Coherent modulation in coupled electro-optomechanical photonic crystal resonators : Floquet dynamics and chaos

Guilhem Madiot

université
PARIS-SACLAY

Coherent modulation in coupled electro-optomechanical photonic crystal resonators: Floquet dynamics and chaos

Thèse de doctorat de l'Université Paris-Saclay

École doctorale n° 572, Ondes et Matière (EDOM)
Spécialité de doctorat: Nanophysique
Unité de recherche: Université Paris-Saclay, CNRS, Centre de Nanosciences et de Nanotechnologies, 91120, Palaiseau, France
Référent: Faculté des sciences d'Orsay,

Thèse présentée et soutenue à Palaiseau le 10/12/2020, par

Guilhem Madiot

Composition du jury:

Emmanuelle Deleporte Professeur, ENS Paris-Saclay	Présidente
Sébastien Hentz Directeur de recherche, CEA LETI, Grenoble	Rapporteur & examinateur
Kien Phan Huy Maître de conférences, FEMTO-ST, Univ. Franche Comté	Rapporteur & examinateur
Lukas Novotny Professeur, ETH Zurich	Examinateur
Ariel Levenson Directeur de recherche, C2N / CNRS	Directeur de thèse
Rémy Braive Maître de conférences, C2N / Univ. de Paris	Invité

Thèse de doctorat

NNT: 2020UPASP076

Remerciements

Je remercie chaleureusement mon encadrant Rémy Braive de m'avoir fait confiance en 2015 pour effectuer un stage au LPN, et de m'avoir renouvelé cette confiance pour poursuivre cette thèse il y a quatre ans. Merci Rémy pour ton investissement inconditionnel et quotidien auprès de tes doctorants, qui contribue largement à notre épanouissement dans cette belle équipe. De la fabrication en salle blanche à la relecture minutieuse de mon manuscrit, en passant par les manips, les analyses, les simulations, tu as su me guider dans chaque étape sans jamais me restreindre.

Un grand merci à Franck Correia qui a débarqué en post-doc à mi-parcours de ma thèse pour rejoindre l'aventure "NOEMS couplés". Nos débats constants, les nouvelles idées ont été, je crois, indispensables à l'aboutissement d'une bonne moitié de ma thèse! Ta bienveillance et ta bonne humeur constante font de toi un collègue extrêmement précieux.

Merci également à mes deux prédécesseurs Viktor Tsvirkun et Avishek Chowdhury pour leurs magnifiques travaux de thèses sans lesquels les miens n'auraient pas été les mêmes. J'en profite pour souhaiter tous mes vœux de réussite à Gladys Jara-Shulz qui débute sa thèse sur les membranes électro-optomécaniques couplées!

Je remercie Sylvain Barbay, qui m'a initié à la dynamique nonlinéaire et souvent (re)mis sur les rails. Je retiens aussi nos nombreuses discussions, qu'elles soient scientifiques ou culinaires.

Merci à Karl Pelka pour son implication dans le développement d'un cadre théorique pour nos expériences en optomécanique. J'ai appris beaucoup de cette collaboration, et ce n'est pas fini! Merci à son encadrant André Xuereb.

Je remercie vivement les membres du jury Emmanuelle Deleporte, Lukas Novotny, Kien Phan Huy et Sébastien Hentz d'avoir pris le temps de lire et évaluer mon travail. Je remercie en particulier les deux derniers cités, rapporteurs de ma thèse, pour leurs questions, suggestions et commentaires enrichissants.

Un grand merci à Julien Chaste pour sa disponibilité et pour m'avoir appris à faire des soudures propres, entre autres.

Merci à Ariel Levenson et à Fabrice Raineri, qui m'ont tout deux régulièrement aidé et conseillé sur des sujets divers et variés.

Merci à tous ceux qui m'ont aiguillé, conseillé et corrigé durant les très longues heures en salle blanche, et en particulier à Abdou Harouri, Dorian Sanchez, Laoges Thao, Alan Durnez et Stéphane Guilet. Merci également à Medhi Idouhamd et Alain Péan, pour leur efficacité au service informatique. Merci au personnel administratif et de la direction du C2N et, en particulier, à Joelle Guitton. Un grand merci au personnel d'entretien de nos lieux de travail.

Durant trois de mes quatre années de thèse, j'ai eu de plaisir d'enseigner au département d'optique de l'IUT d'Orsay. Je remercie donc vivement Loic Rondin pour sa confiance et ses conseils tout au long de cette expérience.

Parce que le temps du doctorat ne se résume par à celui la physique, il me faut également remercier ceux qui ont rendu cette aventure vivante, exaltante et qui, à bien des égards, m'ont simplement permis d'appréhender chaque jour sereinement. En particulier cette sérénité doit beaucoup à la belle ambiance qui, de Marcoussis à Palaiseau, règne dans mon bureau. Ainsi je remercie mes amis "co-bureaux" Quentin, Francesco et Giuseppe, mais aussi David, Maxime, Mathias, John, Loredana, Bruno, Robert, Léa, Malik, Gabriel, Anirudh, Federico, Alexandre et à l'ensemble du groupe TONIQ pour les rapports amicaux qui l'animent.

Un grand merci à mes collocs Minou, Sylvain, Antoine et Thomas pour les moments inoubliables passés à la Mastoc. Merci à mes parents, à mes frères et sœurs, à mes amis, pour leur soutien tout au long de mes études et pour les beaux moments passés, présents et futurs. Enfin, un grand merci à Cynthia pour sa présence à mes côtés depuis maintenant quatre ans.

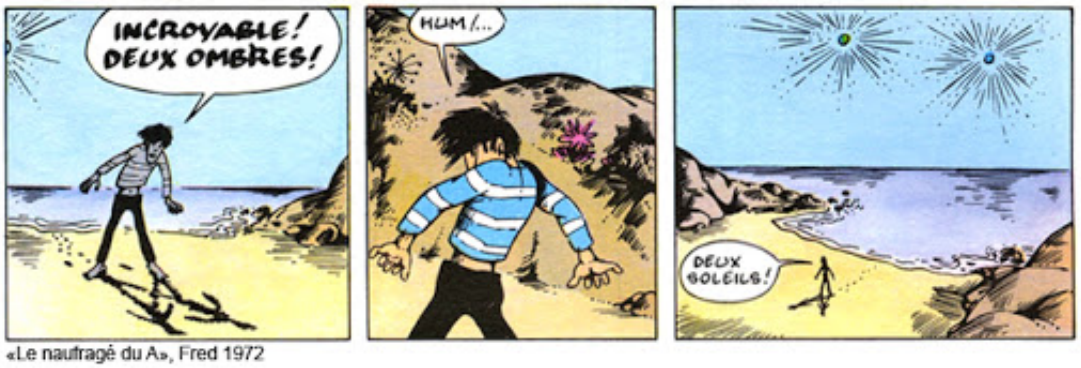

«Le naufragé du A», Fred 1972

Contents

Chapter 1

General introduction

1.1 From single to coupled resonators

A resonator is an oscillating system whose response exhibits an enhancement when periodically excited close to a particular frequency: the *resonant frequency*. From the description of tidal forces involved in the Earth/Sun/Moon system [Garrett, 1972] to nuclear magnetic resonance [Rabi et al., 1938], through musical instruments, resonance is omnipresent in nature. This ubiquity is extremely fruitful when it comes to making analogies between very different systems. At this point all we need to know about a resonator is that, in its simplest picture, it can be described with two quantities. The first is the resonance frequency, or natural frequency, Ω, and the second its quality factor, or Q-factor, Q. The latter is a dimension-less quantity defined by the ratio of total energy stored in the system by energy loss per oscillation cycle. Alternatively, one can write $Q = \Omega/\Gamma$ with Γ the spectral linewidth of the resonance. The Q-factor gives an important indication on the dissipative aspects of a resonator: the more isolated from the environment, the higher its Q-factor. If by any physical process two resonators are capable of influencing each other, they are said to be *coupled*. In this preliminary discussion, we specifically focus on the case of a pair of coupled resonators with the same nature.

1.1.1 Normal modes

The simplest model for coupled resonators uses driven harmonic oscillators acting on each other via a restoring force. Two well-known examples for which this model applies are given in fig. 1.1: a pair of masses linked by a spring, or two capacitively coupled RLC circuits. The schematics feature the subsystem properties: mass and spring constant in the first system, and resistance, capacitance and inductance in the second. In both examples the coupled resonators share their intrinsic properties into new resonances

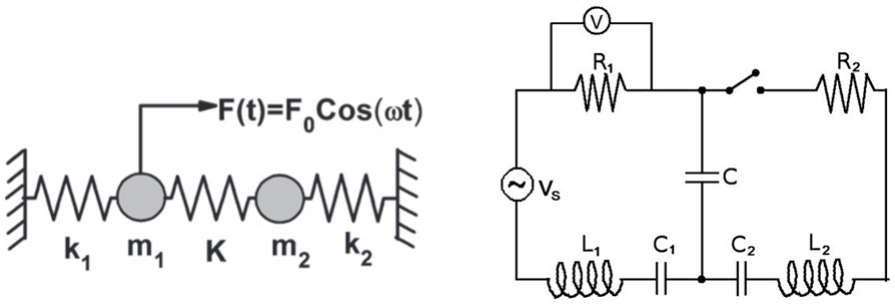

Figure 1.1 – Two examples of driven coupled harmonic oscillators: spring-coupled masses (left) and capacitively coupled RLC circuits (right). Schematics taken from [Satpathy et al., 2012].

called the *normal modes*. Thus even if the subsystems have exactly the same natural frequency, the whole generally displays two distinct resonances with spectral positions and linewidths given by the subsystems frequencies, dissipation rates and by the coupling strength. Each normal mode is a mixture, or *hybridization*, of the original uncoupled eigenmodes. This phenomenon can be visualized with two simple pendula whose masses are linked by a spring (see fig. 1.2). Here, the system normal modes correspond to an in-phase or an out-of-phase motion of the masses, respectively referred as the symmetrical and the anti-symmetrical modes.

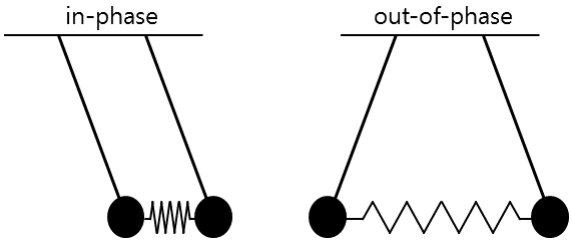

Figure 1.2 – Normal modes of two pendula coupled with a spring.

This model will be the corner stone of our experiments. Expressed in the appropriate formalism, depending on whether optical or mechanical resonators are used, the eigenmode analysis of the systems can always be interpreted with this simple approach for sufficiently weak driving force. For higher driving force, the system enters into nonlinear regimes inherent to all physical systems.

1.1.2 Nonlinear resonators

A resonator can display a nonlinear response when strongly excited or when highly interacting with its environment. Among the typical effects produced by nonlinear resonance,

bistability is quite emblematic. This refers to the situation where there exist two stable states at which the system can find an equilibrium. Bistability is often caused by a dependence of the resonator's natural frequency on its response amplitude, as commonly described in optics through the Kerr-type nonlinearities [Braginsky et al., 1989] or equivalently in mechanics and electronics with the Duffing model [Lifshitz and Cross, 2009]. Chaos is another possible dynamical regime emerging in a driven oscillator. It appears when the oscillation becomes fully unstable and somehow never finds an equilibrium. In these circumstances, the dynamics is simultaneously deterministic and completely unpredictable beyond a certain temporal horizon. These kind of regimes persist and generalize when several oscillating systems are coupled. All these aspects are encored in the study of nonlinear dynamical systems. This large field of mathematics finds applications in all fields of science. Coupled nonlinear oscillations are studied to understand and, possibly, to take advantage of their complex dynamics, as testified by the large theoretical corpus covering the topic (see for example [Kozłowski et al., 1995; Wirkus and Rand, 2002; Kenfack, 2003]).

To experimentally explore these systems, it is necessary to conceive reproducible resonant systems displaying reasonably fast dynamics. Moreover they must be sufficiently nonlinear and accurately controllable. All these conditions are fulfilled at the nanometer scale. Additionally, and although this mays sound obvious, nanoresonators are small. This implies that they can be assembled in arrays gathering a lot a structures all coupled to each other. This is a great advantage for the study of collective behaviors, like synchronization [Acebrón et al., 2005] or pattern formation [Acebrón et al., 2005; Abrams and Strogatz, 2004]. However, as for any kind of experimental system, the growth of complexity must be progressive. Thus it seems essential to focus on the coupling mechanisms dictating the dynamics of a pair of resonators before considering larger arrays.

1.1.3 Other motivations

The use of coupled resonators presents other multiple interests. For example, in the last years, the study of exceptional points has pointed out the rich potential of coupled linear resonators whose properties are correctly related [Miri and Alù, 2019]. Such phenomenon nonetheless requires a fine control of the subsystem properties. Indeed the subsystems do not necessarily have the exact same intrinsic natural frequencies and Q-factors, which can lead to many configurations leading to behaviors ranging from subtly to considerably different. These behaviors spark many classical analogies with quantum effects studied in atomic physics, like Rabi oscillations [Spreeuw et al., 1990; O'Connell et al., 2010], Fano resonances [Satpathy et al., 2012] or electromagnetically induced transparency [Liu et al., 2016].

Interestingly a resonator can be put in interaction with additional degrees of freedom,

in which information can be stored or modified. For example a mechanical or optical resonator can be used to mediate the state of a quantum dot [Yeo et al., 2014; Najer et al., 2019]. Permitting several of these resonators to couple can add another level of complexity by enabling the quantum information to be coherently transferred. The strong coupling regime, in which the energy is transferred between the resonators faster than it is dissipated, is ideal for such operation [Niemczyk et al., 2010; Okamoto et al., 2013; Pernpeintner et al., 2018].

1.2 Nanomechanical resonators

The mechanical properties of nanometer scale systems are the object of intense research anchored in the field of nanomechanics. With the technological progresses in micro and nano-fabrication within the last two decades, it is now possible to realize nanomechanical resonators sustaining frequencies ranging from the kHz to several tens of GHz, and displaying very high quality factors. These aspects offer a unique opportunity to study the motion at the mesoscale, halfway between the classical and quantum worlds. Moreover, the elastic properties of a material are often intrinsically related to its thermal, optical and electrical properties. Therefore, nanomechanical resonators are generally useful in metrology, allowing high sensitivity measurements of motion [Mason et al., 2019], mass [Chaste et al., 2012], force [Rugar et al., 2004], torque [Wu et al., 2017], and so on. This also explains the transdisciplinarity of nanomechanics from physics to other fields, like biology [Tamayo et al., 2013].

1.2.1 Electromechanical systems

The integration of electrostatically actuated mechanical devices has enabled the proliferation of micro and nano electromechanical systems (MEMS and NEMS) in on-board technologies, mostly for sensing operations. Thus a smartphone typically uses about ten MEMS enabling continuous accelerometry, magnetometry or gyroscopic motion measurement. More importantly, nanomechanical resonators are subject to many intrinsic nonlinearities due to their high aspect-ratio. Finally, they are tunable, i.e. there exist a panel of methods enabling fine control of the resonator properties [Zhang et al., 2015]. Beside this wide field of technological applications, the NEMS are also very useful for the examination of nonlinear dynamics. They are also easily integrable with magnetomotive, piezoelectric or electrostatic actuation. These aspects simply permit to realize nonlinear dynamics experiment in an acceptable timescale, with high accuracy and reproducibility. The stiffness of a resonator – its ability to resist at an elastic deformation – is very likely to be nonlinear in a nanomechanical system. This implies that a sufficiently high displacement is likely to modify the resonance frequency. In consequence, the amplitude

response of the strongly-driven system can exhibit bistability [Antoni et al., 2012]. While this kind of effect is generally undesired in the NEMS industry, it also present numerous interests for sensing [Venstra et al., 2014], memory [Bagheri et al., 2011], or amplification applications [Chowdhury et al., 2017, 2020], for example.

1.2.2 Optomechanical systems

The momentum carried by light can displace matter. This *radiation pressure* force can be exploited, for example, to trap and cool atoms in an optical tweezer [Ashkin, 1970; Ashkin et al., 1986]. On larger objects however, this effect is mostly negligible, thus a hiker's speed is usually not modified whether he or she is facing the sun or not. It is possible to enhance this effect using optical cavities such that the mechanical eigenmodes of macroscopic objects can be driven [Dorsel et al., 1983] or cooled [Cohadon et al., 1999]. These two examples rely on a Fabry-Pérot cavity made of two mirrors of which one is fixed while the other is free to move, as schematized in fig. 1.3. Here, the intracavity field, fed by a laser, pushes the movable mirror via the radiation pressure force. The frequency difference between the laser and the cavity resonance – the laser detuning – is modified if the cavity length is altered which results in a change of the force. Thus with this simple mechanism, the optical and mechanical resonators are coupled, as they mutually influence each other. This representation is commonly used to depict an optomechanical cavity and the associated coupling mechanisms [Aspelmeyer et al., 2014]. Note that we do not refer an optomechanical cavity as a matter of "coupled resonators" as it involves two resonators that do not have the same nature and operate in very different frequency domains. Dynamical backaction occurs in an optomechanical cavity when the photon lifetime κ^{-1} in the cavity is of the order of the mechanical oscillation period Ω_m^{-1} [Braginski and Manukin, 1967]. This condition enables a delay dynamics to take place between the motion and the intracavity intensity. It can be exploited to coherently remove or add energy to the mechanical resonator, depending on the laser detuning. In electromagnetic micro-resonators, the high photon lifetime and the small mode-volume enable highly nonlinear physics to be studied. In particular, the strong co-localization of photon and phonon modes permits to reach highly efficient optomechanical interactions. Thus the quick development of micro-resonators in the 2000's has brought a huge contribution to optomechanics as many of the proposed photonic devices are also the center of phononic modes. We show some typical devices in fig. 1.4: i) a micro-torroidal resonator [Verhagen et al., 2012] operating in the near-infrared domain; ii) a superconducting LC circuit operating in the microwave domain [Teufel et al., 2011]; iii) a single-crystal diamond microdisk where NV color centers quantum states can be manipulated trough the spin-strain interaction [Mitchell et al., 2016]; iv) a levitated liquid Helium drop enabling ultra-strong optomechanical coupling regime [Childress et al., 2017] or v) a Bragg micropillar

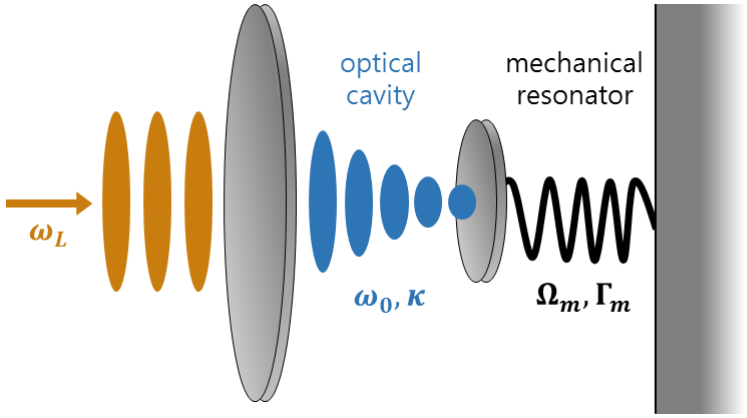

Figure 1.3 – schematic of an optomechanical cavity. A laser (orange) injects an optical cavity formed by two mirror whose one is fixed (left) while the other is movable (right). The intracavity field (blue) can thus mechanically act of the latter

resonator sustaining 300 GHz phononic modes [Esmann et al., 2019]. These system are very different but nonetheless share the same feature of enabling a high Q/V[1] optical mode to be strongly confined to the vibrational eigenmodes of the system. It turns out that photonic crystals are particularly well adapted in this purpose.

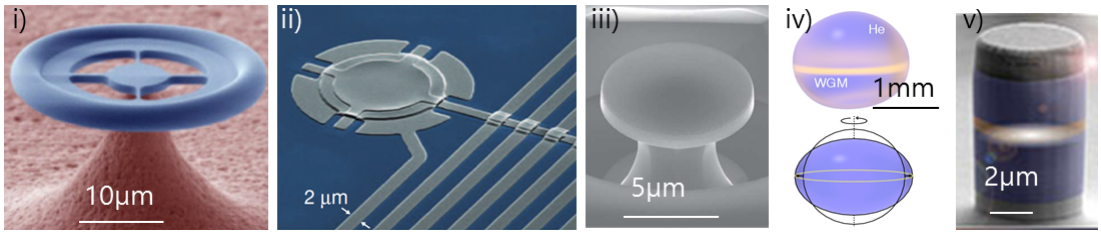

Figure 1.4 – Few examples of optomechanical systems: i) [Verhagen et al., 2012], ii) [Teufel et al., 2011], iii) [Mitchell et al., 2016], iv) [Childress et al., 2017] and v) [Esmann et al., 2019].

1.2.3 Photonic crystals for NOEMS

A photonic crystal (PhC) is a periodic dielectric structure in which the electromagnetic waves can not propagate at some particular frequency ranges. These forbidden spectral bands, or *photonic band gaps*, are extremely useful to control the electromagnetic radiation propagation in materials [Joannopoulos et al., 2008]. Dielectric periodicity along one, two or three spatial directions are commonly refereed as 1D, 2D and 3D PhC. While the latter case remains barely studied due to fabrication constraints, 1D and 2D PhC are nowadays commonly used for a large panel of applications including photonic waveguides

[1] Q/V: Q-factor to mode volume ratio

[Johnson et al., 2000], optical fibers [Russell, 2003], microcavities [Vahala, 2003] and mirrors [Lousse et al., 2004]. The latter two items are particularly interesting for the following discussion.

Suspended photonic crystals use the total internal reflexion along at least one dimension (two for the nanobeams) in order to confine light. The high index contrast between the material and the surrounding air guarantees the spatial confinement over this axis, the other two being imposed by the photonic crystal. This configuration is particularly useful for realizing NOEMS devices as the suspension introduce the needed mechanical degree of freedom. One strategy for realizing PhC microcavities consist in the insertion of defects in a well defined PhC structure. The crystal must be designed such that the desired resonance frequency lies in the photonic band gap. Then, by artificially inserting a defect in the crystal definition, one locally allows the light to propagate in the material at a frequency originally forbidden. By engineering the photonic crystal design as well as the defect, it possible to create extremely localized photonic modes showing high Q/V ratio. This strong confinement is at origin of many nonlinear light-matter interactions, including radiation pressure forces used for cavity optomechanics experiments.

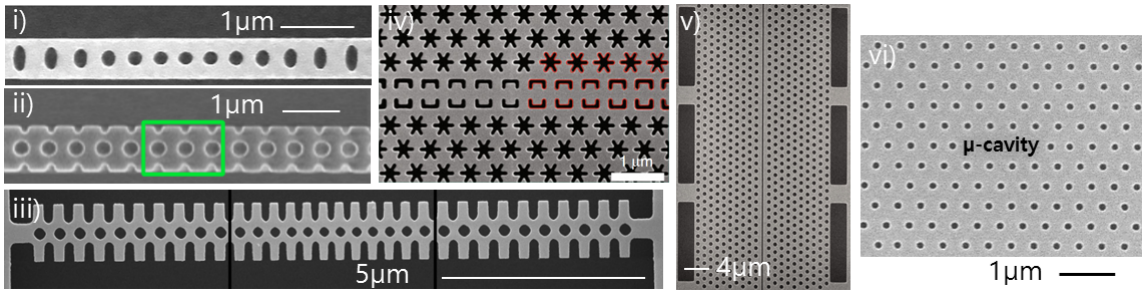

Figure 1.5 – Optomechanics systems using specifically photonic crystal microcavities i) [Chan et al., 2012a], ii) [Ghorbel et al., 2019], iii) [Navarro-Urrios et al., 2014], iv) [Ren et al., 2020] and v) [Safavi-Naeini et al., 2010]. vi) Adopted design for the following study.

Among the very rich literature dealing with photonic crystal optomechanics, we show few designs in fig. 1.5. In 1D photonic crystal nanobeams, the optical field is confined by total internal reflexion along two directions. The defect can be introduced via the apodization of the design alone the third direction. This is consist in smoothly changing the hole shapes, the crystal spacing or the hole sizes towards the center of the microcavity. Respective examples are shown in i) a silicon nitride nanobeam mechanically isolated by a phononic crystal shield [Chan et al., 2012a]; ii) a GHz piezoelectric nanobeam resonator showing low phase noise self-sustained oscillations regime [Ghorbel et al., 2019]; iii) a *phoXonic crystal* nanobeam [Navarro-Urrios et al., 2014]. This novel approach consists in gathering the concept of photonic crystal and phononic crystal in a same device. The phoXonic crystals can trap phonons and photons in a very small volume, such that

the electromagnetic field and mechanical distributions efficiently overlap. The 2D photonic crystals are less commonly used in optomechanics experiments. Two examples are shown here with iv) a 2D crystal combining photonic and phononic bandgaps thanks to the *snowflake* lattice [Ren et al., 2020], v) a high-optical Q optomechanical cavity using a triangular lattice of holes [Safavi-Naeini et al., 2010], vi) L3 defect cavities used in hybrid optomechanical devices [Gavartin et al., 2011; Tsvirkun et al., 2015].

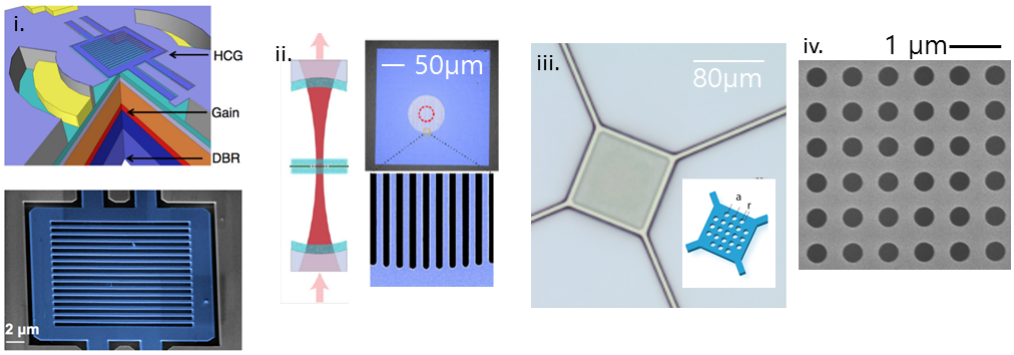

Figure 1.6 – Optomechanics with suspended photonic crystal reflectors: i) [Yang et al., 2015]; ii) [Stambaugh et al., 2015]; iii) [Norte et al., 2016] and iv) [Antoni et al., 2011]

Photonic crystals can also be used for the realization of highly reflective micro-mirrors. Suspended membranes equipped with a 2D photonic crystal fill both mechanical and optical requirements for achieving optomechanical and electromechanical experiments. For example in fig. 1.6 we show examples where suspended photonic crystal membranes are used for building i) an optomechanical laser [Yang et al., 2015], ii) a "membrane-in-the-middle" experiment [Stambaugh et al., 2015] or iii) achieving optomechanical cooling of a trampoline resonator [Norte et al., 2016]. iv) An engineered square lattice of holes enables both out-of-plane reflectivity enhancement – the surface is structured to act as a mirror in a specific spectral range – and mass reduction of the membrane [Antoni et al., 2011; Makles et al., 2015].

1.2.4 Coupled nanoresonators in the literature

This is a large topic, here we show several examples of experimental realizations in which resonators are coupled, for either applicative or fundamental research purposes in the frame of NOEMS. In the optical domain, coupling is usually achieved using the exponentially decaying intensity field leaking off the resonators, or *evanescent field*. in fig. 1.7a, we show i) two waveguide-coupled enclosed micro-ring resonators enabling optical filtering operations [Hryniewicz et al., 2000]; ii) two 1D PhC nanobeams separated by a thin air-gap [Deotare et al., 2009]; and iii) A 2D photonic crystal molecule made of two engineered defect cavities for coupled nanolasers investigation [Hamel et al., 2015]. The

last example involves iv) three to five coupled micro-disks enabling the synchronization of micromechanical oscillators [Zhang et al., 2012].

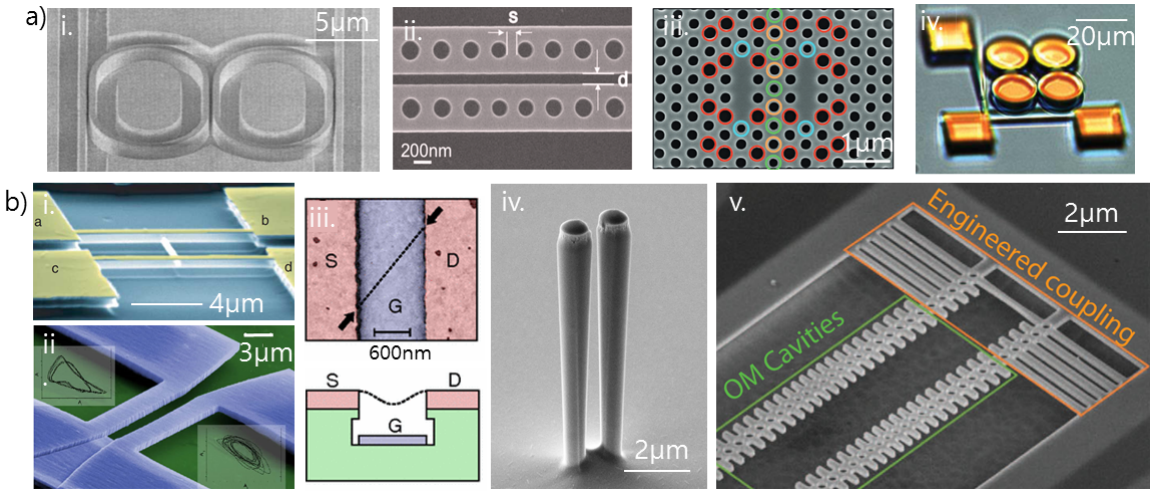

Figure 1.7 – Few examples of coupled optical cavities a.i) [Hryniewicz et al., 2000], ii) [Deotare et al., 2009], iii) [Hamel et al., 2015] or coupled mechanical resonators b.i) [Shim et al., 2007], ii) [Karabalin et al., 2009], iii) [Eichler et al., 2012] , iv) [Doster et al., 2019] and v) [Colombano et al., 2019]

In the mechanical domain, there also several realizations of coupled nanoresonators. Few examples are show in fig. 1.7b. The most common approach consists in coupling suspended nanobeams, either using i) a physical junction [Shim et al., 2007] or ii) strain coupling at the clamping regions [Karabalin et al., 2009]. Under certain condition it is also possible to perform internal mode coupling within a unique resonator. For example in iii) two eigenmodes belonging to the same carbon nanotube interact via internal nonlinearities [Eichler et al., 2012]. Internal coupling can also be caused by internal strain [Faust et al., 2012]. Strain coupling can be used in other geometries such as iv) nano-pillars [Doster et al., 2019]. Finally, we show v) two mechanically coupled photonic crystal nanobeams [Colombano et al., 2019]. The engineering mechanical coupling permits two optomechanical cavities to synchronize. Here we exclusively showed situations where the coupling is caused by purposely connecting two nanomechanical systems.

Ultimately in [Lin et al., 2010] the concepts of mechanical and optical coupling are gathered on the same structure between two optomechanical cells, enabling profound analogies with atomic physics. More generally, bi-dimensional optomechanical crystals are structures combining phononic and photonic band gaps to manipulate a large number of optomechanical degrees of freedom [Safavi-Naeini and Painter, 2010].

1.3 Our systems of study

In this thesis, we use coupled optomechanical or electromechanical resonators in the study of nonlinear dynamical regimes. We focus on suspended bi-dimensional photonic crystal rectangular membranes, in line with previous doctoral researches focusing either on optomechanics [Tsvirkun, 2015] and on electromechanics [Chowdhury, 2016]. With the novel design adopted in each case, coupling is obtained respectively in the optical domain or in the mechanical domain.

1.3.1 Design

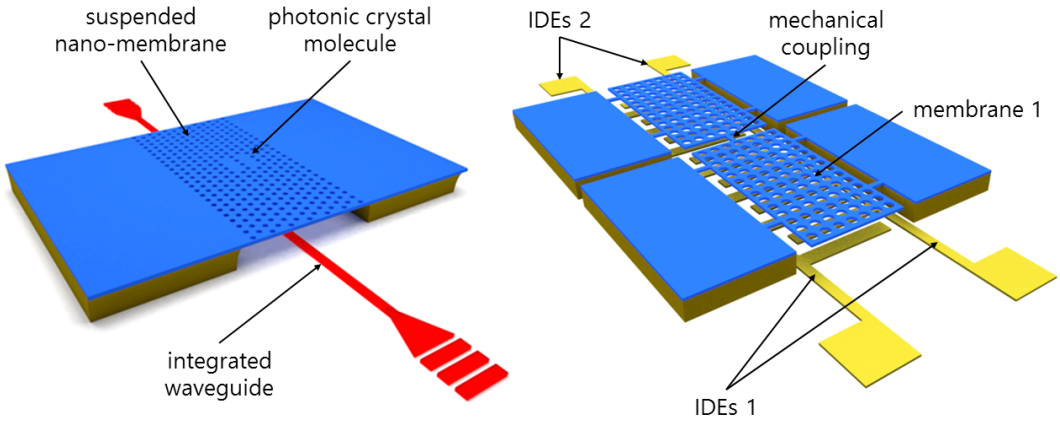

Figure 1.8 – Designs of a) the optomechanical and b) of the electromechanical integrated platforms.

To be more concrete, the first system consists in an hybrid optomechanical system made of a suspended InP nano-membrane with an integrated SOI waveguide underneath. Here we propose to use *photonic crystal molecules* instead of a single defect-cavity, in order to read-out the Brownian motion of the membrane (see fig. 1.8a). Here the concept of coupled resonator is thus introduced in the optical domain, between at least two micro-resonators. The system is probed by injecting light at the waveguide input and analyzing the waveguide transmission. The circulating field evanescently couples to the defect cavities such that mechanical noise, optomechanically transduced in the optics, can be measured.

The second system is based on a very similar nano-mechanical resonator. However, the InP nano-membrane is now electro-capacitively driven by a pair of gold interdigitated electrodes on which a voltage is applied. In opposition with first system, the motion is now resonantly driven. Thus it reaches much higher amplitudes, up to a nonlinear regime. Here we want to duplicate the system and add a junction between the resonators (see

fig. 1.8b). The coupling therefore operates in the mechanical regime. The mechanical motion is accessed by optomechanically probing the Fabry-Pérot cavity defined between the substrate and the photonic crystal membrane (see fig. 1.6 image iv.).

Beside numerous conceptual similarities, including in their design and fabrication developments, these systems rely on distinct physical processes, which is why they are mostly treated independently in this manuscript.

1.3.2 Clean-room fabrication process

The fabrication of our nano integrated platforms is described in this section. The electromechanical (EM) and the optomechanical (OM) platforms are based on the same process. When necessary, the specifications of one design will be pointed out. The entire process can be summarized in three important steps : the BCB heterogeneous bonding, the electron-beam lithography of the photonic crystal and the InP etching using ICP[2] technique.

1.3.2.1 Choice of indium Phosphide

Indium phosphide is a III-V semiconductor. This material is commonly used for the fabrication of integrated telecom-wavelength active photonic devices, taking advantage of its direct band-gap for embedding quantum wells or quantum dots in the InP layer. Already used for the realization of photonic crystal nanolasers in our clean-room facilities [Halioua et al., 2010; Marconi et al., 2016], this material was chosen for the conception of optomechanical photonic crystal membranes regarding the well mastered technological aspects involving this material. In the optomechanical experiments, we actually take benefits from an InGaAs quantum dots layer for technical purposes, like the optical fiber alignment procedure. Although we do not investigate this aspect in the following work, the quantum dots can also be at the center of interesting dynamics involving the optomechanical aspects of our system [Tsvirkun et al., 2016].

1.3.2.2 Improvements of the clean room process

The optimization of most of the stages in the following process was realized during the previous PhD projects in our group. Although the general picture stays unchanged, the process has been consequently improved by combining two e-beam lithography steps into a single one. The photonic crystal (PhC) pattern was indeed defined in a first place using a PMMA positive resist. This implied to transfer the PhC pattern to an additional SiN sacrificial layer. Then, the PhC pattern was transferred to the III-V layer using ICP etching. A second e-beam lithography was achieved to define the mechanical structures

[2] ICP : Inductively Coupled Plasma

followed by a second ICP etching. Gathering these two step offers several advantages. First, because the PhC and the mechanical support are defined at one, any misalignment of these elements is rejected because only one e-beam lithography alignment procedure is now necessary. The current design is also time saving and therefore less expensive.

Furthermore, the structures release was obtained using wet chemical under-etching combined with critical point drying technique. We have optimized a dry etching technique using an isotropic plasma allowing to overcome the critical step of suspended structure in liquid medium.

1.3.2.3 IDEs fabrication

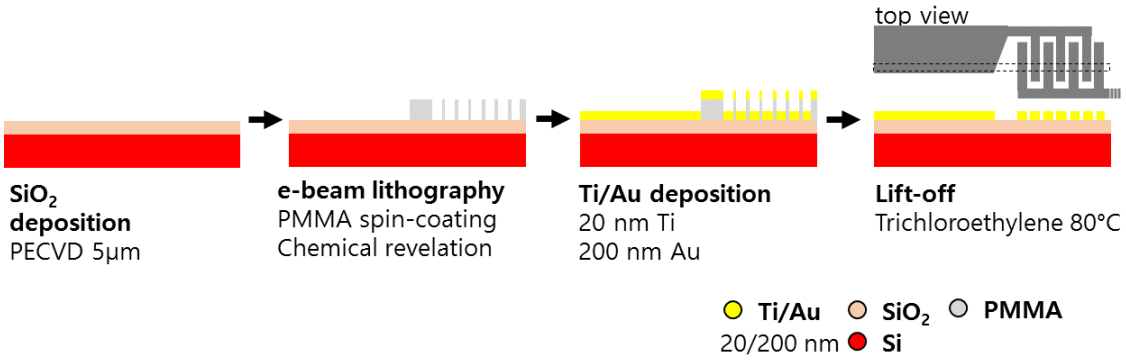

Figure 1.9 – fabrication of the gold interdigitated electrodes

The main difference between the OM and EM fabrication processes is the platforms' basis. The SOI waveguides used for the optical access of the OM cavities are designed and fabricated by LETI. However, the interdigitated electrodes (IDEs) that we require for the coupled NEMS actuation are designed and fabricated in our group. The IDEs process (see fig. 1.9) relies on an electron beam lithography of a PMMA positive resist. The silicon substrate is preliminary cleaned with acetone in an ultrasound bath. A few microns thin SiO_2 layer is deposited by PECVD[3] to electrically isolate the IDEs from the substrate. A A7-PMMA positive resist is spin coated on the chip and insolated with the electron beam. The mask is generated with a 1 nm resolution, which is enough given the mask requirements. Indeed the minimum separation between the pair of IDEs is 1 µm. The insolated resist is chemically removed in a MIBK/IPA[4] (1:3) solution. The remaining resist that might have stayed in the tight area, typically at the IDEs regions, is removed in a 0_2 plasma. The chip surface is metallized with 20 nm of titanium and 200 nm of Gold. The titanium allows a better adherence of the electrodes on the SiO_2 surface. Finally, the remaining (not insolated) PMMA resist is removed with thrichloroethylene.

[3]PECVD : Plasma-Enhanced Chemical Vapor Deposition
[4]IPA : Isopropanol

1.3.2.4 Heterogeneous integration: InP membrane on SOI

The epitaxial InP layer transfer onto the SOI waveguides circuit is an essential part of the process. Both EM and OM devices require a fine control of the gap between the InP membrane and the substrate. In the first case, this gap directly tunes the electromechanical coupling, i.e. the efficiency of the electro-capacitive force exerted by the IDEs of the membranes. In the second case, the external coupling between the defect cavities and the waveguide is extremely dependent on this distance, making its control even more critical. One NEMS chip contains many structure, about 10 systems for the NEMS samples, and up to 320 for the SOI waveguides based OM systems. These structures are spread out over basically 1 cm^2. It is therefore necessary for the bonded III-V substrate to be perfectly parallel to the bottom plane.

The III-V substrate consists in an epitaxial InP layer (265 nm) grown on top of an thin etch-stop InGaAs layer (1 µm). This last is encapsuled between the layer of interest and a thick InP substrate. In order to allow suspension of the InP structures, and to control the air gap depth, a SiN sacrificial layer is deposited by PECVD.

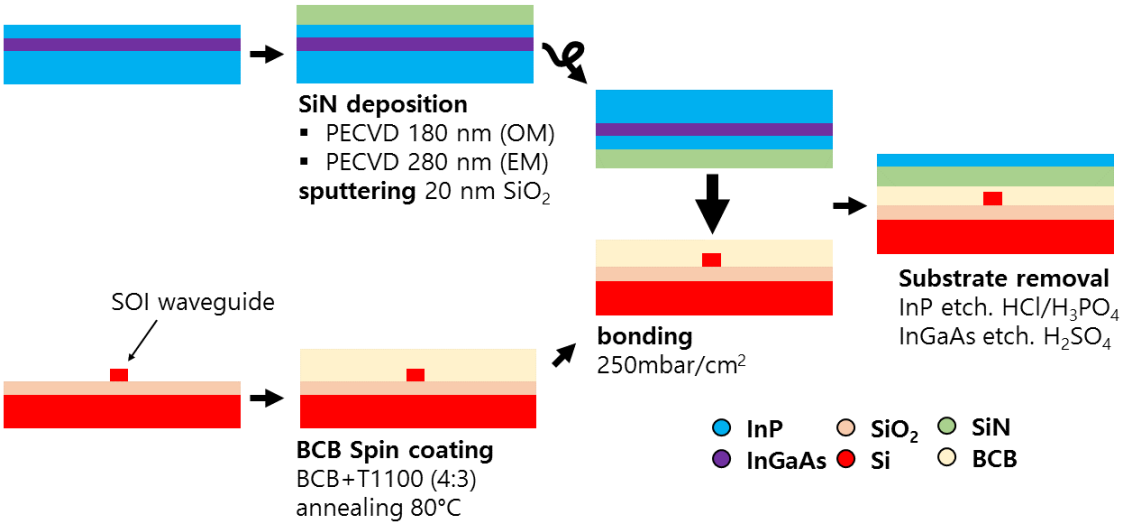

Figure 1.10 – III-V BDB bonding on top of SOI waveguides

The heterogeneous integration of our III-V substrate on top of the SOI waveguides can be achieved by employing divinylsiloxane-disbenzocyclobutene (DVS-BCB) (see fig. 1.10). Diluted in mesitylene, this polymer provides an adhesive that matches with our high degree of planarization condition. It is also convenient for its high resistance to chemical/physical etchings that will be performed in the next steps of the process. Finally, DVS-BCB is transparent in the telecommunication wavelengths, which is essential for the SOI waveguides refractive indexes contrast requirements. The solution of BCB-T1100 (4:3) is spin coated on the SOI chip and annealed at 80^{o}C.

The III-V substrate is carefully positioned on the region of in interest of the SOI. The whole is placed in the bonder, between the bottom metallic plate and a top plexiglass press. After the vacuum is obtained in the machine, the sample is brought to 320^{o}C for the BCB to melt. Then a 250 mbar/cm^2 force is applied on the chip for about two hours. Finally, the temperature and pressure are both slowly ramped back to ambient conditions. After the bonding, the BCB layer is as small as 30 nm. This value should be added to the SiN layer thickness in order to obtain the air gap height.

The III-V substrate is removed by HCl chemical etching. The InP crystalline planes can be anisotropically etched by using a HCl/H_3PO_4 (3:1) solution. Eventually, this can be helped by using convective agitation of the solution. It takes approximately 2h30 for the full substrate etching to be done. Once the InP substrate is removed, the etch-stop InGaAs layer is etched with a $H_2SO_4/H_2O_2/H_2O$ (3:1:1) solution.

1.3.2.5 Photonic crystal drawing

The e-beam lithography of the mechanical resonators is done with hydrogen silsesquioxane (HSQ) as a negative resist. For the resist adherence on the InP surface to be improved, a 5 nm thick SiO_2 layer is deposited with PECVD. The sample is thermalized at 160°C before the spin coating. The HSQ XR-1541 6% resist is spin-coated on the sample. The obtained HSQ film thickness is theoretically of the order of 100 nm after annealing.

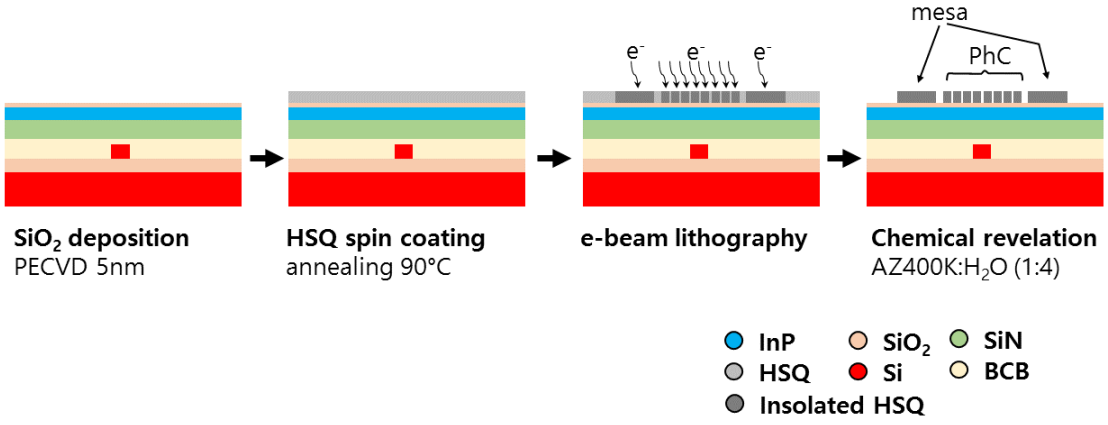

Figure 1.11 – Single e-beam lithography step using negative HSQ resist

The quality of the photonic crystal is critical for the photonic properties. The cylindrical holes are treated by the lithograph as a serie of successive rings. Another crucial point is the alignment of the structure with either the waveguides or the electrodes. A resolution of about 40 nm is possible thanks to markers previously drawn on the sample. Once aligned, the sample is exposed to the electron beam. A solution of diluted AZ400K

(1:4) is used for the revelation. The surface is observed with a SEM[5] to check the PhC holes quality and the alignment.

The HSQ mask is transferred to InP by ICP etching (see fig. 1.12). This step is achieved with a 600 W $HBr/O_2/He$ $(8/0.4/40)$ plasma. Here again, we ensure the quality of the mask transfer by observing the sample in the SEM. The remaining HSQ and SiO_2 is removed by chemical etching into a 10% AF solution for 2 minutes. This etching time is critical since a longer time might allow the AF solution to etch the SiN layer and therefore initiate the under-etching of the mechanical structures.

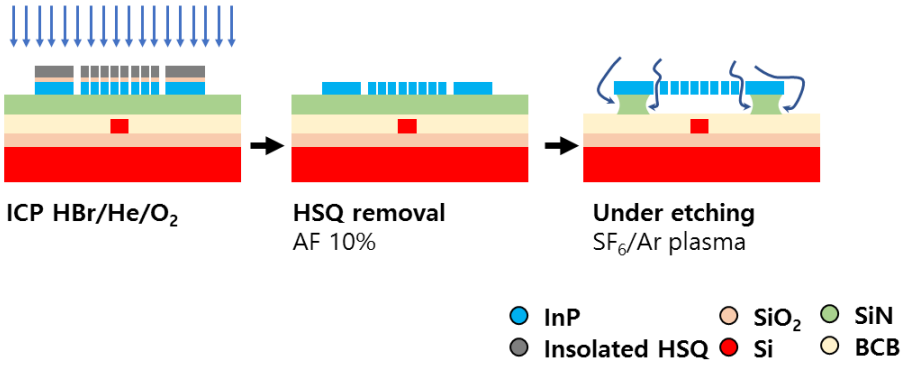

Figure 1.12 – InP etching using ICP and dry under-etching

1.3.2.6 Membrane release

The final clean-room process to be achieved is the release of the micro membranes. The very short air-gap ($\approx$ 300 nm) under the micro-membranes leads to important surface effects during the evaporation of any liquid phase surrounding the mechanical system. Ambient conditions evaporation would lead the membranes to be brought to the underneath plane and sticked to it by van der Waals interactions. To overcome this and as discussed above, the previous samples were submitted to a 10% AF solution for 15 minutes in order to remove the SiO_2/HSQ layers and to underetch the mechanical membranes. The chip was transferred into an IPA solution and then placed in a supercritical dryer. A dry underetching technique has been preferred for this work. We use a SF_6/Ar (50 sccm:10 sccm) plasma generated at 500W. At this point, the mechanical structures must be underetched and the clean room process is ended. For each system of study, the final configuration is shown with a schematic on figs. 1.13a and 1.13b with an example of colorized SEM image.

[5]SEM : Scanning Electron Microscope

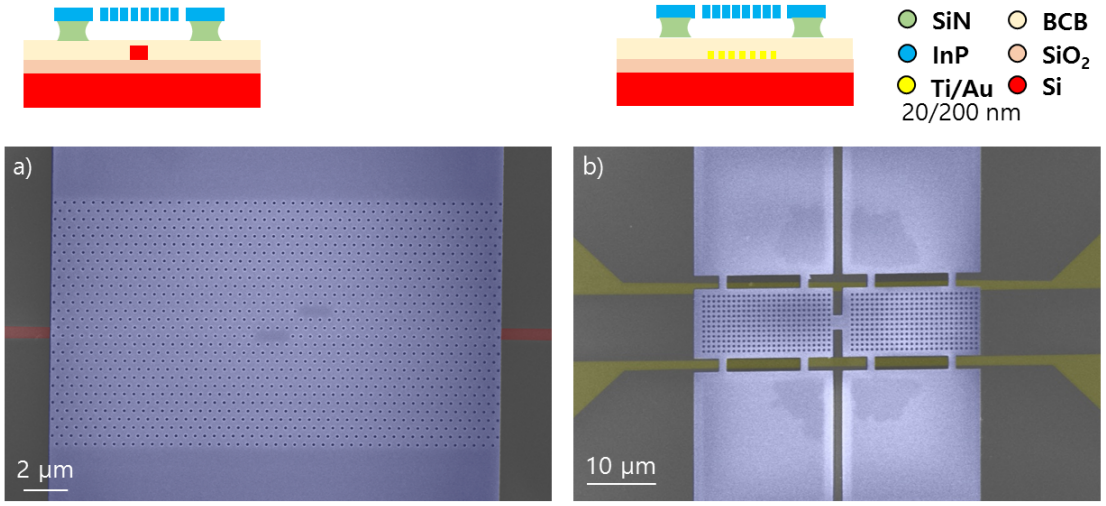

Figure 1.13 – Colorized SEM images a) Suspended PhC molecules with two defect cavities (blue) and integrated SOI waveguide (red) b) Pair of suspended PhC membranes mechanically coupled with a rectangular junction (blue) and underneath independent pair of IDEs (yellow).

1.3.3 Manuscript organization

The experiments realized on the fabricated devices are detailed in the following five chapters. They are embedded in two parts, one focusing on the optomechanical photonic molecule platform (part I), the other being dedicated to the coupled electromechanical membranes system (part II).

The photonic aspects of the optomechanical platform are described in chapter 2. On top of the details concerning the photonic crystal design, we provide a model for the optical modes description based on Coupled Mode Theory (CMT). The integrated waveguide transmission spectrum is theoretically predicted as a function of the system parameters. The different coupling geometrical configurations are discussed with regards to the experimental results. The major nonlinearity arising in the system is the thermo-optic effect is also described theoretically and experimentally in this chapter. The mechanical aspects of the system are discussed in chapter 3. We first focus on the mechanical eigenmodes of the structure. The experimental observation of the mechanical noise spectra compared with the FDTD simulations performed on the structure. The optomechanical interaction, which permits this characterization, is discussed via two different approaches. The first uses a very simplistic model assuming purely dispersive optomechanical processes in the system, thus enabling the single photon optomechanical coupling strength to be measured. Secondly, we model in a more reasonable way the system by introducing the dissipative mechanisms through which the mechanical noise in imprinted in the optics. This way the role for the different contribution can be estimated experimentally. Finally

a toy-model is introduce to account for the thermo-mechanics effects that manifests via a frequency shift of the mechanical modes when the optical modes are resonantly injected. All the optomechanical aspects treated in this chapter show significant discrepancies depending on the probed optical mode. The third and last chapter on this first part treats the nonlinear dynamics experiments performed on this system. Using a periodic modulation of the input laser, we observe Floquet dynamics revealed by the emergence of mechanical sidebands in the noise spectrum. These sidebands becomes more ample and tend to desymmetrize when the input power is increased. Using a theoretical model developed by our collaborators at University of Malta, Karl Pelka and André Xuereb, the phenomenon is understood as a non-trivial multi-timescales dynamics involving the mechanical resonator and a thermo-optic nonlinear photonic mode. In the last experiment, we propose to demonstrate vibrational resonance amplification using the bistability generated by such thermo-optic resonator.

The structure of the second part is comparable to the first. We start by describing fully the system of interest design in chapter 5. This includes the mechanical resonators but also the electro-capacitive actuation and the optomechanical readout description. The theoretical model starts with a pair of driven-coupled-damped harmonic oscillators. The important notions are added to the discussion when needed. The experimental characterization lingers on the measurement of the mechanical properties: frequencies, damping rates and coupling. The latter can be measured by crossing the natural frequencies of the resonators, which we attempt electro-statically and thermo-mechanically. The displacement and force calibrations of the system are performed on a particular device that we re-use exclusively in the nonlinear dynamics experiment. The use of stronger drive leads to mechanical saturation lead by a shift of the mechanical frequency. This nonlinear effect is the cornerstone of this last experimental chapter (chapter 6). Using the Duffing model, that we adapt to suit the coupled resonators, the device is carefully characterized and calibrated in its nonlinear regime. The use of periodic low-frequency modulation of the applied force, we observe a period-doubling cascade route-to-chaos dynamics, in good agreement with the model. The study is realized with the use of adapted tools for the data analysis. In particular, the employment of bifurcation diagrams and the numerical computations of the largest Lyapunov exponent permits to drive these conclusions. The investigation is mainly led via the use of two experimental buttons which are the modulation amplitude and the modulation frequency. This second parameter interestingly reveals the origin of the dynamics to lie in the resonator dissipation rate, which we verify by tuning the pressure of the vacuum chamber, in which the sample is placed. Using a two-drive actuation scheme, the two normal modes of the systems are simultaneously activated. We show, still with help of our Duffing model, that the modes are actually nonlinearly coupled to each other. This orthogonality breaking concretely permits the synchronization of the normal modes amplitude all along the

bifurcation structure. In the chaotic regime, we attentively describe the imperfect phase synchronization of the normal modes via a statistical approach. The final experiment consists in an attempt to characterize the randomness of the binary sequences that one can generate from a chaotic time trace. The details as well the key-aspects of this protocol are examined.

We finally summarize these results and conclude in chapter 7. We also give few perspective that seem interesting with regards to their potential. Supplemental information are shown in the appendix section. Each part ends with a table summarizing all the key notations involved.

Part I

Optomechanics with photonic crystal molecules

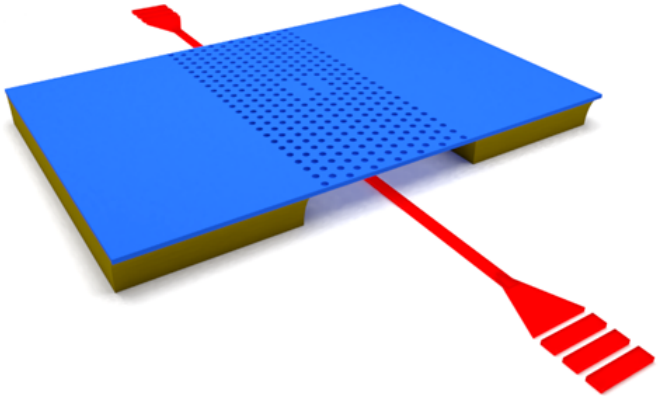

Hybrid integrated optomechanical platform

The hybrid integrated optomechanical platform is studied in this first part. We will first focus on the optical properties of the system in chapter 2. This includes the design of the 2D photonic crystal molecules, made by arranging several defect cavities in clusters allowing them to evanescently couple. The addition of the integrated waveguide to the system permits to drive these localized optical modes which can be modeled though the coupled mode theory. Several geometries are then experimentally observed and discussed. Finally we focus on the thermo-optic nonlinearity which we observe to be the dominating nonlinear effect in this system. In chapter 3 the mechanical properties are investigated via the optomechanical interactions. The simulated and experimental mechanical frequencies are compared. The vacuum optomechanical coupling is estimated for different coupled optical/mechanical mode using a phase-modulation technique. This discussion is deepened to an evaluation of the dispersive and dissipative contributions to the optomechanical coupling. This is possible by scanning the optical resonance while measuring the mechanical mode, which goes with a shift of the mechanical frequency. This shift is discussed using a thermo-mechanics toy-model.

The nonlinear dynamics resulting from the modulation of the input laser field is studied in chapter 4. We experimentally demonstrate how such excitation leads to the transfer of the modulation sidebands from the optical domain to the mechanical domain. The number of sidebands can be increased by driving the system in a thermo-optic nonlinear regime. These unbalanced sidebands amplitudes are sustained with a theoretical framework encompassing these different aspects, namely the optomechanical interactions and the thermo-optic effect. The latter allows to the reach optical bistabilities that are imprinted into the mechanical resonator frequencies through the thermo-mechanic process. Relying on this, we use the mechanical frequency for the characterization of the bistability in preparation of an experiment of vibrational resonance. In this process, a weak-amplitude low-frequency square signal is amplified using a high frequency periodic signal.

Chapter 2

Nanophotonic platform description

In this chapter, we describe the optical properties of the integrated platform. We introduce different configurations for two defect-cavities to couple within a suspended photonic-crystal (PhC). We give a theoretical background for the description of coupled cavities accessed via a waveguide through the coupled mode theory. The photonic molecules are then experimentally characterized. Finally we give a description of the thermo-optic effect which is the dominant nonlinear process standing in this system.

2.1 Photonic platform design

Most of the optimization for the photonic crystal geometry is learned from previous research in the lab [Tsvirkun, 2015]. The key-elements are given at first, followed by an extension towards photonic molecules made of several defect cavities enclosed in the same crystal.

2.1.1 Single L3-defect cavity

The periodic arrangement of the refractive index in a dielectric material leads to a band structure of the material dispersion diagram. In particular this concept can be exploited for manipulating the light at the nanoscale. A 2D photonic crystal (PhC) corresponds to a periodicity over two spatial directions while the dimension of the material in the 3rd direction is reduced below the optical wavelength thus allowing total internal reflection in the membrane. The latter is made of a 260 nm thick indium phosphide (InP) layer with refractive $n_0 = 3.16$ [Pettit and Turner, 1965] thus enabling a high index contrast. In our system, a triangular lattice of cylindrical holes allows the insertion of an optical band-gap in the near-infrared domain.

Several types of defect can be inserted in the PhC lattice allowing an optical state to exist in the optical band-gap. The line defects are achieved by removing consecutive

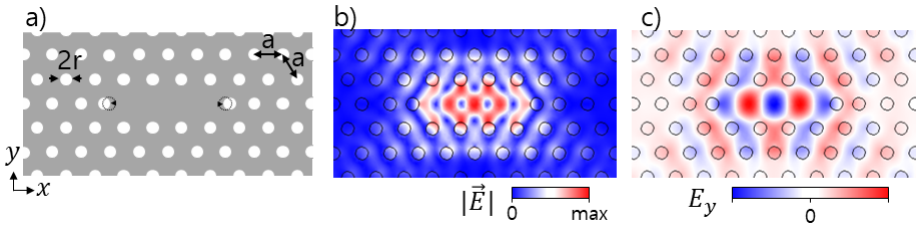

Figure 2.1 – a) Single cavity design with hole radius r and crystal parameter a. The cavity neighboring hole positions are shifted with $0.2a$. b) Distribution of the electrical field intensity in the defect. c) Distribution of the y component the electrical field E_y

holes over a given line in the crystal. A full line missing permits the light to be guided along the defect axis, therefore constituting a waveguide. However if the line has a finite length, the light is confined in the 3 spatial directions, giving rise to an optical cavity. It has been shown that the L3 defects [Akahane et al., 2003], obtained by removing three consecutive holes over a line, can achieve high optical quality factors. We adopt this strategy for designing the photonic molecules on our suspended InP membrane.

The triangular lattice PhC is characterized by a lattice constant $a = 420$ nm and a hole radius r (see fig. 2.1a). The lattice parameter is optimized for an optical band-gap centered at 1550 nm. The PhC defect cavities must sustain a fundamental optical resonance around 1550 nm which is achieved for $r = 100$ nm. A change in the hole radius of the order of 10 nm shifts the L3 microcavity resonance wavelength by about 20 nm. The quality factor of a L3 defect-cavity can be improved by engineering the crystal. In particular, the positions of the holes at the extremities of the defect can be shifted along the cavity axis [Sauvan et al., 2005]. The optimum shift is given by $0.2 \times a$ where a is the crystal lattice constant. The 260 nm thick PhC slab is modeled with Finite Element Method software such that the electrical field distribution is simulated in the single defect cavity. The magnitude of the electrical field $|\vec{E}|$ in the defect is represented at the fundamental resonance in fig. 2.1b. The field is dominated by the transverse electrical field component E_y whose distribution is represented in Figure 2.1c. While the field intensity is maximum inside the defect, it exponentially leaks out the cavity. This evanescent field in the PhC plane is exploited for coupling several L3-defects to each other.

2.1.2 Photonic crystal molecule

By analogy with the ability of atoms to bind into chemical molecules, a cluster of optical microcavities exchanging energy is sometimes refereed as a "photonic molecule" [Bayer et al., 1998; Mukaiyama et al., 1999]. The spatial confinement of the optical modes as well

as energy-splitting resulting from such coupling motivate this terminology. As discussed with the single L3-defect, the evanescent field intensity distribution is anisotropic around the cavity. Interestingly, the strength of this coupling not only depends on the distance between the cavities but also on their orientation regarding the crystal lattice. Indeed, it appears that the evanescent field reaches a maximum intensity in the diagonal directions, while it is weak in the longitudinal x and y directions [Atlasov et al., 2011]. Thus a higher coupling is expected in these directions for a given separation between two cavities. In order to evidence this feature, several designs of photonic molecules are considered. Here we focus on "diatomic" photonic molecules, i.e. involving only two defects. However, more complex molecules can be designed and propose alternative coupling considerations. This point is the object of a discussion in appendix A. These different configurations are shown in figs. 2.2a to 2.2c (left) with the associated distribution of the electrical field component E_y for the anti-symmetrical (middle) and symmetrical (right) normal modes.

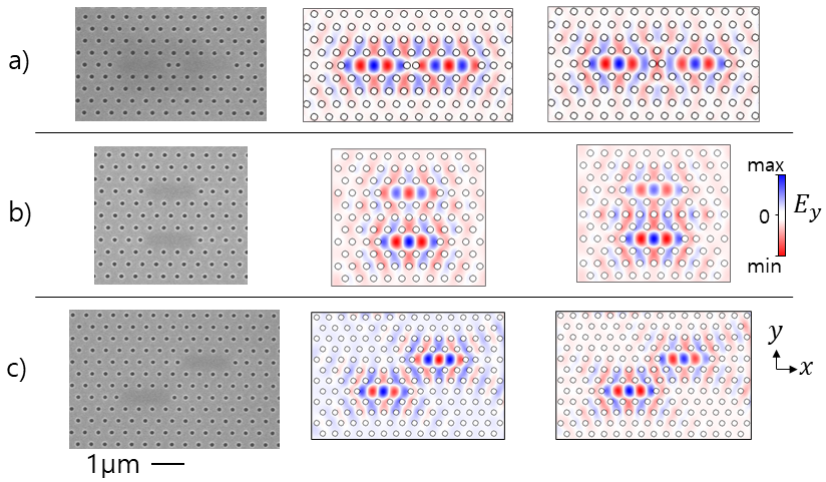

Figure 2.2 – SEM image of the PhC molecule (left) and associated distribution of E_y for the anti-symmetrical (center) and symmetrical modes (right) in the a) horizontal (2H2), b) vertical 2V3 and c) diagonal (2D2) configurations.

In addition to the coupling orientation, the distance between the cavities can be used for tuning the coupling. In the vertical configuration, two cavities must be separated by an odd number of rows in order for their centers to remain aligned in the y direction. We introduce a nomenclature to categorize the photonic molecules. n cavities separated by p holes (or rows of holes) constitute a nXp photonic molecule where X refers to the coupling orientation and can be V,H or D respectively for 'vertical' (along y), 'horizontal' (along x) and 'diagonal' (along x ans y). Moreover, the simulations of the electrical field distributions come with the resonant frequencies, which permits to estimate the couplings in each configuration. These simulated couplings are provided together with the experimental data (see section 2.3.2).

In the next section, we will investigate on the coupled mode theory of the coupled-waveguide photonic molecules. Although the energy splitting will still be dominated by the direct coupling between the cavities, we will discuss how an indirect mechanism, allowing the cavities to couple through the waveguide, can play a role in the normal mode spectral positions and linewidth.

2.1.3 SOI waveguide integration

The PhC membrane is suspended over a SOI waveguide enabling an integrated access to the photonic molecule. The ridge waveguide can be injected on either side through the available grating couplers. The traveling wave is localized in the guide and exponentially decays around it such that it can couple to the PhC cavities. This evanescent coupling is given both by the waveguide cross-section dimensions and by the distance between the guide and the membrane. This gap is fixed by the fabrication process, which is common to an entire chip. In practice it is given by the cumulative thickness of the deposited SiN and SiO_2 layers (resp. 180 nm and 20 nm), that are further removed for at the under-etching step. Therefore the waveguide and the cavity are separated by 200 nm. Different waveguide geometries are available on a chip such that several configurations can be explored. In the case of two PhC cavities, all waveguides are provided with identical height $h = 220$ nm but their width can vary from 250 nm to 550 nm.

2.2 Coupled mode theory

This section describes how several optical cavities can be coupled together with a waveguide. The formalism used to describe such systems is the time-domain Coupled Mode Theory (CMT) [Miller, 1954; Fan et al., 2003; Haus, 1984]. When one optical cavity exchange energy with a waveguide, we observe the input propagating mode couples with the cavity at the resonance frequency. However, when a second cavity is coupled to the waveguide and/or to the first one, both direct and indirect coupling between the cavities can lead to a mode splitting. The influence of the different couplings is investigated here in order to ideally modelize our systems. The aim of this part is to derive an expression for the amplitude transmitted through an optical waveguide on the one hand. On the other hand, we want to rewrite the coupled master equations for the cavity amplitudes in terms of normal modes. This we help to simplify the calculations a lot when we will consider an optomechanical coupling.

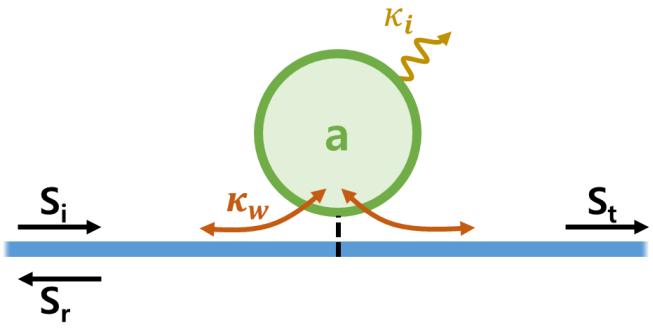

Figure 2.3 – Schematic of a waveguide-coupled bi-directional optical cavity.

2.2.1 Single cavity

We preliminary study the simple case of a single Standing-Wave (SW) cavity coupled to a non-dissipative waveguide. The cavity with resonance frequency ω_0 (or wavelength $\lambda_0 = 2\pi c/\omega_0$) is coupled both to an optical waveguide with an external decay rate κ_w and to the environment through an intrinsic decay rate κ_i as described in fig. 2.3. The total dissipation loss rate of the cavity κ is the sum of these two contributions: $\kappa = \kappa_i + \kappa_\mathrm{w}$. The optical linewidth of this resonator is given by 2κ. The excitation of the cavity occurs through the external coupling with the waveguide in which an incident wave of amplitude s_i and frequency ω_L travels. The input power launched to the cavity writes $P_\mathrm{in} = |s_i|^2$ so the corresponding photon flux is $P_\mathrm{in}/\hbar\omega$. The analysis of this single-port system can be done either using the reflected wave or the transmitted wave carrying respective amplitudes s_r and s_t. In the experiments, we will measure the waveguide transmission $T = |s_t/s_i|^2$.

The master equation for the cavity amplitude a is given by:

$$\frac{\mathrm{d}a}{\mathrm{d}t} = -(j\omega_0 + \kappa_i + \kappa_\mathrm{w})a + \sqrt{\kappa_\mathrm{w}}s_i(t) \tag{2.1}$$

By choice, we place ourselves in the rotating frame $e^{-j\omega t}$. The steady state solution of the resonator amplitude is

$$a(t) = \frac{\sqrt{\kappa_\mathrm{w}}s_i(t)}{\kappa_i + \kappa_\mathrm{w} - j(\omega_L - \omega_0)} \tag{2.2}$$

The energy stored in the optical resonator is therefore $|a|^2$. Note that the energy conservation implies that $|s_i|^2 = |s_t|^2 + |s_r|^2 + 2\kappa_i|a|^2$.

The transmitted amplitude reads $s_t = e^{-jK\Delta z}[s_i - \sqrt{\kappa_\mathrm{w}}a(t)]$ with K the propagation constant in the waveguide and Δz the distance between the input and the output[1]. We can deduce the complex transmission $\tau = s_t/s_i$ expressed in terms of quality factors

[1] The reflected amplitude reads $s_r = s_t - s_i$

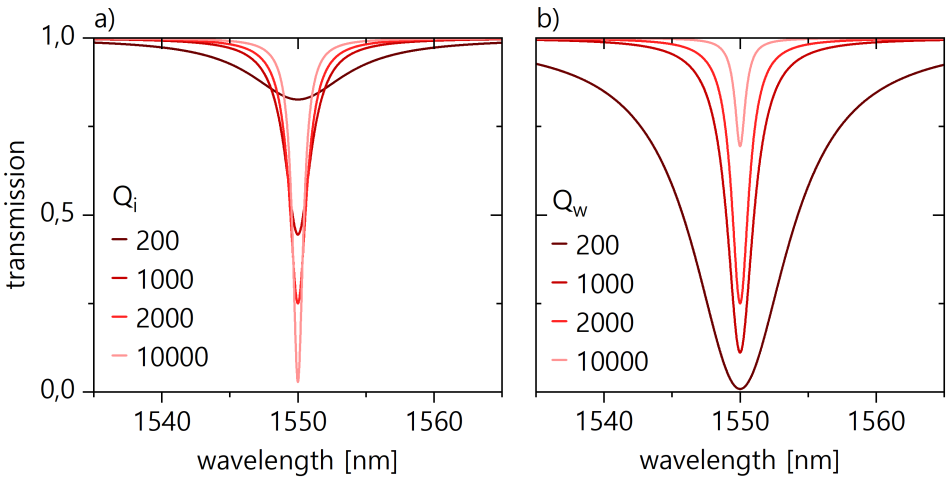

Figure 2.4 – Transmission spectrum of a single cavity coupled to a waveguide with resonance centered at 1550 nm. a) The influence of Q_i is studied for Q_w=2000. b) The influence of Q_w is studied for Q_i=2000.

$Q_i = \omega_0/2\kappa_i$, $Q_\mathrm{w} = \omega_0/2\kappa_\mathrm{w}$ and normalized detuning $\delta = \frac{\omega_L - \omega_0}{\omega_0}$:

$$\tau = e^{-jK\Delta z}\left(1 - \frac{\frac{1}{Q_\mathrm{w}}}{-2j\delta + (\frac{1}{Q_i} + \frac{1}{Q_\mathrm{w}})}\right) \tag{2.3}$$

Finally we deduce the transmission $T = |\tau|^2$:

$$T = \frac{4\delta^2 + \frac{1}{Q_i^2}}{4\delta^2 + (\frac{1}{Q_i} + \frac{1}{Q_\mathrm{w}})^2} \tag{2.4}$$

Both dissipative components affects the depth and the linewidth of the resonance dip in the transmission spectrum as shown in figs. 2.4a and 2.4b. The spectral linewidth is given by the total dissipation rate κ so both components similarly influence this property. However only the external losses determines the amount of optical power injected to the cavity. At resonance, the transmission writes $T_0 = (Q_w/Q_t)^2$ with $Q_t = (Q_i^{-1} + Q_\mathrm{w}^{-1})^{-1}$ the total quality factor of the cavity. Therefore the condition $Q_i \gg Q_\mathrm{w}$ is required for maximizing the resonance depth, so that the resonance linewidth is limited by the external losses. Such situation is refereed as over-coupling regime.

2.2.2 Two coupled cavities

The problem is now extended to a pair a SW cavities coupled to each other both directly and indirectly through the waveguide. Several configurations can be discussed but this study is first approached in a general frame. In order to simplify the problem, we consider two cavities (1) and (2) with identical resonance frequencies ω_0 and internal decay rate

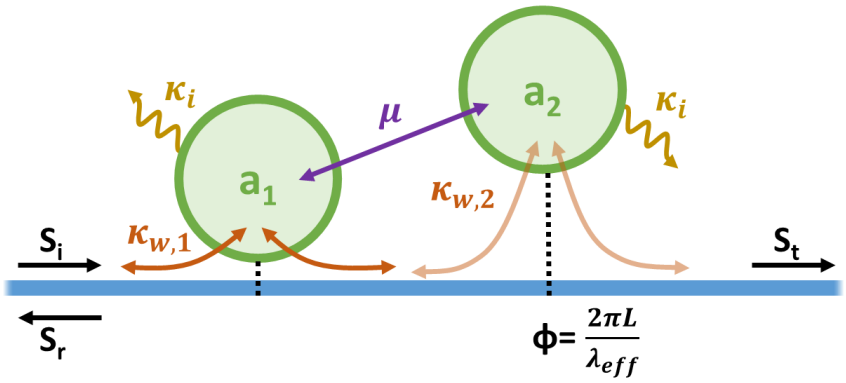

Figure 2.5 – Two cavities coupled to a waveguide with a direct coupling μ and an indirect coupling through the waveguide.

κ_i. This assumption relies on the design of the photonic crystal (PhC). Indeed the PhC defects, that constitute the optical resonators, are never placed close enough to the crystal edge such that their properties are different to each other. The cavities are also both coupled to the waveguide with external decay rates $\kappa_{\mathrm{w},1}$ and $\kappa_{\mathrm{w},2}$. We introduce a direct coupling rate between the cavities μ. Finally, the parameter ϕ designates the phase shift in the waveguide between the cavities. Assuming a distance L between the cavities and an effective refractive index in the waveguide n_{eff}, this phase shift writes $\phi = 2\pi n_{\mathrm{eff}} \frac{L}{\lambda}$. The problem is schematically described in fig. 2.5.

The dynamics of the cavity amplitudes a_1 and a_2 are given by the following set of coupled equations.

$$\begin{aligned} \dot{a_1} &= -(j\omega_0 + \kappa_1)a_1 + (j\mu + e^{-j\phi}\sqrt{\kappa_{\mathrm{w},1}\kappa_{\mathrm{w},2}})a_2 + \sqrt{\kappa_{\mathrm{w},1}}s_i \\ \dot{a_2} &= -(j\omega_0 + \kappa_2)a_2 + (j\mu + e^{-j\phi}\sqrt{\kappa_{\mathrm{w},1}\kappa_{\mathrm{w},2}})a_1 + e^{-j\phi}\sqrt{\kappa_{\mathrm{w},2}}s_i \end{aligned} \tag{2.5}$$

where $\kappa_1 = \kappa_i + \kappa_{\mathrm{w},1}$ and $\kappa_2 = \kappa_i + \kappa_{\mathrm{w},2}$ are respectively the total loss rates of the cavity 1 and 2. In this system, both cavities are driven at the same frequency but with different forcing amplitudes due to the unbalanced external losses $\kappa_{\mathrm{w},1} \neq \kappa_{\mathrm{w},2}$. These forces are also out of phase by the phase shift ϕ. Note also that the direct coupling μ appears in the imaginary part of these equations because it constitute a coherent process. The indirect coupling occurring through the waveguide involve a complex number indicating that this coupling is both coherent and dissipative. We discuss this point by studying the normal mode properties.

2.2.2.1 Normal mode properties

The introduction of a coupling between two nearly identical resonators leads to a splitting in the spectrum. It is usually rather easy to obtain the eigenfrequencies of a system of coupled linear resonators. Here, we need to pay attention to the coupling terms in the

equation of motion (2.5). Indeed these terms are not imaginary valued but own a real part that contributes to the dissipation processes. We introduce an energy-coupling μ' and a loss-coupling κ' such that $\kappa' + j\mu' = e^{-j\phi}\sqrt{\kappa_{\mathrm{w},1}\kappa_{\mathrm{w},2}} + j\mu$. We deduce:

$$\begin{aligned} \mu' &= \mu - \sin\phi\sqrt{\kappa_{\mathrm{w},1}\kappa_{\mathrm{w},2}} \\ \kappa' &= \cos\phi\sqrt{\kappa_{\mathrm{w},1}\kappa_{\mathrm{w},2}} \end{aligned} \tag{2.6}$$

For an exact treatment of this problem, one can diagonalize the matrix M obtained from eq. (2.5):

$$M = \begin{pmatrix} \kappa_1 + j\omega_0 & \kappa' + j\mu' \\ \kappa' + j\mu' & \kappa_2 + j\omega_0 \end{pmatrix} \tag{2.7}$$

This matrix has complex eigenvalues whose real part give the normal modes decay rates while their imaginary part give the eigenfrequencies. As the analytic expressions for these eigenvalues are quite complicated, we assume identical external couplings $\kappa_{\mathrm{w},1} = \kappa_{\mathrm{w},2} = \kappa_{\mathrm{w}}$ such that the expressions for the energy-splitting $\Delta\omega$ and loss-splitting can be simplified and interpreted.

$$\begin{aligned} \Delta\omega &= 2|\mu + \kappa_{\mathrm{w}}\sin(\phi)| \\ \Delta\kappa &= 2|\kappa_{\mathrm{w}}\cos(\phi)| \end{aligned} \tag{2.8}$$

This complex coupling therefore results in a level repulsion, given by $\Delta\omega$ (or equivalently $\Delta\lambda = \Delta\omega \times \frac{2\pi c}{\omega_0^2}$). This can be interpreted by identifying a symmetrical and an anti-symmetrical normal mode. This spectral splitting is made of two contributions that can interestingly counter-balance when $\sin\phi = -\mu/\kappa_{\mathrm{w}}$. Since $\sin\phi$ is bounded, it can occur only if $\kappa_{\mathrm{w}} \geq \mu$ which implies that the normal modes overlap (assuming the overcoupling regime $\kappa_i \ll \kappa_{\mathrm{w}}$,smalliteChutinan). In order to take advantage of such situation, one must be able to finely control the phase shift such that this singular point can be evidenced. The indirect coupling also leads to an imbalance between the normal modes linewidths as soon as $\phi \neq \pm\pi/2$. Moreover, depending on the sign of $\cos(\phi)$, the broader normal mode is not always the same. Interestingly, the phase shift ϕ plays an important role in the dissipative properties of this system. For example, one can set this phase to any multiple of π in order to reduce the linewidth of a given normal mode down to $2\kappa_i$. This linewidth is then limited by the cavities internal loss κ_i and in such configuration, the normal mode does not couple to the waveguide such that it can not be neither injected nor observed. In an indirect observation of the system spectral response, this invisible resonance is called a *dark mode*, or *dark state*.

As it will be shown when discussing the transmission spectra, the introduction of a contrast in the cavities external couplings ($\kappa_{\mathrm{w},1} \neq \kappa_{\mathrm{w},2}$) forbids the existence of a dark mode.

2.2.2.2 Transmission spectra

The stationary solutions are found by taking an amplitude of the form $a_k = A_k e^{-j\omega t}$ where A_k is the complex amplitude of the cavity k in the rotating frame. This calculation is almost exactly performed in [Li et al., 2010] but assuming $Q_{\mathrm{w},1} = Q_{\mathrm{w},2}$. As this assumption is not desired, we adapt the calculation and find that the expression for the complex transmission stays the same with the substitution $Q_{\mathrm{w}} \to \sqrt{Q_{\mathrm{w},1}Q_{\mathrm{w},2}}$:

$$\tau = e^{-j\phi}\left[\frac{1+\gamma_1+\gamma_2+\gamma_1\gamma_2\left(e^{j\phi}+j\frac{\sqrt{Q_{\mathrm{w},1}Q_{\mathrm{w},2}}}{Q_c}\right)\left(e^{-j\phi}-j\frac{\sqrt{Q_{\mathrm{w},1}Q_{\mathrm{w},2}}}{Q_c}\right)}{1-\gamma_1\gamma_2\left(e^{-j\phi}-j\frac{\sqrt{Q_{\mathrm{w},1}Q_{\mathrm{w},2}}}{Q_c}\right)^2}\right] \tag{2.9}$$

Where $\gamma_k = \frac{-1/Q_{\mathrm{w,k}}}{1/Q_i+1/Q_{\mathrm{w,k}}-2j\delta}$ is the transfer function of a single cavity coupled to a guide with parameters $Q_{i,k}$ and $Q_{\mathrm{w,k}}$ as seen above. $Q_c = \omega_0/2\mu$ is the quality factor associated to the direct coupling. This expression is complicated and involve many parameters. It is not very useful to explicit an expression for the transmission $T = |\tau|$. We plot the transmission spectrum from eq. (2.9) assuming several geometrical configurations.

Let's first consider a simple case where only the cavity 1 is coupled to the waveguide. In practice this configuration is obtained when one cavity is placed far from the integrated waveguide but still couples to the other cavity. The resulting transmission can be computed by setting $\kappa_{\mathrm{w},2} = 0$ or similarly by taking $Q_{\mathrm{w},2} \to \infty$. The phase shift in the waveguide is not defined anymore and can be arbitrarily set to zero (see fig. 2.6a). The transmission spectrum displays two resonance dips separated by a splitting proportional to Q_c^{-1}. When the direct coupling is set to zero, the situation is analog to the single cavity treated previously.

Another case to describe is the horizontal configuration where both cavities equally couple to the waveguide ($\kappa_{\mathrm{w},1} = \kappa_{\mathrm{w},2}$, see fig. 2.6b). In our experiments we encounter this situation when both cavities are aligned in the waveguide direction so they are equally spaced from it. We have seen in section 2.2.2.1 that the complex coupling results in a splitting both the normal mode frequencies and loss rates. In the transmission plot, the resonance dips periodically appear and disappear with the phase shift ϕ. When $\phi = 0\ [2\pi]$, the cavities are excited in-phase such that only the symmetrical normal mode can be driven. Similarly, when $\phi = \pi\ [2\pi]$, the cavities are excited out-of-phase such that only the anti-symmetrical mode can be excited. In intermediate values of the phase shift, the positions and linewidths of the normal modes vary as described by eq. (2.8).

The most general configuration is obtained when the cavities are coupled diagonally in the slab. Then the cavities unequally couple to the waveguide and the phase shift can be arbitrary valued. The description of the transmission spectrum does not differ

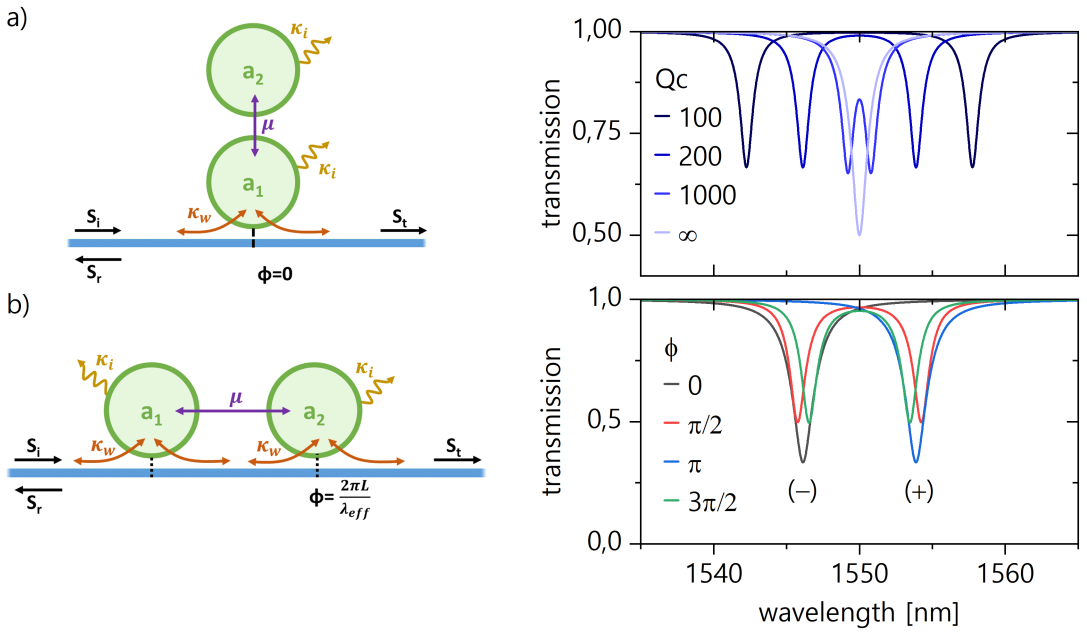

Figure 2.6 – a) Vertical configuration: only one cavity coupled to the waveguide. A mode splitting is observed. b) Horizontal configuration: both cavities couple to the waveguide with the same decay rate. The phase shift ϕ determines the balance in the normal mode external loss rates. All data are plotted with $Q_i = Q_{\mathrm{w},1} = Q_{\mathrm{w},2} = 2000$.

much from the previous case. The fact that the external loss rates are different only forbid the normal mode to become dark when the proper phase shift is established. This comes from the fact that the system is now driven in an unbalanced way since more power is injected in a cavity than in the other. As an illustration, we show in figs. 2.7a and 2.7b the transmission spectrum in color scale as a function of the phase shift. In both situations, the product $\sqrt{Q_{\mathrm{w},1}Q_{\mathrm{w},2}}$ is fixed such that the colormaps looks extremely similar. However in one case, the external loss rates are equal ($Q_{\mathrm{w},1} = Q_{\mathrm{w},2}$) while in the other we introduce a contrast ($Q_{\mathrm{w},1} = 5Q_{\mathrm{w},2}$). The subtle difference between these plots can be seen when ϕ is a multiple of π. In the first case one normal mode becomes dark (its depth vanishes) while in the other, both couple to the waveguide. In both cases, the total linewidth (indicated with the black dashed lines) are limited by the intrinsic losses are do not reach zero.

To go further, it can be verified that it is possible to recover a dark mode despite unbalanced external couplings by breaking the frequency matching between the cavities. By doing so, the energy injection is balanced back for one of the normal modes such that it can become dark at the appropriate phase shift. However the injection imbalance is enhanced for the other normal mode.

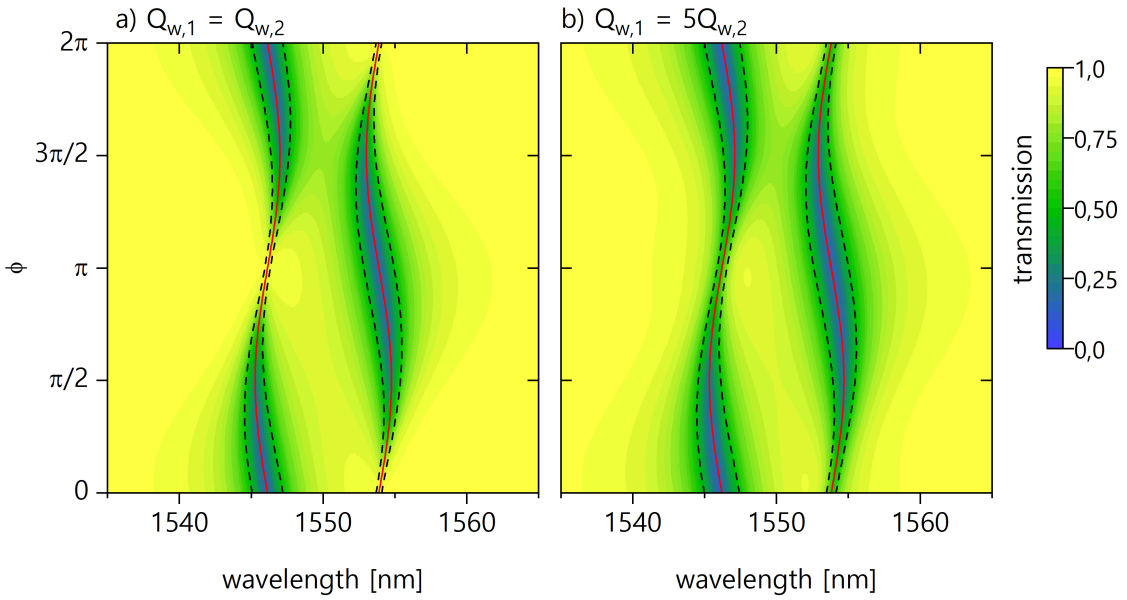

Figure 2.7 – Transmission spectrum plotted as a function of the phase shift with $Q_i = 2000$, $Q_c = 200$ and $\sqrt{Q_{\mathrm{w},1}Q_{\mathrm{w},2}} = 894$. a) $Q_{w_1} = Q_{w_2}$: the contrast between the normal mode amplitudes is maximum such that every π, one normal mode becomes dark. b) $Q_{w_1} = 5Q_{w_2}$ the contrast between the amplitudes is limited.

2.3 Complete optical characterization of the investigated structures

The optical setup and the alignment procedure enabling the characterization of the optical transmission through the waveguide are presented here. We introduce a method to distinguish the optical resonance belonging to several integrated photonic molecules. Finally, we discuss the influence of the system geometry on the measured optical couplings.

2.3.1 Optical setup

The chip is placed on a vertical holder that is itself fixed on a 3D motorized stage. The whole is put into a vacuum chamber. The pressure does not influence the optical properties so the alignment of the optical setup can be performed at room pressure. A window available at a chamber feed-through is used for imaging the sample with a white light source focused at the sample with an objective and reflected towards a CCD camera (see fig. 2.8b). The same optical path is used for pumping the quantum dots with a 820 nm diode laser. It results in a photoluminescent emission around 1550 nm that is scattered in all direction (see fig. 2.8a). In particular, a part of this light couples to the

SOI waveguide and scatters out of the grating couplers. These bright spots – at each grating coupler and at the PhC position – can also be imaged with an infrared camera placed behind the sample, the Silicon substrate being transparent at this wavelength. A hole in the sample holder and another window in the chamber are meant for this purpose. This method facilitates the alignment of the optical fibers on the grating couplers for injecting and collecting the integrated system.

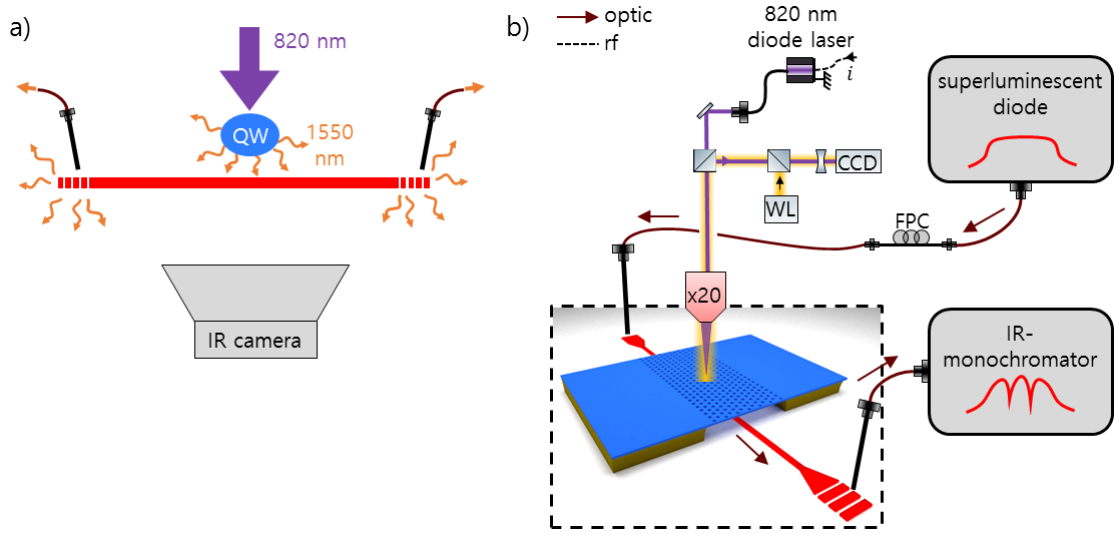

Figure 2.8 – a) Procedure for the fiber alignment. A 820 nm laser pumps the quantum wells in the InP layer resulting in a photoluminescent emission around 1550 nm. An infrared camera images the emission spots at both grating couplers and at the PhC position. b) SOI waveguide transmission characterization setup. A SLD broadband source is injected in the system and analyzed at the output with a monochromator coupled to an InGaAs camera.

The alignment procedure starts by placing a single-mode optical fiber above each side of the waveguide. The injection is optimized for a proper angle between the fiber and the grating coupler. In principle this angle depends on the injected wavelength although the optimization is always performed at 1550 nm and this dependence is not critical within the spectral band we are working on. In practice the optimal angle is around 80° and can be adjusted on the fiber holders for each side. Next the position of each fiber needs to be precisely adjusted. For this purpose each fiber holder is fixed on a remotely controlled 3D positioning stage. The fibers are independently displaced for maximizing the output power while the quantum wells are pumped with the free-space diode laser. Once that both optical fibers are positioned, the waveguide can be injected on one side with a superluminescent diode source (SLD). The light is collected on the other side and sent to an infrared monochromator coupled to an InGaAs camera cooled

with liquid Nitrogen. Thus the transmission spectrum can be characterized in the SLD spectral band, i.e. from 1500 nm to 1600 nm roughly.

Note that the photoluminescence process can be used for the characterization of the photonic crystal molecules. In this case the light back-scattered towards the pumping laser is collected with a dichroic mirror and sent to the monochromator.

2.3.2 Transmission spectrum interpretation

Three PhC membranes are suspended over each waveguide in order to increase the number of available structures on a chip. The radii of the holes in the photonic crystals are respectively set to 90, 100 and 110 nm so their resonances are properly separated. Indeed, the resonance wavelength of a L3 defect cavity tends to increase when the holes radii decrease. However, it is still not always straightforward to associate a resonance dip to a given structure, in particular under strong coupling where the spectral splitting is so high that the resulting span overlaps with the one of another structure. To accurately identify the normal modes to a PhC membrane, the 820 nm diode laser is successively focused on all the structures on a chip. By changing the power of this laser, a thermo-optic shift of the resonance dip positions occurs in the transmission spectrum. In fig. 2.9, this effect is illustrated with a waveguide coupling to three 2V3 photonic molecules with different hole radii. The transmission spectrum displays several dips among which only two shift when the diode laser is turned on. After repeating this measurement with the diode laser focused on the other two PhC membranes, the three pairs of resonance dips are finally identified. From the central wavelength at each photonic molecule – obtained by taking the mean value of both normal modes positions – we find that a change of $+10$ nm in the PhC holes radii leads to a shift of -20 nm of the cavity natural resonance.

2.3.3 Experimental analysis of the photonic molecules

The physical properties of the photonic molecules can now be accessed from the experimental characterization of the waveguide transmission by taking advantage of the theoretical description of the system provided by the coupled mode theory. From the measurement presented in fig. 2.9, it appears that the spectrum has not a flat intensity in the typical range 1550-1600 nm. Although the SLD source does have a quite flat intensity in this range, this evidence the pass-band behavior of the SOI grating couplers. Importantly the normalization of the spectrum, which is an essential prerequisite for fitting the data, must account for this filter. For this purpose, a Gaussian is adjusted on the data such that only the resonance dips significantly discard from this Gaussian. Dividing the spectrum with this latter provides the transmission, i.e. a quantity normalized such that it dwells between 0 and 1 and is close to 1 off an optical resonance.

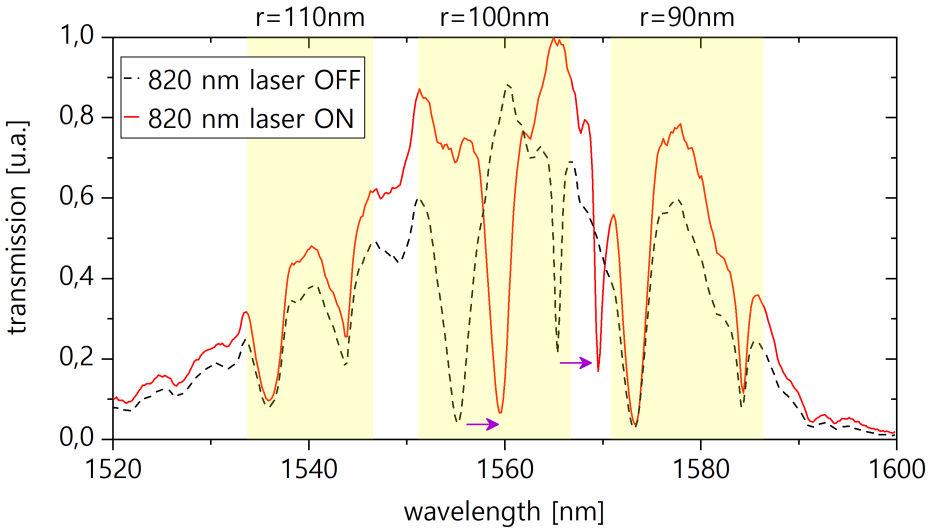

Figure 2.9 – Effect of the 820 nm diode laser on a typical transmission spectrum in a 2V3 photonic molecule. Only the resonances dips associated to the heated membrane shift by about 5 nm (see arrows). Finally each pair of normal modes (contained in a given yellow stripe) is associated to a photonic crystal hole radius r (indicated on top).

A typical waveguide transmission generally displays three pairs of dips – one for each crystal that it couples to – and we focus here and the central doublet, i.e. associated to a hole radius of 100 nm. The transmission is plotted for three different geometries in fig. 2.10a: 2H3, 2V3 and 2D2. These photonic crystal molecules are all coupled to a 300 nm wide waveguide such that their resonance linewidths compare. The data are fitted using eq. (2.9). The set of fitting parameters depends on the configuration. In particular the phase shift ϕ and the external coupling quality factor $Q_{\mathrm{w},1}$ and $Q_{\mathrm{w},2}$ can be constrained by the geometry as discussed in section 2.2. With 7 fitting parameters, it can not be guaranteed that the set on which the fit converges is accurate. However, as soon as the fit agrees on the dip positions, it indicates that the natural cavity resonance wavelength and the direct coupling quality factor are relevant for discussion. The other returned parameters are convenient for a general discussion about the system losses but should considered as uncertain. Thus we focus here on the doublets spectral separation for each system, i.e. the mode splitting. As expected, it is found that the diagonal configuration offers a larger spectral separation. The splitting in the 2H3 structure presented here actually barely overcomes the resonance linewidth.

More generally, the splittings are evaluated in several other structures suspended over waveguides of different dimensions, which should not affect so much the result, and over two different sample. They are plotted as a function of the cavity separation distance (in unit of number of holes or lines) for each geometry in fig. 2.10b. We distinct the two sample with the orientation of the symbols. In complement, the splittings are evaluated

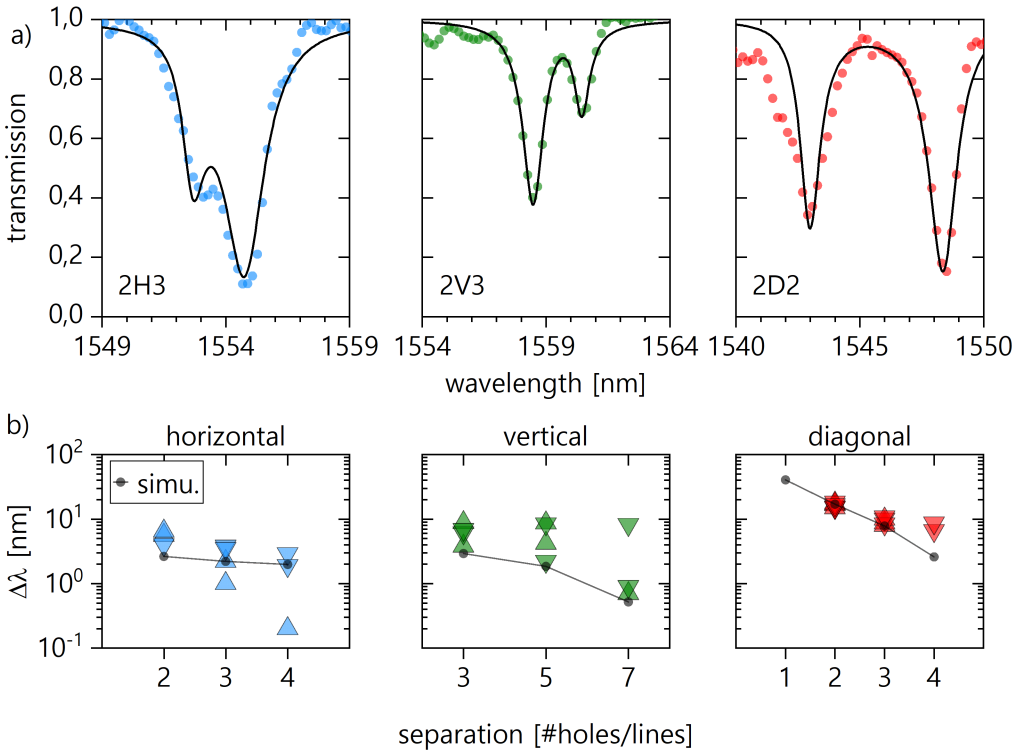

Figure 2.10 – a) Measured normalized transmission (colored dots) with fits (black lines) for three different configurations. b) Measured mode splitting for several structures studies on two samples (difference of symbol orientations) as a function of the spacing between the defects. The simulated splittings (black) are obtained only considering the photonic crystal.

using FDTD simulations for each geometry. The general tendency for the experimental data agrees with the intuition and the simulations: a higher separation between the cavities leads to a lower coupling. This evolution is clear for the horizontal and diagonal geometries. However for the vertical one, it seems that some structures display a coupling significantly higher than in the simulations. Note that for low couplings, typically in the 2H4 and 2V7 configurations, the indirect coupling occurring though the waveguide and involving the phase shift ϕ might become the dominant coupling process. As the waveguide is not taken into account in the simulations, one must have this in mind when comparing with the experiments as this might explain discrepancies. Note that a splitting of about 30 nm is numerically evaluated in a 2D1 structure, which is not very convenient for the experiments as the equipment are mainly restricted to an operating spectral range centered at 1550 nm and typically limited with a 50 nm span. A small deviation to 1550 nm for the cavity resonance wavelength would therefore quickly lead a resonance of the photonic molecule to be unattainable. In consequence, as this simulation precedes the sample fabrication, the diagonally coupled molecules are always designed with a

separation higher than 2 lines.

The optical quality factors are extremely variable from one structure to another. On the few spectra that could be correctly fitted, it comes out that the average intrinsic quality factor is about 10^3 and never overcomes 10^4 which is quite low compared to the state of the art for optical microcavities. The external quality factor depends on the distance between the cavity and the waveguide as well as on the width of the SOI waveguide. Importantly in the vertically coupled cavities, two resonance dips are always observed. This indicates that both cavities couple to the waveguide with unbalanced couplings. In the theoretical description, we assume that in this configuration the further cavity has an external quality factor $Q_{\mathrm{w},2} = +\infty$. We conclude that this is incorrect. Therefore the corresponding spectra (e.g. with the central plot in fig. 2.10a), are fitted with the unique constraint $\phi = 0$ as the cavities are notwithstanding coupled in-phase with the waveguide.

2.4 Thermo-optic nonlinearity

In a photonic device, the strong confinement of light is responsible for several types of nonlinearities that can be exploited for a large variety of applications. Here we focus on the thermo-optic effect where the temperature growth in the material induced by light absorption is responsible for a significant shift of the dielectric index. In an optical cavity, this effect is enhanced such that it can red-shift the cavity resonance frequency. If the input field intensity passes a certain threshold, the resonance lineshape becomes bistable. Such behavior can be evidenced by scanning forward and backward the laser frequency over the resonance, or equivalently, by sweeping up and down the input laser intensity.

This effect can be modeled using nonlinear time-domain CMT [Uesugi et al., 2006; Gao et al., 2017]. Given an optical cavity with resonance frequency ω_0, intrinsic and external loss rates κ_i and κ_{w}, the cavity energy in the stationary regime reads $|a|^2$ with a the cavity amplitude given by eq. (2.2). As κ_i refers to the total intrinsic loss rate, it includes the thermal absorption process that is relevant here. We introduce the linear absorption rate in the cavity κ_{abs} such that the power absorbed by the driven cavity is $\kappa_{\mathrm{abs}}|a|^2$. The resulting temperature growth in the cavity related to the absorbed power through the material thermal resistance R_{th} (in units of K.W^{-1}). It leads to a temperature shift in the cavity $\Delta\theta = R_{th}\kappa_{\mathrm{abs}}|a|^2$. Finally, this temperature shift induces a red-shift of the cavity wavelength frequency given by

$$\Delta\lambda = \frac{\lambda_0}{n_0}\frac{\mathrm{d}n}{\mathrm{d}\theta}\Delta\theta \tag{2.10}$$

with $\lambda_0 = 2\pi c/\omega_0$ and n_0 respectively the resonance wavelength and the refractive index

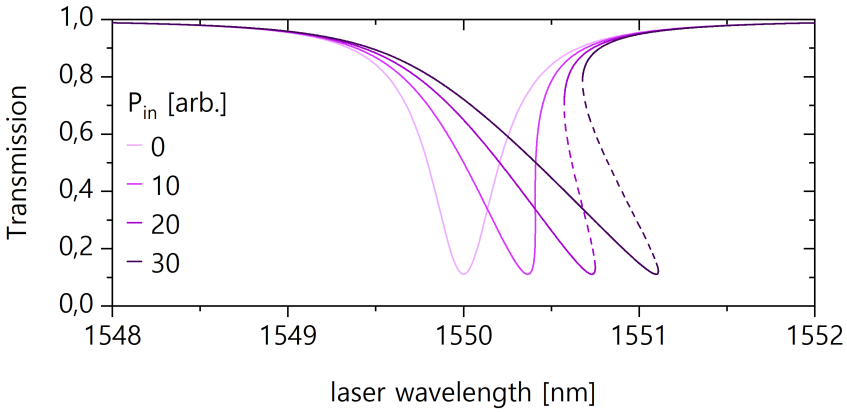

Figure 2.11 – Theoretical nonlinear single port transmission of a waveguide coupled to a cavity submitted to thermo-optic effect. Higher input power leads to a linear shift of the resonance position. The resonance evidence bistable regime at sufficiently high input power P_{in}. The stable (unstable) solutions are plotted with straight (dashed) lines. Parameter used: $\lambda_0 = 1550$ nm, $Q_i = 10^4$, $Q_{\mathrm{w}} = 5000$.

at room-temperature ($\theta_0 = 293$ K). Injecting the input-power dependent resonance frequency $\omega_0' = 2\pi c(\lambda_0 + \Delta\lambda)^{-1}$ in the coupled-waveguide single cavity amplitude yields a new shape for the transmission dip. In fig. 2.11, we plot the nonlinear transmission for values of the input power. Beside the linear shift of the resonance wavelength which constitutes the corner stone of this model, the resonance dip clearly bends with increasing input power. Over a certain threshold, the transmission – in coherence with the cavity energy solution – displays up to three solutions, one being unstable (dashed lines), while the other two are stable. The span of this bistability window grows with the input power.

In order to experimentally observe this hysteretic behavior, the transmission must be characterized by scanning the resonance in both directions. This is not possible with the SLD source that was used so far. We rather use a tunable laser instead and inject the waveguide through the aligned injection fibers. The output laser field is sent to a low-power photodetector and the DC response is checked on an oscilloscope. Therefore, the waveguide transmission is now triggered in real-time, provided that the transmission can be re-normalized. The input power is estimated by measuring the off-resonance transmission ζ of the integrated waveguide and assuming the injection and the collection efficiency to be equal. Therefore, with P_{inj} the optical power sent in the injection fiber, the input power writes $P_{\mathrm{in}} = \sqrt{\zeta} P_{\mathrm{inj}}$. In fig. 2.12a, the resonance wavelengths of an optical mode is plotted as a function of the calibrated input power. This mode is actually the $(+)$ normal mode of a 2V3 photonic molecule. The associated transmission response is measured for several input power values such that the wavelength associated to minimum transmission is reported with an experimental uncertainty. The resonance

wavelength can be fitted using eq. (2.10). Taking a value $\frac{\mathrm{d}n}{\mathrm{d}\theta} \approx 1.9892 \times 10^{-4}$ K^{-1} from [Della Corte et al., 2000] and with the InP refractive index $n_0 \approx 3.16$ [Pettit and Turner, 1965], we can estimate the cavity temperature change $\Delta\theta \approx 4$ K at the maximum injected power $P_{\mathrm{in}} \approx 1.6$ mW. For low power the observed transmission dip can be fitted with the linear transmission expression such that the internal and external Q-factors are determined. In fig. 2.12b, with $P_{\mathrm{in}} \approx 325$ µW, we find $Q_i \approx 4400$ and $Q_{\mathrm{w}} \approx 9500$. Injecting these Q-factors as well as the power-dependent resonance wavelength into the transmission expression, the similar fit can be performed on the data collected for higher injected power. For example, with $P_{\mathrm{in}} \approx 1.3$ mW and using Mathematica to estimate the multivalued solution, we fit the data using the nonlinearity $\mathcal{R} = \frac{\lambda_0}{n_0}\frac{\mathrm{d}n}{\mathrm{d}\theta} R_{th}\kappa_{\mathrm{abs}}$ and find $\mathcal{R} \approx 1.6 \times 10^{14}$ nm/W. Finally we can estimate the product $R_{th}\kappa_{\mathrm{abs}} \approx 1.62$ K.fJ^{-1}. Although the fit accurately matches with the width of the observed dip, and also retrieves the presence of a bistable region, we note a disagreement in the size of the bistability. This discrepancy is probably the result of a too high scan-speed of the laser wavelength [Rodriguez et al., 2017]. In practice, this later is set at 10 nm/s in order to prevent oscillations in the laser output power, which would have corrupted the measured transmission. This results in an averaging effect of the transmission near the bistability edges. In the experimental data, the jumps of the optical states are not abrupt as it should, but follow the photodetector response lifetime (≈ 6 ms).

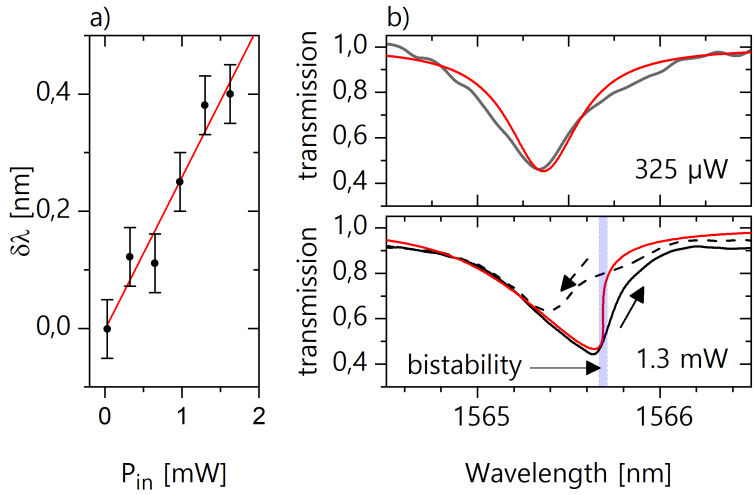

Figure 2.12 – a) Thermo-optic shift of the (+) optical mode of a 2V3 photonic molecule. The power dependence of the shift is fitted with a line (red). b) Measured waveguide transmission at $P_{\mathrm{in}} = 325$ µW and 1.3 mW. Higher input power leads to thermo-optic bistability (transparent stripe) evidenced by scanning the resonance forward (straight) and backward (dashed) at 10 nm/s. The resonance dips are fitted with the transmission including the thermo-optic nonlinearity.

In [Brunstein et al., 2009], a study of the thermal properties of a similar InP suspended photonic-crystal membrane provides an estimation for the thermal resistance $R_{th} \approx 1.7 \times 10^4$ K.W^{-1}. Relying on this value, we deduce the linear absorption rate in the system $\kappa_{\text{abs}} \approx 95$ GHz.

In this section, we have modeled and quantified the thermo-optic nonlinearity in a typical coupled-waveguide optical cavity. The extension of this model to coupled optical cavities, achievable by adapting the linear coupled mode theory described in section 2.2, is not of interest here. Overall the thermo-optic effect has an important impact in the following experiments as it manifests itself at the typical input powers used for probing the mechanical noise spectra of the suspended membranes. Coupled to thermo-mechanical processes, it will allow us to model the mechanical frequency shifts induced by the power absorbed in the microcavity.

2.5 Conclusion on the optical aspects

In this chapter, the waveguide-coupled photonic crystal molecules are investigated theoretically and experimentally. We have detailed the optical setup with which the structures can be characterized. As expected with the numerical simulations, the optical coupling decreases when the cavities are distanced from each other. The horizontal and vertical configurations provide similar couplings while the diagonal configuration enables a higher coupling. The effect of the relative positions of the cavities over the integrated waveguide is clearly visible in the balance of the normal modes spectral linewidth as their external Q-factors are basically determined by this geometry. Finally we focus on the thermo-optic effect which is presumably the dominant nonlinearity is this system. The phenomenon is described for a unique optical mode which appears to be successful while the extension of the thermo-optic model to coupled resonators would imply a much more complicated theoretical frame.

It comes out that this system, conceptually quite simple, carries a very rich physics. In particular, the existence of both a direct coupling – within the crystal – and an indirect coupling – through the waveguide in which the circulating light experiences a phase shift ϕ – gives rise to various lineshapes for the resonance dips in the transmission spectrum. One spectacular example is the existence of dark modes, that do not couple with the waveguide when ϕ is a multiple of π. The mechanism of this behavior can be understood as a destructive interference of the transmitted wave at the dark mode frequency, disabling the injection coupling. Alternatively, it can been seen as the result of an out-of-phase excitation scheme, where the dephasing between the optical resonators applied drives (given by ϕ) is in conflict with the photonic mode symmetry. Therefore, it seems extremely interesting to have a fine control of ϕ for several reasons. First, the

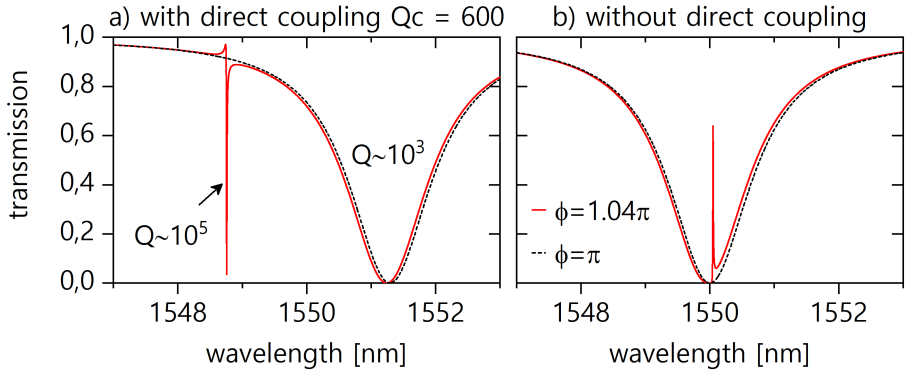

Figure 2.13 – Transmission spectrum plotted with $\lambda_0 = 1550$ nm, $Q_i = 10^6$, $Q_{\mathrm{w},1} = Q_{\mathrm{w},2} = 2 \times 10^3$ a) with direct coupling $Q_c = 600$ or b) without direct coupling ($Qc = +\infty$). The phase shift $\phi = \pi$ (black dashed) leads to a dark mode while a small shift to $\phi = 1.04\pi$ (red) leads to a high Q resonance (a) or antiresonance (b).

evidence of a dark mode paradoxically implies not to observe a resonance dip. Obviously, the evidence of the dark mode presence is conditioned to the ability of changing the system coupling parameters such that it becomes observable. This systems offers a parameter, ϕ, whose control permits exactly this. In optomechanics, the optical linewidth plays a very import role as it dictates the sensitivity to mechanical displacement. One could imagine a system in which the normal modes linewidths can modified by finely controlling the phase shift. At a value of ϕ leading to a dark mode, a tiny change permits the mode to couple back with a high quality factor . This is illustrated in fig. 2.13a with realistic values $Q_i = 10^6$ and $Q_{\mathrm{w}} = 2 \times 10^3$. The mode can reach a total Q higher than 10^5 which corresponds to a linewidth of about 3 GHz. This corresponds to the typical mechanical frequency confined in the L3 defect which opens the way for a very rich configuration for cavity optomechanics experiments in the resolved sideband regime – i.e. when the mechanical frequency overcomes the optical linewidth. An equivalent result can be obtained without the direct coupling between the cavities as shown is fig. 2.13b. In this system, the cavities would only communicate through the waveguide and could therefore be arbitrarily far from each other.

Chapter 3

Optomechanical characterization

The optomechanical properties of the suspended photonic crystal are investigated here. After an analysis of the mechanical eigenmodes of the structure using finite-element method (FEM) simulations, the system is experimentally characterized through the optomechanical interactions. The total optomechanical couplings are measured and discussed. A thermo-mechanical effect is finally evidenced and discussed through a toy-model.

3.1 Mechanical properties

We now focus on the mechanical properties of the suspended photonic crystal. After an overview of the membrane mechanical eigenmodes in the MHz domain, the noise spectrum of the structure is experimentally observed through the optomechanical interaction. We compare the observed eigenfrequencies with the FEM simulations.

3.1.1 Eigenfrequency analysis

The InP photonic crystal is defined over a 10×20 rectangular surface. This membrane is partially clamped on two opposite sides as shown in fig. 3.1. The free-standing part of this structure is limited to this rectangle since the under-etching process is achieved through the crystal holes.

As any solid state object, the PhC slab can vibrate at some particular discrete eigenfrequencies [Kittel, 2005; Cleland, 2013]. These vibrations are favored by the mechanical degree of freedom introduced when suspending the membrane. The eigenfrequency analysis of a mechanical structure can be performed analytically in the case of simple geometries, e.g. for a singly or doubly clamped nanobeam or for unclamped rectangular membranes [Hauer et al., 2013]. In order to obtain the eigenfrequencies and associated displacement field distributions in more complex structure, we use the Finite-Element

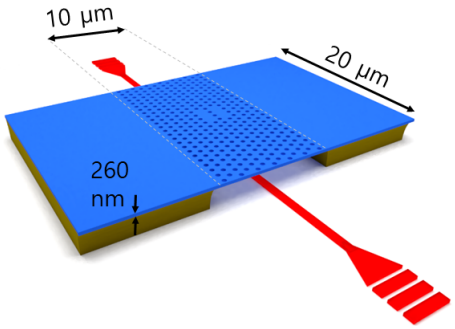

Figure 3.1 – Schematic of the optomechanical hybrid platform. The InP layer (blue) is suspended over a 20×10 µm^2 area thus defining the mechanical resonator. The SiN layer (brown) thickness is very exaggerated here. The SOI waveguide (red) lies below the membrane.

Method (FEM) software COMSOL Multiphysics [COMSOL, 2018]. The model inputs the membrane geometry, but do not integrate the array of holes since it considerably increases the simulation time. It is verified that the presence of the photonic crystal in the model does not change the shapes of the mechanical modes. The mechanical properties of InP used for the simulation include an effective Young's modulus $Y_{\text{eff}} = 17$ GPa, the Poisson's ratio (0.36) and the density (4810 kg.m^{-3}). Note that the Young modulus of bulk InP is significantly higher (60 GPa). Here the use of lower value is justified by the presence of the holes [Cepkauskas and Jianfeng, 2005], the use of thin layers and also by the presence of a InGaAs quantum well layer in the middle, which are all expected to impact the elastic and thermal properties of the material. Comparable value (20 GPa) was used with a similar device in [Gavartin et al., 2011]. In fig. 3.2a, the total displacement fields of the first 10 mechanical eigenmodes are shown. These modes involve most of the suspended material such that the effective mass of these modes compare with the actual mass of the suspended membrane. These "drum modes" yield in the MHz domain but higher order modes can be found up to few GHz. In particular, the mechanical modes confined in the L3-defect micro-cavity constitute an interesting ground for cavity optomechanics experiments, as the higher mechanical frequency is efficiently coupled to the optics [Gavartin et al., 2011]. Additionally, the clustered defect cavities are expected to house not only coupled optical modes but also coupled phononic normal modes, enabling the study of multimode cavity optomechanics. However, these GHz modes could not be observed in this work and we therefore focus on the drum modes of the membranes in this discussion. From the displacement field of the eigenmodes, we identify the mode indexes (m, n) where m (n) refers to the number of antinodes in the x (y) direction. This categorization of the modes is particularly well adapted for the description of a free rectangular membrane whose eigenfrequencies and associated displacement fields can

analytically expressed as a function of m and n.

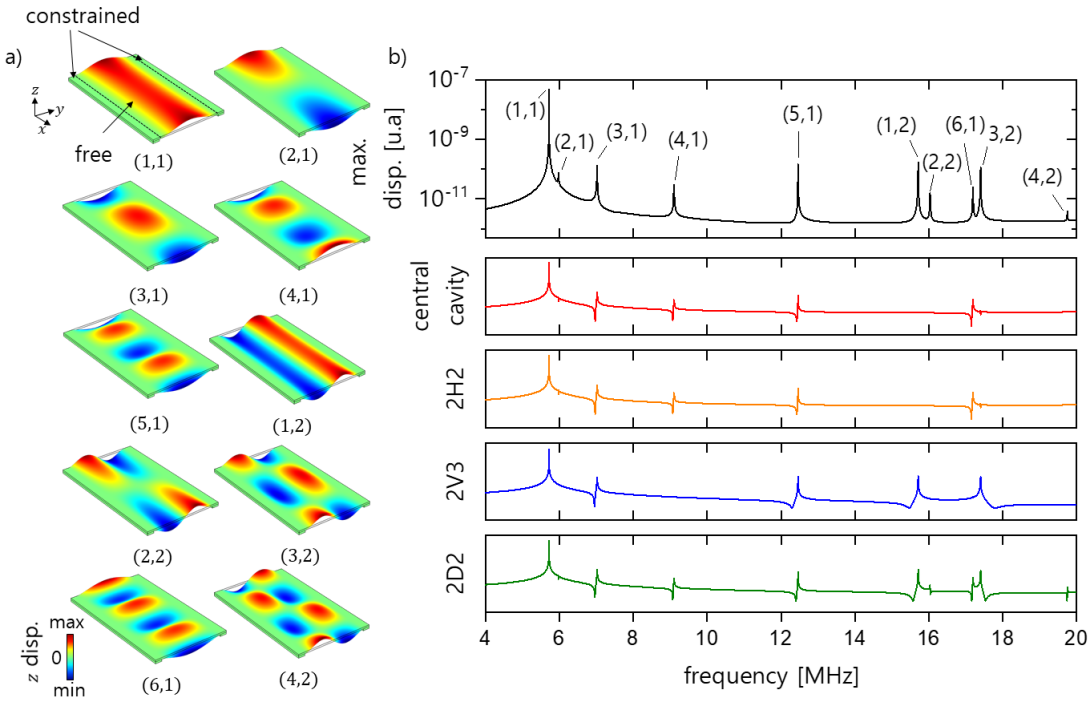

Figure 3.2 – a) First 10 mechanical eigenmodes displacement component (z) distributions fields. Each mode is labeled with its mode indexes (m, n). The constrains imposed in the simulations are indicated on the fundamental mode $(1, 1)$. b) Simulation total displacement in response with imposed frequency. From top to bottom : maximum response in the membrane, response in the central L3 cavity and then response in the 2nd cavity for the 2H2, 2V3 and 2D2 photonic molecules.

By imposing an harmonic excitation to the system, the fft-domain response of the membrane can also be simulated. As the displacement fields display some nodes, we plot the maximum total displacement of the membrane in fig. 3.2b (black line). Each displacement peak is labeled with the corresponding mode indexes. Interestingly, some modes have very low amplitude, e.g. the second mode $(2, 1)$ or the 10th mode (4,2). Starting with this observation, it seems rightful to wonder which of these modes will *a priori* be observable in the experiments. Indeed, the coupling strength between the mechanics and the optics, i.e. the optomechanical coupling basically depends on the strength of the overlap function between the $\overrightarrow{E}$ field and the displacement field distributions [Johnson et al., 2002]. If the displacement is weak, this coupling might be too low for the mode to be observed. More precisely, the displacement field must display significantly high amplitude where the photonic modes are confined. A qualitative approach therefore consist in checking the local displacement at the optical cavity positions. As described in section 2.1.2, the cavity positions depends the photonic molecule configuration. How-

ever, there is always a cavity placed at the membrane center. The fft-domain total displacement response at the center of this cavity is plotted with a red line in fig. 3.2b. As a matter of fact some eigenmodes yield zero amplitude at this point, suggesting that they will poorly couple with the photonic mode confined in this cavity. Similarly, the displacement field in the 2nd cavity for the 2H2, 2V3 and 2D2 configurations are plotted below with respectively orange, blue and green lines. The 2nd cavity of the 2H2 configuration, which is slightly shifted along the x axis from the central cavity, is submitted to a very similar displacement than this latter. However, when the second cavity is shifted along the (y) axis as in the 2V3 configuration, the eigenmodes arising in the displacement spectrum (blue line) are not the same. For example the modes $(4,1)$ and $(6,1)$ are visible in the 2H2 configuration but not in the 2V3, and the opposite in true for the modes $(1,2)$ and $(3,2)$. Finally, in the diagonal configuration 2D2, where the cavity in shifted both along the x and the y axis, the displacement spectrum (green line) displays all the eigenmodes of the membrane indicating that this configuration might be a good candidate for sensing as many mechanical modes as possible.

3.1.2 Mechanical noise spectrum measurement

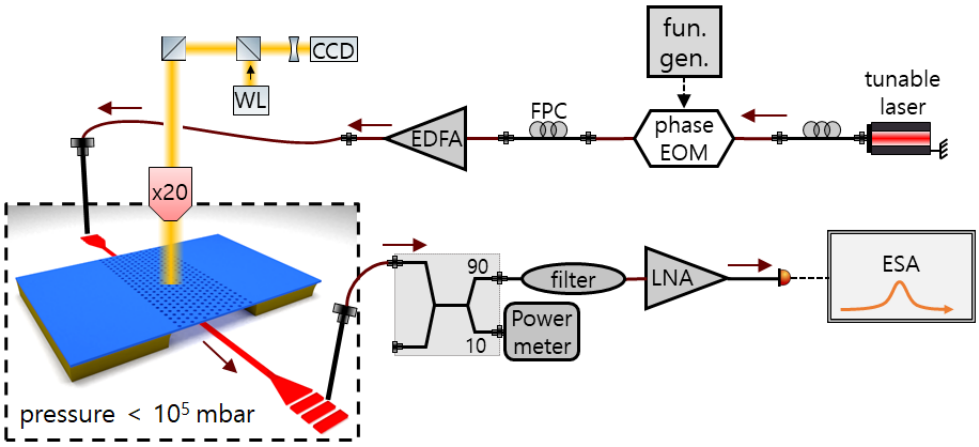

Figure 3.3 – Experimental setup implemented for the optomechanical characterization of the membranes.

As the system is put at finite-temperature, the mechanical eigenmodes of the suspended membrane are driven by thermal noise. The system naturally vibrates in a superposition of all its eigenmodes. The displacement associated to this displacement is very weak as the mechanical is not resonantly driven. However, this motion can still modulate the light field injected in the optical cavity through the optomechanical interaction.

After aligning the fiber at the waveguide grating couplers as indicated in section 2.3.1, the vacuum chamber is pumped below 10^{-5} mbar. A tunable laser is used to inject the

photonic crystal molecule (see fig. 3.3). The laser field is preliminary polarized with a fiber polarization controller (FPC) and amplified in an Erbium-Doped Fiber Amplifier (EDFA). The output signal is filtered and amplified in a low-noise amplifier (LNA). A photodetector converts the optical signal into a RF wave that is studied with an electrical spectrum analyzer (ESA). The ESA returns a noise spectrum $P(\omega)$ in units of dBm. The power spectral density (PSD in units of mW/Hz) is given by $S_P(\omega) = 10^{P(\omega)/10}/\mathrm{RBW}$ with RBW the resolution bandwidth of the ESA.

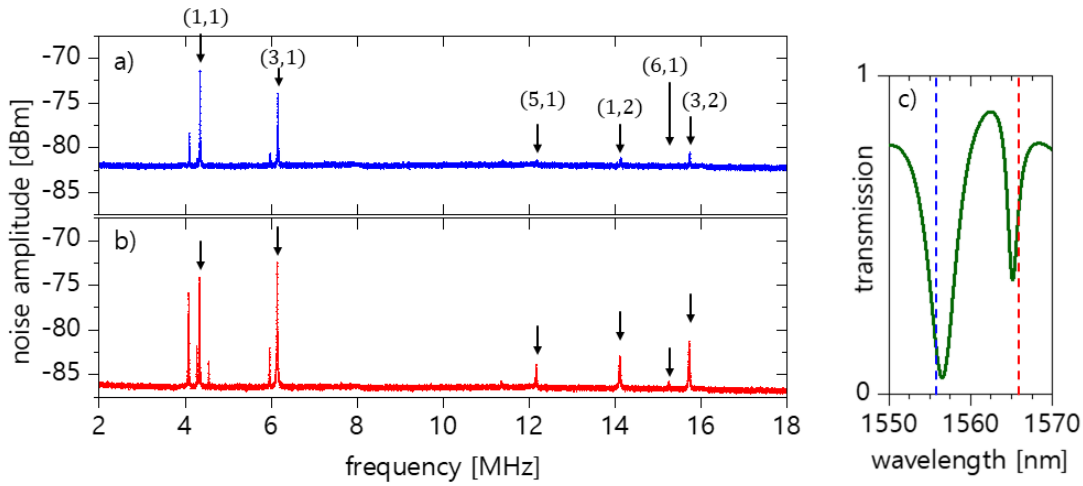

Figure 3.4 – Noise spectrum of a 2V3 PhC membrane obtained by resonantly driving: a) the anti-symmetrical optical mode with $\lambda = 1556$ nm b) the symmetrical optical mode with $\lambda = 1566$ nm. The arrows point at the modes belonging to the probed membrane. Each peaks is labeled with the corresponding mode indexes. c) Fit on the associated transmission spectrum characterized with a SLD source with the laser positions for each mode (dashed lines).

A typical noise spectrum is shown over a large frequency range by driving resonantly either the symmetrical (fig. 3.4a) or anti-symmetrical (fig. 3.4b) photonic mode. The transmission spectrum associated to this 2V3 structure is indicated in fig. 3.4c as a landmark. Both photonic modes being coupled to the same mechanical structure, the spectra are strongly correlated in terms of peak positions. However, these peaks have different amplitudes since the corresponding mechanical modes do not couple equally with the photonic modes. Some of the mechanical modes do not belong to the probed structure but the other two PhC membranes suspended over this waveguide. Although the laser does not probe resonantly these photonic molecules, it is still modulated by the mechanical noise. This is a signature of a dissipative optomechanical coupling of certain mechanical modes with the waveguide.

Each mechanical mode can then be identified to a displacement field distribution by

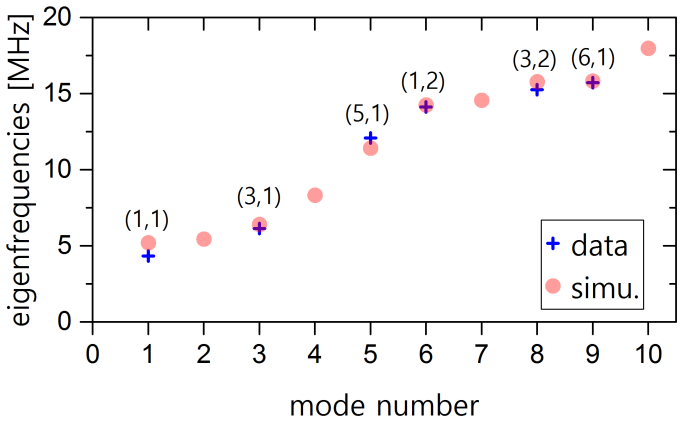

Figure 3.5 – Comparison between the measured (blue crosses) and simulated (red disks) mechanical eigenfrequencies. The data are provided by the 2V3 structure. The FEM simulation uses an effective Young modulus of the pierced InP nano layer $Y_{\text{eff}} = 17$ GPa.

comparing the experimentally measured frequencies with the eigenfrequencies found in FEM simulation. Here we assume that, among the eigenmodes found in the simulations, only those with a significant displacement amplitude at the cavity positions are coupled into the optics. According to what was discussed in section 3.1.1, we assume that modes $(2,1)$, $(4,1)$, $(2,2)$ and $(4,2)$ dot not coupled – or at least inefficiently couple – to the optics in the 2V3 configuration. By sorting the first 10 eigenmodes by ascending frequencies, the observed and simulated mechanical frequencies are compared in fig. 3.5. There is a consistent match between these two. As discussed previously, the simulation uses the effective Young modulus of the pierced nano-membrane $Y_{\text{eff}} = 17$ GPa to match the frequencies. There are still some small discrepancies between the observed and simulated eigenfrequencies. This can also come from the geometry simplifications in the simulation, as the absence of the photonic crystal holes, but it can also be explained by the misevaluation of the free-standing InP volume. Indeed the under-etched area can be slightly different than the defined 10×20 µm^2 mechanical membrane, e.g. if the under-etching step is prolonged a little too much.

In order to distinguish the mechanical modes sustained by the probed membrane from the others, it is also possible to shine the 820 nm diode-laser at the membranes and observe a thermal shift of the resonances. The thermal load of the laser of the mechanical structure induces a change of the material density which shifts the internal stress in the mechanical resonator. This photothermal effect displaces the mechanical resonances towards low or high frequencies depending on the initial stress in the structure. In figs. 3.6a to 3.6c, we show the mechanical spectrum obtained when heating either of the three membranes. These latter are refereed as A, B or C with respective hole radius 90 nm, 100 nm and 110 nm. Let's recall that the larger the hole radius, the

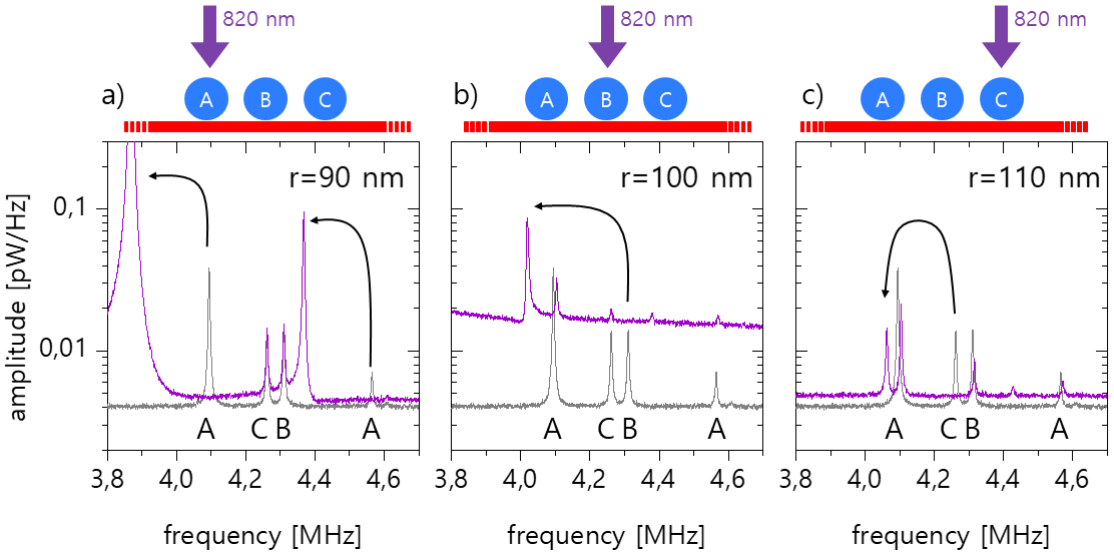

Figure 3.6 – Mechanical noise spectrum measured by driving membrane B optical mode, with $\lambda = 1564$ nm (grey lines). Identical measurement performed when using the 820 nm laser for heating (purple lines): a) the membrane A, b) the membrane B and c) the membrane C. The mechanical frequency shifts (black arrows) belong to the heated membrane.

larger the photonic mode resonance wavelength. In each case, the injected tunable laser wavelength is set to 1564 nm such that it resonantly probes the anti-symmetrical photonic mode of the structure B when the diode laser is off. The mechanical spectrum thus obtained is shown with grey lines is each configuration. This measurement shows 4 mechanical peaks. When heating the membrane A, two of these mechanical frequencies shift towards lower frequencies. We therefore identify these peaks as sustained by the membrane A. Moreover the corresponding optical modes drifts such that it is resonantly driven by the tunable laser. This leads to an enhancement of the mechanical peaks amplitudes. The amplitude of the 1st peak, that is hidden by the figure scale, increases up to 2.84 pW/Hz. This consequent amplification of the mechanical noise might also be the result of more complicated interactions involving the quantum dots that are pumped by the diode laser [Tsvirkun et al., 2016]. Such dynamics is not further investigated in this work. Heating the membrane B or C both lead to the shift of one of the remaining mechanical frequency such that all the modes that ultimately be identified to a given membrane. Note that, when heating the membrane B, the optical resonance is shifted toward lower wavelengths. Thus the tunable laser no longer drives resonantly the optical resonance dip and the resulting increase in the transmission explains the higher noise floor in the spectrum.

3.2 Optomechanical couplings

The lecture of the mechanical is enabled by the optomechanical interactions standing in the system. A basic description of an optomechanical cavity is based of the frequency modulation of the optical cavity by the mechanical motion. In this frame the coupling can be measured using a phase modulation of the input laser field. At first, we apply this method to calibrate several mechanical resonances read either through the symmetrical or the anti-symmetrical optical resonances. Then we propose a more advanced model that now also includes the dissipative optomechanical contributions. In order to quantify these contributions, we scan a laser on the optical resonances. This experiment evidence a thermo-mechanical shift of the mechanical frequencies which is understood in the frame of a toy-model.

3.2.1 Calibration of the single-photon coupling strength

The optomechanical single-photon coupling strength g_0 [Aspelmeyer et al., 2014] is at center of the interactions occurring in an optomechanical cavity where only the optical resonance frequency is affected by the mechanical motion. It can be estimated experimentally by comparing the mechanical mode amplitude with the amplitude of a calibrated near-resonant phase modulation signal [Gorodetksy et al., 2010; Schliesser et al., 2008]. The optical field injected in the integrated waveguide is preliminary modulated with a phase Electro-Optic Modulator (EOM) in which a sinusoidal signal is sent with amplitude V_{mod} and frequency f_{mod} (see fig. 3.3). The induced phase modulation of the optical field reaches a phase shift given by $\beta = \pi V_{\mathrm{mod}}/V_\pi$ where $V_\pi = 3.5$ V is the voltage at which the device provides a phase-shift of π. The modulation frequency is set close to the mechanical resonance to be calibrated. In these conditions, the optomechanical coupling is given by

$$g_0 \approx \sqrt{\frac{1}{2\overline{n}} \frac{\beta^2 \Omega_{\mathrm{mod}}^2}{2} \frac{\Gamma_m}{4\mathrm{RBW}} \frac{S_P(\Omega_m)}{S_P(\Omega_{\mathrm{mod}})}} \tag{3.1}$$

where $\overline{n} = k_B\theta_0/\hbar\Omega_m$ is the mean phonon number in the mechanical oscillator at temperature θ_0 (293K in our experiment). The power spectral density is measured with a resolution bandwidth RBW. The mechanical resonance is fitted with a Lorentzian lineshape allowing to extract the mechanical resonance frequency Ω_m and the mechanical linewidth Γ_m. The modulation peak is fitted with a Gaussian function. For each fit the peak power is also obtained such that the ratio $S_P(\Omega_m)/S_P(\Omega_{\mathrm{mod}})$ is accurately determined.

This technique is applied to a 2V3 structure to measure the coupling between the optical modes and five mechanical eigenmodes. The fitted PSD measured with $\mathrm{RBW} = 20$ Hz at the fundamental mode is shown in fig. 3.7a and fig. 3.7b respectively for the

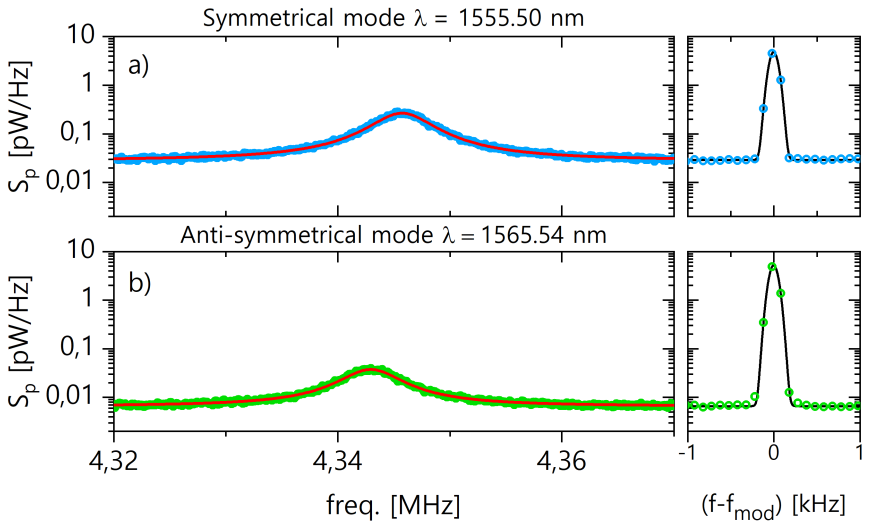

Figure 3.7 – Experimental calibration of the optomechanical coupling g_0 between the fundamental mechanical mode and either a) the $(-)$ optical resonance or b) the $(+)$ optical resonance. In each case, the resonance is fitted with a Lorentzian lineshape (left) and the modulation signal is fitted with a Gaussian peak (right).

$(-)$ photonic mode ($\lambda = 1555.50$ nm) and the $(+)$ photonic mode ($\lambda = 1565.54$ nm). The modulation frequency is set to $f_{\mathrm{mod}} = 4.281$ MHz and the modulation amplitude to $V_{\mathrm{mod}} = 6$ mV. The fitted modulation peak is shown over a different frequency scale. The optomechanical couplings are evaluated using the experimental parameters. This protocol is reproduced for the next 4 mechanical modes and the results are presented in table 3.1. The 3rd and 4th mechanical modes were not measurable through the optical mode $(+)$. This experimental calibration provides an order of magnitude for the optomechanical coupling rate reached in our system. In our system the coupling mechanism in our system can not be reduced to a simple modulation of the cavity frequency by the mechanics. The dissipation rates are also affected by the motion. In the following the relative weights of the dissipative and dispersive contributions will be modeled and estimated.

3.2.2 Dispersive and dissipative optomechanical couplings

Here we describe how the mechanical displacement modulates the optical field propagating in the waveguide, through the photonic molecule. It involves several contributions whose nature, either dispersive or dissipative, is discussed. In order to experimentally access the mechanical noise spectrum, we exploit the optomechanical interactions standing in the waveguide/PhC system. In section 2.2, the coupled mode analysis of the integrated photonic system enables a complete description of the waveguide transmission

Mech. mode index	$\Omega_m/2\pi$ [MHz]	$\Gamma_m/2\pi$ [kHz]	Q_m	$g_0/2\pi$ [Hz] MODE $(-)$	$g_0/2\pi$ [Hz] MODE $(+)$
$(1,1)$	4.34	5.56	778	485.0	174.6
$(3,1)$	6.15	7.61	1237	514.1	227.7
$(5,1)$	12.18	17.63	691	1420.8	$\varnothing$
$(1,2)$	14.13	23.49	601	985.3	$\varnothing$
$(6,1)$	15.74	16.25	969	1843.5	380.2

Table 3.1 – Experimentally measured frequency Ω_m, linewidth Γ_m, quality factor $Q_m = \Omega_m/\Gamma_m$ for 5 mechanical resonances. The calibrated optomechanical coupling g_0 is obtained either through the $(-)$ or the $(+)$ photonic resonances in this 2V3 photonic molecule.

and the influence of the coupling parameters. Now we need to describe how a tiny perturbation for each of these parameters, caused by the mechanical displacement of the suspended PhC, can affect the transmitted signal [Wu et al., 2014; Tsvirkun et al., 2015]. We write down an expression for the transmission derivative involving several optomechanical contributions:

$$\frac{\mathrm{d}T}{\mathrm{d}x} = \left[\sum_k G_{\omega_k}\frac{\partial T}{\partial \omega_k} + G_\mu \frac{\partial T}{\partial \mu} + \sum_k G_{\kappa_{i,k}}\frac{\partial T}{\partial \kappa_{i,k}} + \sum_k G_{\kappa_{w,k}}\frac{\partial T}{\partial \kappa_{w,k}} + G_\phi \frac{\partial T}{\partial \phi}\right] \tag{3.2}$$

with G_{ω_k}, G_μ, $G_{\kappa_{i,k}}$, $G_{\kappa_{w,k}}$ and G_ϕ the derivatives $d\cdot/dx$ where $\cdot$ refers respectively to the frequency of cavity k, the coupling rate, the internal dissipation rate of cavity k, the external dissipation rate of cavity k and the phase. At this stage already, we can glimpse how complicated this descriptions is going to be. Indeed, the number of optomechanical contributions is too important for an efficient analysis of the data on the one hand, and for a rigorous and rational interpretation on the other hand.

In fact, it is not necessary to take into account a 2-cavity model for the transmission as soon as i) the optical drive frequency is set near an optical resonance and ii) the optical modes are well resolved in the optical spectrum. In particular this second condition implies that the Fano interferences resulting from low-Q cavities or low coupling rate should not be significant enough to prevent the description of each optical normal mode with a Lorentzian lineshape.

By assuming that each normal mode behaves as the result of a single waveguide-coupled cavity, we simplify the model by using a new expression for the transmission derivative:

$$\frac{\mathrm{d}T}{\mathrm{d}x} \approx G_{\omega_0}\frac{\partial T}{\partial \Delta} + G_{\kappa_i}\frac{\partial T}{\partial \kappa_i} + G_{\kappa_\mathrm{w}}\frac{\partial T}{\partial \kappa_\mathrm{w}} \tag{3.3}$$

with $\Delta = \omega_L - \omega_0$, κ_i and κ_w respectively the laser detuning, the internal loss rate and

the external loss rate of the single optical resonator. Here the transmission is given by eq. (2.4) but can be rewritten in terms of the relative detuning $\Delta/2\kappa_t$ where $\kappa_t = \kappa_i + \kappa_{\mathrm{w}}$ is the total amplitude decay rate of the mode:

$$T = \frac{(\Delta/2\kappa_t)^2 + (\kappa_i/2\kappa_t)^2}{(\Delta/2\kappa_t)^2 + 1/4} \tag{3.4}$$

In practice in the experiments, we will consider either the $(-)$ or the $(+)$ photonic mode with their respective resonance frequency and linewidth $\omega_\pm$ and $2\kappa_\pm$.

Now the global optomechanical interaction involves only three contributions G_{ω_0}, G_{κ_i} and $G_{\kappa_{\mathrm{w}}}$. The first one reflects how the mechanical displacement affects the optical frequency and therefore form the dispersive part of the coupling. In opposition the two other contributions participate to the dissipative part of the interaction. Under a small modification of the cavity properties, the resonance dip in the transmission spectrum is modified as shown in fig. 3.8 (top). At a given detuning Δ, the intensity changes by an amount given by the partial derivative associated to the changing parameter. These partial derivatives are plotted in fig. 3.8 (bottom) as a function of the detuning, assuming a critical coupling regime $\kappa_i = \kappa_{\mathrm{w}}$[1].

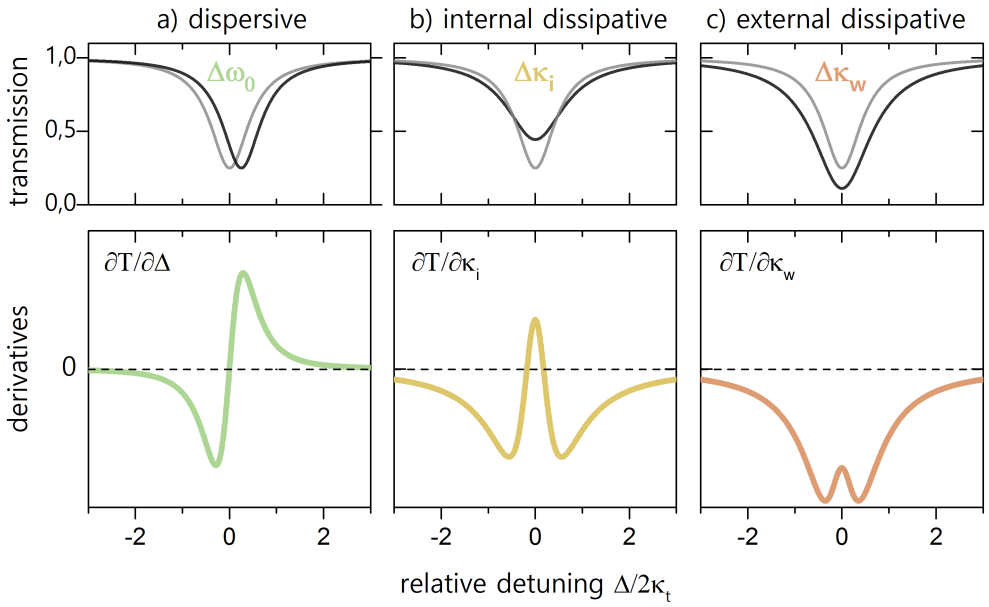

Figure 3.8 – Impact of a variation of the resonant frequency (a), the intrinsic loss rate (b) and the external loss rate (c) on the transmission spectrum (top). The associated partial derivatives (bottom) correspond to the respective contributions to the optomechanical coupling. Plot realized at the critical coupling ($\kappa_i = \kappa_{\mathrm{w}}$).

[1] The influence of the coupling efficiency $\kappa_{\mathrm{w}}/\kappa_t$ on these sensitivity functions is studied in details in [Tsvirkun, 2015] , Sec.2.3

3.3 Influence of the detuning

As the transduction of mechanical motion into the optical field is enhanced by the cavity, it is interesting to scan the optical resonance to investigate on the interactions between the cavity and the mechanics. In this experiment we scan the optical modes around the resonance and record the mechanical noise spectrum for a given eigenmode. From the data we can extract the amplitude of the mechanical peak amplitude and position as a function of the detuning for each optical mode. The first permits to evaluate the dissipative and dispersive contributions to the optomechanical coupling. The frequency shift is discussed through a toy-model based on a thermo-mechanical process.

3.3.1 Optomechanical contributions

The optomechanical interactions can not be reduced to the single-photon coupling strength g_0 calibrated in the previous section. Actually, as discussed in section 3.2.2, the transduction of a mechanical signal into the transmitted optical wave occurs through a dispersive process – in which the cavity frequency is perturbed by the motion – but also through a dissipative process, where the cavity loss rates are perturbed. In order to evaluate the balance between these contributions, only the optical frequency can be experimentally played with. Indeed our modeling relies on the linear coupled mode analysis of the photonic platform and the laser intensity must therefore be set sufficiently low so that no nonlinear regime is reached. In practice, the thermo-optic nonlinearity described in section 2.4 tends to distort the optical resonance dip and provokes hysteretic behaviors. The goal in the following experiment is therefore to measure the mechanical mode while scanning either the $(-)$ or the $(+)$ optical resonances with the laser. The evolution of the mechanical peak amplitude as a function of the detuning thus enables an evaluation of the optomechanical couplings.

The measured power spectral density relates to the mechanical oscillator PSD S_{xx} (in units of m^2/Hz) with [Bunch et al., 2007] :

$$S_P(\omega) = S_P^{(n)} + \eta^2 S_{xx}(\omega) \tag{3.5}$$

where the constant offset $S_P^{(n)}$ is the white noise of the detectors. The parameter η reflects how well the mechanical signal is converted in the electrical signal detected by the ESA[2]. Here we split this conversion coefficient with

$$\eta = \chi \times \frac{\mathrm{d}T}{\mathrm{d}x} \tag{3.6}$$

where χ involves several parameters such as the photodetector conversion efficiency, the optical and electrical power losses or the ESA load impedance. The optomechanical cou-

[2] $s_x^0 = \sqrt{S_P^{(n)}/\eta^2}$ is the displacement sensitivity of the experimental setup (in units of $\mathrm{nm}/\sqrt{\mathrm{Hz}}$)

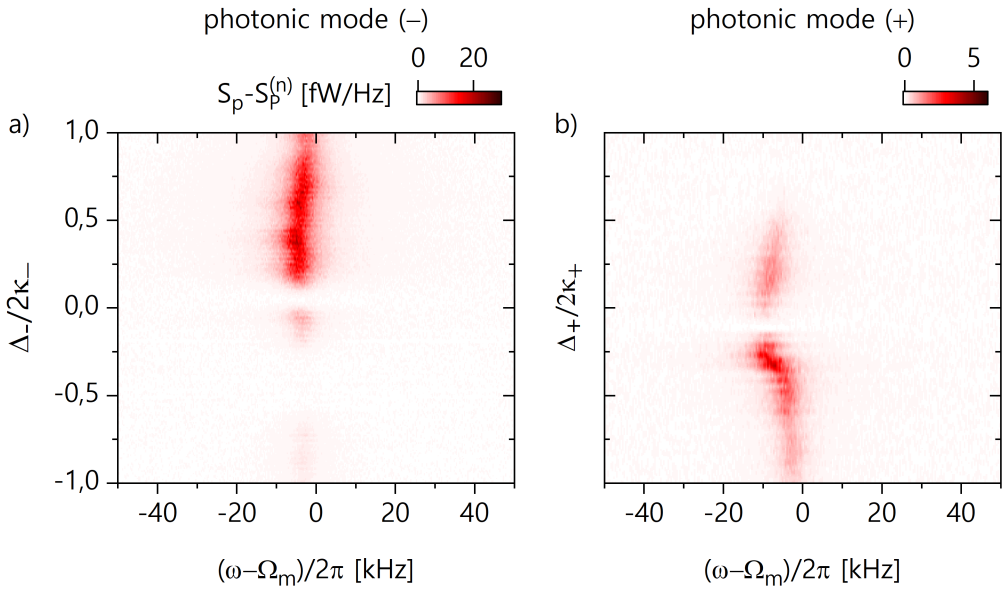

Figure 3.9 – Influence of the detuning on the fundamental mechanical mode lineshape with $P_{\rm in} = 480$ µW. a) The laser scans the optical mode $(-)$ and the noise spectrum is accessed through this same laser. b) Similarly with the optical mode $(+)$.

pling is given by $\mathrm{d}T/\mathrm{d}x$ which can be expanded in partial derivatives of the transmission (see eq. (3.3)).

Additionally, the mechanical oscillator PSD is given by the equipartition theorem [Albrecht et al., 1991]:

$$S_{xx}(\omega) \propto \frac{\Gamma_m}{(\omega^2 - \Omega_m^2)^2 + (\omega\Gamma_m)^2} \tag{3.7}$$

with Ω_m the oscillator frequency and Γ_m its mechanical linewidth. Note that the exact formulation permits to calibrate the mechanical displacement by assuming the effective mass $m_{\rm eff}$ of the mechanical mode. However in this section we only give a qualitative description of the optomechanical contributions. This can be done without the calibration of the detection scheme (χ) and of the mechanical displacement, given by evaluating the effective mass $(m_{\rm eff})$.

This experiment is performed on a 2V3 photonic molecule sustaining two optical resonances at $\lambda_- = 1557.27$ nm and $\lambda_+ = 1565.55$ nm. The internal Q of the cavities is estimated above $Q_i = 10^4$ and their respective external Q are $Q_{\rm w}^- = 470$ and $Q_{\rm w}^+ = 6680$. We measure the mechanical noise spectrum around the fundamental resonance centered at $\Omega_m = 2\pi \times 4.34$ MHz. The ESA averages 50 spectra with a resolution bandwidth $\mathrm{RBW} = 50$ Hz. This measurement is automatized to be reproduced while the laser frequency scans the optical resonance $(-)$. For each spectrum, the noise floor $S_P^{(n)}$ is estimated by averaging the PSD away from the mechanical resonance. The net mechanical noise PSD $S_P(\omega) - S_P^{(n)}$ is presented as a function of the relative

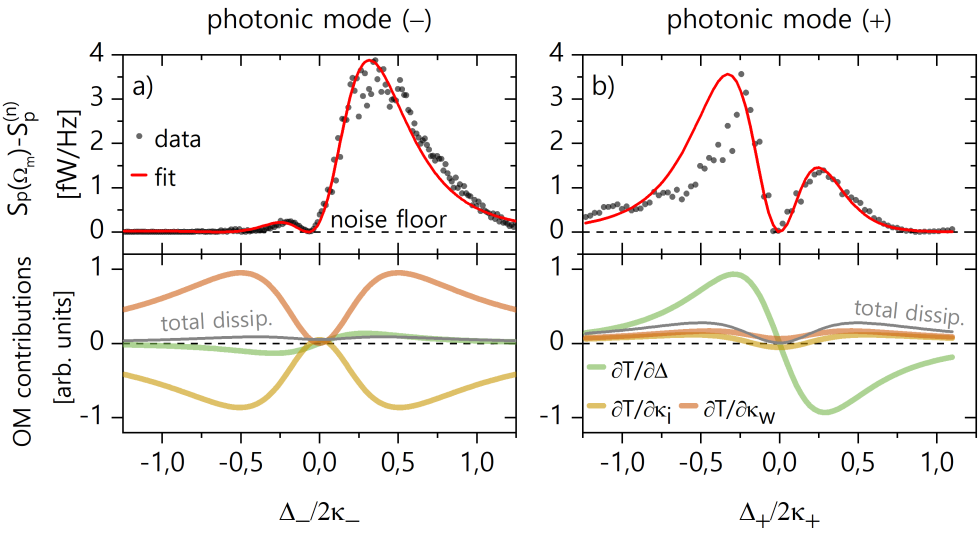

Figure 3.10 – Net amplitude of the mechanical peak obtained by fitting a) the data presented in fig. 3.9a and b) the data presented in fig. 3.9b. The fit considers a weighted sum of the partial derivatives of the transmission with the weights as fitting parameters. These three weighted functions are plotted below for reference.

detuning $\Delta_-/2\kappa_-$ in fig. 3.9a. This measurement is reproduced while scanning the other optical resonance. The mechanical mode transduction in the optics clearly depends on the detuning as its peak amplitude varies. We also note a pronounced shift of the mechanical frequency near the optical resonances. This is more manifest for the mode $(+)$ as discussed further on.

For each value of the detuning, the PSD $S_P(\omega)$ is fitted using eq. (3.5) returning the mechanical frequency Ω_m, the mechanical linewidth Γ_m and resonant PSD amplitude $S_P(\Omega_m)$. We focus on the latter to obtain the different optomechanical contributions. The net mechanical peak amplitude is indeed directly proportional to the transduction constant η^2. We show the net amplitude obtained from figs. 3.9a and 3.9b respectively in figs. 3.10a and 3.10b. It is therefore possible to fit this quantity, plotted as a function of the relative detuning, with $(\mathrm{d}T/\mathrm{d}x)^2$ (given by eq. (3.3)) since no other parameter included in η is expected to vary with the detuning. Again, as the experimental calibration parameter χ is not known, a quantitative evaluation of the optomechanical couplings is not possible. Only the relative strengths of the different contributions can be obtained here. The net amplitude is fitted using the uncalibrated optomechanical coupling strengths χG_{ω_0}, χG_{κ_i} and χG_{κ_w}. The three partial derivatives are plotted below, weighted by the corresponding strength. The total dissipative contribution, defined by $G_{\kappa_w}\frac{\partial T}{\partial \kappa_w} + G_{\kappa_i}\frac{\partial T}{\partial \kappa_i}$, is also plotted (gray line) to be compared with the dispersive contribution $G_{\omega_0}\frac{\partial T}{\partial \Delta}$. The fit yields a satisfactory agreement with the experimental data.

The fit evidence a clear imbalance between the dispersive and dissipative contributions to the optomechanical coupling. For the optical mode $(-)$, that carries a total optical quality factor $Q_- \approx 470$, the coupling is dominated by the two dissipative components. From the fit, we estimate $G_{\kappa_{i,-}}/G_{\omega_-} \approx 4.38$ and $G_{\kappa_{w,-}}/G_{\omega_-} \approx -4.61$. However for the optical mode $(+)$, for which we evaluate $Q_+ \approx 6680$, the dispersive contribution g_{ω_+} dominates the optomechanical coupling and the dissipative components $G_{\kappa_{i,+}}/G_{\omega_+} \approx 0.12$ and $G_{\kappa_{w,+}}/G_{\omega_+} \approx 0.09$ are weak. This shows that the balance between the dispersive and dissipative processes participating to the optomechanical interaction does not only depend on the displacement field distribution of the mechanical mode, but also on the optical resonance properties. Nonetheless, the signs of the dissipative contributions are such that the total dissipative component (gray line) remains comparable to the dispersive component. Thus for both modes the total dissipative component compares with the dispersive contribution.

3.3.2 Thermo-mechanics effect

The mechanical frequency shift observed when scanning the optical modes is now investigated through a simple thermo-mechanics model. We plot the frequency shift $\delta\Omega_m$ as function of the relative detuning $\Delta_-/2\kappa_-$ and $\Delta_+/2\kappa_+$ respectively in figs. 3.11a and 3.11b. The reference frequency (when $\delta\Omega_m = 0$) is given by the fit as discussed in the following.

Preliminary, it seems necessary to comment on the fact that this shift can not be described via the optical spring effect (OSE) as introduced in the theory of cavity optomechanics [Aspelmeyer et al., 2014]. Injecting our system parameters, including the optical linewidths, the mechanical frequency and the dispersive optomechanical coupling, the theory indeed predicts a shift below 1Hz, namely 3 to 4 order of magnitudes below the shift actually observed in our experiments. Additionally the mechanical linewidth Γ_m extracted for the fits is constant with the detuning. This is an additional indication that dynamical backaction is negligible in this optomechanical system. It seems more reasonable, given the importance of thermal effects in the optics, that this frequency shift finds its origin in a thermo-mechanical effect.

Temperature growth in the bulk is expected to create material dilatation which modifies the mechanical properties of the structure. We derive a model based on a 1D mechanical resonator characterized by the membrane effective Young's modulus Y_{eff} and submitted to an internal stress σ_0 at ambient temperature [St-Gelais et al., 2019]. When submitted to a temperature effective variation $\Delta\theta_{\text{mech}}$, the resonator equilibrium position (originally $x_0 = \sigma_0/Y$) is shifted by an amount $|\Delta x/x_0| = \alpha\Delta\theta_{\text{mech}}$ with α the thermal expansion coefficient of the material. The sign of this shift depends on whether the material is initially submitted to a compression internal stress ($\Delta x/x_0 < 0$) or to a

tensile internal stress ($\Delta x/x_0 > 0$). As this model will be applied to a structure in which the mechanical frequency decreases with the temperature, we will assume σ_0 to be compressive in the following. The new internal stress is then given by $\sigma = \sigma_0 - Y\alpha\Delta\theta_{\mathrm{mech}}$. As the mechanical frequency is proportional to $\sqrt{\sigma}$, it can be expressed as a function of the temperature effective growth with

$$\Omega_m = \Omega_{m,0}\sqrt{1 - \frac{Y}{\sigma_0}\alpha\Delta\theta_{\mathrm{mech}}} \tag{3.8}$$

with $\Omega_{m,0}/2\pi$ the mechanical frequency at room temperature.

In order to relate the effective temperature shift to the photothermal processes involved in the experiment, we suppose that this quantity is proportional to the power dissipated in the optical cavity. In the description of the thermo-optic nonlinearity (see section 2.4), the temperature shift inside the cavity is related to the cavity energy $|a|^2$ through the linear absorption rate κ_{abs} of the cavity and the material thermal resistance R_{th} such that $\Delta\theta_{\mathrm{cav}} = R_{th}\kappa_{\mathrm{abs}}|a|^2$.

However, contrary to the thermo-optic effect in which only the temperature of the micro-cavity matters, our thermo-mechanical model involves the temperature shift of the entire membrane. As the photonic modes are localized in the defect cavities, the temperature distribution in the membrane should be inhomogeneous. Moreover, the temperature influence on the mechanical frequency should also depend on the overlap between the mechanical displacement field and the temperature distribution such that a heat source placed close to the clamping regions should influence less on the mechanics than the same source placed at a displacement antinode. With these few considerations, it appears that the temperature shift in the cavity is different from the effective temperature on the membrane. We introduce a constant $\xi = \Delta\theta_{\mathrm{mech}}/\Delta\theta_{\mathrm{cav}}$ depending *a priori* both on the system geometry (photonic molecule orientation and position) and on the considered mechanical eigenmode.

The mechanical frequency extracted from the fits of the mechanical spectra (see figs. 3.9a and 3.9b) is plotted as a function of the relative detuning for each optical mode in figs. 3.11a and 3.11b. The data points are fitted with the expression $\Omega_m = \Omega_{m,0}\sqrt{1 - A|a|^2}$ with using the free parameters $\Omega_{m,0}$ and $A = \frac{Y\alpha\xi\kappa_{\mathrm{abs}}R_{th}}{\sigma_0}$. The cavity energy $|a|^2$ is given by eq. (2.2). The fit accurately describes the mechanical frequency shift. The ambient temperature frequency $\Omega_{m,0} \approx 2\pi \times 4.35$ MHz is subtracted to the data in order to represent the frequency shift $\delta\Omega_m = \Omega_m - \Omega_{m,0}$.

To comment of the validity on this model, it is interesting to extract a value for the parameter ξ. We use the effective Young's modulus of the InP membrane $Y \approx 17$ GPa (see simulations in section 3.1.1) and its thermal expansion $\alpha = 4.6 \times 10^{-6}\mathrm{K}^{-1}$ [Glazov et al., 1977][3]. The values for the linear absorption rate and the thermal resistance are

[3] See http://www.ioffe.ru/SVA/NSM/Semicond/InP/ for more details on InP constants.

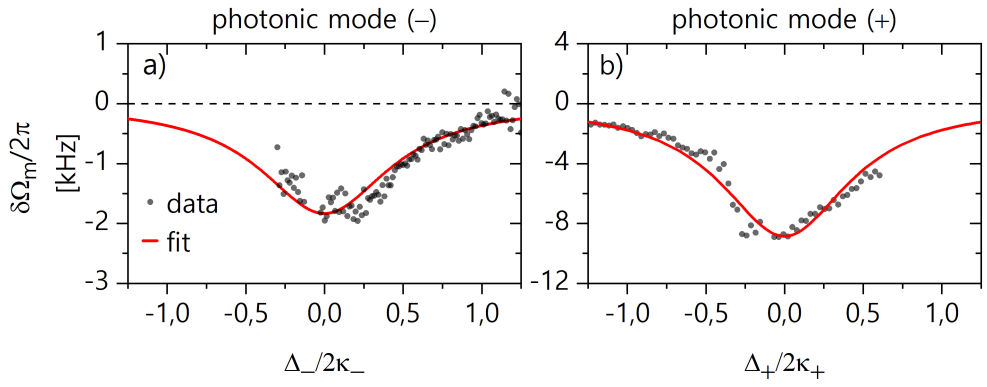

Figure 3.11 – Fundamental mechanical mode frequency shift when scanning a) the $(-)$ optical mode or b) the $(-)$ optical mode. The data (dots) are obtained by fitting the mechanical peak and are fitted (red lines) with the scaled cavity internal power.

taken from the study of thermo-optic effect with the same structure, where the fit of the nonlinear transmission gives the product $\kappa_{\mathrm{abs}} R_{th} \approx 1.62$ K.fJ^{-1}. Finally, the internal compressive stress in the membrane can be estimated from the mechanical frequency and the material density ($\rho = 4810$ kg.m^{-3} for InP), relying on the analytic expression of the fundamental eigenfrequency (using the general expression given in [Hauer et al., 2013] with $\mathrm{m} = \mathrm{n} = 1$) in a rectangular membrane with dimensions $L_x \times L_y$:

$$\Omega_{0,0}/2\pi = \frac{1}{2}\sqrt{\frac{\sigma_0}{\rho}\left[\frac{1}{L_x^2} + \frac{1}{L_y^2}\right]} \tag{3.9}$$

For our fundamental eigenmode of the 10×20 µm^2 membrane, we find $\sigma_0 \approx 29.0$ MPa. Finally, one can evaluate the cavity-to-membrane temperature shift ratio for the fitting parameter A. The values $\xi_- \approx 0.61$ and $\xi_+ \approx 0.98$ are respectively found for the $(-)$ and the $(+)$ optical modes. It can be interpreted that the mode $(+)$ heats more efficiently the mechanics than the mode $(-)$. As the temperature in the cavity is higher than the mean membrane temperature, this parameter is expected to be lower than one. It can be numerically estimated by simulating the thermal equilibrium in the structure with Comsol. The cavity volume is set at a temperature $\theta_0 + \Delta\theta$ by inserting a heat source inside. The bottom of the SiN layer, that are in contact with the Silicon substrate in our chip, is constrained to ambient temperature θ_0. At the thermal equilibrium, the simulation provides the temperature distribution on the structure (see fig. 3.12a). The dissipated power (heat source) is swept such that the mean temperature shift of the membrane can be plotted as a function of the mean cavity temperature (see fig. 3.12b). The slope gives the cavity-to-membrane temperature shift ratio $\xi = 0.22$. We also verify that the temperature in the cavity is linear with the dissipated power in the heat source, which is important to confirm that ξ is constant in our model. The simulation inputs the

thermal conductivity of InP and of SiN (resp. $\sigma_{th}^{\mathrm{InP}} = 0.68$ W.cm^{-1}.K^{-1} and $\sigma_{th}^{\mathrm{SiN}} = 0.1$ W.cm^{-1}.K^{-1}) [Glazov et al., 1977].

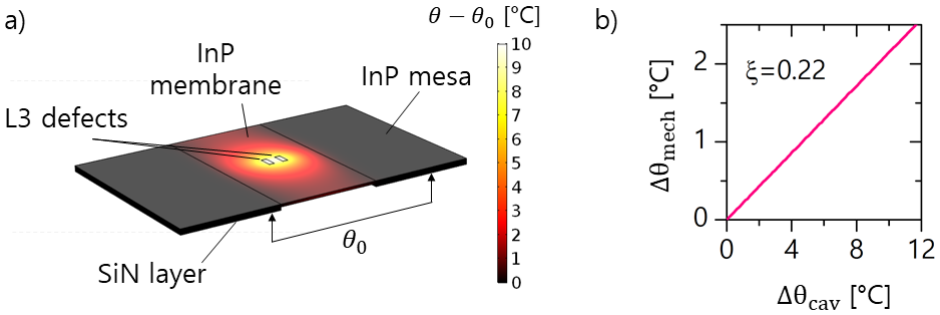

Figure 3.12 – a) Temperature distribution at equilibrium. The ambient temperature θ_0 is imposed on the membrane clamps. b) The mean temperature shift $\Delta\theta_{\mathrm{mech}}$ in the membrane is evaluated as a function of the mean temperature shift $\Delta\theta_{\mathrm{cav}}$ in the L3 defects with Comsol. The simulated membrane-to-cavity temperature shift ratio $\xi = 0.22$ is given by the slope.

There are many sources of uncertainty in this toy-model, starting with all the material constants that do not consider the InGaAs quantum well layer present in the membrane, as well as the geometrical approximations – e.g. the expression used to calculate the compressive stress is valid for an unclamped rectangular membrane. As the values that are found for the temperature shift ratio yields below 1 with a coherent order of magnitude, we conclude that the model agrees qualitatively with the observed physics[4].

With this model it is clear that the distortion of the optical lineshape under thermo-optic effect would transduce directly in the mechanical frequencies. In particular, by injecting higher input power, a bistability can emerge in the system near the resonance wavelength (see section 2.4). Thus by scanning the optical resonance with an input power enabling such hysteretic behavior to occur, it is expected that the mechanical modes also experience hysteretic shift of their frequency. We perform this experimental test with an input laser power $P_{\mathrm{in}} = 1.3$ mW. The resulting noise spectrum is plotted as a function of the laser detuning regarding the resonance of optical mode $(-)$ in fig. 3.13a and mode $(+)$ in fig. 3.13b. The optical mode $(-)$ has low optical Q and is not distorted enough to become bistable at this input power. The frequency shifts slightly to lower frequency and the mode amplitude evolves similarly to the low input power situation shown previously. However, when the optical mode $(+)$ in scanned, the frequency of the fundamental mechanical mode clearly displays an abrupt jump around

[4]It could be interesting to enrich the toy model with temperature dependent elastic constants, which is not the case here, see e.g. [Branicio et al., 2009]

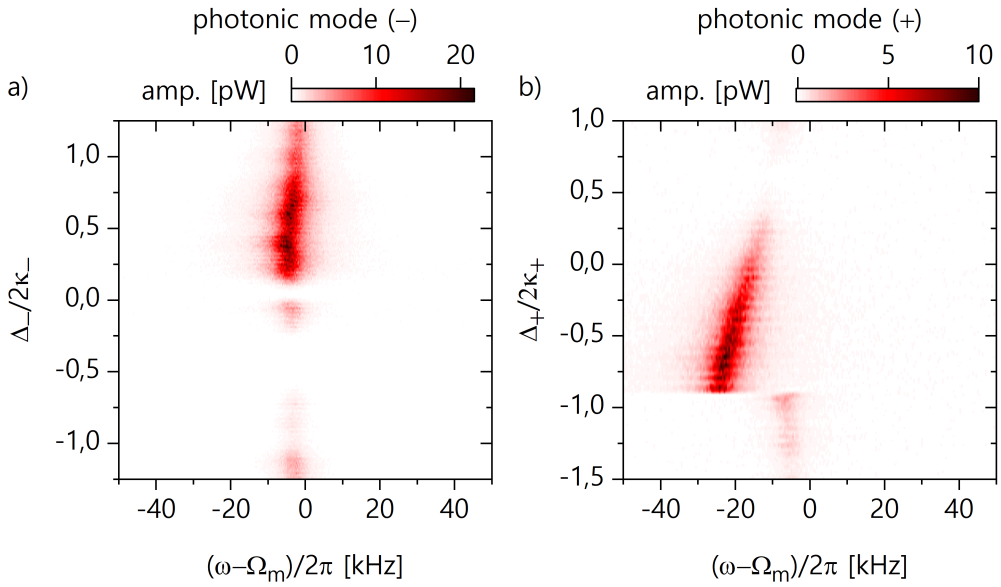

Figure 3.13 – Influence of the detuning on the fundamental mechanical mode lineshape with $P_{\mathrm{in}} = 1.3$ mW. a) The tunable laser scans the optical mode $(-)$ and the noise spectrum is accessed either through this same laser. b) Similarly by scanning the optical mode $(+)$. The thermo-optic nonlinear response is imprinted in the mechanical frequency through the photo-thermal process.

$\Delta_+/2\kappa_+ \approx 1.25$. Note that here the measurement is performed with increasing laser wavelength ($\Delta_+/2\kappa_+$ is swept from 1 to -1.5) [5]. Here again the contrast between the observations made on the two optical modes is very pronounced. This is only caused by the difference of external quality factors

With the experiments shown in this section, the mechanical properties are accessed through the same laser used for driving a given optical mode. In appendix B, we show additional measurements in which a first laser is used to scan an optical mode – possibly inducing thermo-mechanical shifts due to its power – while a second "passive" tunable laser drives the other optical mode at constant wavelength and low power. This way, the mechanical mode frequency shift and the variation of its amplitude are accessed in an alternative way.

[5] The reverse sweep is not shown but realizable. However, as a time-lapse of few seconds is required to record each mechanical spectrum, it is not possible to continuously sweep the laser wavelength. In addition our laser shows a better intensity stability when scanning forward than backward. Thus the backward scan induces perturbations that provoke jumps of the optical state.

3.4 Conclusion on the optomechanical properties

In this chapter, the mechanical properties of a suspended photonic crystal molecule are studied through the optomechanical interaction. The mechanical eigenmodes are investigated via the optical noise spectrum readout. This transduction process act unequally on the different eigenmodes depending on the considered photonic molecule geometry. This can be qualitatively understood and verified. A more rigorous approach would consist in the FEM simulation of the optomechanical couplings involved in all these geometries. Such simulations rely on the estimation of the overlap between the electrical field distribution associated to a given photonic mode and the displacement field at a given mechanical resonance. Two main contributions can be estimated. The "moving boundaries" contribution evaluates the change in the dielectric properties of the material when the dielectric boundaries are altered, e.g. when the holes' edges are distorted. The "photoelastic constribution" uses the photoelastic properties of the material to account for a change in the bulk permittivity. These two contributions can be estimated with analytical expressions [Eichenfield et al., 2009] and numerically evaluated to engineer the optomechanical coupling in photonic crystal microcavities [Chan et al., 2012b]. However such simulations are resource and time consuming because the whole mechanical membrane must be modeled with a fine mesh in order to realistically take the photonic crystal into account. They are more adapted to optimize the optomechanical coupling in co-localized photonic and phononic modes. Indeed, in such case the simulation can usually be performed using only the cavity and neglecting most of the suspended structure (or using a fine mesh only in the cavity).

In this system, the mechanical motion can influence both on the dissipative and dispersive features of the optical resonator. Interestingly with coupled optical modes, the dominant contribution involved in the coupling between the normal modes and on given mechanical mode is not necessarily the same. Although hardly exploitable in our system due to low optical quality factors, this aspect could be of great interest for multimode optomechanics experiments. As an example it has been shown that for a given optical linewidth to mechanical frequency ratio, there is an optimum dissipative to dispersive optomechanical couplings ratio in the frame of mechanical cooling experiments. With coupled optical modes, it is therefore possible to explore several optomechanical regimes experienced by the same mechanical mode. Multiple theoretical proposals exploit the balance between these two contributions for the realization of quantum operations such as cooling [Weiss and Nunnenkamp, 2013] or squeezing [Tagantsev et al., 2018]. However, in our structures, the optical quality factor does not permit to approach the resolved sideband regime, in which the quantum experiments can be performed.

Thermal effects are also found to play an important role in this system. In parallel with the thermo-optic effect discussed in section 2.4, we observe that the mechanical

frequencies are also affected by the photothermal absorption in the cavity. Relying on a toy-model, this effect is described as a non negligible thermal shift of the full membrane when the loaded-cavity temperature increases.

Chapter 4

Nonlinear dynamics

In this last chapter of this first part, we describe two experiments exploiting the nonlinear properties of the system. First we use the optomechanical interaction to transfer send modulation tones, generated by intensity modulation of the input field, to the mechanical domain. This interaction is understood in the frame of a theoretical model using Floquet dynamics approach. In presence of a Kerr-type optical nonlinearity[1], this effect is enhanced and altered such that the mechanical noise spectrum sideband peaks now show imbalance amplitudes. In practice we use thermo-optic nonlinearity to achieve this effect, in a bistable regime. Secondly, we rely on the latter for the demonstration of vibrational resonance amplification of a weak signal.

4.1 Sideband generation via input field modulation

In the following we study the effect of modulated optical drive on the optomechanical system. We first describe the spectral properties of the modulated input laser field. The theoretical frame for the optomechanics description is then established via a Floquet approach. The experimental results follow, from the low optical power regime – where only optomechanical features are observed – to thermo-optical regime. We finally present experimental results whose understanding goes beyond the frame of our model, and give an intuitive explanation of the physics involved.

4.1.1 Input field modulation

The following dynamics is induced by modulating the input field with a Mach-Zender intensity electro-optical modulator (EOM). The function transfer of such device can be expressed in the laser frequency rotating frame as a function of the modulation frequency

[1] A linearity that leads the resonant frequency of the cavity to be shifted by the intra-cavity field.

Ω_{mod} and modulation amplitude V_{mod}:

$$\mathcal{T} = \frac{e^{j\phi_0}}{2}\left[1 + e^{j\left(-\pi/2+\beta\cos(\Omega_{\mathrm{mod}}t)\right)}\right] \qquad \text{with} \qquad \beta = \pi\frac{V_{\mathrm{mod}}}{V_\pi} \tag{4.1}$$

The half-wave voltage V_π is a specificity of the modulator, it corresponds to the voltage to apply such that the Mach-Zender output changes from constructive to destructive interference. The modulator transfer function can alternatively be written in terms of Bessel functions $\mathcal{J}_k(\beta)$ using the Jacobi-Anger expansion:

$$\mathcal{T} = e^{j\phi_0}\left[\frac{1 - j\mathcal{J}_0(\beta)}{2} + \sum_{n=1}^{+\infty} j^{n+1}\mathcal{J}_n(\beta)\cos(n \times \Omega_{\mathrm{mod}}t)\right] \tag{4.2}$$

Thus the input field carries all harmonics of the modulation tone with amplitudes given by the above expression.

4.1.2 Theoretical model: a Floquet dynamics approach

In sideband resolved optomechanical system, quantum manipulations of photons and phonons can be performed via a modulation of the input laser field [Farace and Giovannetti, 2012; Clerk et al., 2008; Mari and Eisert, 2009]. In particular it was shown recently that input modulation in a resolved sideband optomechanical system can be used to achieve quantum measurements [Qiu et al., 2019] or to reach new types of optomechanical instabilities [Shomroni et al., 2019]. Here we study the effect of driving laser modulation in an unresolved sideband optomechanical system. The following theoretical developments have been driven by Karl Pelka and André Xuereb, from University of Malta, in the frame of a collaboration dedicated to the understanding of the following experimental results. The model describes one mechanical mode coupled to one optical mode. Here we only write the linearized optomechanical equations describing the optical (resp. mechanical) mean field $\overline{a}$ ($\overline{b}$) and fluctuating component $\delta\hat{a}$ ($\delta\hat{b}$):

$$\begin{aligned}
\dot{\overline{a}} &= \Big[j(\Delta - g_0[\overline{b} + \overline{b}^*]) - \kappa_t\Big]\overline{a} + \mathcal{E}_0\mathcal{T}e^{-j\phi_0} \\
\dot{\overline{b}} &= -\left(j\Omega_m + \frac{\Gamma_m}{2}\right)\overline{b} - jg_0|\overline{a}|^2 \\
\dot{\delta\hat{a}} &= \left(j\Delta - \kappa_t\right)\delta\hat{a} - jg_0\left(\overline{a}[\delta\hat{b} + \delta\hat{b}^\dagger] + \delta\hat{a}[\overline{b} + \overline{b}^*]\right) + \sqrt{\kappa_{\mathrm{w}}}\delta\hat{a}_{\mathrm{in}} \\
\dot{\delta\hat{b}} &= -\left(j\Omega_m + \frac{\Gamma_m}{2}\right)\delta\hat{b} - jg_0(\overline{a}^*\delta\hat{a} + \overline{a}\delta\hat{a}^\dagger) + \sqrt{\Gamma_m}\delta\hat{b}_{\mathrm{in}}
\end{aligned}$$

The optical cavity is driven with a laser of amplitude $\mathcal{E}_0$ and carrying fluctuation given by $\delta\hat{a}_{\mathrm{in}}$. The mechanical resonator is driven by the thermal fluctuations $\delta\hat{b}_{\mathrm{in}}$. The laser frequency ω_L is detuned from the optical resonance frequency ω_0 by an amount $\Delta = \omega_L - \omega_0$. The optical cavity total decay rate is κ_t while the external decay rate is

κ_{w}. The mechanical mode has frequency Ω_m and damping rate $\frac{\Gamma_m}{2}$. Finally, g_0 is the single-photon coupling strength, i.e. the dispersive optomechanical coupling. The next development of the model consists in applying Floquet techniques [Malz and Nunnenkamp, 2016] in order to obtain an expression for the cavity fluctuation power spectral density (PSD of $\delta\hat{a}$), which is the quantity we investigate experimentally by measuring the noise spectrum of the output optical field. The model predicts the presence of mechanical sidebands resulting from the coupling between the added modulation tone and associated harmonics with the mechanical degree of freedom, via the optomechanical interaction (see fig. 4.1).

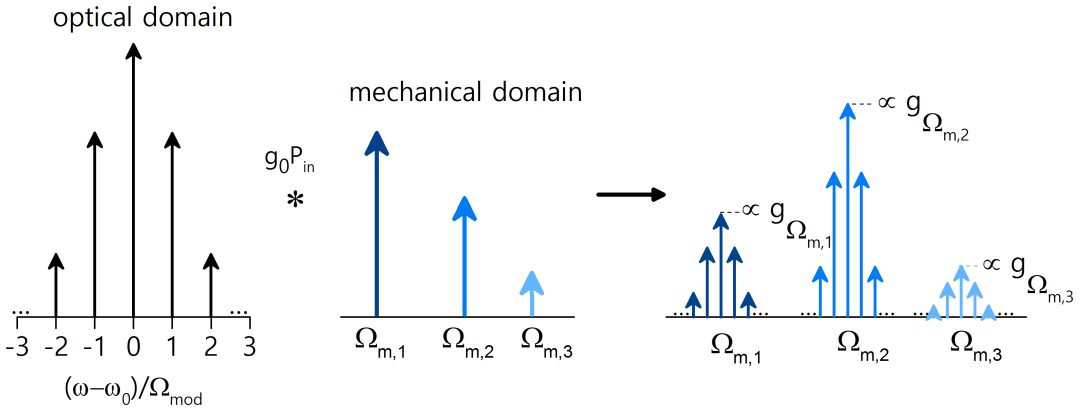

Figure 4.1 – The modulation tone present in the input optical field (left) is transferred to the mechanical domain where several mechanical resonances yield with their respective displacement amplitude. The resulting optical noise spectrum shows the optomechanically transduced mechanical peaks, each with its respective optomechanical coupling. Each peak is surrounded by the modulation harmonics.

4.1.3 Low laser power: optomechanical sidebands

The input field modulation is obtained with an intensity EOM placed before of the vacuum chamber optical insertion (see fig. 4.2). The injection in the EOM is optimized with a fibered polarization controller (FPC). The other FPC is kept before the amplification in the EDFA in order to properly couple the circulating laser field with the photonic modes. The modulation is given by sending a periodic RF signal to the EOM via a function generator. This latter outputs the signal $V_{\mathrm{mod}}\cos(\Omega_{\mathrm{mod}}t)$ where V_{mod} and Ω_{mod} are the modulation amplitude and frequency. The half-wave voltage of the EOM is calibrated to $V_\pi = 7.5$ V. Together with the tunable laser wavelength λ and output power, it gives to the user four parameters to play with in the following experiments. In practice, concerning the laser power, we will continue to refer to the estimated circulating power

P_{in}.

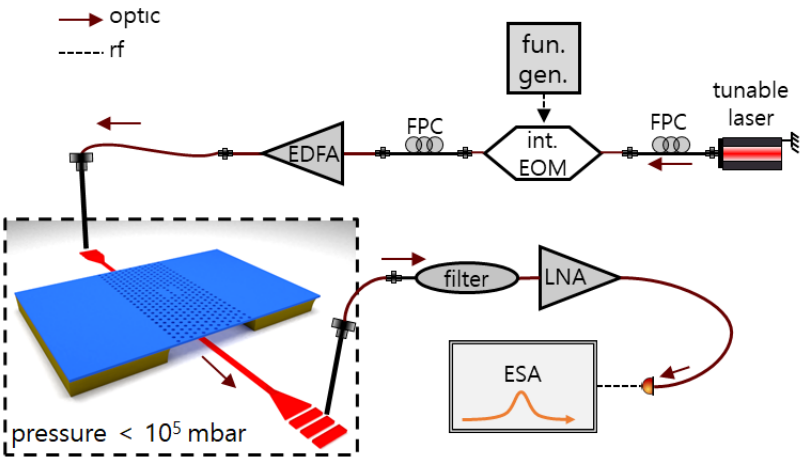

Figure 4.2 – The setup now includes a fibered intensity modulator placed before the waveguide input.

We focus on the 2V3 photonic molecule that was already extensively studied so far[2]. In the first place we try to avoid the prevalence of thermal effects by using a relatively low circulating power $P_{\text{in}} = 325$ µW. We set the modulation with $V_{\text{mod}} = 2$ V and $\Omega_{\text{mod}} = 2\pi \times 50$ kHz. The noise spectrum measurements shown in the following focus on the fundamental mechanical resonance (mode index (1,1)). Its central frequency, at room temperature, is estimated to $\Omega_{m,0} = 2\pi \times 4.34$ MHz. The mode has mechanical quality factor $Q_m = \Omega_m/\Gamma_m \approx 778$. The first measurement consists in measuring the noise spectrum of the output field as a function of the laser wavelength, for each optical mode. The resolution bandwidth is set to 50 Hz. The laser wavelength is swept upward on each mode in order to cover the same spectral range that in the measurements shown in section 3.3.

The results are shown in figs. 4.3a and 4.3b. Here we use directly the net amplitude, obtained by removing the noise level from each spectrum. For both optical modes, the mechanical resonance amplitude and frequency evolve as described previously. However, this main peak ("order 0") is followed by small replica equidistantly positioned from the order 0 position. In the following we will refer to these replica as sidebands. The frequency difference is given exactly by Ω_{mod} (order ± 1 at $\Omega_m \pm \Omega_{\text{mod}}$). In the case of the mode $(+)$, in fig. 4.3b, for which the thermo-mechanic shift of Ω_m is more pronounced, we clearly see that the sideband frequencies experience the same shift. Still in the case of this particular mode, we observe the order 2 sidebands (at $\Omega_m \pm 2\Omega_{\text{mod}}$) but only for a very restricted range of wavelength 1565.57 to 1565.62 nm. These second order sidebands are not visible when the optical mode $(-)$ is driven. The model indicates that the sidebands

[2]see thermo-optic effect in section 2.4, and all the measurements shown in chapter 3

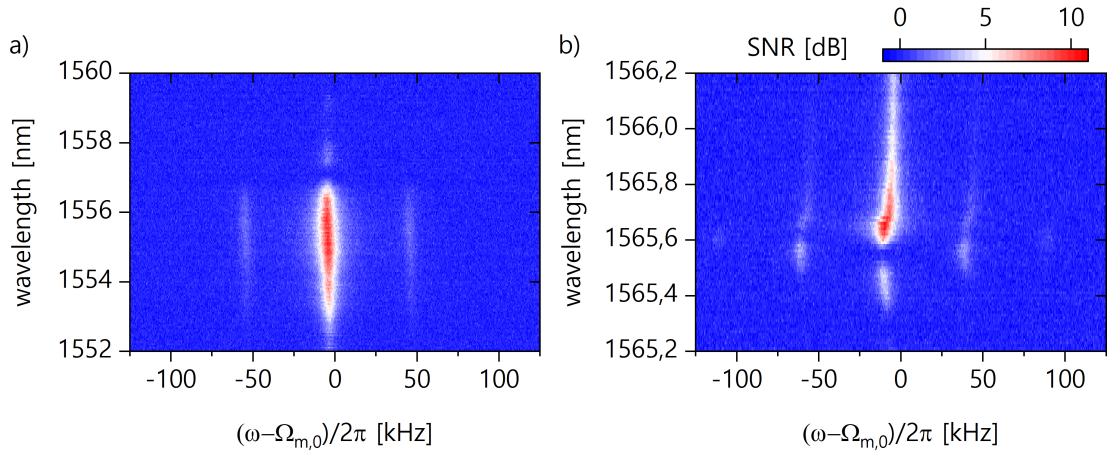

Figure 4.3 – Noise power spectrum signal-to-noise ratio measured as a function of the laser wavelength for the optical mode $(-)$ (a) and for mode $(+)$ (b). The modulation uses $V_{\mathrm{mod}} = 2$V and $\Omega_{\mathrm{mod}}/2\pi = 50$ kHz. Measured with input power $P_{\mathrm{in}} \approx 0.3$ mW.

amplitude depends to the optomechanical coupling. In the meantime, we have shown in the previous measurements that, in this structure, the optomechanical coupling between this mechanical mode and the optical mode $(-)$ is dominated by dissipative processes. As the present model accounts only for a dispersive optomechanical process, it is possible that this explains why there are fewer sidebands with lower amplitude when the mode $(-)$ is driven. However, this intuitive explanation has not yet been confirmed by the theory. For this purpose, the model should be adapted in order to account for the dissipative optomechanical contribution. In the following, we will focus on mode $(+)$, which mainly couples dispersively with the mechanics.

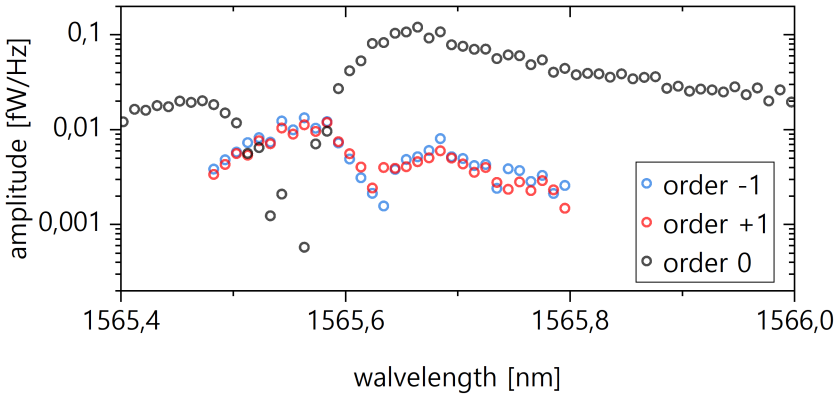

Figure 4.4 – Peak net amplitudes obtained from fig. 4.3b. Mechanical peak (order 0) in black, sidebands of order $+1$ (red) and -1 (blue).

For each spectrum (i.e. each value of λ), we fit the peaks with Lorentzian lineshapes

such that the noise floor and the amplitudes, frequency and linewidth or the sidebands and of the order 0 can be extracted. In absence of thermo-optic effect, the model predicts balanced sidebands, which we want to verify as a function of the detuning. For this purpose, we show the amplitudes of the mechanical mode and the first order sidebands in fig. 4.4. These data can be collected only when the fit is successful, i.e. only when the amplitude is high enough. The sidebands have indeed the same amplitude, according to this measurement.

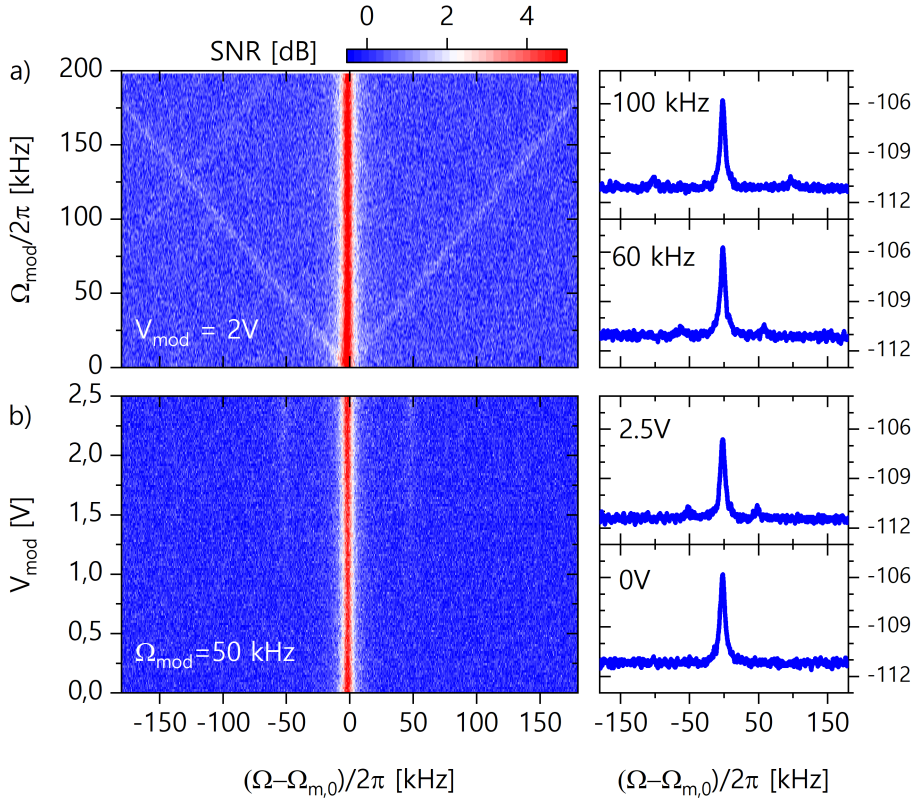

Figure 4.5 – Noise power spectrum measured as a function of a) the modulation frequency and b) the modulation amplitude. Right side: typical averaged mechanical spectra. Measured with $\lambda = 1565.75$ nm and $P_{\mathrm{in}} = 0.36$ mW.

We now set the laser wavelength to $\lambda = 1565.63$ nm, such that the order 0 peak amplitude is maximum, in order to check the influence of both modulation parameters, Ω_{mod} and V_{mod}. In fig. 4.5a, the modulation amplitude is set to $V_{\mathrm{mod}} = 2$ V. The color scale is set tight enough to visualize the first order sidebands. Note that at this particular wavelength, the second order sidebands are not visible as discussed with the previous figure. This measurement permits to verify the sidebands relative position from the order 0 is given by the modulation frequency. From 75 kHz to the top of the heat map, a sideband belonging to another mechanical mode can be observed. This mode is sustained by a different photonic molecule structure – suspended over the same

waveguide – displaying a resonance is the same spectral region. This is verified with the experimental techniques detailed in sections 2.3.2 and 3.1.2.

A complementary measurement is done with $\Omega_{\mathrm{mod}} = 2\pi \times 50$ kHz while V_{mod} is swept. The resulting heat map is shown in fig. 4.5b. In the present regime, as illustrated with the typical spectra on the right, the order 0 and clearly dominant compared to the sidebands. Actually these latter are hardly visible for $V_{\mathrm{mod}} < 1.5$ V. One method, in order to increase there amplitude, consists in using higher laser input power sent to the system.

4.1.4 Thermo-optic regime: sideband imbalance

The thermo-optic nonlinearity in the system is added to the theoretical description. For this purpose we introduce the cavity temperature variation $\Delta\theta(t)$ which follows the following dynamics:

$$\frac{d\Delta\theta(t)}{dt} = \kappa_{\mathrm{th}}\Big[R_{th}\kappa_{\mathrm{abs}}|\overline{a}|^2(t) - \Delta\theta(t)\Big] \tag{4.3}$$

with R_{th} the thermal resistance, κ_{abs} the absorption rate of the cavity and κ_{th} the thermalization rate. The first constant depends on the photo-absorptive properties of the system while the second relies on the thermal diffusion processes, which is why they are expected to be different. Beside, the optical resonance frequency is now modeled as a function of this temperature offset and of the resonance frequency ω_{cav} in absence of laser drive:

$$\omega_0 = \omega_{cav}\Big(1 + \frac{1}{n_0}\frac{dn}{d\theta}\Delta\theta(t)\Big) \tag{4.4}$$

This implies that the laser detuning is modulated by the cavity temperature. Moreover, although the modulation signal is a sinus, the thermal response is ruled by a competition between absorption and relaxation. In consequence, this nonlinear oscillation will lead to imbalance sideband amplitudes, e.g. the amplitude of sidebands -1 and $+1$ are not the same anymore, generally speaking (see fig. 4.6).

We inject the system such that the circulating power is $P_{\mathrm{in}} = 1.3$ mW. In these conditions, the optical mode $(+)$ becomes bistable between 1565.7 nm and 1566.8 nm. This is verified manually by scanning the mode in both directions and evaluating the hysteresis edge positions, in absence of intensity modulation. The modulation is set with $\Omega_{\mathrm{mod}} = 2\pi \times 50$ kHz and $V_{\mathrm{mod}} = 2$ V. We scan the optical mode $(+)$ in two configurations. The first consists in using a first low-intensity laser, with intensity modulation, for the scan, and a second laser driving the optical mode $(-)$ with $\lambda_- = 1554.7$ nm for a passive readout of the mechanical resonance. The probe laser is also filtered in order to get rid of the cross-talks. More details about this two-lasers driving scheme are given in appendix B. The resulting heat map in shown in fig. 4.7a. The laser

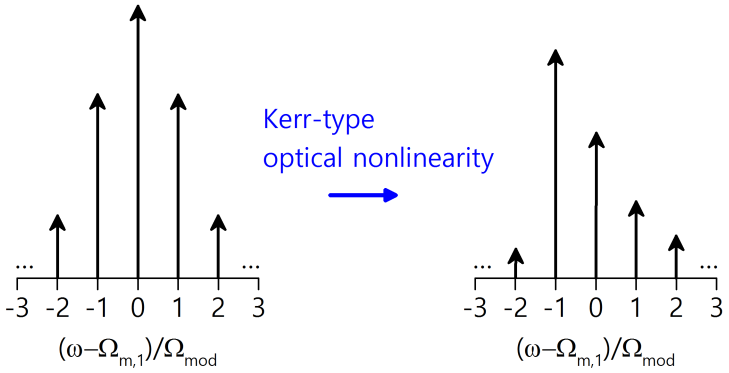

Figure 4.6 – In the linear regime of the optical resonator, the modulation harmonics are directly transferred in the mechanical rotating frame with balanced sideband amplitudes (left). The Kerr-type nonlinearity di-symmetrize the sidebands (right).

probing the other mode do not see this additional tone. This indicates that there is no optomechanical process that couples the optical modes together, through the mechanics. It also simply confirm that, as soon as the probing laser has sufficiently low intensity, the optical normal modes are orthogonal and therefore uncoupled.

The second configuration is the standard direct readout using only one laser, that was used so far. The measurement can be seen in fig. 4.7b. In both cases, the order zero peak experiences a similar frequency shift. The modulation sidebands however only appear in the laser field sent to the mode (+), i.e. that is initially modulated.

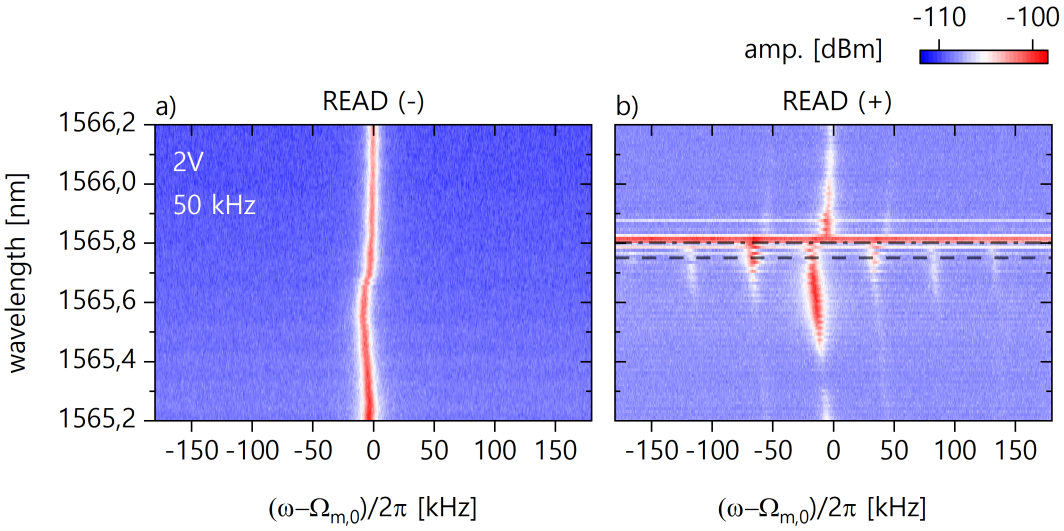

Figure 4.7 – Noise power spectrum measured a) indirectly using a probe laser with wavelength $\lambda_- = 1554.7$ nm and b) directly with the scanning laser at power $P_{\text{in}} = 1.3$ mW.

Now we specifically focus on fig. 4.7b for which there are several interesting features to discuss. Firstly, all the peaks experience an abrupt jump of their respective central frequency around 1565.8 nm. This is related to the optical bistability. The mechanical frequency jump is well understood from our preliminary measurements in the previous chapter. As all the sidebands' positions are constrained by the mechanical frequency and the modulation frequency, they display the exact same hysteretic behavior. Secondly, we note that now up to three sidebands are observed on each side of the order 0. Finally, as particularly visible with the first order sidebands (± 1), their amplitudes are not balanced anymore. Near the bistability edge, highlighted with the horizontal dash-dotted line at $\lambda = 1565.8$ nm, the noise level quickly grows above the peak amplitudes. This feature is not understood from the theoretical model and will be the object of a discussion later on. For now, we focus at the center of the bistable region, at $\lambda = 1565.75$ nm (dashed horizontal line).

4.1.4.1 At the bistability center

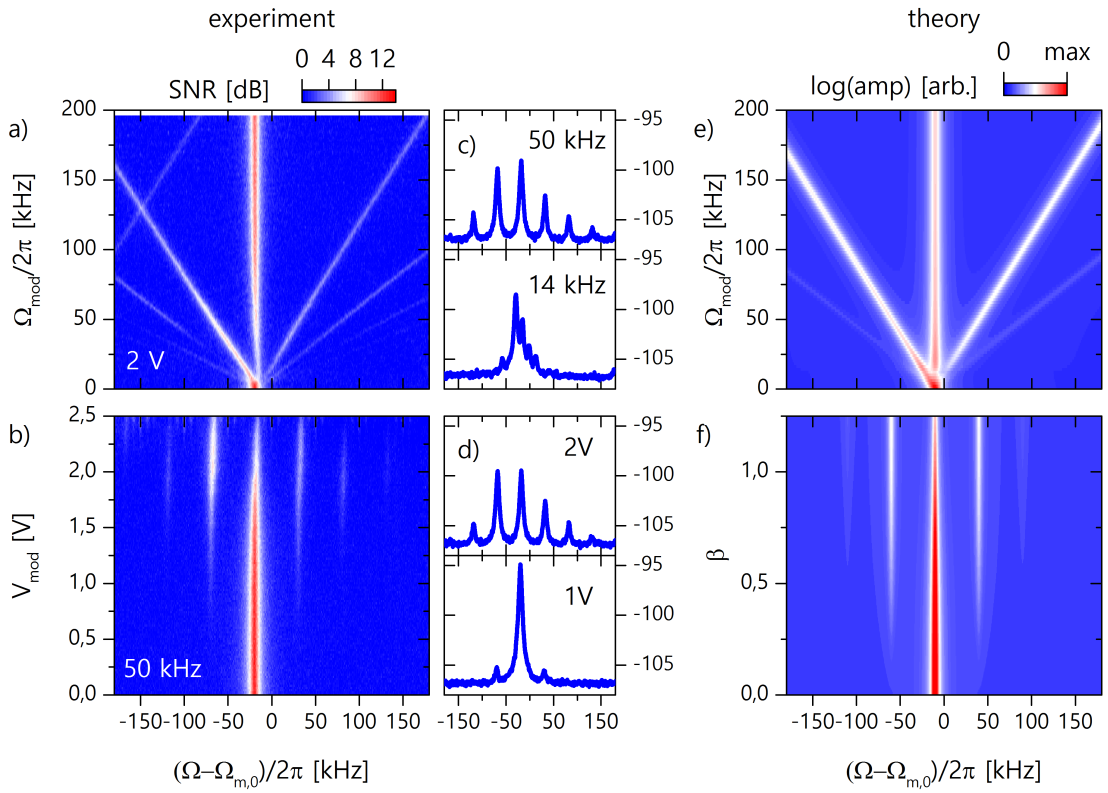

Figure 4.8 – Noise power spectrum measured as a function of a) the modulation frequency and b) the modulation amplitude. c)-d): averaged mechanical spectra. Measured with $\lambda = 1565.75$ nm and $P_{\text{in}} = 1.3$ mW. e)-f) Numerical simulations.

We map the noise spectrum near the fundamental mechanical resonance as a func-

tion of the modulation frequency (for $V_{\mathrm{mod}} = 2$ V) in fig. 4.8a and as a function of the amplitude depth (for $\Omega_{\mathrm{mod}} = 2\pi\times = 50$ kHz) in fig. 4.8b. These measurements emphasize the imbalance between the sidebands amplitude. We note that the effect of more modulation depth seems to be equivalent to slower modulation as both tend to balance the sidebands' amplitudes back. We also remark that the sidebands of order -1 dominates the order $+1$ when V_{mod} is sufficiently high and Ω_{mod} sufficiently low (see averaged spectra in figs. 4.8c and 4.8d). In this case, we finally see a diminution of the order 0 amplitude. For example for $V_{\mathrm{mod}} = 2$ V and $\Omega_{\mathrm{mod}} = 2\pi \times 14$ kHz, the amplitude of the mechanical peak is lower than the -1 order sideband.

By imputing the calibrated physical quantities in the model, the power density spectrum can be evaluated as a function of the experimental variables. These quantities include the optical and mechanical modes frequencies and linewidths, the estimated circulating power and the thermo-optic properties of the mode. Several parameters are kept free, as the modulation depth calibration, the thermal absorption and thermalization rates and the single-photon optomechanical coupling g_0. The latter is actually estimated in section 3.2.1 but, as discussed earlier, this calibration is not perfectly reliable since it is valid only for purely dispersive optomechanical coupling. The numerous free parameters as well as the complexity of the solutions did not enable a quantitative modelization of the experiment. However the main features are present in the theoretical heat maps shown in figs. 4.8e and 4.8f. Here we plot the decimal logarithm of the power spectral density. The relative sideband amplitudes is well captured by the model, except for the order 0 which is not found as low as in the experiments for $\Omega_{\mathrm{mod}} < 2\pi \times 50$ kHz (or equivalently for $V_{\mathrm{mod}} > 2$ V).

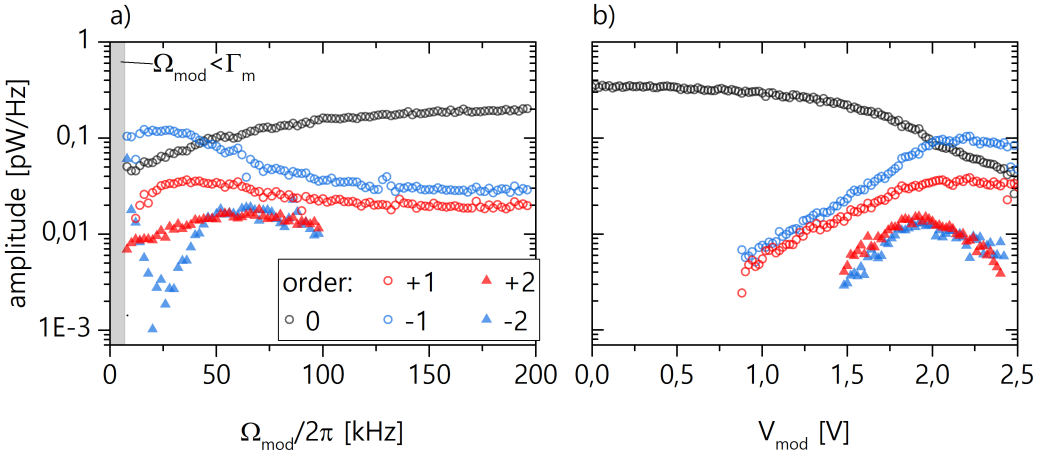

Figure 4.9 – Peak amplitudes obtained from figs. 4.8a and 4.8b.

The peak amplitudes are extracted from the data by fitting the spectra one by one. The evolution of these amplitudes, shown in figs. 4.9a and 4.9b confirm the opposite

tendency observed as a function of the modulation parameters. Note that for $\Omega_{\mathrm{mod}} < \Gamma_m$, highlighted by a transparent stripe in fig. 4.9a, the fits are not successful as the sidebands can not be resolved. The confidence intervals associated to these amplitudes, and given by the fit of each peak, are lower than the symbol sizes. This imbalance is therefore a significant effect.

According to the model, the different timescales involved in the thermal absorption and thermalization operations are responsible for these features. In fact, the second process is presumably much slower than the first one. As a result, the detuning is not sinusoidally modulated which tends to favor some particular harmonics of the modulation frequency in the output optical field. As these harmonics are captured by the mechanics through the optomechanical interaction, it comes out that the optomechanical sidebands have unbalanced amplitudes for a given order. When the modulation frequency increases, it becomes harder for the cavities to thermalize. Thus, after some threshold, the thermal effects becomes weak. As a result, the sidebands tend to balance as observed in fig. 4.9a around $\Omega_{\mathrm{mod}}/2\pi = 25$ kHz. This threshold frequency basically corresponds to the cut-off frequency of the thermo-optic bistability as discussed in the context of vibrational resonance, using a similar structure, in section 4.2. The cut-off frequency is basically given by the thermalization times in the cavity.

symbol	meaning	typical value
Γ_m^{-1}	mechanical damping time	200 µs
Ω_m^{-1}	mechanical displacement period	4 µs
$\kappa_{\mathrm{th}}^{-1}$	thermalization time in the material (fits from fig. 4.17)	$3-4$ µs
$\kappa_{\mathrm{abs}}^{-1}$	cavity linear absorption time[3] (fit from fig. 2.12b)	10 ps
κ^{-1}	cavity lifetime	5 ps

Table 4.1 – typical time constants involved in the experiment

Beyond the frame of the present experimental characteristics, the model suggests the use of multimode optomechanics. For this, one would require a system sustaining several mechanical modes with a reasonably low intermodal frequency $\Delta\Omega$. Then the modes must be strongly coupled to the optical cavity mode, such that parametric amplification of the mechanical motion can be achieved, with the presence of radiation pressure induced mechanical bistabilities [Bagheri et al., 2011]. In this configuration, one

[3] This value is the most uncertain in this table as it is not provided by a direct measurement but deduced after assuming the thermal resistance $R_{th} \approx 1.7\times10^4$ K.W^{-1} that was estimated in [Brunstein et al., 2009]

can use a modulation of the input field with a modulation frequency precisely matching $\Delta\Omega$, and with the laser frequency driving the optomechanical system in the blue-detuned regime. It becomes therefore possible to address both mechanical modes at the same time thanks to the multiple tones generated in the optical field. This configuration becomes particularly interesting in presence of optical Kerr-type nonlinearity as the modulation sidebands transferred to the mechanical domain are now imbalanced such that the mechanical modes can be asymmetrically addressed. In particular, as we have seen from the experimental results, the modulation depth constitutes a control parameter to chose which sideband dominate. With this parameter, one could control which mechanical mode is bistable or not. This conceptual scheme, that naturally emerges from our Floquet dynamics theoretical model can be adapted to a "many-mode" optomechanical system. It thus opens the way towards the realization of logic gates using multimode optomechanical system.

4.1.4.2 At the bistability edge

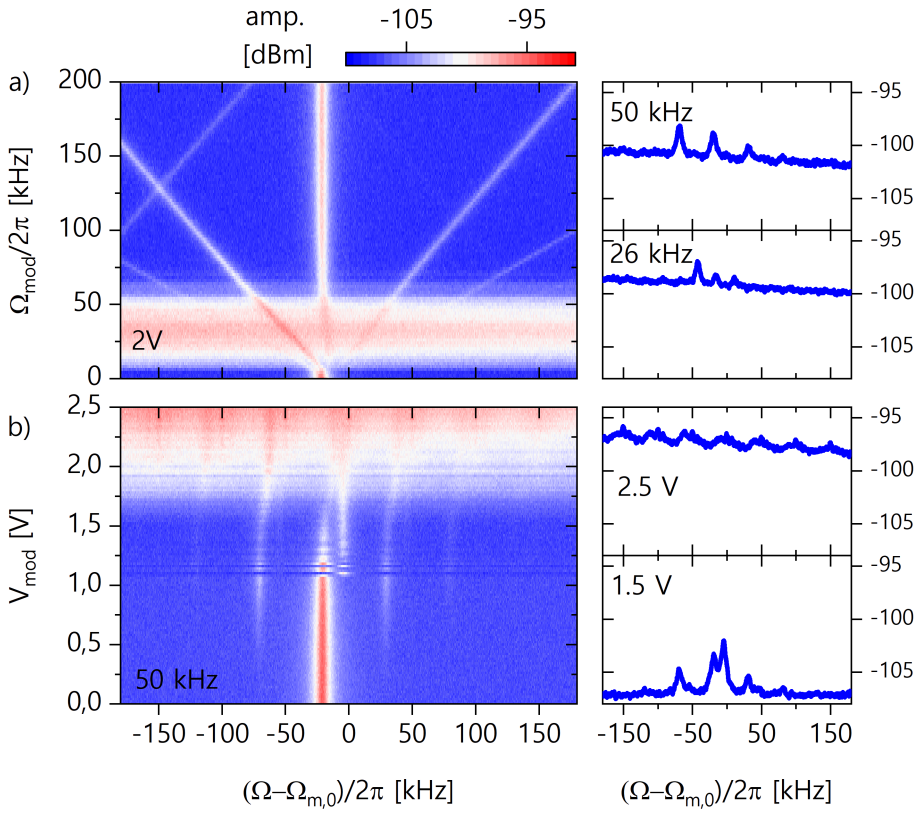

Figure 4.10 – Noise spectrum measured as a function of the modulation frequency (a) and amplitude (b). Right side: typical averaged mechanical spectra. Obtained with $\lambda = 1565.85$ nm and $P_{\text{in}} = 1.3$ mW.

When the intensity-modulated laser is positioned at the edge of the thermo-optic bistability, the noise floor increases by about 10 dB. This effect was sighted in fig. 4.7b. We now take a closer look to this peculiar regime. The noise power density spectrum is measured one more time as a function of the modulation parameters. This time the laser wavelength is placed at $\lambda = 1565.80$ nm. The results are presented in figs. 4.10a and 4.10b. Firstly, one can verify that the noisy region is recovered at the set of parameters used for the laser wavelength scan: at $\Omega_{\mathrm{mod}} = 2\pi \times 50$ kHz and $V_{\mathrm{mod}} = 2$ V. However the measurements show that this regime appears only for sufficiently high modulation depth (typically $V_{\mathrm{mod}} > 1.75$ V here) and only in a restricted range of modulation frequency. From $V_{\mathrm{mod}} = 1$ to 2 V, the optical state tends to switch stability. As the mechanical frequency is thermo-mechanically shifted by the intracavity field, it shows several abrupt changes from the low-power value $\Omega_m - \Omega_{m,0} = 0$ to the shifted value $\Omega_m - \Omega_{m,0} \approx= -21$ kHz. As the measurement of a single spectrum is averaged several seconds, if the switching occurs during the measurement, it leads to an averaging effect such that the spectrum displays several times the same peaks at different positions. This is the case for example of the reported spectrum measured at $V_{\mathrm{mod}} = 1.5$ V. This observation motivates the real-time investigation of the optical cavity under modulated drive that is the object of the next section.

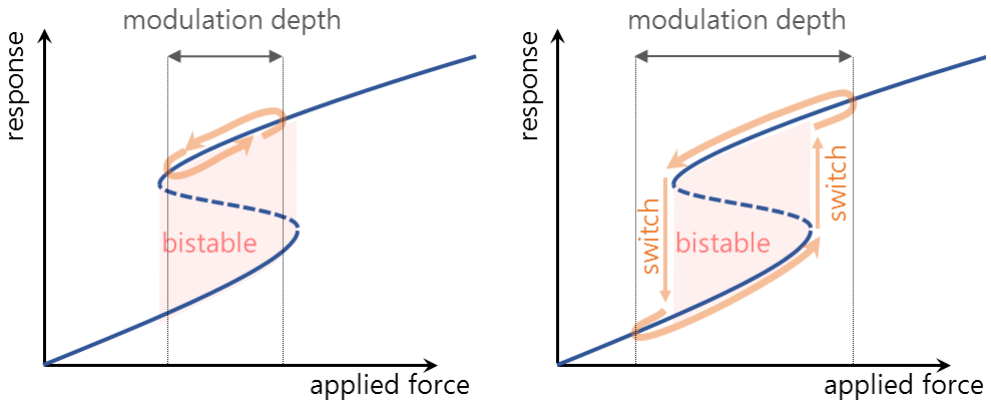

Figure 4.11 – Schematic of the response of a nonlinear optical resonator as a function of the applied force (dark blue). The system displays a bistable regime (red transparent stripe).

The averaged spectra extracted from the map (on the right side) seem to indicate that the mechanical peaks, including the sidebands, do not add up to this high noise level. These peaks are indeed drowned into the noise. The noise floor, at the maximum noise level, is oscillating with a period given by Ω_{mod} and also decreases slowly by approximately 1.2 dB over the 350 kHz spectral span. These elements conduct to the conclusion that this high noise level is the consequence of an optical dynamics that do

not relate to the optomechanical features of the system. In seems more probable that the modulation near the thermo-optic bistability edge leads to non trivial oscillations of the optical state. Such oscillations are also more likely to occur when the modulation depth is increased, as the system explore a wider range in the parametric response space. This is illustrated with a schematic in fig. 4.11. The dark blue curve schematically represent the response of the nonlinear system as a function of the applied force. Here the intensity modulation of the input laser corresponds to a modulation of the applied force and the modulation depth is represented by the black arrow size. If the depth is small enough, the system trajectory (orange arrows) lies on a stable branch (left situation) while it starts switching is the depth passes a certain threshold. This representation is slightly simplistic as it does not account for the modulation of the detuning that comes with the force modulation. In other words with this schematic, the shape of the response itself should be modulated. Moreover, the dynamical evolution of this response depends on the heating and cooling duration.

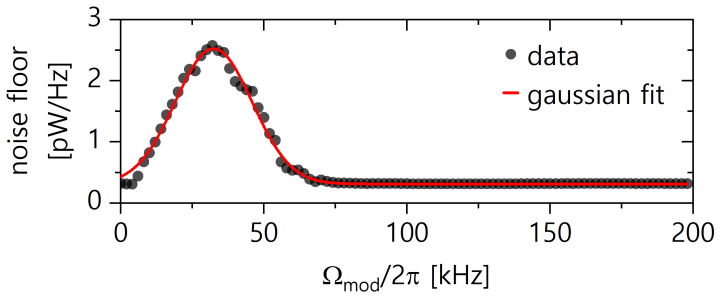

Figure 4.12 – detected noise floor obtained from fig. 4.10a.

In fig. 4.10a, the noisy region is limited to a specific range. By extracting the noise level for each line, that we report in fig. 4.12, this frequency range is more precisely determined. It appears that the noise floor follows a Gaussian distribution centered around 30 kHz with a width of about 25 kHz. At high frequencies, the absence of oscillations probably signifies that the modulation is too fast for the optical resonator to reply, such that the trajectory do not reach the opposite edge of the bistability and, therefore, lies on the same stable state. For low modulation frequency however, the response adiabatically follows the excitation. The noise level at the mechanical frequency is probably not impacted by the dynamics of the optical resonator that occurs at low frequency. Because of the complex evolution of the bistable response curve, due to these different time scales involved in the modulation process, it is not simple to apprehend the effect of the modulation frequency on the oscillation regime.

This phenomenon has been observed on other structures on which it was possible to performed further measurements. For example in figs. 4.13a and 4.13b we show respectively the optical noise spectrum for different modulation amplitude (with fixed

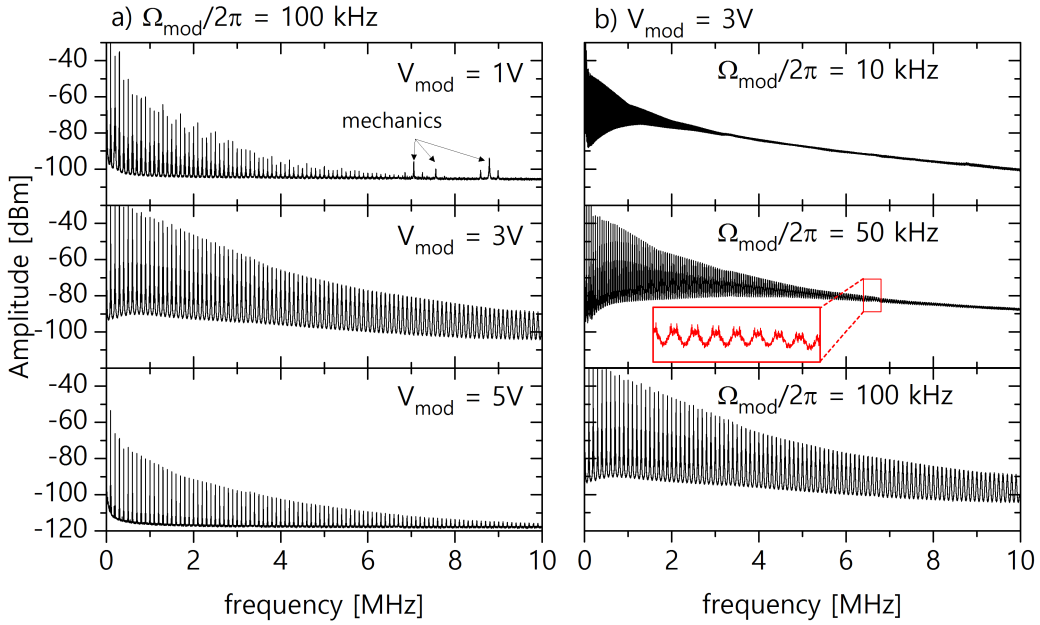

Figure 4.13 – Frequency-domain response of the optical field in a 2D4 photonic molecule. The system is driven near an optical resonance with intensity modulation. a) The modulation amplitude is varied with $\Omega_{\mathrm{mod}} = 50$ kHz. b) The modulation frequency is varied with $V_{\mathrm{mod}} = 2$ V. The mechanical modes (shown with arrows) are quickly hidden by the modulation peaks. inset: the frequency pattern for $V_{\mathrm{mod}} = 2$ V and $\Omega_{\mathrm{mod}} = 50$ echoes to the observation in the previous results (see fig. 4.10b inset at 2.5 V).

modulation frequency 100 kHz) and for different modulation frequency (with fixed modulation amplitude 3 V). In this system[4], several mechanical modes can be observed between 7 MHz and 9 MHz, as indicated with the arrows, but are quickly hidden by the modulation peaks resulting from the periodic jumps of the system. In particular for $V_{\mathrm{mod}} = 2$ V and $\Omega_{\mathrm{mod}} = 50$ kHz, the optical spectrum shows a periodic pattern very similar to the one discussed in fig. 4.10b (inset at 2.5 V), as emphasized with the inset in red in fig. 4.13b.

4.2 Vibrational resonance in thermo-optic bistability

Vibrational resonance has been introduced in [Landa and McClintock, 2000] as an analogy with stochastic resonance [Dykman et al., 1995], in which noise is added to a bistable system enabling the amplification of a weak signal. In vibrational resonance however, the amplification is achieved and controlled by replacing the noise with a high frequency

[4] This system correspond to a 4D4 photonic molecule that we further investigate in the vibrational resonance experiment, in the following section.

(HF) periodic signal as soon as the amplitude of the latter passes a certain threshold. Nevertheless the mechanisms involved in these two phenomena leads to the same result. The added signal (either noise of a HF signal) permits to distort the nonlinear response lineshape of the system. This way, the system can freely switch from one stable state to the other. Originally unable to flip the resonator state, the weak signal can experience amplification if the amplitude difference between the two stable states overcomes the amplitude of the weak signal.

Vibrational resonance has been theoretically studied in different type of nonlinear systems, e.g. in neural network [Deng et al., 2010], in excitable systems [Zaikin et al., 2002] or in biological networks [Rajasekar et al., 2012]. Several experimental demonstration have also been conducted in electronic circuits [Ullner et al., 2003], macroscopic bistable laser [Chizhevsky et al., 2003] or electro-mechanical Duffing resonator [Chowdhury et al., 2020] for example. In the following, we focus on a thermo-optic bistability for realizing the vibrational resonance amplification of a weak low-frequency signal. Several conditions are required for amplifying a signal with this method. First, it only operates for sufficiently weak signals. If the modulation amplitude is initially already high enough to induce switches in the bistability, this method is not adapted to perform amplification. The threshold modulation amplitude V_t separates the regime in which the system state accurately follows the modulation ($V_{\mathrm{mod}} > V_t$) from the regime where the system state stays unchanged – or hardly flips – under modulation ($V_{\mathrm{mod}} < V_t$). This second situation is required for performing the amplification. Secondly, as it all relies on the faculty for the system to switch stable state, the weak signal frequency must be low enough for this switching to occur, i.e. lower than a cut-off frequency Ω_{c}. Finally, the frequency of the HF signal must be high compared to the modulation frequency $\Omega_{\mathrm{hf}} \gg \Omega_{\mathrm{mod}}$ but smaller than the resonator frequency. Here since we consider an optical resonator with a resonance frequency of the order of 10^{14} Hz, the range in which the HF signal frequency must be picked is basically limited by the equipment. Both the cut-off frequency and the threshold amplitude must be estimated before proceeding to the vibrational resonance experiment. Interestingly in our system, this characterization can be performed both by measuring the transmitted optical field or with the mechanical frequency in which the optical state is encoded.

4.2.1 Bistability characterization

We focus on a 4D4 photonic molecule (4 defect-cavities diagonally separated by four lines of holes). More details about the 3 or 4 cavities photonic molecules are given in appendix A. A scanning electron micrograph of the molecule is shown in fig. 4.14a. In the associated spectrum shown in fig. 4.14b, four resonance dips are identified, with unbalanced optical linewidths. When driven with an estimated input power $P_{\mathrm{in}} = 240$

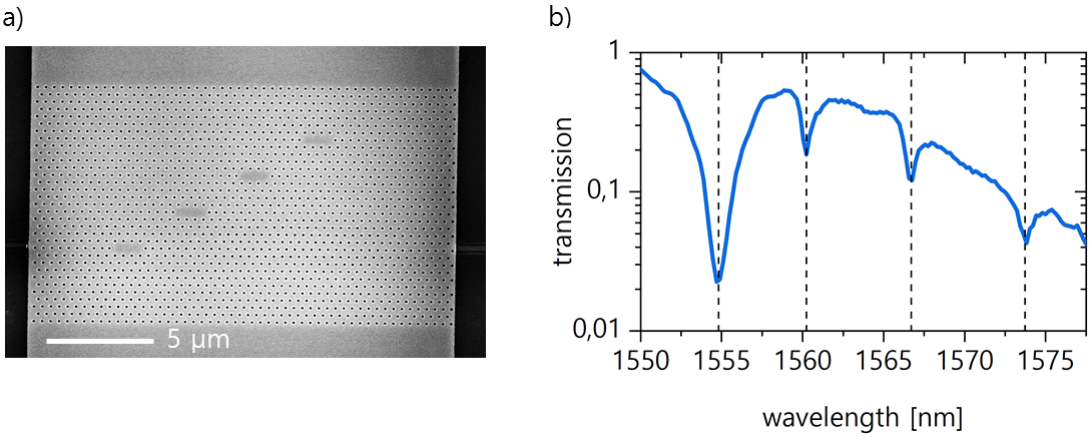

Figure 4.14 – a) SEM image of a 4D4 photonic molecule. b) Transmission spectrum of the system. The four dips correspond to the optical eigenmodes of the system.

µW, the molecule response displays a strong thermo-optic shift of the resonances, more pronounced for the 2nd and 3rd dips. The thermo-optic bistability could not be directly characterized due to the strong instabilities of the input optical fiber under high laser power. However, by measuring the mechanical noise spectrum as a function of the laser wavelength, the thermo-mechanical shift of the mechanical frequencies enable to visualize the optical state. Scanning the laser wavelength forward provides the map presented in fig. 4.15. In this measurement, the scan is realized over the 2nd and 3rd optical resonances while the 1st resonance, much broader and therefore barely nonlinear, is ignored. It appears clearly that both the 2nd and 3rd resonances are bistable as evidenced by the jumps in the mechanical frequency. By manually scanning downward the laser wavelength, we access the jump-up positions of the optical states. This way the hysteretic trajectory of the mechanical frequency is recovered and indicated with oriented black dashed lines.

4.2.2 Thermo-optic switching time

When the optical resonator state flips, it requires a certain time to reach its new stability. Under modulation, the optical state is asked to flip twice a modulation cycle, which is possible only is the switching time τ_s is short enough. Therefore, the maximum modulation frequency allowing the system to accurately flip twice a period is given by $\Omega_c/2\pi \sim 2\tau_s^{-1}$. It is possible to estimate the cut-off modulation frequency by measuring the typical switching time of the system. The idea is to modulate the input input slowly enough such that the transitory regime, in which the system leaves a stable state to reach the other one, can be measured. For this purpose, the laser wavelength is set at the center of the bistability ($\lambda = 1566.75$ nm) and modulated in the EOM with a square

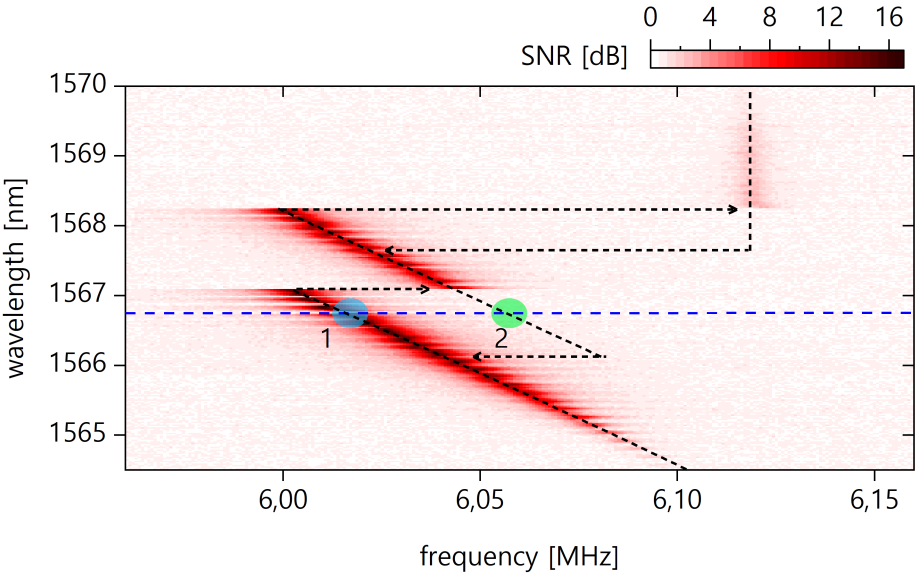

Figure 4.15 – Mechanical noise spectrum mapped while the laser wavelength is scanned upward in the 4D4 photonic molecule. The hysteretic mechanical frequency shift is indicated with dashed black arrows. The frequency corresponding to each optical state (green and blue disks resp. for the cold and hot states) are identified at wavelength $\lambda = 1566.75$ nm (blue dashed).

signal carrying amplitude V_{mod} and frequency Ω_{mod}. In principle, there is no fundamental difference between a sine or a square signal in this experiment. However, the second allows abrupt jumps of the optical state under modulation, which simplifies the data analysis. At the waveguide output, a fiber splitter allows to trigger the transmitted signal via a fW sensitivity photodetector in parallel of the broad band detection used so far for the noise spectrum analysis. This new detector returns an electrical voltage V_{out} that is triggered in the oscilloscope, together with the reference modulation signal.

With a modulation amplitude $V_{\mathrm{mod}} = 2$ V and frequency $\Omega_{\mathrm{mod}} = 10$ kHz, the system response is recorded over several hundred of modulation cycles. The data are averaged cycle by cycle are plotted in fig. 4.17. During one cycle, the resonator, initially set in the cold state (high transmission), transits towards the hot state and then returns back to the cold state at half a cycle. This transitory regime manifests as an exponential decay from one state to the other. When the resonator is stabilized in a state, we should observe a plateau: a constant value of the transmission. Instead, we observe a slowly decaying value because the photodetector we use filters out the DC component of the signal. Fitting the averaged data with a function $f(t) = A\exp(-t/\tau_{\mathrm{s}}) + B$ provides the switching time 4.4 µs and 3.4 µs respectively for the heating time and the cooling times. The significance of the difference between these two values is not established but both values are clearly coherent with previous estimations (1 µs. in [Brunstein et al., 2009]).

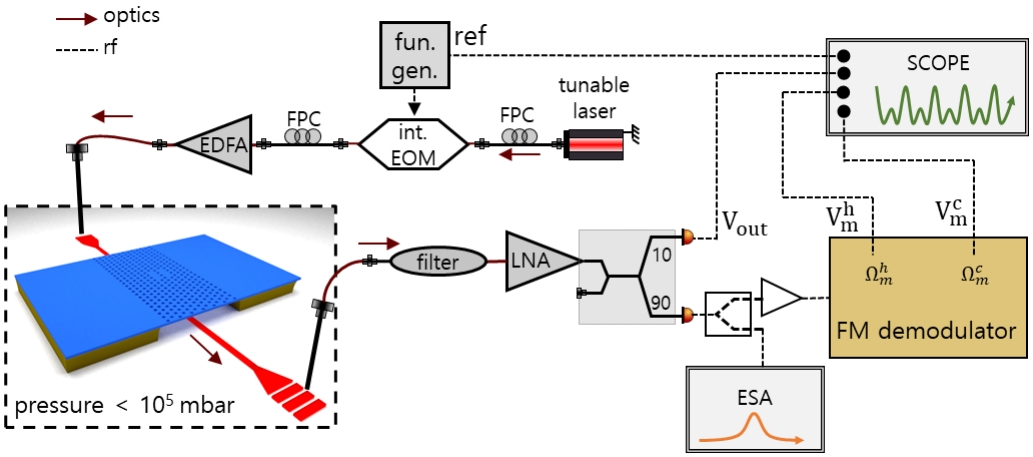

Figure 4.16 – The experimental setup now includes a fW sensitivity photodiode whose DC outputs is sent to an oscilloscope. An electrical power splitter now allows a simultaneous read out of the noise spectrum in the ESA and a two-channels FM-demodulation after amplification of the signal. The demodulation amplitudes are sent to the oscilloscope. Finally, the latter also inputs the modulation signal for reference.

The corresponding cut-off frequency, as discussed above, is of the order of 125 kHz. In the literature similar measurements have been performed in various systems. Depending of the type of optical resonator (micro-rings, Fabry-Pérot, 1D or 2D photonic crystal resonators), on the material and of the type of nonlinearity, this decay time can be of several milliseconds [Jang and Chen, 2003], or as low a few hundred of nanoseconds [Qiu et al., 2017]. Note also that this cut-off frequency corresponds to the maximum modulation frequency allowing sideband imbalance in the previous experiments. Indeed, Above this frequency, the thermo-optic effect becomes negligible as the thermal variations of the cavities remain week. This is indeed what we have observed in fig. 4.9a; where the first order sidebands amplitudes tend to balance around 125 kHz.

In this characterization, the trace of the optical state in the mechanical frequency is possible only because the modulation frequency is way below the mechanical linewidth ($\Omega_{\mathrm{mod}} \ll \Gamma_m$). Therefore the optomechanical sidebands, that we describe in the previous section, are all gathered at the mechanical frequency such that there is enough noise amplitude for the signal to be analyzed. At higher modulation frequency, the same study would be possible only through the optical transmission output, as soon as it lies below the cut-off frequency.

4.2.3 Threshold amplitude

The switching between optical stable states can be driven by the field modulation only if the modulation amplitude passes a certain threshold. Vibrational resonance amplification

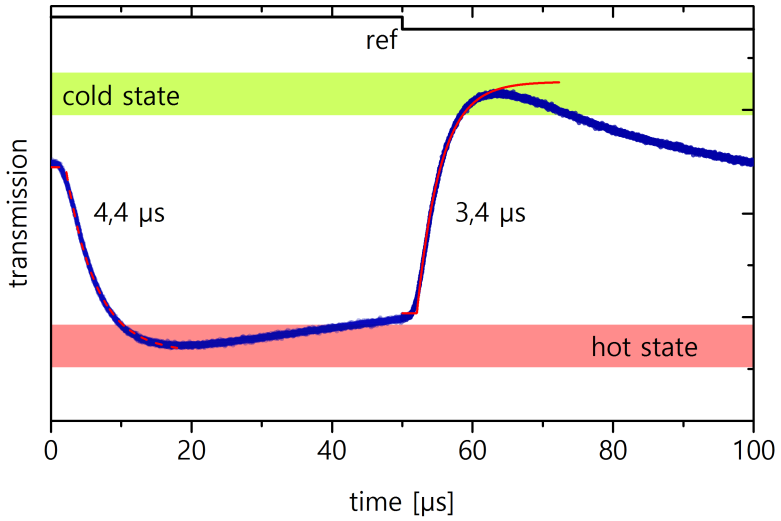

Figure 4.17 – Thermo-optic bistability switching time characterization. The data are obtained by averaging one hundred traces with 1 modulation period duration. The fit (red lines) inputs an exponential decay (dashed) or growth (straight) respectively. The reference modulation signal is shown for indication.

can be demonstrated on modulation signal with amplitude set below this threshold, and therefore we need to calibrate it. The method used for this purpose is straightforward: increase the modulation amplitude and check the optical response. When the amplitude is high enough, the optical state should flip at the modulation frequency. The latter must be lower than the cut-off frequency.

In our case, the optical state can be accessed both though the transmission signal or through the position of the mechanical mode in the noise spectrum. Here we focus on the two aspects. On one side, we record the transmission response in the oscilloscope. On the other side, the output signal is analyzed in the ESA via a fast photodetector. From the spectrum, we determine the two positions of the mechanical peak $\Omega_{\mathrm{m}}^{\mathrm{c}} = 2\pi \times 6.0572$ MHz and $\Omega_{\mathrm{m}}^{\mathrm{h}} = 2\pi \times 6.0164$ MHz respectively for the cold and hot optical states (see fig. 4.15). The RF signal is therefore amplified and demodulated using a lock-in amplifier. Two demodulation channels are used at frequencies $\Omega_{\mathrm{m}}^{\mathrm{c}}$ and $\Omega_{\mathrm{m}}^{\mathrm{h}}$ and with passband filter width of 1 kHz. The two corresponding demodulation signal amplitudes $V_{\mathrm{m}}^{\mathrm{h}}$ and $V_{\mathrm{m}}^{\mathrm{h}}$ are recorded in the oscilloscope.

The resulting time traces are shown for three values of the modulation amplitudes in fig. 4.18a. In each case, we show from top to bottom the reference modulation signal, the transmission signal and the demodulation amplitudes. Below $V_{\mathrm{mod}} = 950$ mV, the output signal show a square modulation following the drive. However, the amplitude of this signal does not correspond to optical switching in the bistability. In fact the optical state remains in its initial state. This is confirmed by the constant high noise amplitude at

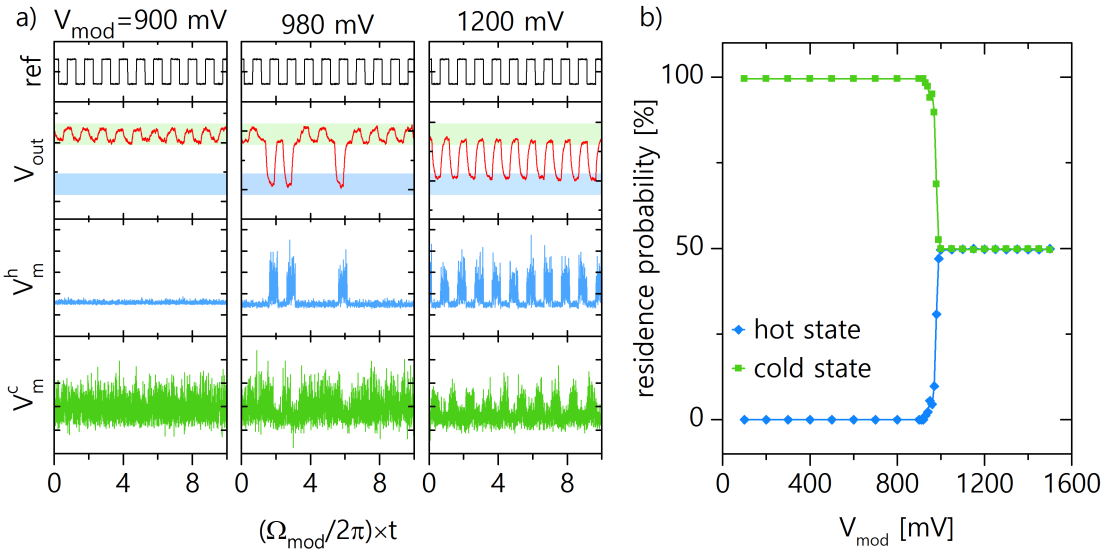

Figure 4.18 – a) For $V_{\mathrm{mod}} = 900$, 980 and 1200 mV, from top to bottom: reference modulation signal, transmitted signal V_{out} and demodulated noise amplitude at the hot (cold) state mechanical frequency $\Omega_{\mathrm{m}}^{\mathrm{h}}$ ($\Omega_{\mathrm{m}}^{\mathrm{c}}$). b) Probability for the optical state to be in the hot (blue) or cold (green) state. Measurement performed for $\Omega_{\mathrm{mod}} = 2\pi \times 10$ Hz. The probability evaluation uses the time-trace $V_{\mathrm{m}}^{\mathrm{h}}$ of length 20 s. The voltage is compared to an arbitrarily defined threshold to determine whether the system lies in the cold or in the hot state.

the cold mechanical frequency. Meanwhile the noise amplitude at the other mechanical frequency stays constant low. Around $V_{\mathrm{mod}} = 980$ mV, the optical state starts to flip. It is however not perfectly mastered by the modulation. The jumps are perfectly correlated whether the optical output or the mechanical frequency position is checked. Finally, over $V_{\mathrm{mod}} = 1$ V, the optical state switches are perfectly synchronous with the modulation reference signal.

For a given time trace, one can calculate the residence probability of the optical state. It simply consists in measuring the amount of time spent by the system in the cold (or hot) optical state. To do so, a threshold line is arbitrarily chosen in between the two corresponding amplitude levels. The probability for the system to set in the cold state is 100% for low modulation amplitudes (see fig. 4.18b). It quickly go down to 50% around the threshold amplitude $V_t = 980$ mV. The threshold amplitude V_t is clearly characterized with this measurement. Note that the evaluation of the residence probability can be equivalently performed using V_{out} or $V_{\mathrm{m}}^{\mathrm{h}}$ while $V_{\mathrm{m}}^{\mathrm{c}}$ is too noisy to obtain such a clear threshold curve. The statistical error associated to the residence probability is not plotted but verified to be significantly low, i.e. typically lower than 10%.

4.2.4 Amplification via high frequency modulation

Now that the cut-off frequency and the threshold modulation amplitude are calibrated, we investigate the amplification of a weak signal via a high-frequency intensity modulation. The input modulating signal writes:

$$V_{\mathrm{ref}} = V_{\mathrm{mod}}\mathrm{SQ}(\Omega_{\mathrm{mod}}t) + V_{\mathrm{hf}}\cos(\Omega_{\mathrm{hf}}t) \tag{4.5}$$

where $\mathrm{SQ}(x) = \mathrm{sign}(\sin(x))$ is the square function. With this electro-optical modulating signal, the optical field carries both signals.

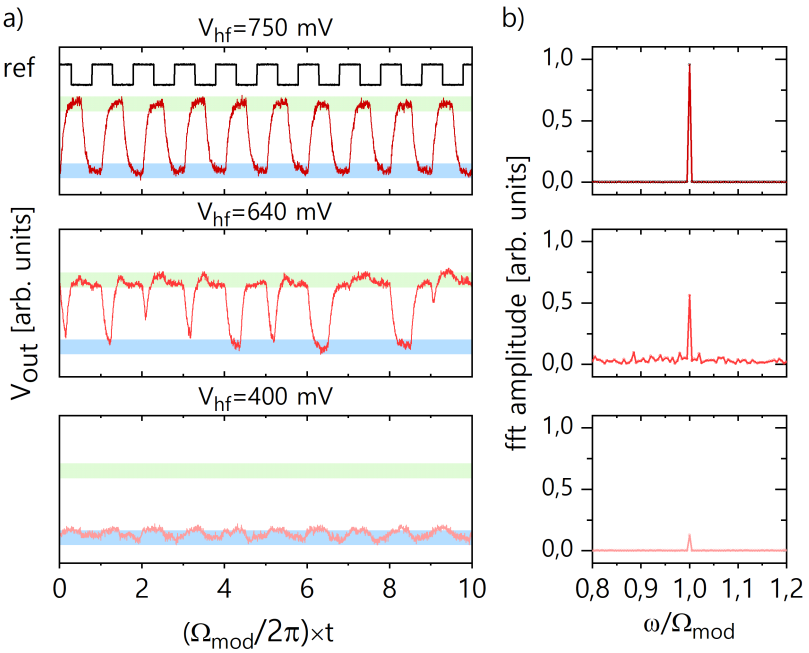

Figure 4.19 – a) Time-domain and b) frequency-domain transmitted signal V_{out} for three values of the high frequency signal amplitude $V_{\mathrm{hf}} = 800,\ 1280$ and 1500 mV. $\Omega_{\mathrm{hf}} = 2\pi \times 80$ kHz

When $V_{\mathrm{mod}} < V_t$ and $V_{\mathrm{hf}} = 0$, we know that the square signal can not flip the optical state. However, the increase of V_{hf} comes with a significant distortion of the bistability until the switching process can be re-activated. First, we try with $V_{\mathrm{mod}} = 500$ mV. We also chose a frequency $\Omega_{\mathrm{hf}} = 2\pi \times 80$ kHz and record the output optical response for increasing value of V_{hf}. The results are show in fig. 4.19a through three examples. While at 400 mV the system stays on the hot state and no flip occur, we observe a transition around 640 mV. Here the state inaccurately flips. The maximum fidelity – i.e. correlation between the flips and the reference square signal – is obtained around $V_{\mathrm{hf}} = 750$ mV. In each case, we plot the fft spectrum of the time trace. At frequency Ω_{mod}, a peak testifies the presence of the low-frequency square modulation. Its amplitude increases

when the switching process starts. In parallel of these measurements, the noise amplitude at the mechanical resonance frequency have also been recorded in order to compare its dynamics with the output optical field. However, because of the HF signal injection, the mechanical peak share its amplitude with the surrounding optomechanical sidebands. As a result, this amplitude is too low to be accurately analyzed.

The amplification factor $G_{V_{\mathrm{mod}}}$ is given by the ratio of the peak amplitude at V_{hf} by its value when $V_{\mathrm{hf}} = 0$:

$$G_{V_{\mathrm{mod}}} = \frac{\widetilde{V}_{\mathrm{out}}(\omega = \Omega_{\mathrm{mod}}, V_{\mathrm{hf}})}{\widetilde{V}_{\mathrm{out}}(\omega = \Omega_{\mathrm{mod}}, V_{\mathrm{hf}} = 0)} \tag{4.6}$$

For a given low-frequency signal amplitude V_{mod}, this factor is evaluated as a function of the high-frequency signal amplitude V_{hf}. This measurement is reproduced for several values of V_{mod}. The resulting amplification curves of shown in fig. 4.20. By definition, amplification occurs when $G_{V_{\mathrm{mod}}} > 0$. It is the case for modulation amplitudes higher than 50 mV. This value set a threshold under which the weak signal can not be amplified. In fact, at this value, an amplification is observed but only in a very limited range of HF signal amplitudes and the corresponding amplification factor is below 2. For higher values of V_{mod}, we observe an clear amplification up to 10. The range of V_{hf} in which this occurs is basically centered around 650 mV, except for the case $V_{\mathrm{mod}} = 100$ mV. Moreover, the width of this amplitude range yields a maximum for $V_{\mathrm{mod}} = 200$ mV. At this value, we find an amplification higher than 7 between $V_{\mathrm{hf}} = 500$ and $V_{\mathrm{hf}} = 750$ mV.

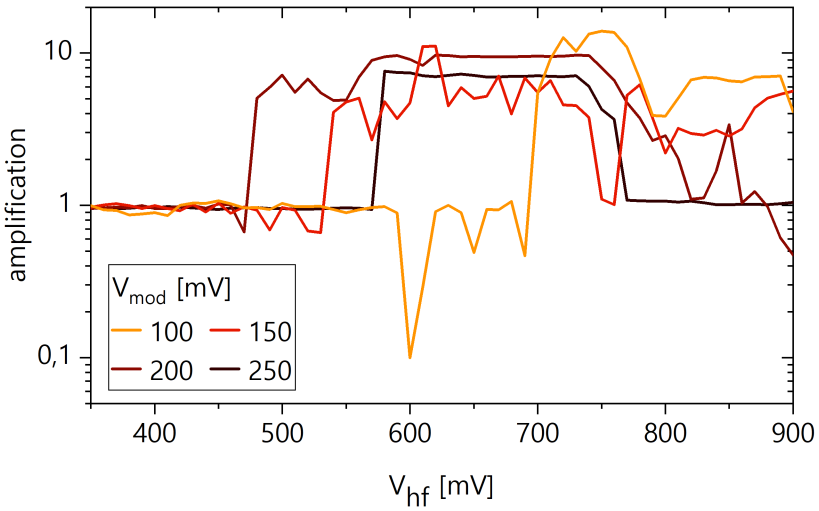

Figure 4.20 – Amplification factor as the function of the high-frequency signal amplitude for different modulation signal amplitudes. The amplification factor is given by the amplitude of the fft-domain signal peak at V_{hf} divided by its equivalent at $V_{\mathrm{hf}} = 0$. HF signal has frequency $\Omega_{\mathrm{hf}} = 2\pi \times 80$ kHz

In summary, we have demonstrated amplification of a weak signal using vibrational

resonance in a waveguide-coupled thermo-optic microresonator. The preliminary characterization of the bistable system is possible both through the waveguide transmission optical field and through the thermo-mechanical effect induced in the optomechanical cavity. This experimental results are not backed-up theoretically, although the mechanism of vibrational resonance is well understood in the literature. In complement of this experimental demonstration, it would be appreciable to draw a quantitative theoretical analysis of the phenomenon, based on the thermo-optic model. It would also be interesting to reproduce the experiment in an higher quality factor optical resonator, such that the mechanical resonances would get actively involved in the dynamics which would be a suitable basis for nonlinear optomechanics experiments.

4.3 Conclusion on the nonlinear dynamics experiments

All along this chapter, the effect of an intensity modulated drive on a thermo-optic optomechanical cavity is investigated through different aspects. First, using low intensity input laser, we describe and observe optomechanical sidebands surrounding the mechanical resonances. This effect results from the optomechanical interaction which enable a transfer of the modulation tones from the optical domain to the mechanical domain. The qualitative result yield in the apparition of sidebands surrounding the mechanical resonances in the noise spectrum of the output laser field. At higher input power, the effect of thermo-optic nonlinearity in the optical resonator leads to an asymetrization of these sidebands, as soon as the modulation frequency stands below a certain value. The phenomenon is understood as the result of asymmetrical heating and cooling processes occurring in the bistable resonator but is generally obtainable with other Kerr-type optical nonlinearities. The laser frequency happens to play an important role in the dynamics of the system. At the edge of the bistability, a new regime occurs for particular ranges of modulation depth and frequency. It manifests through an important elevation of the noise floor, which seem to derive from non-trivial oscillations in the optical domain. The lack of experimental data do not permit to properly understand this nonlinear dynamics yet. Thus it seems reasonable that these high amplitude oscillations are driven by modulation of the hysteresis cycle. In the second run of experiments, we focus on another optomechanical system in which the thermo-optic bistability in now exploited for the amplification of a weak low-frequency modulating signal. The effect, that occurs under the influence of a high-frequency period signal, is known as *vibrational resonance*.

Table of variables for Part I

Symbol : Meaning	Typical value (Units)
General	
$\hbar$: reduced Planck constant	1.055×10^{34} (J.s)
k_B : Boltzman constant	1.381×10^{-23} (J.K^{-1})
c : speed of light in vacuum	2.99×10^{8} (m.s^{-1})
θ_0 : ambient temperature in the lab	293 (K)
Material constants of indium phosphide	
n_0 : refractive index [Pettit and Turner, 1965]	3.16
$\frac{dn}{d\theta}$: thermo-optic coefficient [Della Corte et al., 2000]	1.9892×10^{-4} (K^{-1})
α : thermal expansion [Glazov et al., 1977]	4.6×10^{-6} (K^{-1})
$\sigma_{th}^{\mathrm{InP}}$: thermal conductivity [Glazov et al., 1977]	0.68 (W.cm^{-1}.K^{-1})
ν : Poisson's ratio [Dargys and Kundrotas, 1994]	0.36
Y : Young's modulus [Dargys and Kundrotas, 1994]	60 (GPa)
Y_{eff} : Effective Young's modulus in the PhC membrane (guess)	17 (GPa)
ρ : density [Dargys and Kundrotas, 1994]	4810 (kg.m^{-3})
Coupled mode theory	
s_i, s_t : resp. waveguide complex incident and transmitted amplitude	
$\tau = s_t/s_i$: normalized waveguide transmission complex amplitude	
$T = \lvert\tau\rvert^2$: normalized waveguide transmission intensity	
$P_{\mathrm{in}} = \lvert s_i\rvert^2$: waveguide incident power	< 1 (mW)
$a_\bullet$: complex amplitude of cavity $\bullet$ with $\lvert a_\bullet\rvert^2$ its stored energy	
ω_0 : cavity resonance frequency	$2\pi \times 193$ (THz)
κ_i : internal amplitude loss rate	
κ_{w} : external amplitude loss rate	
κ_t : total amplitude loss rate with $\kappa_t = \kappa_i + \kappa_{\mathrm{w}}$	
Q_i : internal Q-factor with $Q_i = \omega_0/2\kappa_i$	1500
Q_{w} : external Q-factor with $Q_{\mathrm{w}} = \omega_0/2\kappa_{\mathrm{w}}$	$10^2 - 10^4$
Q_t : total Q-factor with $Q_t^{-1} = Q_i^{-1} + Q_{\mathrm{w}}^{-1}$	
μ : cavity direct coupling rate	$2\pi \times 0.1 - 1$ (THz)
$Q_c = \omega_0/2\mu$: cavity direct coupling Q-factor	$Q_c \approx 10^2 - 10^3$
ϕ : phase shift in the WG between the cavities	0 – 2π
$\delta = \frac{\omega - \omega_0}{\omega_0}$: normalized detuning	$\pm 1/Q_{opt}$
Nonlinear CMT: thermo-optic effect	
κ_{abs} : linear absorption rate [fit figs. 2.12a and 2.12b]	95 (GHz)
R_{th} : thermal resistance of the cavity [fit figs. 2.12a and 2.12b]	1.7 $\times 10^4$ (K.W^{-1})
$\Delta\theta = \theta - \theta_0$: temperature elevation in the cavity	up to 10 K

Symbol : Meaning	Typical value (Units)
Nanophotonic platform geometry	
r : photonic crystal hole radius	90 - 110 (nm)
a : photonic crystal lattice constant	420 (nm)
h : SOI waveguide height	220 (nm)
w : SOI waveguide width	250 to 550 (nm)
Mechanics	
$\Omega_m/2\pi$: mechanical resonance frequency	1-10 (MHz)
$\Gamma_m/2\pi$: mechanical damping	1-10 (kHz)
m_{eff} : resonance effective mass	186 (pg)
σ_0, σ : internal stress at room temperature and at θ, respectively.	~ 30 (MPa)
Optomechanics - experimental	
$\omega_L/2\pi$, λ : Driving laser frequency and wavelength, respectively	
G_{ω_0}: dispersive optomechanical coupling	~ 1 (GHz/nm)
$G_{\kappa_i}, G_{\kappa_w}$: resp. internal and external dissipative optomechanical couplings	~ 1 (GHz/nm)
$g_0/2\pi$: vacuum single photon optomechanical coupling rate	$10^2 - 10^3$ (Hz)
$\Omega_{\mathrm{mod}}/2\pi$: modulation frequency	0-200 (kHz)
V_{mod} : modulation amplitude	0-3 (V)
χ : calibration constant (not determined)	
$\sqrt{\zeta}$: waveguide injection/collection efficiency	≈ 10 %
V_π: half voltage of the intensity (or phase) EOM	phase-EOM 3.5 (V) int-EOM 7.5 (V)
$\beta = V_{\mathrm{mod}}/V_\pi$: EOM modulation depth	
Optomechanics - theory	
$\frac{\Delta_i}{2\kappa_i} = \frac{\omega_L - \omega_i}{2\kappa_i}$: reduced laser detuning to resonance with ω_i and $2\kappa_i$ resp. the resonance frequency and linewidth	
$\overline{a}$, $\delta\hat{a}$: resp. optical mean field and fluctuating components	
$\overline{b}$, $\delta\hat{b}$: resp. mechanical mean field and fluctuating components	
Vibrational resonance experiment	
$\Omega_{\mathrm{m}}^{\mathrm{c}}$, $\Omega_{\mathrm{m}}^{\mathrm{h}}$: mechanical freq. at the cold or hot optical state, respectively	
$V_{\mathrm{m}}^{\mathrm{c}}$, $V_{\mathrm{m}}^{\mathrm{h}}$: amplitude of the noise spectrum at $\Omega_{\mathrm{m}}^{\mathrm{c}}$ and $\Omega_{\mathrm{m}}^{\mathrm{h}}$, respectively	
V_{hf}, Ω_{hf} : resp. high-frequency input signal amplitude and freq.	
V_{out} : transmitted power, directly measured at the waveguide output	
$G_{V_{\mathrm{mod}}}$: amplification gain	

Part II

Chaotic dynamics of coupled electro-optomechanical nanoresonators

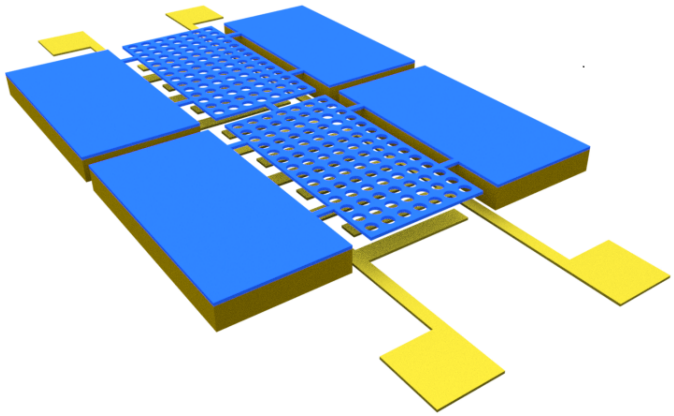

Coupled electro-optomechanical resonators

This second part is dedicated to the study of the nonlinear dynamics in coupled electro-optomechanical resonators. The system involves two mechanical resonators that are coupled mechanically with a small junction. Each resonator is excitable with a pair of interdigitated electrodes. Their respective displacement can also both be accessed independently using an optomechanical readout. In chapter 5, we describe the system and introduce the basic concepts required in the study of coupled resonators in the linear regime. Relying of this basis, a calibration of the mechanical properties, including the natural frequencies, the damping rates and the spring coupling, is established. It is also possible to calibrate the displacement and the applied electrocapacitive force.

Under strong excitation, the systems enters in a nonlinear regime. This is studied in chapter 6. The stationary response of the system is first modeled with a model of coupled driven Duffing oscillators. We demonstrate how the modulation of the force leads to chaos and investigate both the influences of the driving frequency, the modulation amplitude and of the modulation frequency. Several experimental bifurcation diagrams, that highlight this nonlinear dynamics, reproduced numerically thanks to the Duffing-Duffing model. Then, using a double-drive excitation on the system eigenmodes, several synchronization regimes are investigated. In particular in the chaotic regime, the phase dynamics experience a particular type of dynamics, refereed as imperfect phase synchronization, that we characterize statistically. Relying on our system chaotic dynamics, we apply a random number generation (RNG) protocol to our experimental time traces. We characterize this protocol in the frame of our particular system. A regime of perfect phase synchronization, that we can predict numerically, presents an immediate interest for performing synchronized bichromatic RNG.

Chapter 5

Design and characterization of the system

The main steps of the clean-room fabrication of the opto-electromechanical platform has been studied in the introduction. In this chapter we detail the geometry of the structures. The single-membrane design has been previously optimized within our group so the focus is on the coupling properties. We describe the optical readout as well as the electro-capacitive actuation before starting the mechanical characterization in the linear regime. In this context, the theoretical concepts are introduced when necessary. Finally we perform a calibration of the mechanical displacement and of the applied force which will be of great use in the next chapter for the modeling of the nonlinear dynamics.

5.1 Coupled NEMS platform design

To introduce the coupled membrane system, we first go back to the single membrane design with which the previous experiment have been performed. Relying on a simple linear model of coupled harmonic resonators, the strategy adopted for coupling the membranes is discussed. The resulting system mechanical eigenmodes are obtained using Finite Element Method simulations. The geometry of the interdigitated electrodes, which enable a capacitive actuation of the resonators, is finally precised.

5.1.1 Nanomembranes geometry

The mechanical resonators are extremely similar to those used in the optomechanics experiments. They consist in 20×10 μm^2 rectangular membranes with a thickness 260 nm given by the InP epitaxial layer (see fig. 5.1). The membranes are suspended over a 380 nm air-gap and are attached to the rest of the InP layer through two pairs of 1 μm wide and 2 μm long bridges positioned of each side of the membrane longer edge.

The clamping positions of these bridges are chosen to maximize the internal mechanical quality factor of the membrane fundamental resonance. One may also want to use longer or thinner bridges in order to increase the Q-factor but this comes with a higher risk of mechanical failure under strong excitation.

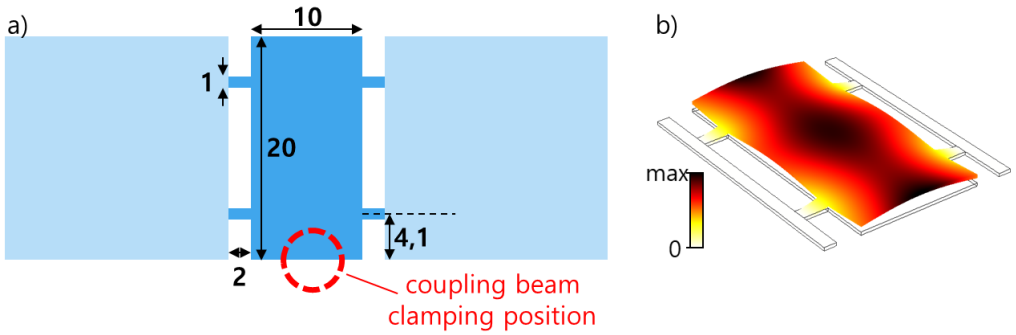

Figure 5.1 – a) Geometry of a single membrane. The dimensions are given in units of µm. The mesa structure (lighter blue) maintains the suspended resonator (darker blue). b) Total displacement of the single membrane at its fundamental mode simulated with finite element method.

In the past works [Chowdhury, 2016], the nonlinear regime of this structure has been the object of several studies. These latter include superharmonic resonance [Chowdhury et al., 2016] or weak signal enhancement using stochastic resonance [Chowdhury et al., 2017] or vibrational resonance [Chowdhury et al., 2020]. All these demonstrations are based on the Duffing oscillator model. In the next, we start from this geometry to obtain a system of two coupled nanomembranes. At each step of this study from the design to the study of complex nonlinear dynamics, we will attempt to identify the effect of the coupling on the physics.

5.1.2 Mechanical coupling

Conceptually, the straightforward way to couple two mechanical resonators is to attach a spring between them. It is necessary to go through the basic description of two coupled resonators before discussing the chosen design. Although it would be adequate to consider two identical resonators for a basic approach of the physics, the fabricated nano-components always slightly differ to each other which induces a natural frequency mismatch between the coupled membranes. In order to stay general, we consider two non identical harmonic oscillators A and B with natural frequencies Ω_A and Ω_B, damping rates Γ_A and Γ_B and identical mass m. This assumption relies on the fact that the two membranes are nearly identical and should have the same mass. Later on we will note that the natural frequencies of the resonators are different. As the natural frequency

is given by $\Omega_{A,B}^2 = k_{A,B}/m_{A,B}$ with $k_{A,B}$ the resonator's spring constant, it indicates that this latter is different from a membrane to another. In fact, it is probable that both parameters $k_{A,B}$ and m can vary but assuming that only the spring constant is responsible for the natural frequency mismatch does not change the following results. The resonators are coupled through a bi-linear interaction potential $V_{\text{int}} = -\frac{1}{2}mG(x_A - x_B)^2$ and no external force act on the system. Therefore the master equations for this system can be written:

$$\begin{cases} m\ddot{x_A}(t) + m\Gamma_A\dot{x_A}(t) + m\Omega_A^2 x_A(t) + mG\left[x_A(t) - x_B(t)\right] = 0 \\ m\ddot{x_B}(t) + m\Gamma_B\dot{x_B}(t) + m\Omega_B^2 x_B(t) + mG\left[x_B(t) - x_A(t)\right] = 0 \end{cases}$$

The identical masses assumption implies a symmetrical coupling $G_A = G_B = G$. It is convenient to consider the self-coupled frequencies $\omega_{A,B}^2 = \Omega_{A,B}^2 + G$. For a better readability, we stop writing the time dependence of the variables $x_{A,B}$ and $\dot{x}_{A,B}$:

$$\begin{cases} \ddot{x}_A + \Gamma_A\dot{x}_A + \omega_A^2 x_A - Gx_B = 0 \\ \ddot{x}_B + \Gamma_B\dot{x}_B + \omega_B^2 x_B - Gx_A = 0 \end{cases} \tag{5.1}$$

The first objective is to describe the eigenfrequencies of this system. These are the frequencies at which the system naturally responds, when relaxing after a perturbation for example. When submitted to a periodic excitation, the response amplitude of the system is also maximum at the resonance frequency. When two identical resonators are coupled, the mechanical system displays two resonances often refereed as symmetrical and anti-symmetrical modes (or bonding and anti-bonding, depending on the context).

A matricial approach is helpful for obtaining the frequencies $\omega_\pm$ and damping rates $\Gamma_\pm$ of the normal modes. We can assume $\Gamma_{A,B} \ll \omega_{A,B}$ since we expect mechanical quality-factors of the order of $Q_m \approx 500 - 1000$ from the previous work based on a single membrane. The values of $\omega_\pm$ and $\Gamma_\pm$ obtained by the diagonalization of the Jacobian of eq. (5.1) as described in [Zanette, 2018]:

$$J = \begin{pmatrix} 0 & 0 & 1 & 0 \\ 0 & 0 & 0 & 1 \\ -\omega_A^2 & G & -\Gamma_A & 0 \\ G & -\omega_B^2 & 0 & -\Gamma_B \end{pmatrix} \tag{5.2}$$

The eigenvalues of J can be written $\lambda_\pm = -\Gamma_\pm + i\omega_\pm$. A simple analytic expression for $\omega_\pm$ can be given by neglecting the dissipation:

$$\omega_\pm^2 = \frac{\omega_A^2 + \omega_B^2}{2} \pm \frac{1}{2}\sqrt{(\omega_A^2 - \omega_B^2)^2 + 4G^2} \tag{5.3}$$

By simplifying the problem with identical natural frequencies ($\omega_A = \omega_B = \omega_0$, and as soon as $G < \omega_0^2$), one would find the expression $\omega_\pm^2 = \omega_0^2 \pm G$. Coupling two

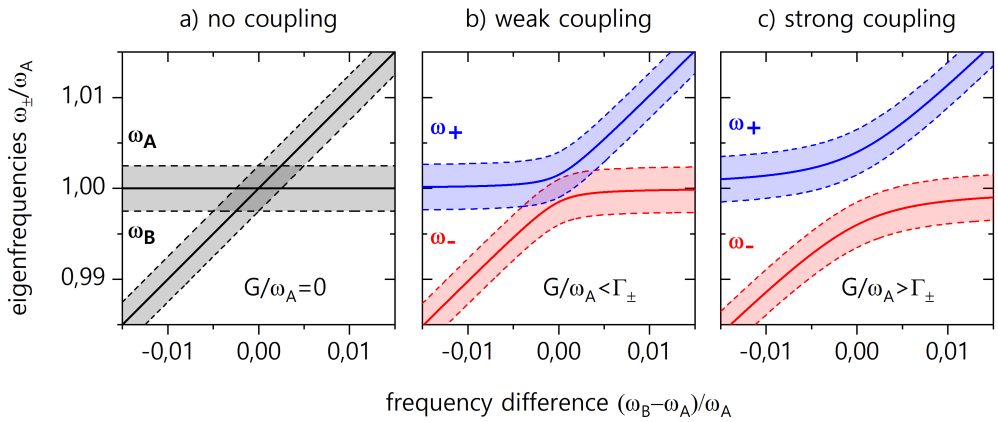

Figure 5.2 – Eigenfrequencies (straight lines) and associated spectral linewidth (dashed lines delimited transparent stripes) resulting from coupled undamped resonators as a function of the natural frequency difference. Computed using $\Gamma_A = \Gamma_B = \omega_A/200$ and a) $G/\omega_A = 0$, b) $G/\omega_A = 0.4$ and c) $G/\omega_A = 0.8$.

resonators leads to a level repulsion as soon as these resonators natural frequencies are close enough to each other. In fig. 5.2, the eigenfrequencies deduced from eq. (5.3) are represented as a function of the natural frequency difference $(\omega_B - \omega_A)/\omega_A$. For a non-zero spring coupling G, an avoided-crossing is observed in the spectrum and the splitting at $\omega_A = \omega_B = \omega_0$ is given by G/ω_0.

However, this does not guarantee the two normal modes to be resolved in the mechanical spectrum. The dissipation rates $\Gamma_\pm$ has to be taken into account. Their general expression are quite complicated bu they can be numerically deduced from the Jacobian diagonalization in order to know whether or not the spectral resolution criterion $G/\omega_0 > \Gamma_\pm$ is satisfied.If the mechanical modes overlap near the avoided-crossing point, the resonators are weakly coupled, while the opposite situation is refereed as strong coupling [Zanotto, 2018].

In order to produce a pair of coupled mechanical membranes, the geometry described above is simply duplicated and a coupling element is added between the membranes. In practice, we will use a rectangular nanobeam clamped on each membrane. Its geometry must maximize coherent energy transfer between the two mechanical modes. In particular, we will perform this optimization for the fundamental resonances. The displacement field of the single membrane fundamental mode has a maximum displacement at the center of its width as shown in fig. 5.1. We note ℓ and w respectively the length and the width of this coupling beam(see fig. 5.3a). These two geometrical parameters have a strong influence on the mechanical coupling. The dimensions are tuned to maximize the coupling between the fundamental modes although coupling might still occur for higher order modes. This optimization is done by computing the system mechanical

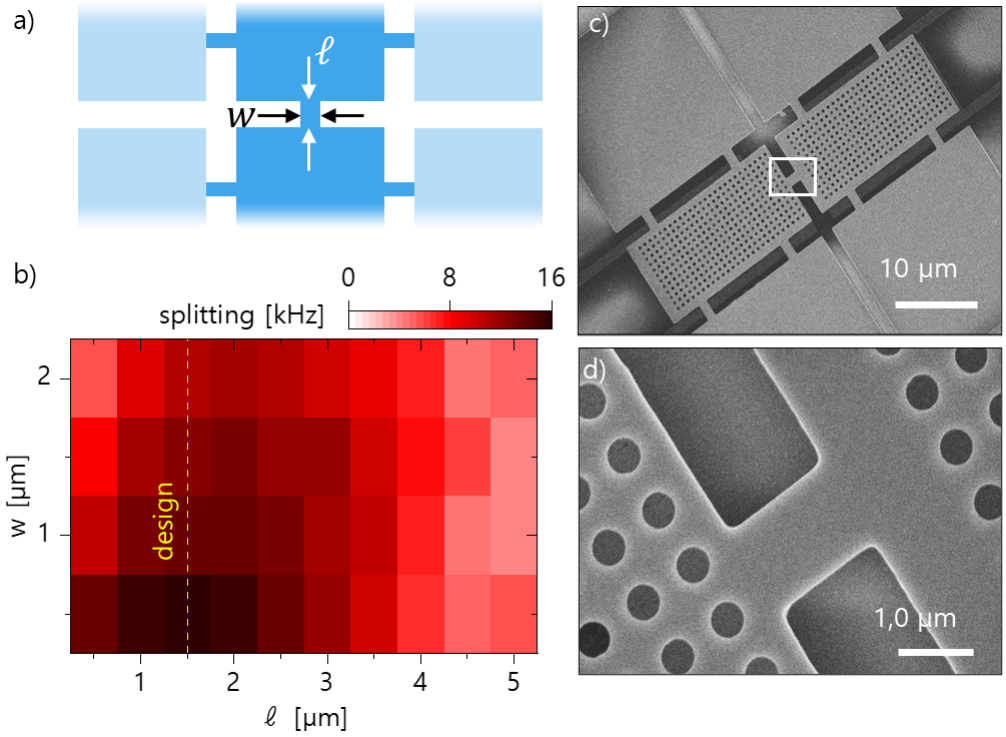

Figure 5.3 – a) schematic of the coupled membranes with the introduction of a $\ell \times w$ coupling beam. b) Simulated frequency splitting of fundamental mechanical mode as a function of the coupling beam dimensions c) SEM image of the ensemble. d) SEM image of a $1,5 \times 1,0$ µm^2 coupling beam.

eigenfrequencies with COMSOL Multiphysics. The frequency difference between the fundamental symmetrical mode and the fundamental anti-symmetrical mode is checked while the dimensions are tuned. The resulting colormap in fig. 5.3b shows that a maximum coupling occurs whenever $\ell = 1.5$ µm. All the structures are designed using this coupling length while the width is changed from 0.5 to 2 µm in order to try exploring several coupling regimes. SEM micrographs of the structure is shown in fig. 5.3c and a zoom on the coupling junction in fig. 5.3d. The mechanical ensemble geometry including two membranes coupled with a 2×1 µm^2 is now tested with Comsol simulations. The mechanical modes displacement fields are obtained and compared with the equivalent results for a single membrane. In fig. 5.4, the first 10 mechanical modes are illustrated by mean of their normal displacement fields and sorted by increasing frequency. For each of these mode, the decomposition into a symmetrical and an anti-symmetrical modes is shown. The displacement color scale is not common to all images as we want here to point at the relative displacement within a given deformation mode.

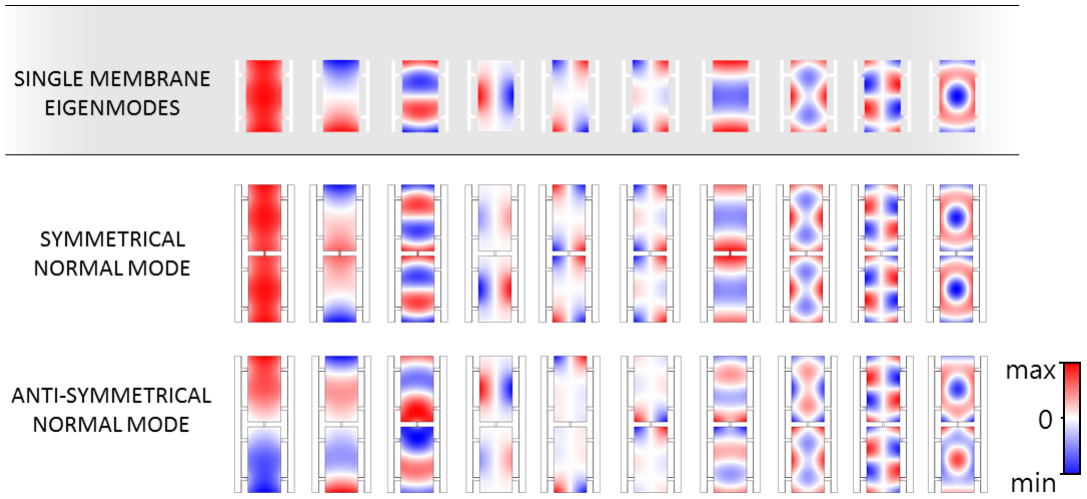

Figure 5.4 – Simulated out-of-plane displacement fields for 10 mechanical eigenfrequencies. The mechanical coupling induces a level repulsion leading each mode to decompose into an anti-symmetrical mode (top) and a symmetrical mode (bottom).

5.1.3 Interdigitated electrodes

Each membrane is suspended over a pair a gold interdigitated electrodes (IDEs). This actuator is schematically represented in fig. 5.5a. By applying a difference of electrical potential between these electrodes, an electrical field is produced around the IDEs. In particular the electrical field distribution shows significant normal component to the membranes plane. Although the InP layer is not doped, residual carriers can thus be driven by this electrical field. This strategy is particularly efficient at the membrane fundamental resonance as the electrical field normal component distribution overlaps particularly well with the corresponding out-of-plane displacement field.

The optimization of the IDEs geometry is performed by maximizing the force applied on the membranes for a given applied voltage. The description of this force will be the object of a discussion in section 5.2.2.2 but basically, it is proportional to the derivative of the capacitance with the membrane position $\partial C/\partial x$. This quantity can be expressed as a function of the material constants as well as the IDEs geometry. Such approach, as detailed in [Makles, 2015], permits to map $\partial C/\partial x$ as a function of the interdigit separation a and the air-gap height as shown in fig. 5.6. The capacitive force increases as the air-gap height is reduced. In practice, each membrane is suspended over a pair of IDEs so it is possible to drive the system from either side. As shown in the SEM images figs. 5.5b and 5.5c, the shortest distance between the two sets of IDEs is given by the length of the coupling beam. As a function of the digit-separation a, the force displays a maximum (see fig. 5.6). Finally the electrodes width is chosen as half the digit-separation (i.e. $a/2$) since this value also maximizes the quantity $\partial C/\partial x$, and therefore the force.

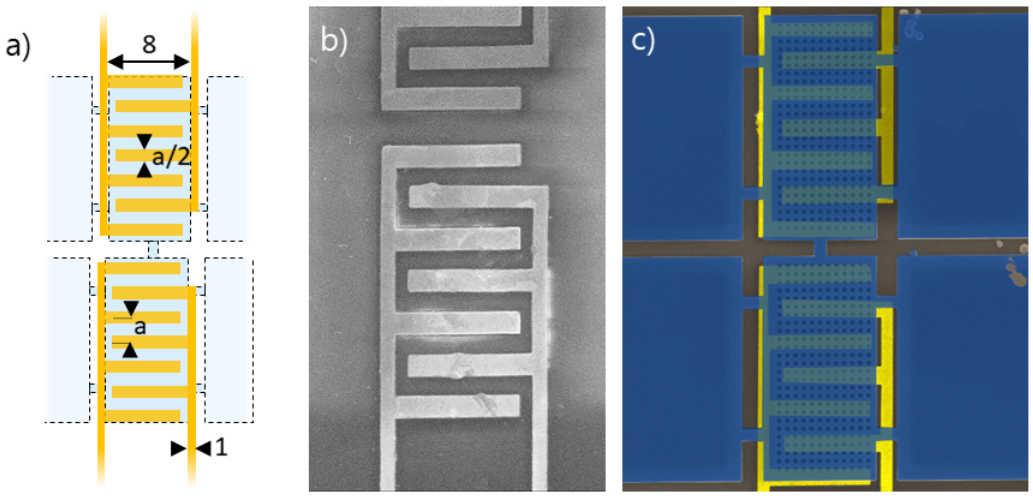

Figure 5.5 – a) Full schematic of the system including two coupled membranes suspended over their respective pair of IDEs. The IDEs dimension are indicated in units of µm. b) SEM image of a pair of IDEs before the BCB bonding. c) colorized SEM image of the ensemble. Each InP membrane (blue) are suspended over a pair of IDEs (yellow).

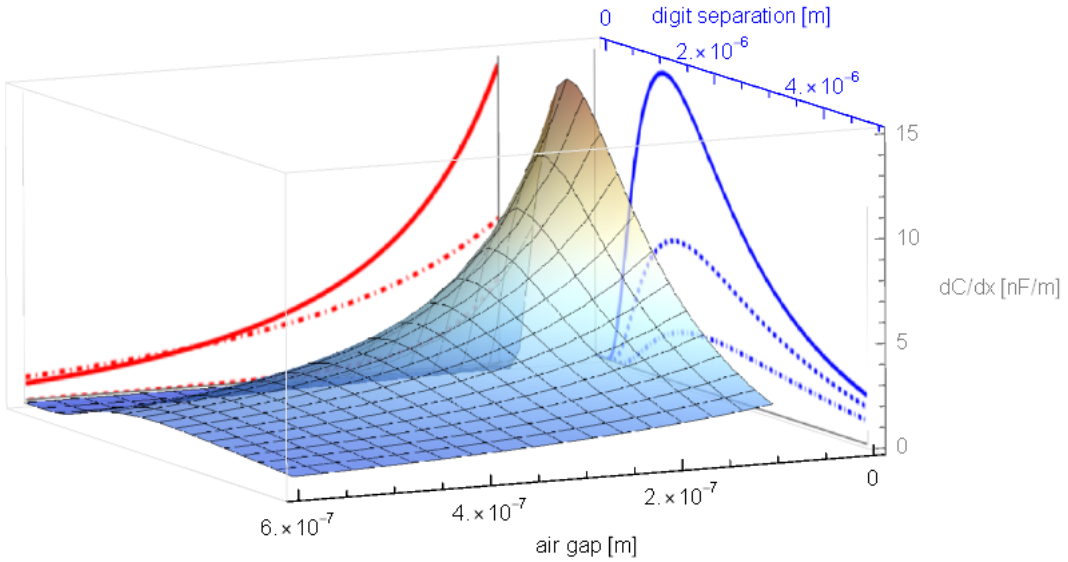

Figure 5.6 – The quantity $\partial C/\partial x$ is mapped as a function of the IDEs digit separation and the air gap dimension. The projection are shown for a gap fixed to 380 nm, 200 nm and 100 nm (resp. blue straight, dashed and dash-dotted) and with the digit separation fixed to 1.5 µm, 3 µm and 0.5 µm (resp. black straight, dashed and dash-dotted). The straight lines correspond to the chosen design.

5.2 Experimental setup

The mechanical resonator displacement optical readout and electro-capacitive actuation schemes are detailed in this section. The Fabry-Pérot cavity formed by the IDEs and the associated suspended membrane, which acts as a deformable mirror, is spectrally characterized. Secondly, we introduce a model of the force exerted by the IDEs on the membrane.

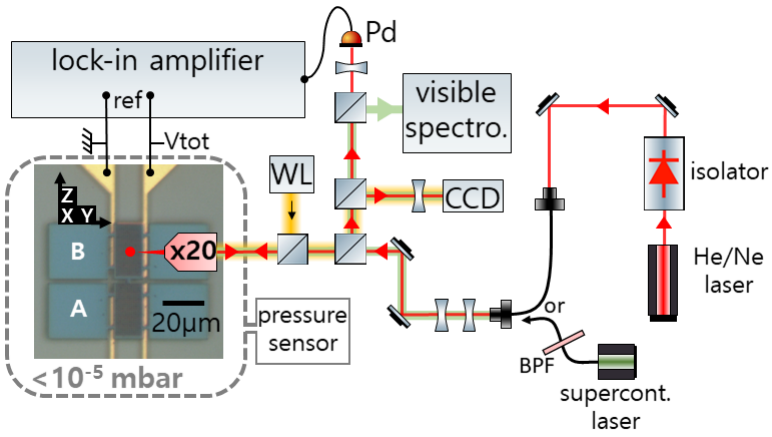

Figure 5.7 – Optomechanical characterization setup. The supercontinuum laser (green) is used to characterize the Fabry-Pérot cavity made by the IDE/membrane system. The Helium-Neon laser (red) is used for the mechanical displacement readout. A white light collimated source (orange) is used to image the structures.

5.2.1 Optical readouts

For the optical properties The system membrane/IDE constitutes an optical cavity we can probe for measuring the mechanical displacement (see schematic in fig. 5.8a). In order to characterize this cavity we use a supercontinuum laser preliminary filtered with a 500-770 nm band pass filter (BPF). The laser field initially circulates in an optical fiber at the output of which the beam is collimated back in free-space. The spot size is reduced using a telescope made of 2 converging lenses. The laser beam is then identically focused on the membrane center giving rise to a beam waist of approximately 5 µm. The white light beam is focused on the sample thanks to a $\times$20-microscope objective so the light spot shines an area containing more than an ensemble of membranes. The reflected light is sent to a CCD camera whose output can be acquired in real time on our computer. The reflected beam is analyzed with a visible spectrometer (see setup in fig. 5.7). The sample holder is loaded on a 3D nano-positioning stage that we remotely control. In order to image the sample and place correctly the laser on the membrane,

we aligned a collimated white light source parallel to the laser beam. We normalize the resulting reflectance spectrum with a reference measurement obtained by pointing the laser at a gold planar surface available on the chip. The normalized reflectance (see fig. 5.8b) shows an absorption dip typical from Fabry-Pérot cavity resonance and centered around 630 nm with an optical Q-factor of about 10. Despite this low Q-factor ~ 10 this dip matches with the Helium-Neon (He-Ne) wavelength $\lambda = 633$ nm which is used to optically readout the membranes displacements.

For the mechanical properties The intensity stabilized He-Ne laser is isolated from the setup to avoid any reflection to disturb the cavity. We coupled the free-space laser beam to an optical fiber in order to limit the beam divergence along the setup. The reflected beam is sent to a 10Hz-100MHz broadband photodetector for further signal analysis on the output electrical signal using the lock-in amplifier.

Note that the mechanical readout could also be performed with a Michelson interferometer by using a local oscillator to the optical setup, allowing a higher optical power in the photodetector. The drawback of this approach is the decorrelation of the mechanical noise between the reference arm and the system of interest due to their distance on the experimental table. Thus the mechanical response is read with a higher amplitude but the noise at low frequency (i.e at the measurement timescale 1-100 Hz) perturbs the measurement.

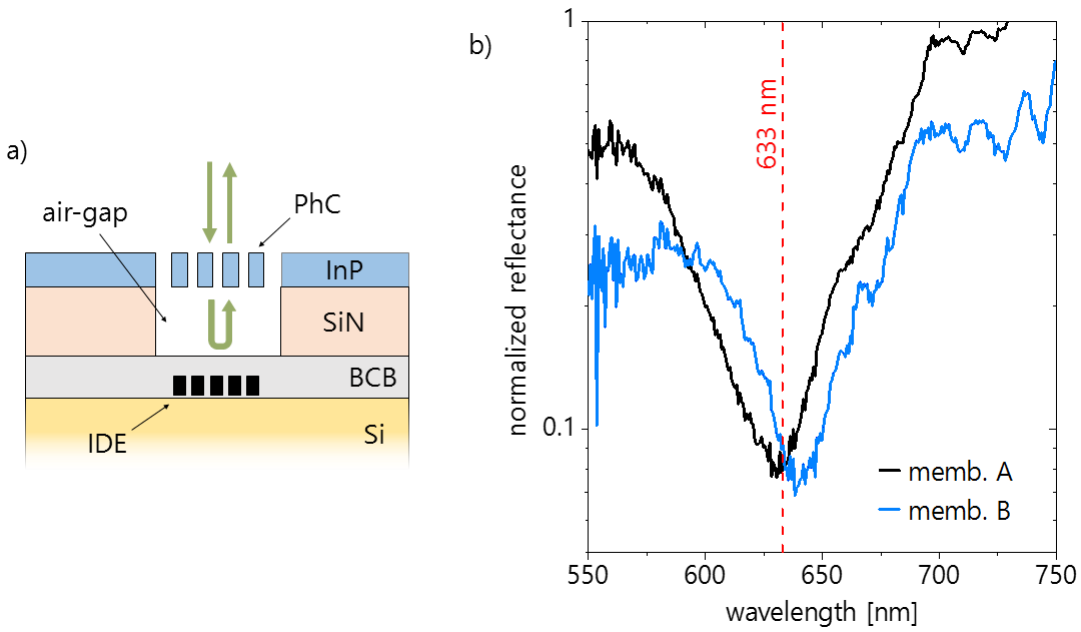

Figure 5.8 – Reflectance spectra obtained on the membranes. A resonance dip is visible near the He-Ne laser wavelength (red dashed line).

Optomechanical coupling This system constitutes an optomechanical Fabry-Pérot cavity whose optical frequency shift per displacement is given by [Aspelmeyer et al., 2014]:

$$\mathcal{G} = |\frac{\partial \omega_c}{\partial x}| = \frac{\omega_c}{L} \tag{5.4}$$

where $\omega_c = \pi \times c/L$ is the fundamental resonance frequency of a Fabry-Pérot cavity of length L. Assuming an homogeneous refractive index of the air-gap volume – which is not perfectly true given the presence of a BCB layer – and using $\omega_c = 2\pi \times c/\lambda_0$ and $L = 380$ nm, we obtain $\mathcal{G} \approx 2\pi \times 1230$ GHz/nm. The corresponding optomechanical coupling between this optical cavity and the fundamental mode of our mechanical resonator is $g_0 = \mathcal{G} x_{zpf}$ with $x_{zpf} = \sqrt{\hbar/2m_{\text{eff}}\Omega_m}$ is the zero point fluctuation amplitude of this mechanical mode and Ω_m its angular frequency. For a resonance frequency $\Omega_m = 2\pi \times 2.2$ MHz and a simulated effective mass $m_{\text{eff}} = 186$ pg, we find $g_0 \approx 2\pi \times 170$ MHz.

Of course the extremely low optical quality factor ($Q_{\text{opt}} \approx 10$) of this cavity prevents any significant dynamical backaction to be observed as the resolved sideband regime can be achieved for $\Omega_m > \gamma_{\text{opt}}$ while we obtain $\Omega_m \approx 10^{-8} \times \gamma_{\text{opt}}$!

5.2.2 Electromechanical actuation

We have discussed the experimental setup used for the mechanical displacement readout. Now we will describe how our electromechanical structures can be driven. After the technical description of the electrical connections from the chip to the lock-in amplifier, we can model the capacitive force exerted by the set of interdigitated electrodes.

5.2.2.1 Electrical connections

The chip is stuck on a ceramic chip-receiver using silver paste. The electrical connections between the sample and this receiver are done with wire bonding connections. We use 25 μm diameter Aluminium wires bonded on the gold pads. The chip-receiver is then encapsulated into a PLCC-to-DIP adapter. This last only has 44 electrical pins which limits the number of structures on the sample. We use 40 pins which fits with 20 pairs of IDEs, or 10 systems of 2 coupled membranes. 40 electrical wires are then tin-welded on these pins in the back on the sample holder. The welds are isolated to each other using heat-shrink sheath. The wires are then contacted to the sub-D 50 plug available at the chamber feed-through. The sub-D 50 output is connected to an electrical board outside the vacuum chamber where 40 independent BNC connections are available with their respective switch in order to excite or ground a desired electrode. Given the mechanical frequency we expect to handle in the following experiments (in the MHz domain), the use of BNC cable is appropriate.

5.2.2.2 Force modeling

We consider that the membrane/IDE system behaves as a position dependent capacitance $C(x)$. By applying total voltage V_{tot} on a set of interdigitated electrodes, the total potential energy stored in the capacitance writes $E(x) = \frac{1}{2}C(x) \times V_{tot}^2$. The force exerted on the membrane derives [1] from this potential energy [Galayko, 2018]:

$$F = \frac{1}{2}\frac{\partial C}{\partial x} \times V_{tot}^2 \tag{5.5}$$

In order to drive the system at frequency ω_d, a static voltage and a AC voltage are applied to the IDEs. The total voltage writes $V_{tot} = V_{dc} + V_{ac}\cos(\omega_d t)$ and the resulting force is:

$$F(x) = \frac{1}{2}\frac{\partial C}{\partial x} \times \left(V_{dc}^2 + \frac{1}{2}V_{ac}^2 + 2V_{dc}V_{ac}\cos(\omega_d t) + \frac{1}{2}V_{ac}^2\cos(2\omega_d t)\right) \tag{5.6}$$

Note that this force is not only resonant but also owns a static component and an off-resonant force that excites the resonator at twice the resonant frequency. In order to understand how this static force influence the mechanical response, we can solve our coupled resonators model with a constant external mass-normalized force $F_{DC} = \frac{1}{2}\frac{\partial C}{\partial x} \times \left(V_{dc}^2 + \frac{1}{2}V_{ac}^2\right)$ applied on one of the resonators. Let's say A. Intuitively, we know that this static forced exerted on the resonator will displace it. Any additional time dependent force will put it in motion around a new equilibrium position. From this point of view, it is coherent to introduce an position offset $x_{A,0} = F_{DC}/\omega_A^2$. Then the master equation for the resonator A becomes:

$$\ddot{x}_A + \Gamma_A\dot{x}_A + \omega_A^2(x_A - x_{A,0}) - Gx_B = 0$$

In our experiments, F_{DC} could either finds its origin in a residual stress in the material, or be an external force imposed by the user. It is interesting to remark that the displacement induced by a static force is Q_m times smaller than the resonant displacement with Q_m the mechanical quality factor. Similarly, the off-resonant forcing term at frequency $2\omega_d$ is not expected to significantly drive the displacement and this will be experimentally confirmed later. Thus the electro-capacitive force can be simplified to its resonant term:

$$F(x) \approx \left|\frac{\partial C}{\partial x}\right| \times V_{dc}V_{ac}\cos(\omega_d t) \tag{5.7}$$

This expression also relies on the assumption of a linear capacitance. Under high mechanical displacements one might require do consider a nonlinear capacitance:

$$\frac{\partial C}{\partial x} = \mathcal{C}_0 + \mathcal{C}_1 x + \mathcal{C}_2 x^2 + \mathcal{C}_3 x^3 + ... \tag{5.8}$$

[1] This partial derivative must importantly be computed at constant charge.

In general only $\mathcal{C}_0$ will be considered but the higher order terms are interesting to keep in mind. The 1st order term $\mathcal{C}_1$ is responsible of a mechanical frequency shift of the resonator which can be useful for tuning the resonator frequency. This effect is often called the "dielectric tuning" of the resonance frequency [Unterreithmeier et al., 2009]. Note that this effect is often exploited in order to generate a force component that act as a modulation of the natural frequency. This leads to a parametric oscillator $\ddot{x} + \Gamma\dot{x} + \omega_0^2\Big(1 + \frac{1}{4}\mathcal{C}_1 V_{ac}^2 \cos(2\omega_d t)\Big)x = f\cos(\omega_d t)$.

The higher terms $\mathcal{C}_2$ and $\mathcal{C}_3$ introduce anharmonic terms in the mechanical potential. In particular, the 3rd order term can shift the mechanical Duffing nonlinearity which could be interesting for further experiments.

5.3 Mechanical characterization

Having set an optical detection mean and discussed the basic principles of the electro-capacitive actuation, we can now characterize our mechanical system. First, we can measure the mechanical response over a large range of the driving frequency and try to identify the different resonances to a given displacement field. We will then focus on the fundamental mechanical resonances and go through the theory of two driven non identical and coupled harmonic oscillators to describe the spectrum shape. We can extract the key-parameters of the membranes from this fit.

5.3.1 Mechanical response spectrum

The mechanical characterization of the system starts with a measurement of its spectral response over a large frequency span. The chip is placed in a vacuum chamber pumped below 10^{-5} mbar. We focus on two membranes connected with a 0.5×1.5 µm^2 coupling beam. The IDEs have interdigit separation of 3 µm and digit width of 1.5 µm. The He-Ne laser beam is focused on the center of the membrane while this same membrane is excited with $V_{dc} = 0.5$ V and $V_{ac} = 2.5$ V. The converted optical signal is demodulated in the lock-in amplifier with a bandpass filter centered at the driving frequency ω_d. The demodulation bandwidth is reduced down to 100 Hz around this reference. The driving frequency is swept from 1 MHz to 20 MHz.

The resulting response amplitude, shown in fig. 5.9, displays a large number of resonance peaks. The fundamental resonance of the system is found around 2.2 MHz and the finite element method (FEM) simulations predict this first resonance to be the symmetrical normal mode resulting from the coupling between the membranes. The second resonance, found at 2.4 MHz here, should therefore be the associated anti-symmetrical resonance although the splitting between these peaks is larger than expected in the simulation. This disagreement occurs because the membrane do not have identical

natural frequencies as assumed in the FEM simulations. For this reason the following peaks can not easily be associated to a given displacement field distribution.

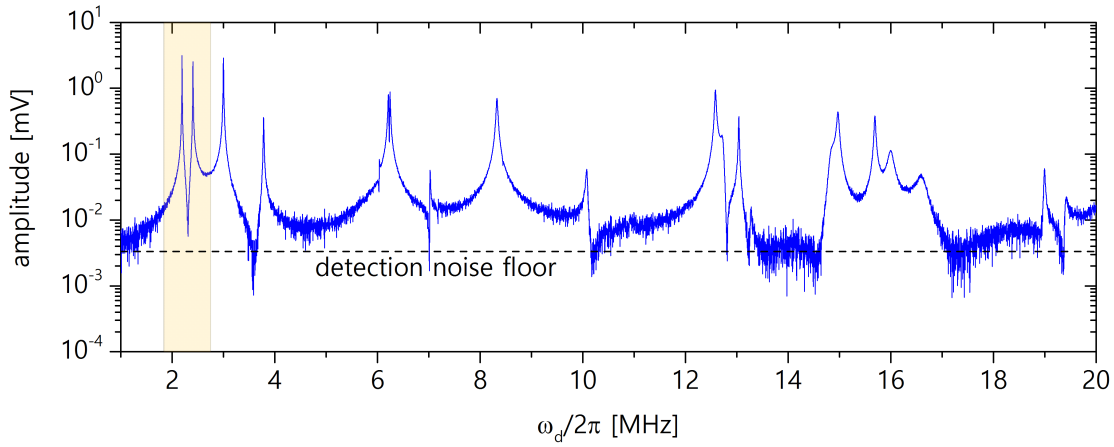

Figure 5.9 – Mechanical response spectrum of the coupled membrane system over a large span. Several resonance peaks are found including the fundamental eigenmodes highlighted in the transparent stripe. Demodulation bandwidth set to $\mathrm{BW} = 100$ Hz. Coupling beam dimension: 0.5×1.5 µm^2.

The amplitude of the mechanical peaks is strongly dependent on the position of the laser spot on the membrane. Indeed, as shown in the expected eigenmode displacement fields in fig. 5.4, the maximum displacement is not necessarily reached at the membrane center. This is less true for the fundamental resonance, for which the displacement does reach a maximum of the membranes centers, but is still quite homogeneous around these points. This mode therefore presents an experimental advantage as its readout does not require a particular attention on the laser spot position: we will simply try to maximize the response signal. Similarly the mechanical linewidths are not all equal as the clamping beam positions are chosen to enhance the mechanical quality factor at the fundamental resonance. The coupling beam dimensions have also been optimized for this particular mode. Consequently in the following work we will always focus on the fundamental eigenmodes (transparent stripe in fig. 5.9) and the laser spot will be placed at the membrane center.

5.3.2 Theoretical response of two coupled resonators in linear regime

The eigenvalues analysis is a very useful and strong method to obtain the exact normal mode frequencies and damping rates. However, in order to fit our experimental data. It is necessary to derive the expressions of the resonators amplitude and phase responses

in the presence of one or two driving forces. We consider two driving harmonic forces at frequency ω_d of respective strength f_A and f_B and delayed with regard to each other with a phase ϕ. The resulting external forces $F_A = f_A \cos(\omega_d t)$ and $F_B = f_B \cos(\omega_d t + \phi)$ are added on the right hand sides in eq. (5.1). The master equations system can be solved by assuming the solutions $x_{A,B}(t) = \mathfrak{Re}\left(\underline{r_{A,B}} e^{i\omega_d t}\right)$ where $\underline{r_{A,B}} = r_{A,B} e^{i\vartheta_{A,B}}$. We choose $r_{A,B} > 0$ and write the following equations in the rotating frame $e^{i\omega_d t}$. We also choose the external drive f_A as the reference of phase. At the stationary regime, $\dot{r}_{A,B}(t) = 0$:

$$\begin{cases} i\Gamma_A \omega_d \underline{r_A} + (\omega_A^2 - \omega_d^2)\underline{r_A} + G\underline{r_B} = f_A \\ i\Gamma_B \omega_d \underline{r_B} + (\omega_B^2 - \omega_d^2)\underline{r_B} + G\underline{r_A} = f_B e^{i\phi} \end{cases}$$

i Normalization:

The number of relevant parameters is reduced by normalizing the problem. We replace all the parameters by their equivalent dimensionless quantities. More importantly the driving frequency ω_d, that is used as unit of time, is now expressed in terms of detuning δ.

$\omega_d t$	$\to t'$	time
$(\omega_B - \omega_A)/\omega_d$	$\to \Delta\omega$	natural frequency mismatch
$(\omega_B - \omega_d)/\omega_d$	$\to \delta$	detuning from resonator B
$(\omega_A - \omega_d)/\omega_d$	$\to \delta - \Delta\omega$	detuning from resonator A
$\Gamma_{A,B}/\omega_d$	$\to \gamma_{A,B}$	damping rates
G/ω_d^2	$\to g$	spring coupling
$f_{A,B}/\omega_d^2$	$\to \tilde{f}_{A,B}$	driving amplitudes

Thus our driving frequency ω_d is fully replaced by only one quantity δ. The choice of ω_B as a detuning reference rather than ω_A is due to the fact that, in our experiments, the resonator B is almost always the one we drive.

Furthermore, if $\omega_d \approx \omega_A, \omega_B$ then $\omega_B^2 - \omega_d^2 \approx 2\omega_d(\omega_B - \omega_d) = 2\delta\omega_d^2$:

$$\begin{cases} i\gamma_A \underline{r_A} + 2(\delta - \Delta\omega)\underline{r_A} + g\underline{r_B} = \tilde{f}_A \\ i\gamma_B \underline{r_B} + 2\delta \underline{r_B} + g\underline{r_A} = f_B e^{i\phi} \end{cases}$$

which directly gives the complex amplitudes:

$$\underline{r_A} = \frac{\tilde{f}_A - g\underline{r_B}}{2(\delta - \Delta\omega) + i\gamma_A} \qquad \text{and} \qquad \underline{r_B} = \frac{\tilde{f}_B e^{i\phi} - g\underline{r_A}}{2\delta + i\gamma_B}$$

Isolating $\underline{r_A}$ and $\underline{r_B}$ gives:

$$\begin{cases} \underline{r_A} = \dfrac{g\tilde{f}_B e^{i\phi} + \Big[2\delta - i\gamma_B\Big]\tilde{f}_A}{g^2 - \Big[2(\delta - \Delta\omega) - i\gamma_A\Big]\Big[2\delta - i\gamma_B\Big]} \\ \\ \underline{r_B} = \dfrac{g\tilde{f}_A + \Big[2(\delta - \Delta\omega) - i\gamma_A\Big]\tilde{f}_B e^{i\phi}}{g^2 - \Big[2(\delta - \Delta\omega) - i\gamma_A\Big]\Big[2\delta - i\gamma_B\Big]} \end{cases} \tag{5.9}$$

The displacement amplitude is then given by $r_{A,B} = |\underline{r_{A,B}}|$ and the resonators phases are given by $\vartheta_{A,B} = \arg(\underline{r_{A,B}})$.

Here again, we won't explicitly write the expressions for r_A, r_B, ϑ_A and ϑ_B since it would not be so relevant and quite complicated without any simplification. These expressions can be computed numerically from eq. (5.9) for any fit purpose. Note also that $|\underline{r_A}|$ and $|\underline{r_B}|$ yield maxima when $\omega_d = \omega_\pm$. In terms of normalized detuning δ, it corresponds to $\delta_\pm = (\omega_B - \omega_\pm)/\omega_\pm$.

5.3.3 Determination of coupling

Now we can start to present the experimental measurements of the mechanical motion in the linear regime. Here the objective is the measurement of coupling. We propose two methods. The first relies on the stationary response of the system as a function of the driving frequency. The resulting spectral response amplitude and phase can be fitted using the linear model. This fit interestingly returns all the intrinsic properties of the system, including the frequencies, damping and the coupling. However, due to this large number of fitting parameters, the accuracy on the coupling evaluation is not optimal. We therefore propose a second method based on the direct measurement of an avoided crossing between the system eigenmodes. This can be achieved by shifting a natural frequency regarding the other one, either via a photothermal absorption process or using a DC induced dielectric tuning of the material.

5.3.3.1 Measurement of the mechanical response

We consider here another[2] system of two coupled membranes, refereed as A and B, and coupled with a 0.5×1.5 µm^2 junction. The membrane B is driven by applying $V_{dc} = 0$ V and $V_{ac} = 0.5$ V on its set of IDEs. With these low values, the mechanical motion is restricted to a linear regime. The membrane A and B are successively read while the driving frequency ω_d is swept over the fundamental resonances preliminary found around

[2] i.e. different from the one presented in fig. 5.9

2.6 MHz. The response amplitude and phase of membrane A (resp. of membrane B) are shown with green dots (resp. blue dots) in fig. 5.10. Both measured amplitudes display two peaks located at $\omega_- = 2\pi \times 2.58$ MHz and $\omega_+ = 2\pi \times 2.63$ MHz while the measured phases execute a phase shift at each resonance. Below 2.55 MHz, the membrane A response amplitude nears the detection noise floor which affects the fit quality and this is particularly visible with the phase response.

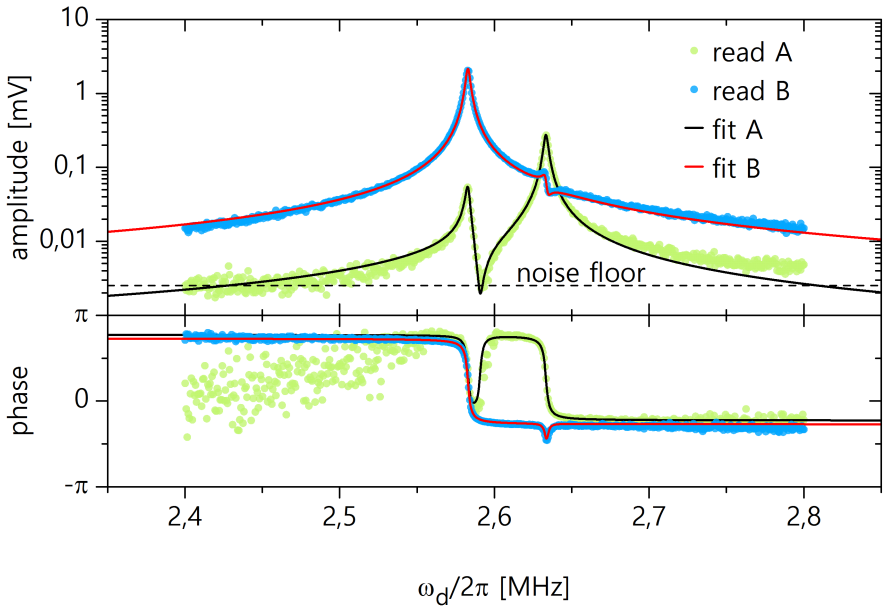

Figure 5.10 – Measurement of the mechanical amplitude and phase responses when membrane B is driven and either membrane A (blue) or membrane B (green) is read. Both the amplitude (top) and the phase (bottom) responses are plotted are fitted. $\mathrm{BW} = 100$ Hz. Coupling beam dimension: 0.5×1.5 µm^2.

Two important pieces of information can be deduced from these responses, and will be confirmed by fitting the data with the theoretical model. The first information comes from the comparison of the amplitude level whether the membrane A or B is read. The membrane B has a higher amplitude because it is the membrane that we excite. A part of the injected power contributes to the mechanical motion, especially when the resonance frequencies are reached. Another part of this power is dissipated which will be discussed further on. By reading A only a small part of the injected power in coherently transferred to membrane A through the coupling beam. The membrane A is somehow driven by the membrane B that is itself driven by the electro-capacitive force. The inefficiency of this indirect process explains why there is less energy stored in the membrane A than in membrane B.

The second observation concerns the relative amplitude of the eigenmodes $(-)$ and $(+)$ in each case. When the membrane A is read, the mode $(+)$ has a higher amplitude than

mode $(-)$ and vice-versa when the membrane B is read. This is the signature of a natural frequency mismatch between the resonators. Indeed, when $\omega_A = \omega_B$, the eigenmodes resulting from strong coupling are perfectly sharing the injected energy: each membrane contributes equally to the symmetrical and to the anti-symmetrical resonances. However, when $\omega_A \neq \omega_B$, each eigenmode still consists in a collective motion of both resonators – at least if $G \neq 0$ – but this time in an unbalanced way. For example here the eigenmode $(-)$ is clearly dominated by the motion of membrane B while $(+)$ is dominated by the motion of A. Interestingly these conclusions about the imbalance both in terms of injected energy and of structural properties can be drawn without an advanced analysis of the data. The presence of coupling is further attested by the presence of a destructive interference dip in the membrane A response (resp. B response) around 2.59 MHz (resp. 2.64 MHz) which is typical of a Fano resonance [Joe et al., 2006; Limonov et al., 2017; Stassi et al., 2017] between the non identical resonators. This effect takes the form of a supplementary shift of the phase response.

The amplitude $R_{A,B}$ and phase $\theta_{A,B}$ are fitted at once in each case with the fitting parameters ω_A, ω_B, Γ_A, Γ_B, G and $\tilde{f}_B$ and using the theoretical expression eq. (5.9). We use the signal quadratures $X_{A,B} = R_{A,B}\cos(\theta_{A,B})$ and $Y_{A,B} = R_{A,B}\sin(\theta_{A,B})$ for the fit optimization since these quantities are homogeneous and continuous. Whether A or B is read, the fitting parameters are exactly the same except $\tilde{f}_B$ that stands for the excitation strength but also for the readout conversion which is not exactly the same whether A or B is read. We find $\omega_B = 2\pi \times 2.583$ MHz, $\omega_A = 2\pi \times 2.633$ MHz, $\Gamma_A = 2\pi \times 2.9$ kHz, $\Gamma_B = 2\pi \times 2.8$ kHz and $G = 4\pi^2 \times 0.021$ MHz^2. Overall the fit is successful and finely recover the experimental data. The eigenfrequency difference $\omega_B - \omega_A = 2\pi \times 50$ kHz is therefore dominated by the natural frequency mismatch. The level repulsion, i.e. the frequency difference caused by the spring coupling is indeed of the order of 1 kHz while it would be equal to $G/\omega_A \approx 2\pi \times 8.3$ kHz with identical resonators.

5.3.3.2 Direct measurement of the coupling via spectral avoided-crossing

The natural frequency mismatch in the coupled nanomechanical resonators is a consequence of the fabrication imperfections and can not be intrinsically set to zero although a consequent effort in the nanofabrication technique might allow to reduce it. In the meantime, a certain number of techniques can be used to tune one resonator frequency regarding the other one [Zhang et al., 2015]. In the following, we attempt two methods for compensating the intrinsic mismatch. The first relies on the photothermal absorption effect and the second on the effect of an electric field on the material.

i Using the photothermal absorption The frequency of a nanomechanical resonator can be altered by a change in the bulk temperature [St-Gelais et al., 2019]. Indeed, the temperature change locally modifies the material density which leads to an additional stress and therefore modifies the resonance frequency. Depending on the initial residual stress in the structure – i.e. at room temperature – the frequency shift can be negative or positive.

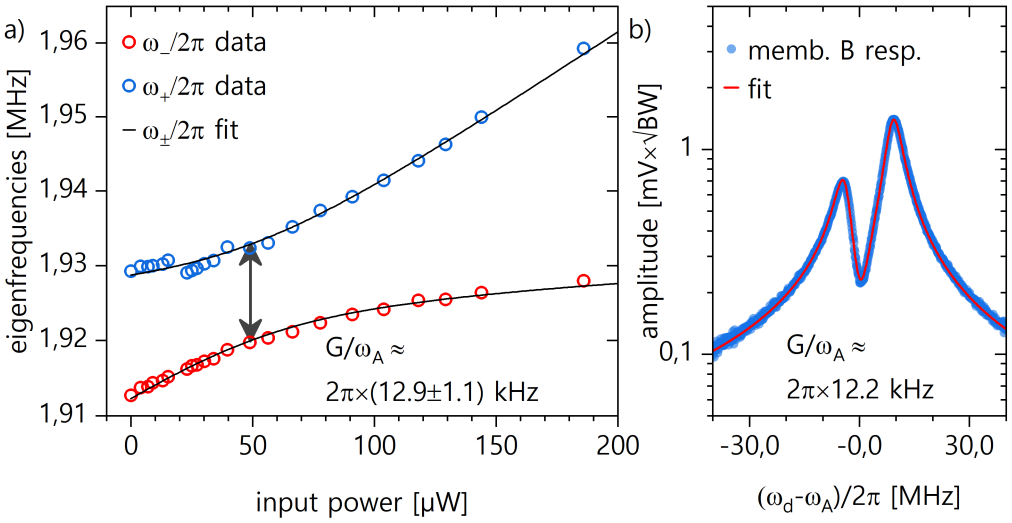

Figure 5.11 – a) Measured eigenfrequencies as a function of the He-Ne laser power sent on membrane A. When the natural frequency of membrane A crosses the one of B (black arrow position), an avoided crossing is observed such that the coupling is directly read from the eigenfrequency difference $G/\omega_A = \omega_+ - \omega_-$. b) Example of fitted amplitude response of membrane B under $V_{ac} = 0.5$V and $\mathrm{BW} = 100$ Hz. Coupling beam dimension: 0.5×1.5 μm^2.

In order to exploit this effect, we use an optical density filter wheel to control the He-Ne laser input power on the sample. This experiment is performed on a pair of membranes coupled with a 0.5×1.5 μm^2 junction. This system was not described so far. We heat the shone membrane by photothermal absorption and observe a change in the normal mode frequencies. In fig. 5.11a, the experimental mechanical eigenfrequencies $\omega_\pm$ are shown for increasing value of the input laser power while the system is driven by applying $V_{dc} = 0$ V and $V_{ac} = 0.5$ V. These frequencies are extracted for the spectral responses obtained by sweeping the driving frequency. We observe an avoided-crossing of the fundamental eigenfrequencies due to strong coupling level repulsion (see section 5.1.2). From our experimental work with the optomechanical structures, made of the same material, we expect a linear shift of the mechanical frequency with the optical power as soon as the shift is small compared to the frequency itself. We assume $\omega_{A,B} = \omega^0_{A,B} + \alpha_{A,B} \times P_{\mathrm{in}}$ with P_{in} the He-Ne laser input power, $\omega^0_{A,B}$ the resonator frequencies when $P_{\mathrm{in}} = 0$ and

$\alpha_{A,B}$ the linear photothermal shift coefficients. The eigenfrequencies are therefore fitted with the imaginary part of the eigenvalues of eq. (5.2). The fitting parameters are the coefficients $\alpha_{A,B}$ and the spring coupling G while the dampings are set to zero (high mechanical quality factor assumption). The fit returns a coupling $G/\omega_A = 2\pi\times 12.9\pm 1.1$ kHz which is coherent with the value 12.2 kHz obtained previously obtained by fitting the spectral response in fig. 5.11b. Note that this latter is measured at an optical power of about 74 µW such that the natural frequencies are slightly different. Indeed the fit, obtained by following the method detailed in section 5.3.3.1, gives $\omega_B - \omega_A = -2\pi \times 5.2$ kHz. The values obtained for the coefficients $\alpha_{A,B}$ are also coherent as the heated membrane (A) has a frequency shift of approximately 224 Hz/µW while the other membrane (B) shifts much less (<17 Hz/µW). It still does probably because of the laser spot size and of the thermal diffusion in the structure. The mechanical modes amplitude being very weak for low probe power, the eigenfrequencies estimation is uncertain. This explains the deviation between data and fit around 25 µW.

ii Using a dielectric tuning The dielectric tuning method has already been mentioned in section 5.2.2.2 and relies on the effect of an applied electric field on the mechanical properties of the material. We focus on the structure whose 1-20 MHz range spectral response was described in fig. 5.9. Here we try to cross the natural frequencies of two non-identical resonators where a frequency mismatch $\omega_A(V_{dc}=0) - \omega_B(V_{dc}=0) \approx 2\pi\times 200$ kHz is initially measured. The use of photothermal effect is prescribed for such important frequency difference because of the irreversible drifts that this would entail. We rather apply a DC voltage on the IDEs of membrane B and check the eigenfrequencies ω_- and ω_+. In order to identify the eigenmodes, a driving voltage $V_{ac} = 0.1 \ll V_{dc}$ is applied so we ensure that the drift is not caused by mechanical nonlinearity.

A static voltage V_{dc} is expected to shift the natural frequency by $\delta\omega = \mathfrak{C}_1 V_{dc}^2$ where $\mathfrak{C}_1$ is the 1st order coefficient in the Taylor expansion of the capacitance derivative (see eq. (5.8)). Therefore we expect the natural frequency of the resonator to shift parabolically $\omega_B(V_{dc}) = \omega_B(V_{dc}=0) + \mathfrak{C}_1^B V_{dc}^2$. The eigenfrequencies ω_- and ω_+ are fitted using the natural frequencies as an input of eq. (5.2). The fit inputs the free parameters $\mathfrak{C}_1^B$, $\omega_A(V_{dc}=0)$ and $\omega_B(V_{dc}=0)$. In fig. 5.12a, the data are shown in terms of frequency shift $\delta\omega_{A,B} = \omega_{A,B}(V_{dc}) - \omega_{A,B}(0)$. The parabolic fits properly capture the observations. As expected the cross effect of the static voltage on membrane A is small but significant. We obtain $C_1^B = -28.1$ Hz/V^2 and the frequency mismatch $\omega_B - \omega_A = 2\pi \times 168$ kHz. In order to compensate the natural frequency mismatch, we need to apply $V_{dc} = 74$ V. This is illustrated in fig. 5.12b where the measured eigenfrequencies are shown and the fits are plotted up to 140 V. Such a voltage can not be applied on the structure which makes this technique fruitless for the observation of an avoided crossing and a direct measurement of the coupling. However, this teaches us

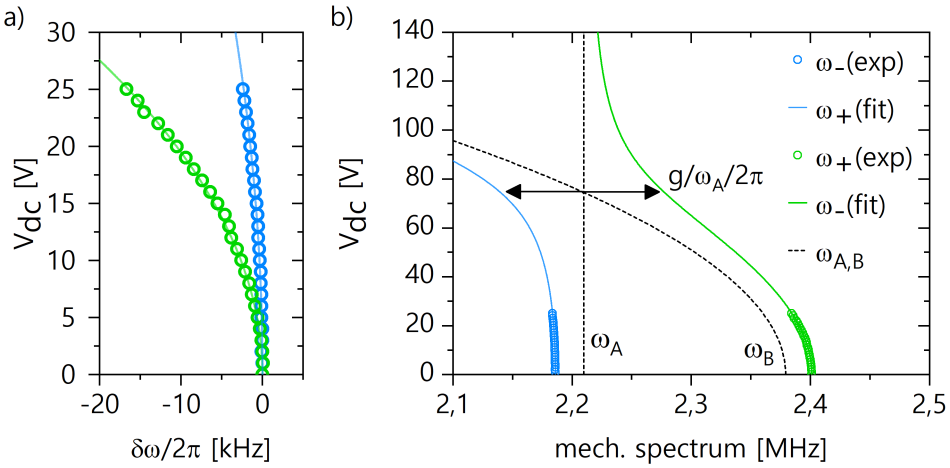

Figure 5.12 – a) Measurement of the eigenfrequencies shift $\delta\omega_{A,B} = \omega_{A,B}(V_{dc}) - \omega_{A,B}(0)$ under static voltage V_{dc} applied on membrane B. b) The fits consider a parabolic shift of the self-coupled frequencies ω_A and ω_B (black dashed) that we use to solve the eigenmodes frequencies ω_- and ω_+ (respect. blue and green lines) resulting from the given coupling G. An avoided crossing is predicted at $V_{dc} = 88$ V when natural frequencies cross. Coupling beam dimension: 1.0×1.5 µm^2.

that the dielectric effect can easily be neglected in the force modeling.

5.3.4 Internal and external mechanical damping rates

The spectral linewidth of a resonator is given by its total damping rate. This latter can be the result of several dissipative processes. For the mechanical systems we consider, the damping rate can be split in an internal and an external component respectively $\Gamma^{\text{int}}_{A,B}$ and $\Gamma^{\text{ext}}_{A,B}$. The internal losses result from the inelastic processes in the material. During the motion, the potential energy loaded in the mechanical resonator is not fully converted in kinetic energy but partially absorbed by the substrate. A part of this energy can also be converted in heat due to local frictions caused by the fabrication imperfections. This internal component can be optimized by working on the geometrical design, in particular on the dimensions of the clamping bridges, and on the nano-fabrication techniques. The external losses are caused by the interactions of our system with the environment. It mainly includes the effect of friction of the surrounding air molecules with the mechanical resonator. This effect can be limited by decreasing the pressure in the vacuum chamber. The total damping rate is the sum of these two terms $\Gamma_{A,B} = \Gamma^{\text{int}}_{A,B} + \Gamma^{\text{ext}}_{A,B}$. In the case of two coupled resonators, each eigenmode has its own damping rate Γ_- and Γ_+. These damping rates are generally not equal in particular for non identical resonators. However they are equal as soon as $\Gamma_A = \Gamma_B$ which we find is the case here.

In order to estimate the internal damping rates of the resonators, we perform a study

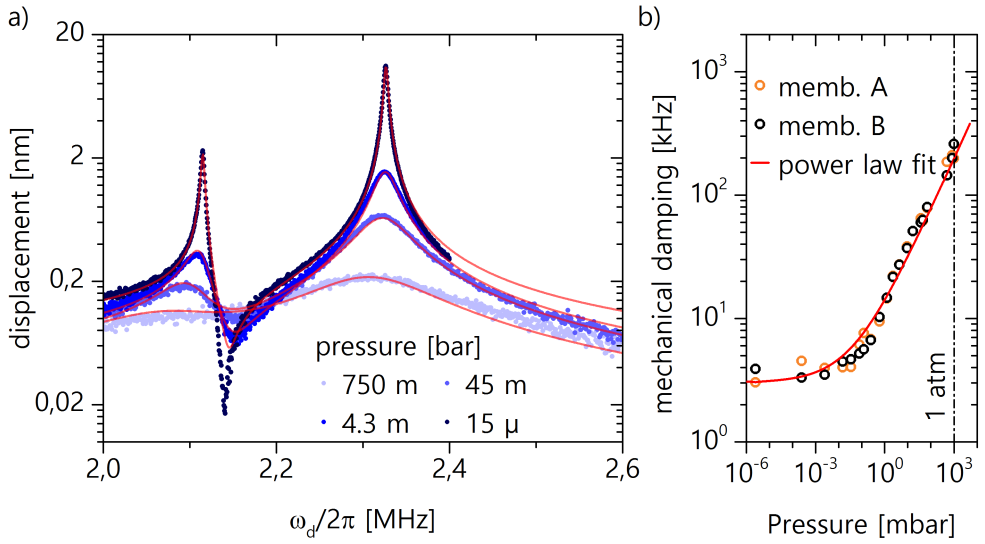

Figure 5.13 – a) Measured spectral response amplitude of the system at different pressure condition in the vacuum chamber. The amplitude is normalized by the maximum. Each curve is fitted using the coupled resonators model. b) The mechanical damping rates are extracted from the fit in a) and plotted as a function of the pressure. A power law fits the data in the drag-limited regime. $\mathrm{BW} = 100$ Hz. Coupling beam dimension: 1.0×1.5 µm^2.

of the system mechanical properties as a function of the pressure vacuum chamber. The experiment is performed with the same structure studied in the previous experiment. The system is driven with $V_{dc} = 2V$ and $V_{ac} = 0.5$ V. These settings guarantee an excitation of the mechanical displacement in its linear regime. The fundamental resonances are spotted around 2.2 MHz and are observed by placing the He-Ne laser on the membrane on which the drive is applied.

Initially the pressure P is stabilized to its lowest value after several weeks of pumping: $P \approx 15$ µbar. The chamber is then isolated from the pump using a valve and the pump is switched off. Starting from this point, the valve is briefly opened in order to progressively increase the pressure in the chamber. The valve is closed and the mechanical spectral response of the fundamental resonances is recorded after few minutes of stabilization. The pressure is given by a vacuum probe placed on the chamber side. This operation is repeated for increasing pressure in the chamber until the chamber is set at atmospheric pressure.

All the measured mechanical responses are fitted using both the amplitude and the phase response so the natural frequencies, damping rates and couplings are obtained for each value of the pressure. In fig. 5.13a, the amplitudes are shown in several cases with the associated fit. A significant broadening of the resonances occurs with higher pressure while their position remains constant. The natural damping rates are plotted as

a function of the pressure P in fig. 5.13b. We observe a regime in which the damping rates exponentially grow with the pressure as shown with the fit performed using a power-law (red line). This illustrates the friction-limited regime of the damping rates where most of the mechanical losses are due to the presence of air molecules around the structure. However, below $P = 10^{-3}$ mbar, a plateau is observed. This corresponds to a regime where the total damping rates are dominated by their internal component. From these results we find that below 10^{-3} mbar, the quality factor can not be significantly improved. The internal damping rates are found to be around 3 kHz. This technique of damping-control through the vacuum chamber pressure is exploited in the following chapter to check the influence of dissipation on the nonlinear dynamics.

5.3.5 Displacement calibration

It has been shown that a simple model of coupled harmonic resonator efficiently describes the stationary response of the driven coupled membranes. It allows the calibration of all the temporal parameters: the frequencies, the damping rates and the coupling rate. However the amplitudes $|r_{A,B}|$ are measured in mV and require a displacement calibration to be converted in nm.

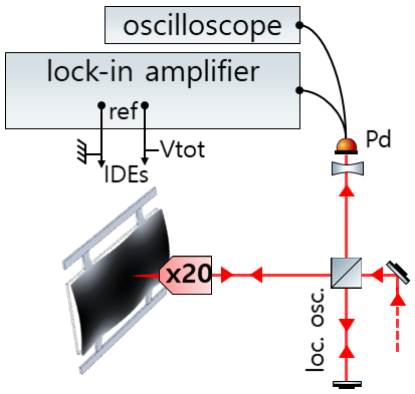

Figure 5.14 – Experimental Michelson setup used for the displacement calibration. A local oscillator is introduced.

We perform a calibration by comparing the electrical signal oscillations amplitude resulting from a given mechanical displacement and from the displacement of a calibrated piezo positioning motorized stage. The first step consists in the calibration of this piezo stage. We point the He-Ne laser at one membrane and optimize the spot position for maximizing the mechanical response of a given mechanical mode. We establish a local oscillator on the optical table in order to achieve a Michelson interferometer (see fig. 5.14). The photodetector now inputs an interfering signal whose intensity writes $I_d \propto 1 + \cos(\Delta\Phi)$ where $\Delta\Phi = 2\pi/\lambda_0 \times d$ is the phase difference induced by the optical path difference d between the interferometer arms.

Displacing the piezo motorized stage by δd along the optical axis direction induces a change δV in the photodetector output signal. So by displacing the stage at constant speed, the output electrical signal is recorded in an oscilloscope and shown in fig. 5.15a. The maximum sensitivity to a small displacement is reached whenever $d = p\lambda/4$. At such operating point, the slope $\alpha = \delta V/\delta d \approx 0.005$ mV/nm can be estimated from the data. We can now set the stage at $\lambda/4$ and resonantly drive the probed membrane with a AC voltage V_{ac}. It results in an resonant oscillations of the membrane that modulates the phase difference $\Delta\Phi$. If the excitation is strong enough, this oscillation of amplitude δV_x is measurable in the oscilloscope although one should make sure not to nonlinearly drive the mechanical system since this calibration relies on a linear model. The corresponding displacement is given by $\delta V_x \times \alpha$. The curve obtained by plotting the displacement as a function of V_{ac} is linear and the slope gives the electromechanical coupling $G_{V_{dc}=0} = 5.7$ nm/V (see fig. 5.15b). This quantity can be kept as a feature of the structure. Of course if the IDEs or the membranes are somehow damaged, $G_{V_{dc}=0}$ will probably decrease but its value does not depend on the way the membrane is probed. In particular, a change in the laser power or the spot position on the membrane does not influence this feature. Afterwards, the local oscillator is removed and the new signal amplitude is observed in the oscilloscope. Its value can be converted to a displacement by comparing with the previous result. The output voltage converts the displacement with a conversion factor $\eta = 0.5$ mV/nm. At this point, the displacement is calibrated in the persistent optical setup.

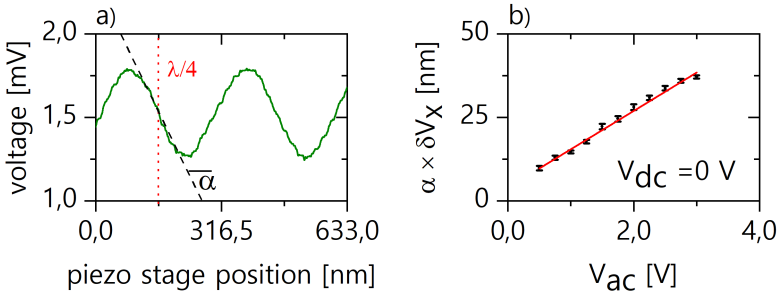

Figure 5.15 – a) Averaged photodetector output voltage as a function of the piezo stage position. The sensitivity is given by the slope at $\lambda/4$. b) Mechanical displacement measured for different value of applied resonant signal V_{ac} (black dots). The measurement is performed for $V_{dc} = 0$ V and the linear fit (red) provides the electromechanical coupling $G_{V_{dc}=0} = 5.7$ nm/V.

As soon as the optical setup is modified, it is possible to quickly recover a displacement calibration of a structure for which this protocol has been applied. The laser spot must be placed such that the mechanical response is maximum. It is then simply necessary to resonantly drive the mechanical mode with $V_{dc} = 0$ V and sweep V_{ac} over

few volts and measure the response. The curve should be linear and the slope gives the electromechanical coupling $G^{\mathrm{mV}}_{V_{dc}=0}$ in units of mV/V. The conversion from electrical signal to mechanical displacement is immediately given by the ratio $G_{V_{dc}=0}/G^{\mathrm{mV}}_{V_{dc}=0}$.

The calibration is performed on a pair of membranes coupled with a 1.5×1.0 μm^2 beam. Their fundamental resonances decompose into a symmetrical and an anti-symmetrical mode with respective frequencies $\omega_- = 2\pi \times 2.163$ MHz and $\omega_+ = 2\pi \times 2.374$ MHz and mechanical damping rate $\Gamma \approx 5$ kHz. This normal mode $(+)$ is dominated by the motion of the membrane B due to an important natural frequency mismatch. A typical amplitude response obtained with $V_{dc} = 0.5$ V and $V_{ac} = 1$ V applied on membrane B is shown in fig. 5.16a. The response is fitted with eq. (5.9) so the membranes parameters are determined. We find the self-coupled frequencies $\omega_A = 2\pi \times 2.187$ MHz and $\omega_A = 2\pi \times 2.345$ MHz and a normalized coupling $G/\omega_A \approx 2\pi \times 130$ kHz. Finally, the displacement calibration has allowed to determine $\eta = 0.5$ mV.nm^{-1}.

5.3.6 Force calibration

The displacement being calibrated it is now possible to calibrate the force exerted by the IDEs on a membrane. For simplicity we consider a single membrane and discuss this choice later. The force exerted by the set of IDEs on the membrane is given by eq. (5.7). The general response amplitude of a driven single harmonic resonator is:

$$A_{\omega_d} = \frac{F/m}{\sqrt{\Gamma^2\omega_d^2 + (\omega_d^2 - \omega_m^2)^2}}$$

with m, ω_m and Γ respectively the mass, natural frequency and damping rate of the resonator. It is driven with a strength F at frequency ω_d. At resonance, i.e when $\omega_d = \omega_m$, the response is $A_{\omega_m} = \frac{F/m}{\Gamma\omega_m}$. We can identify the expressions and obtain:

$$A_{\omega_m} \approx \frac{V_{dc}V_{ac}}{m\Gamma\omega_m}\frac{\partial C}{\partial x} \tag{5.10}$$

The mass of the resonator can be obtain with a COMSOL simulation. It requires to identify the proper displacement field and calculate the associated effective mass $m_{\mathrm{eff}} = \iiint_V \rho r(M) dV(M)$ where ρ is the material density, $dV(M)$ the volume element centered a point M and $r(M)$ its out-of-plane relative displacement. Technically the size of dV is given by the mesh resolution that we choose for the simulation. The remaining unknown parameter $|\frac{\partial C}{\partial x}|$ is precisely giving the force calibration. It can be obtained by evaluating the linear dependence of A_{ω_m} with respect to $V_{dc}V_{ac}$.

Since the force calibration is based on the linear description of the system, it is not necessary to scan the driving frequency ω_d when mapping the parameter space (V_{dc},V_{ac}) because the resonance frequency does not depend of the amplitude in this regime. The mechanical displacement at $\omega_d = \omega_+$ is measured as a function of these

two parameters and plotted in fig. 5.16c. The demodulation bandwidth is set to measured with $\mathrm{BW} = 100$ Hz and each point is averaged 30 times. As expected, the amplitude increases with $|V_{dc}|$ and with V_{ac}. We note that when $V_{ac} < 0.1$ V, the zero displacement line (yellow line) does not occur at $V_{dc} = 0$ V but around -0.11 V. This shift is related to the intrinsic stress into the membrane due the epitaxial layer properties as well as the fabrication technique that was used. Moreover this internal stress that is equivalent to an applied static voltage V_{int} parabolically shifts as a function of V_{ac} because of the contribution $\frac{1}{2}V_{ac}^2$ in the static component of the electro-capacitive force discussed in section 5.2.2.2. Therefore the mechanical mode amplitude is expected to be linear with $V_{dc}^{\mathrm{eff}}V_{ac}$ where $V_{dc}^{\mathrm{eff}} = V_{dc} + V_{\mathrm{int}}$ is the effective DC voltage. The zero displacement line therefore corresponds to a zero value of the effective DC voltage so the applied DC voltage V_{dc} compensates exactly the intrinsic one.

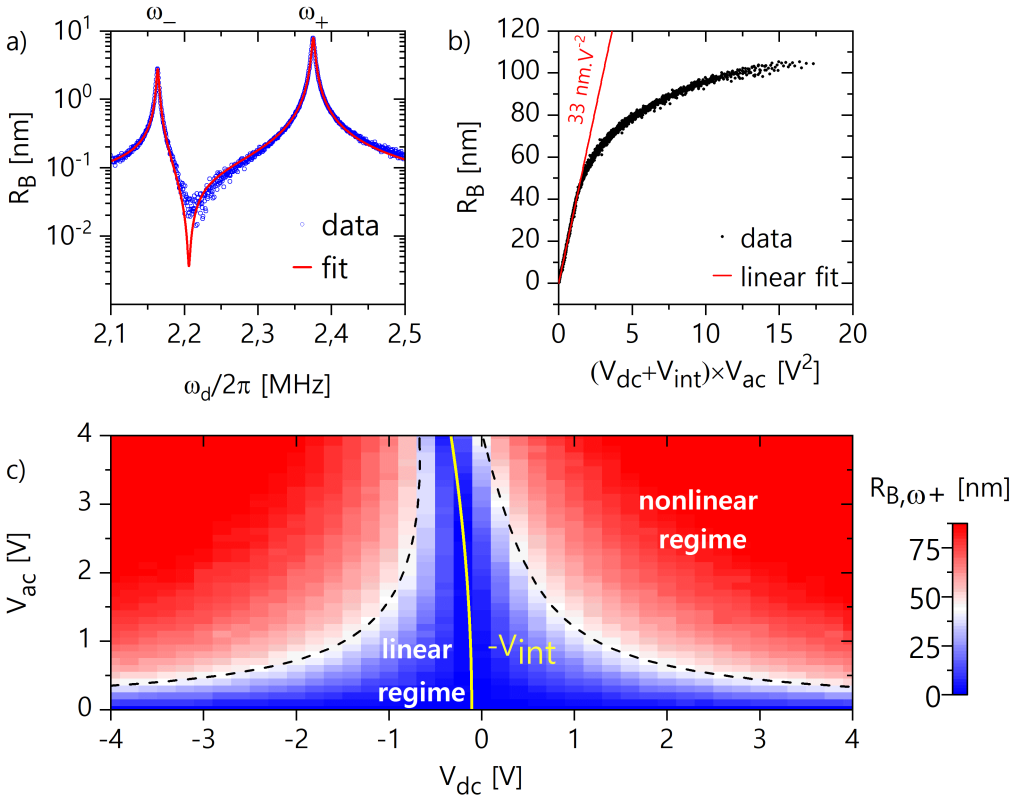

Figure 5.16 – a) Fundamental mode response of the calibrated system with excitation $V_{dc} = 0.5$ V and $V_{ac} = 1$ V. b) The mechanical displacement as a function of $V_{ac}(V_{dc} - V_{\mathrm{int}})$ c) Membrane B experimental resonant response amplitude in (V_{ac}, V_{dc}) parameter space for $\omega_d = \omega_+$. Horizontal and vertical slices are represented for respectively $V_{ac} = 3$ V and $V_{dc} = 2$ V with a linear fit (red line) in the non saturated regime. The iso-$V_{dc}^{\mathrm{eff}}V_{ac}$ curves (black dashed) separate the linear and Duffing-Duffing regimes. $\mathrm{BW} = 100$ Hz. Coupling beam dimension: 1.0×1.5 µm^2.

In fig. 5.16b the displacement is plotted as a function of the product $V_{dc}^{\text{eff}}V_{ac}$. A linear tendency is followed by a saturation starting from $V_{dc}^{\text{eff}}V_{ac} \approx 1.3$ V^2. Above this threshold the system enters in a Duffing regime which will be described further on. We fit the linear regime (red line) and the force calibration can be estimated from the slope using eq. (5.10). For this structure the FEM simulation give an effective mass $m_{\text{eff}}^{\omega_+} \approx 186$ pg so we obtain a force calibration $|\frac{\partial C}{\partial x}| \approx 2.2$ µN.V^{-2}. The experimental uncertainty on this value is hard to estimate especially because of the effective mass that is given by simulations. However, relying only on the experimental measurement, the relative uncertainty is found to be of the order of 50%.

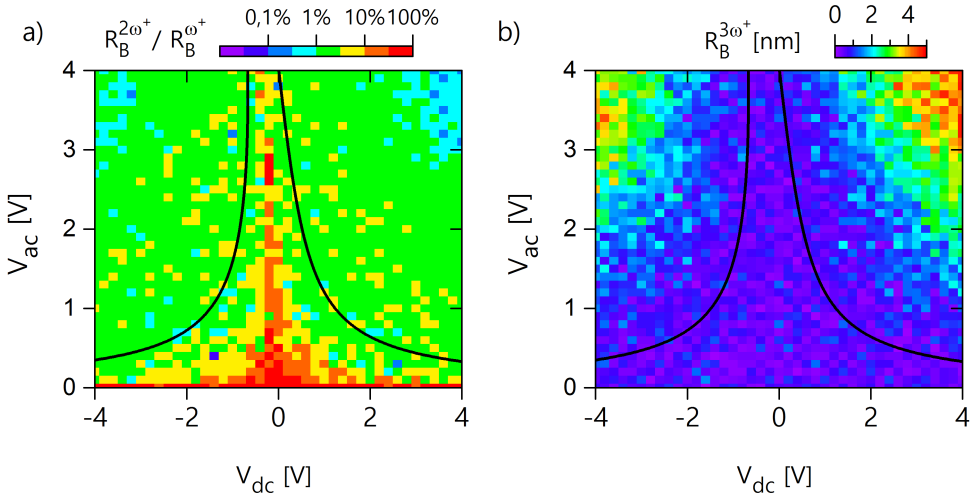

Figure 5.17 – Measured mechanical displacement at $2\omega^+$ (a) and at $3\omega^+$ (b) relative to the displacement at ω^+ as a function of V_{dc} and V_{ac}. The iso-$V_{dc}^{\text{eff}}V_{ac}$ straight black lines delimit the linear and the nonlinear regime.

i 2nd order demodulation: verification of the Force model While the mechanical response at ω^+ is measured as a function of V_{dc} and V_{ac}, we simultaneously demodulate the signal at $2\omega^+$ and at $3\omega^+$. Each filter has a demodulation bandwidth set to $\text{BW} = 100$ Hz. We show the 2nd order relative to the 1st order demodulation response $R(2\omega^+)/R(\omega^+)$ in fig. 5.17a. As discussed in section 5.2.2.2, the force model predict an off-resonant excitation component, at frequency $2\omega_d$, that was considered as negligible but this was not justified so far. This strength component is proportional to V_{ac}^2 and its ratio to the resonant strength component writes $F_{2\omega_d}/F_{\omega_d} = \frac{V_{ac}}{4V_{dc}}$. We observe that for low value of $V_{dc}V_{ac}$ and due to noise, $R(2\omega^+)/R(\omega^+)$ can be of the order of 1. This just indicates that there is no mechanical displacement. The interesting property of this plot is the fact that $R(2\omega^+)/R(\omega^+)$ decreases when the membrane displacement becomes significant. In fact, the mean value is estimated to be lower than

3% over this map. This confirms the weak impact of the off-resonant component of the electro-capacitive force.

ii 3rd order demodulation: indications towards a Duffing nonlinearity The 3rd order demodulation response of the membrane as a function of the excitation parameters is plotted in fig. 5.17b. This time there is no expectation whatsoever of any response at 3 times the resonance frequency since no excitation component oscillates at this frequency. However, it is well known that a Duffing-type nonlinearity involves 3rd order generation. With this map we observe a sudden emergence of this effect when $V_{dc}^{\text{eff}} V_{ac}$ get over a certain threshold, i.e. when the applied strength is big enough. Moreover this threshold seems to coincide with the saturation threshold discussed in this section. This measurement pushes us towards the use of the Duffing resonator for the description of these nonlinear effects.

Chapter 6

Nonlinear dynamics with force modulation

In the previous chapter, we have described the design of the mechanical system and of actuation scheme. We have established an optical setup allowing the calibration of the system relying in particular on the theoretical modeling of driven coupled harmonic resonators. We have voluntarily maintained the system in the linear regime by applying relatively small voltages on the system IDEs. However, it has been observed that displacement saturation occurs when these excitation parameters are increased. The rest of this part relies on the study of this nonlinear regime.

Using the Duffing resonator model, a theoretical model of coupled nonlinear resonators is expanded and applied it to our experimental data. We introduce a low-frequency modulation of the force and discuss the chaotic dynamics that it implies. By taking advantage of this regime, we will describe how the nonlinear coupling between two normal modes can allow them to synchronize in chaos. Several phase synchronization regime can then occur. Finally we apply a protocol of random bit generation from a chaotic signal to our experimental data.

6.1 Duffing-Duffing model

The Duffing model is broadly used for the description of nonlinear mechanical systems. It also has applications in many fields in physics [Korsch et al., 2008], e.g superconducting Josephson amplifier [Roy and Devoret, 2016], ionization plasma [Hsuan et al., 1967] and chimera sates [Clerc et al., 2018]. In our mechanical system, the Duffing nonlinearity emerge from a deviation to the Hooke's law when the mechanical displacement and the structure thickness have comparable order of magnitude. Interestingly in nanomechanical systems this kind of nonlinear regime is easily reached due to the use of thin layers. The Duffing regime leads to bistable states of the mechanical motion. This can be exploited for

several applications and is at the center of the following work. The theoretical description of a single Duffing mechanical resonator has been deeply studied in the literature as well as in the previous works within our research group [Chowdhury, 2016]. We extend this model to linearly coupled resonators. The first step consist in the main derivations of the stationary solutions of a driven ensemble of coupled Duffing resonators. We will discuss the impact of the driving strength and the natural frequency mismatch of these solutions.

6.1.1 Theoretical model

An harmonic oscillator is described through the Hooke's law which stands that the spring force exerted on the mass in motion m is proportional to its displacement from equilibrium position x. $F(x) = k_0 \times x$ with k_0 the spring constant. This gives the resonance frequency $\omega_0^2 = k_0/m$. The Taylor expansion of the spring constant $k(x) = k_0 + k_1 x + k_2 x^2 + ...$ allows a deviation to this linear model and the resulting anharmonic oscillator description complexity grows with increasing order of this expansion. The Duffing model considers a spring constant $k(x) = k_0 + k_2 x^2$ and we introduce the Duffing nonlinearity $\beta = k_2/m$. The physical origin of this nonlinearity can be understood by applying the Euler-Bernoulli equation to a doubly-clamped beam with a position-dependent length [Lifshitz and Cross, 2009].

In our model, we will assume identical Duffing intrinsic nonlinearities in both resonators $\beta_A = \beta_B = \beta$. We adapt eq. (5.1) by adding the nonlinear terms in each resonator master equation. In order both to simplify the calculations and suit the following experiments, we consider only one forced resonator and set $f_A = 0$:

$$\begin{cases} \ddot{x}_A + \Gamma_A \dot{x}_A + \omega_A^2 x_A + \beta x_A^3 - G x_B = 0 \\ \ddot{x}_B + \Gamma_B \dot{x}_B + \omega_B^2 x_B + \beta x_B^3 - G x_A = f_B \cos(\omega_d t) \end{cases}$$

We start from the ansatz $x_A = v_A \cos(\omega_d t) + w_A \sin(\omega_d t)$ and $x_B = v_B \cos(\omega_d t) + w_B \sin(\omega_d t)$ where the quadratures relate to the response amplitude and phase with $r_A^2 = v_A^2 + w_A^2$ and $\vartheta_A = \mathrm{atan2}(v_A, w_A)$ (and similarly for r_B and ϑ_B)[1].

Before injecting the assumed solutions in the master equations, it is useful to preliminary calculate x_A^3 in order to reveal the off-resonant terms oscillating at $3\omega_d$ that can be neglected in the following. It was indeed experimentally verified in eq. (5.10) that the motion at $3\omega_d$ emerges in the nonlinear regime but stays very weak compared to the resonant oscillation. We also expand the expression for the derivatives $\dot{x}_A$ and $\ddot{x}_A$. As the resonant amplitude is expected to vary much slower than resonant oscillations timescale, we can neglect the quadratures second derivatives by assuming $\ddot{v}_A, \ddot{w}_A \ll \omega_d^2 v_A, \omega_d^2 w_A$.

[1] Although the use of complex expressions turned out to be extremely practical for the derivation of the linear solutions, we now promote the use of real quantities in the nonlinear regime.

These preliminary results are injected in the master equations and all quantities are normalized as detailed previously (see section 5.3.2):

$$\dot{v}_A = \frac{1}{2} w_A \left[2(\delta - \Delta\omega) + \frac{3}{4}\tilde{\beta}(v_A^2 + w_A^2) \right] - \frac{1}{2}\gamma_A v_A - \frac{1}{2} g w_B \tag{S.1a}$$

$$\dot{w}_A = \frac{-1}{2} v_A \left[2(\delta - \Delta\omega) + \frac{3}{4}\tilde{\beta}(v_A^2 + w_A^2) \right] - \frac{1}{2}\gamma_A w_A + \frac{1}{2} g v_B \tag{S.1b}$$

$$\dot{v}_B = \frac{1}{2} w_B \left[2\delta + \frac{3}{4}\tilde{\beta}(v_B^2 + w_B^2) \right] - \frac{1}{2}\gamma_B v_B - \frac{1}{2} g w_A \tag{S.2a}$$

$$\dot{w}_B = \frac{-1}{2} v_B \left[2\delta + \frac{3}{4}\tilde{\beta}(v_B^2 + w_B^2) \right] - \frac{1}{2}\gamma_B w_B + \frac{1}{2} g v_A + \frac{1}{2}\tilde{f}_B \tag{S.1b}$$

with the normalized Duffing nonlinearity $\tilde{\beta} = \tilde{\beta}/\omega_d^2$.

This system of equations describes the evolution of our system in terms of quadratures v_A, w_A, v_B and w_B. It presents an interest for the numerical simulations since these quantities are homogeneous to each other. In order to express these solutions in terms of the amplitudes and phases, we perform the reverse transformations $v_A = r_A \cos(\vartheta_A)$, $w_A = r_A \sin(\vartheta_A)$, $v_B = r_B \cos(\vartheta_B)$ and $w_B = r_B \sin(\vartheta_B)$ and take:

$$\begin{cases} \text{(S.1a)} \times \cos(\vartheta_A) + \text{(S.2a)} \times \sin(\vartheta_A) \\ \text{(S.1b)} \times \cos(\vartheta_B) + \text{(S.2b)} \times \sin(\vartheta_B) \\ -\text{(S.1a)} \times \sin(\vartheta_A) + \text{(S.2a)} \times \cos(\vartheta_A) \\ -\text{(S.1b)} \times \sin(\vartheta_B) + \text{(S.2b)} \times \cos(\vartheta_B) \end{cases}$$

The stationary solutions of the amplitudes (r_A,r_B) and phases (ϑ_A,ϑ_B) are given by:

$$\begin{cases} \dot{r}_A = \dfrac{-\gamma_A}{2} r_A + \dfrac{g}{2} r_B \sin(\vartheta_A - \vartheta_B) \\ \dot{r}_B = \dfrac{-\gamma_B}{2} r_B - \dfrac{g}{2} r_A \sin(\vartheta_A - \vartheta_B) + \dfrac{\tilde{f}_B}{2} \sin(\vartheta_B) \\ r_A \dot{\vartheta}_A = \dfrac{-r_A}{2} \left[2(\delta - \Delta\omega) + \dfrac{3}{4}\tilde{\beta} r_A^2 \right] + \dfrac{g}{2} r_B \cos(\vartheta_A - \vartheta_B) \\ r_B \dot{\vartheta}_B = \dfrac{-r_B}{2} \left[2\delta + \dfrac{3}{4}\tilde{\beta} r_B^2 \right] + \dfrac{g}{2} r_A \cos(\vartheta_A - \vartheta_B) + \dfrac{\tilde{f}_B}{2} \cos(\vartheta_B) \end{cases} \tag{6.1}$$

In order to visualize the amplitude responses as a function of the detuning δ, this system is solved using Mathematica for a given set of parameters and in the permanent regime ($\dot{r}_A = \dot{r}_B = \dot{\vartheta}_A = \dot{\vartheta}_B = 0$). In fig. 6.1a, the response of the resonator A is plotted with parameters $\gamma_A = 0.0004$, $\gamma_B = 0.0005$, $\tilde{\beta} = 2 \times 10^{-7}$ and $g = 0.0345$. These normalized parameters, although representative of the typical structures we study, do not correspond to any of them. The response of resonator B is not plotted but the differences have always been discussed in the linear regime (see section 5.3.3.1) and these considerations are still valid here. These solutions show a strong saturation of the displacement as well as a shift in the resonance frequency toward higher frequencies

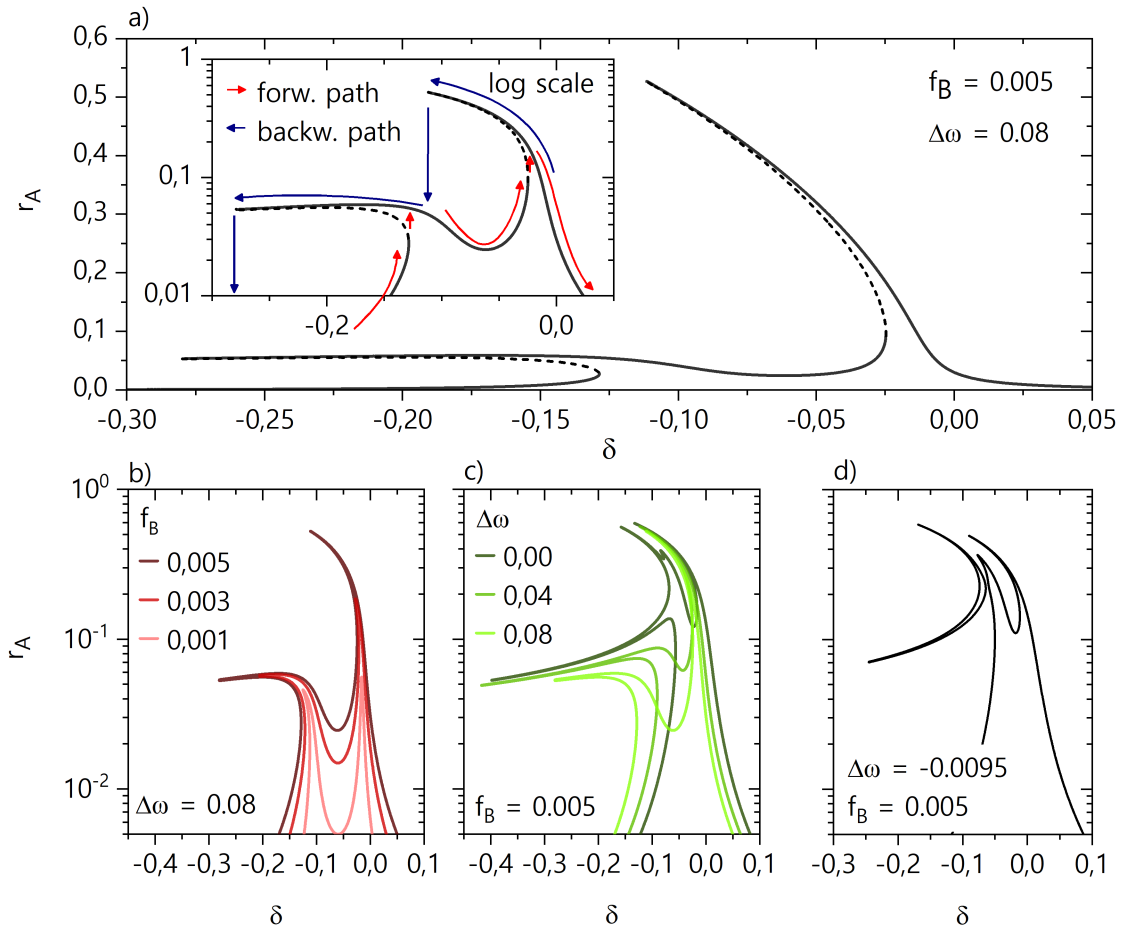

Figure 6.1 – Displacement of the resonator A as function of the detuning δ. We use $\gamma_A = 0.0004$, $\gamma_B = 0.0005$, $\tilde{\beta} = 2 \times 10^{-7}$ and $g = 0.0345$. a) stable (straight line) and unstable (dashed) solutions. Log plot showing the system trajectory when δ is swept up (red) or down (blue). b) Displacement for different strength values. c) for different frequency mismatch values. d) At $\Delta\omega = -0.0095$ we find a solution isolated from the resonances.

(hardening). Note that a negative Duffing constant leads to a shift towards lower frequencies (softening). The deformation of the resonances also comes with a multivalued solution. Some solutions are stable (straight lines) and some are unstable (dashed). By sweeping the detuning up or down, a hysteretic behavior is observed so the system is maintained on the stable solutions. The bistability regions have frequency spans that depends on the nonlinearity βf_B^2 as shown in fig. 6.1b where the same plot is shown but with several value of f_B. For decreasing values of the driving strength, the curve profile tends to the linear case.

The detuning and the driving strengths are experimentally controlled by the user while the coupling g, the dampings $\gamma_{A,B}$ and the frequency mismatch $\Delta\omega$ are intrinsic

to the geometry and the fabrication quality. It is however interesting to observe the effect of the displacement response for different values of $\Delta\omega$ as plotted in fig. 6.1c. Contrary to the single Duffing response, the saturation can get so important that the displacement becomes flat ($\Delta\omega = 0.08$) and even decreases before the bistability edge ($\Delta\omega = 0.04$). The flattening only occurs for one of the eigenmodes. If $\Delta\omega \neq 0$, one can associate each eigenmode to a given resonator. Here we plot the displacement of resonator A and the flattening can be seen on the eigenmode dominated by the motion of B although this imbalance tends to disappear when $\Delta\omega$ vanishes. Despite the fact that a better tuning of the natural frequencies balance the normal mode responses, a qualitative change of these responses is observed when the bistability windows start to overlap. At some particular values of the detuning, more than 2 stable states can be found and the model predicts exotic solutions. An example is show in fig. 6.1d where an isolated loop is presented for $\Delta\omega = -0.0095$. Such basin of attraction have been discussed in similar systems [Kirkendall and Kwon, 2016; Dong et al., 2018].

In this discussion, we have described the important features to be observed in our system but also noted peculiar regimes that can only be achieved with peculiar arrangement of the membranes frequencies and coupling. Although not necessarily observed in the following, these peculiar regimes are not found for unrealistic parameters and could be of great interest in future experiments.

6.1.2 Experimental response plots

The theoretical description of two coupled Duffing resonators was motivated by the observation of a saturation of the mechanical displacement when $V_{dc}V_{ac}$ is increased (see fig. 5.16c). So far, no frequency sweep under such regime has been shown but only the response at the linear resonance frequency $\omega_d = \omega_+$. We focus on the system that was preliminary calibrated and discussed in section 5.3.5. The laser spot is focused on membrane B while the total voltage V_{tot} is applied on the associated IDEs. As the strength applied on the resonator goes as $f_B \propto V_{dc}V_{ac}$, we are free to play with both voltage component to reach the nonlinear regime. We set $V_{ac} = 2.5$ V and sweep the drive frequency ω_d over the resonances for three different values of V_{dc}. The resulting displacement is shown in fig. 6.2a. For $V_{dc} = 1$ V, the resonances are slightly distorted since the system already set in the nonlinear regime as indicated by the calibration map in fig. 5.16c. For $V_{dc} = 3$ V, the resonances are now both bistable. Depending on whether the frequency is swept up or down different solutions are explored and hysteretic jumps are observed at the bistabilities edges. At this point each resonance taken separately qualitatively looks like a single Duffing response. However when $V_{dc} = 5$ V, the displacement response clearly decreases on the upper branch on the anti-symmetrical resonance ($+$) before jumping to the lower stable state. The bistability frequency spans grow with

the applied strength as predicted by our nonlinear model.

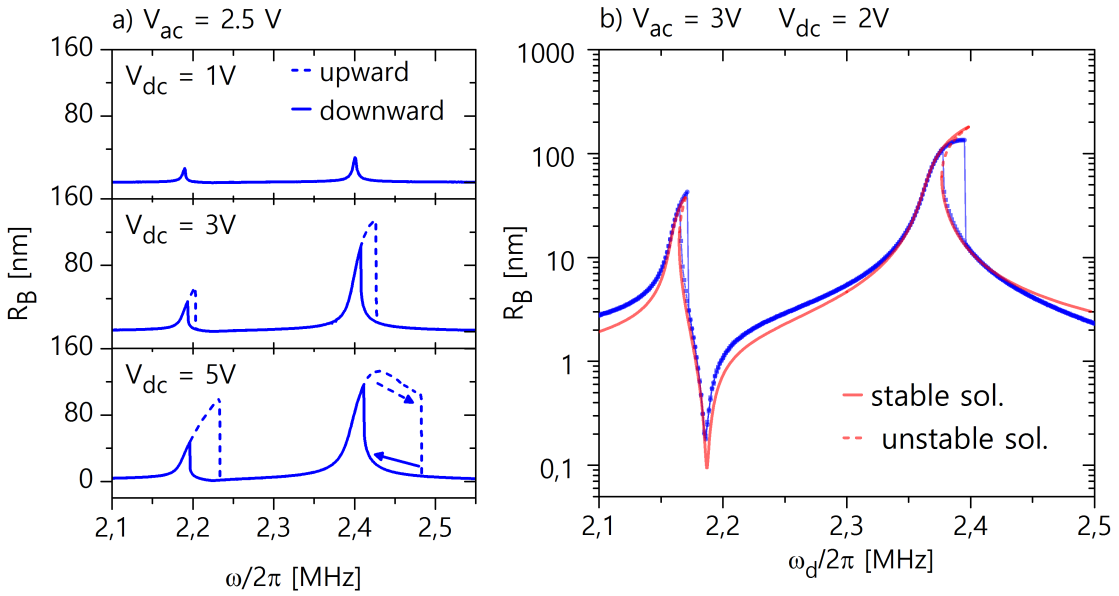

Figure 6.2 – a) Experimental measurement of membrane B displacement while the driving frequency is swept up (dashed) or down (straight). B is driven with $V_{ac} = 2.5$ V and V_{dc} is set to 1 V, 3 V and 6 V (resp. from top to bottom). b) With $V_{dc} = 2$ V and $V_{ac} = 3$ V, the experimental data (blue) are manually fitted with theoretical model (red) by using the linear parameters established previously and using only the Duffing parameter β for the fit.

In fig. 6.2b, the displacement response is measured with $V_{dc} = 2$ V and $V_{ac} = 3$ V. Thanks to the fit performed in linear regime and shown in fig. 5.16a, most of the mechanical properties of this system are already known. The experimental data can be approached with a numerical solution of the Duffing-Duffing model by playing with the nonlinearity β which is the remaining unknown parameter. In practice the knowledge of this parameter relies on the force calibration. By adjusting the value of β in order to get the closest match of the theoretical and experimental bistability edges, we find $\beta \approx (2\pi)^2 \times 6.71 \times 10^{-6}$ MHz^2.nm^{-2}. The theoretical solutions fits quite well with the experimental points. The peak positions and the frequency spans of the bistabilities are properly reproduced as well as the Fano resonance dip at 2.18 MHz. However, the anti-symmetrical resonance $(+)$ amplitude saturation is not recovered and a significant discard occur in this region. This is also the case to a lesser extent for the other eigenmode $(-)$ but this time the experimental mode displace more than in the theory. This disagreement could be explained by many sources starting with an imprecise calibration of the systems parameters. If the natural frequencies and damping are believed to be consistently evaluated, the coupling G could not be directly measured – i.e the

avoided crossing was not observed (see section 5.3.3.2) – for this structure and result from a multi-parameters fit. Thus this parameter is known to critically influence the balance between the eigenmode amplitudes. Moreover the force calibration relies on an imprecise experimental protocol as well as on a finite-element simulation – to determine m_{eff} – that is also source of uncertainty. Of course it can not be excluded that the Duffing-Duffing model is incomplete and can not better describe the experimental data, although it still accurately predict the following nonlinear dynamics experiments.

All the resonator properties are given in table 6.1 as well as the effective mass and calibrated electro-capacitive force. The associated normalized quantities are also given by using a typical driving frequency $\omega_d \sim 2\pi \times 2.3$ MHz. These values are going to be profusely used for modeling the following experiments.

Physical quantities			Normalized quantities
symbol	value	units	expression
ω_A	$2\pi \times 2.187$	MHz	$\Delta\omega = \frac{\omega_B - \omega_A}{\omega_d}$
ω_B	$2\pi \times 2.345$	MHz	$\delta = \frac{\omega_B - \omega_d}{\omega_d}$
Γ_A	$2\pi \times 2.4$	kHz	$\gamma_A = \Gamma_A/\omega_d$
Γ_B	$2\pi \times 4.3$	kHz	$\gamma_B = \Gamma_B/\omega_d$
G/ω_A	$2\pi \times 130$	kHz	$g = G/\omega_d^2$
β	$(2\pi)^2 \times 6.71 \times 10^{-6}$	MHz^2.nm^{-2}	$\tilde{\beta} = \beta/\omega_d^2$
$m_{\text{eff}}^{\omega_+}$	186	pg (computed with finite element simulations)	
F_B	$2.2 \times V_{dc}V_{ac}$	µN	$\tilde{f}_B = \frac{F_B}{m_{\text{eff}}^{\omega_+}\omega_d^2}$

Table 6.1 – List of physical quantities experimentally calibrated (except the effective mass m_{eff} given by Comsol for the coupled membranes anti-symmetrical fundamental eigenmode). Associated normalized quantities used in the numerical simulations. The structure has the coupling beam dimension: 1.0×1.5 µm^2.

6.2 Period-doubling route to chaos with strength modulation

In this section we will study the chaotic dynamics of the coupled nonlinear resonators that occur when the applied force is modulated in amplitude at a low frequency. What "low" means will be discussed later on but basically means that this frequency lies at the dissipative frequency scale $\Gamma_{A,B}$. We first explain how this modulation is experimentally performed and give some key-concept that are required for understanding the resulting dynamics. Then the experimental results are presented starting with the effect of the

modulation on the spectral response amplitude. This measurement, associated with the experimental diagram drawn as a function of the driving frequency ω_d, permits to qualitatively determine how this latter should be set in order to observe chaos. The experimental bifurcation diagrams plotted as a function of the modulation amplitude and frequency are finally performed. The data are compared with the numerical simulations.

6.2.1 Modulation technique

The force amplitude modulation requires a new oscillating component in the applied total voltage $V_{tot} = V_{dc} + V_{ac}\cos(\omega_d t) + V_p \cos(\omega_p t)$. The expansion of the electro-capacitive force expression eq. (5.5) with this new total voltage writes:

$$\begin{aligned} F(t) = \frac{1}{2}\frac{\partial C}{\partial x} \times \Bigg[& V_{dc}^2 + \frac{1}{2}V_{ac}^2 + \frac{1}{2}V_p^2 \\ & + 2V_{ac}\Big(V_{dc} + V_p\cos(\omega_p t)\Big)\cos(\omega_d t) \\ & + \frac{1}{2}V_{ac}^2\cos(2\omega_d t) + \frac{1}{2}V_p^2\cos(2\omega_p t)\Bigg] \end{aligned} \tag{6.2}$$

The static component (1st line) can be neglected as justified in section 5.2.2.2. The off-resonant terms (3rd line) can also be ignored (see section 5.3.5). Finally, the remaining resonant term gives a strength $f_B \propto V_{ac}(V_{dc} + V_p\cos(\omega_p t))$ with respectively the modulation amplitude and frequency V_p and ω_p. As the Fourier transform of such modulated signal shows one component at the carrier frequency and two sidebands located at $\omega_d \pm \omega_p$, we expect to be able to excite the system by using these sidebands. This feature is used in multimode lasers mode-locking operations [Hargrove et al., 1964; Yariv, 1965] for example. Here we can verify the presence of these additional tones is the electro-capacitive force by measuring the system response at different values of the modulation frequency. When this latter is such that $\omega_d \pm \omega_p$ is near one mechanical normal mode, this latter must be driven and therefore respond. The measurement is first performed in the linear regime with $V_{dc} = 3$ V, $V_{ac} = 0.5$ V and $V_p = 2$ V. We plot the response of membrane B, demodulated through a 200 kHz passband filter, as a function of the modulation frequency. As expected, the system is not only driven when the carrier frequency passes the mechanical modes, but also when the modulation sidebands do. Note that nothing happens at the particular modulation frequencies $\omega_p = \frac{p}{n} \times (\omega_+ - \omega_-)$, with p and n two integers, i.e. when the peaks cross each other, because the modes are orthogonal here and are not expected to couple. Thus the present type modulation should not be confused with parametric excitation, e.g. in [Okamoto et al., 2013] where the natural frequency of one resonator is slowly modulated while the system is resonantly driven.

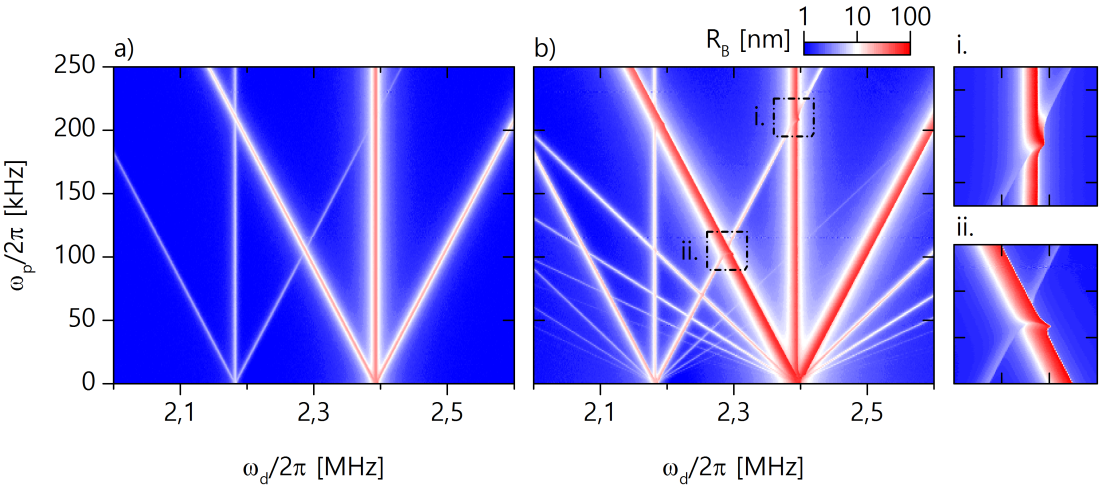

Figure 6.3 – Measured mechanical displacement of membrane B under forward driving frequency sweep, as a function of the modulation frequency. Importantly here we use $\mathrm{BW} = 200$ kHz a) in linear regime: $V_{dc} = 3$ V, $V_{ac} = 0.5$ V and $V_p = 2$ V b) in nonlinear regime: $V_{dc} = 3$ V, $V_{ac} = 1.75$ V and $V_p = 3.5$ V.

When the Duffing regime is reached, a nonlinear interaction occurs between the added modulation tone and the mechanical resonator. As a result, more replica of the main mechanical normal modes are expected. We verify this by using higher driving voltages: $V_{dc} = 3$ V, $V_{ac} = 1.75$ V and $V_p = 3.5$ V. The resulting map, shown in fig. 6.3b, indeed reveals several additional replica (four additional orders). More importantly, as the mechanical modes are nonlinearly driven, they are *a priori* not orthogonal anymore. In consequence, it is expected that some energy transits from the driven mode to the other such that they can couple. This aspect is more carefully discussed later on. For now we simply note the presence of new features at the intersection between the first order replica and the mechanical modes, as pointed out with the zoom inset (i), or when the first orders provided by each mode cross each other (ii). At these crossing positions, it clearly appears that the peaks do not simply overlap but also distort themselves.

It should be emphasized that all these considerations are reminiscent of the optomechanical sidebands described and observed in the first part of the manuscript (see section 4.1). Despite the crucial differences – here the resonantly driven response is read while the Brownian noise is detected in the optomechanical system, we consider here a mechanical bistability whereas the optomechanical system sustains a thermo optic bistability, and so on – both systems can be described with bistable resonators forced with a modulated drive, and responding through a nonlinear process which leads to the presence of replica in the mechanical domain.a

With these clarifications, it is now possible to investigate the dynamics of the system under such modulation by playing with the voltages V_{dc}, V_{ac} and V_p or with the frequen-

cies ω_d and ω_p. In order to reduce this list, we will restrict ourselves by using $V_{dc} = 2$ V and $V_{ac} = 3$ V (which gives the response seen in fig. 6.2b).

6.2.2 Influence of the driving frequency

Before discussing the mechanism through which the bifurcation dynamics arises, let's check the effect of the modulation on the amplitude spectral response. In order to make sure that the probed displacement is spectrally localized at the driving frequency, contrary to the measurements presented in figs. 6.3a and 6.3b, the demodulation bandwidth is reset to 100 Hz such that the sidebands are not visible anymore in the spectral response[2]. In fig. 6.4a, the displacement of membrane B is plotted with the forwardly and backwardly swept driving frequency. As the modulation amplitude is increased from 0 to 3 V, the resonances seem to be distorted and the bistability disappears. This last feature is more visible for the mode $(+)$. Here it is not possible to observe the dynamics that typically takes place at the modulation frequency $\omega_p = 2\pi \times 7$ kHz. It is therefore necessary to use another method for understanding the present physics.

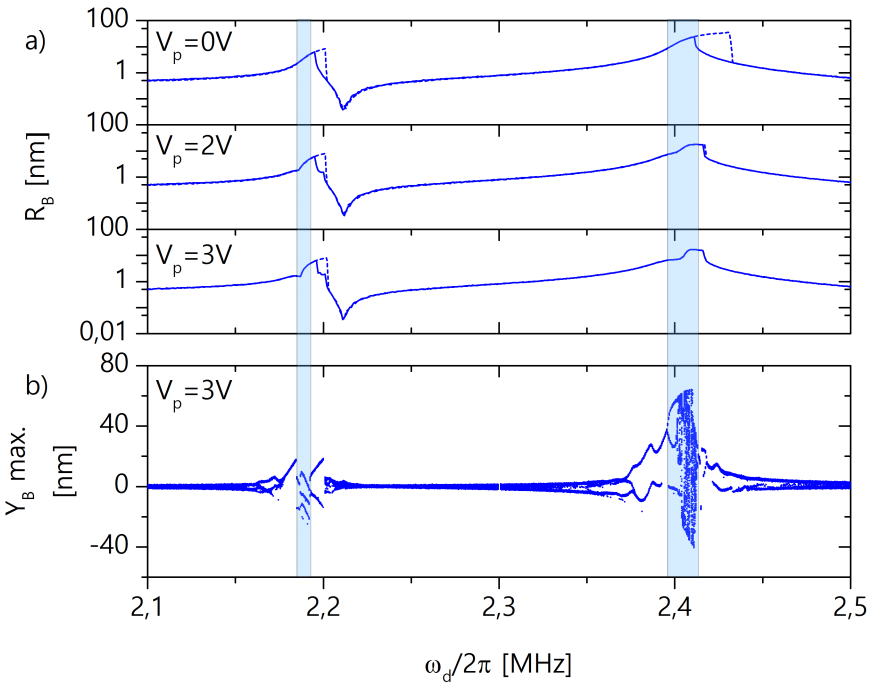

Figure 6.4 – a) For $V_p = 0$,2 and 3 V, displacement response of membrane B under upward (dashed) and downward (straight) sweeps of ω_d. $\mathrm{BW} = 100$ Hz. b) Experimental bifurcation diagram with parameter ω_d at $V_p = 3$ V using $\mathrm{BW} = 40$ kHz. Other parameters: $V_{dc} = 2$ V, $V_{ac} = 3$ V and $\omega_p = 2\pi \times 7$ kHz.

[2]The choice of 100 Hz is arbitrary. The important point is that this value is much below the dynamical features occurring at the modulation frequency (BW $\ll \omega_p$).

To quantify the nonlinear dynamics of a system, the bifurcation diagram is a particularly useful tool. A bifurcation corresponds to a qualitative change of a nonlinear system dynamics under a tiny change of one parameter. As this latter, the bifurcation parameter, is swept over certain range, the system dynamics is evaluated via a figure of merit. In nonlinear sciences, the use of the Poincaré section is often adapted for this purpose. In appendix C, a technical note provides several tools for the time trace analysis. In particular, the Poincaré section construction is explained. Here, it seems interesting to attempt building a bifurcation diagram as a function of the driving frequency ω_d. Using $\omega_p = 2\pi \times 7$ kHz and $V_p = 3$ V, the demodulated amplitude and phase signals provided by the readout of membrane B is recorded while ω_d is swept from 2.1 to 2.5 MHz. In order to access the dynamical effects we seek at typical frequency given by ω_p, the demodulation bandwidth is widened to $\mathrm{BW} = 40$ kHz. It is important both to record data with enough resolution and time-length. We set the sampling frequency to 400 kHz (≈65 points per modulation period) and the acquisition duration to 100 ms (700 modulation periods). Each measurement includes the time vector and the signal quadratures $X_{A,B} = R_{A,B}\cos(\theta_{A,B})$ and $Y_{A,B} = R_{A,B}\sin(\theta_{A,B})$ where A or B refers to the resonator that is probed. The Poincaré section is extracted from each trace using the local maxima of $Y_B(t)$. Plotted as a function of $\omega_d/2\pi$, we obtain the bifurcation diagram presented in fig. 6.4b.

On this diagram, the points found in a given column (i.e. at a given value of the bifurcation parameter) correspond to the projection of the Poincaré section on 1 dimension. If all the points are gathered a given value, it indicates that the time trace maxima always reach the same value. This period-1 dynamics is found generally off the mechanical resonances. However when the driving frequency is close to the resonances, more complicated regimes are found. When the points are spread over a large range of amplitude, it means that the response does not oscillate regularly and never reach the same maximum. This is a feature of chaos as it will be more deeply discussed later. In the following, we want to experimentally investigate this nonlinear dynamics by using the modulation amplitude V_p and frequency ω_p as the bifurcation parameters. This preliminary result indicates how the driving frequency should be set. It appears indeed that the more complex dynamics, highlighted in the blue transparent stripes, is obtained at resonance. More precisely, the low frequency bistability edges seem to be at the center of each of these windows. In the following, we use this position as a reference for the construction of the bifurcation diagrams. This allows the different normal mode dynamics to be compared to each other and permits also a better reproducibility.

6.2.3 Modulation mechanism on the bistable response

It is possible to build oneself an intuition of the mechanism enabling this complex dynamics to occur. So far, the bistable regime has been shown in the spectral response of the system, i.e. when the driving frequency is swept forward and downward. The theoretical displacement obtained for the fixed settings $V_{dc} = 2$ V and $V_{ac} = 3$ V is recalled in fig. 6.5a. For a given eigenmode, the bistable regime is highlighted in red. However, the force amplitude modulation can not be easily imaged with this representation. Instead, the theoretical displacement can be plotted as a function of the applied strength. For this purpose the driving frequency is fixed at the low bistability edge of the normal mode that is investigated. Then the stationary solutions are numerically resolved as a function of the force f_b.

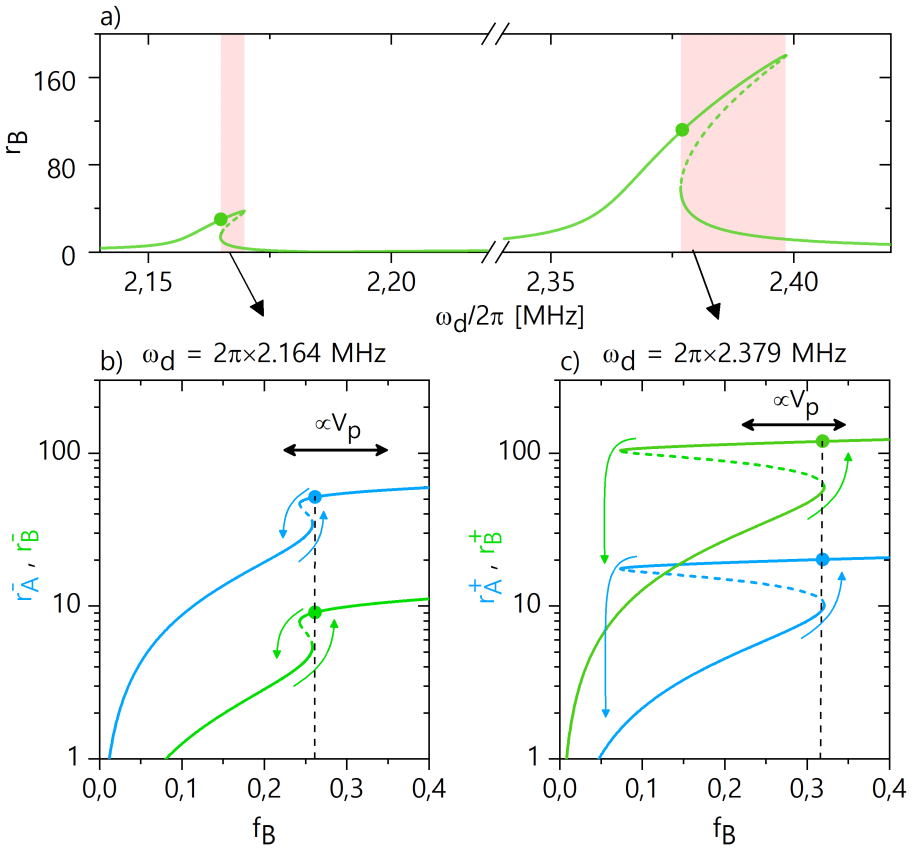

Figure 6.5 – a) Theoretical displacement of resonator B for $V_{dc} = 2$ V and $V_{ac} = 3$V as a function of the driving frequency. b) Theoretical displacement of resonator A (blue) and B (green) for $\omega_d = 2\pi \times 2.164$ MHz as a function of the force amplitude f_B. c) idem for $\omega_d = 2\pi \times 2.379$ MHz.

In fig. 6.5b (resp. in fig. 6.5c), the displacement of resonator A is shown in blue and the displacement of B is shown in green when driving the symmetrical eigenmode $(-)$ with $\omega_d = 2\pi \times 2.164$ MHz (resp. anti-symmetrical eigenmode $(+)$ with $\omega_d = 2\pi \times 2.379$

MHz).

As shown with the black arrows, the strength modulation implies an horizontal displacement on the stable states. The higher V_p the more susceptible for the system to read the other bistability edge and jump to the lower state. Additionally, the modulation frequency plays an important role in the capacity of the system to respond to the drive. If the change in the applied strength is too fast, the system won't be able to respond and maybe will be blind tho the modulation. Therefore it is possible at this point to anticipate that the frequency modulation must not be too large compared to the typical dissipation rate given by $\Gamma_{\pm} \approx \Gamma_{A,B} \approx 5$ kHz.

6.2.4 Experimental bifurcation diagrams

We start the study with the strength modulation amplitude V_p. We recall here that $V_{dc} = 2$ V and $V_{ac} = 3$ V for this study. The modulation frequency is set to $\omega_p = 2\pi \times 7$ kHz. The objective is to evaluate the effects of this modulation on each normal mode and to compare them. We also wish to compare the system dynamics whether the membrane A or B is read which makes 4 different scenarii to explore.

First, the laser spot is focused on membrane A and the driving frequency matches with the symmetrical eigenmode bistability edge $\omega_d = 2\pi \times 2.164$ MHz. A time trace is recorded for each value of V_p between 0 and 3 V. The same experiment is then realized by focusing the laser on membrane B. The bifurcation diagrams are built from the Poincaré section made of the local maxima of $Y_A(t)$ as a function of V_p as shown in (fig. 6.6a). Using $Y_A(t)$ rather than $X_A(t)$ is an arbitrary choice motivated by the higher amplitude of the phase portraits along the Y axis. Then the same experiment is reproduced by probing the membrane B. The corresponding diagram is is shown in fig. 6.6b and each time trace is used to compute the largest Lyapunov exponents (LLEs) shown in red below the corresponding diagrams. The computation of the LLE is discussed in appendix C. For low value of the modulation voltage injected into the normal mode $(-)$, a single branch in the Poincaré section in results from the closed single loop oscillations. In this limit-cycle regime the membranes MHz oscillations envelopes are modulated at ω_p. As the strength is modulated stronger, we observe two consecutive period-doubling bifurcations at $V_p \approx 1.75$ V and $V_p \approx 2.5$ V prior to a window of chaotic dynamics for $V_p > 2.8$ V that we highlight with transparent blue stripes. The presence of chaos is confirmed by the positive LLEs while it is zero for limit cycle oscillations.

Similar measurements are conducted driving the other normal mode $(+)$. The driving frequency is now set to the low-frequency edge of the bistability at $\omega_d = 2\pi \times 2.379$ MHz. We construct the bifurcation diagrams still reading the motion of membrane A (fig. 6.6e) and then membrane B (fig. 6.6f). The phase portraits associated to this case are shown in fig. 6.6g. The bifurcation diagrams of eigenmode $(+)$ also display

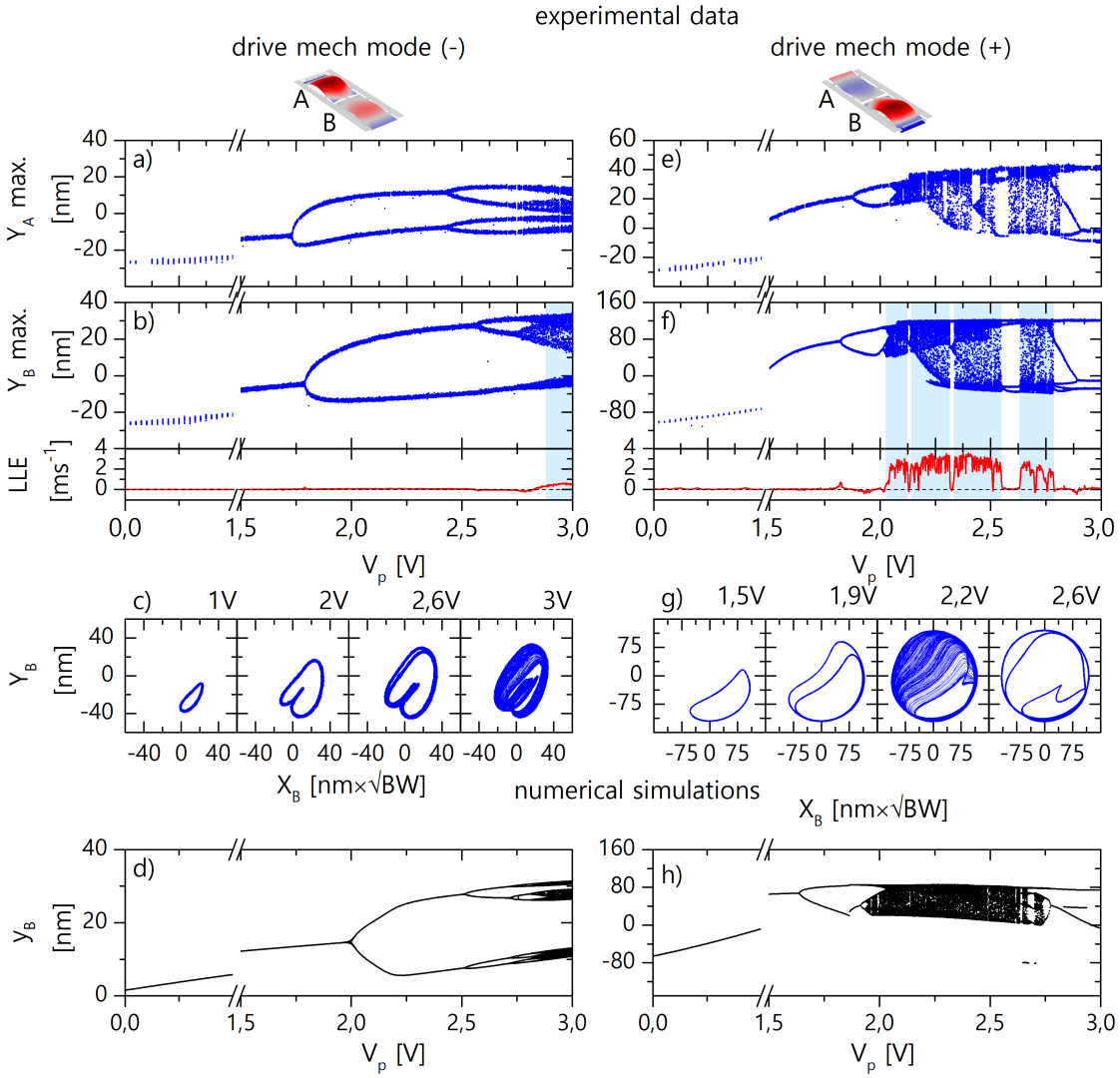

Figure 6.6 – Experimental and numerical bifurcation diagrams under single driving. Measurement and simulations are performed by driving either the symmetrical (left column $\omega_d = 2\pi \times 2.164$ MHz) or anti-symmetrical resonance (right column $\omega_d = 2\pi \times 2.379$ MHz) with $V_{dc} = 2$ V, $V_{ac} = 3$ V and $\omega_p = 2\pi \times 7$ kHz. a)-e) experimental bifurcation diagrams built by sweeping V_p and reading membrane A. b)-f) idem by reading B and with the associated largest Lyapunov exponents (LLE). c)/f) Phase portraits at different dynamical regimes. d)/f) Numerical simulation of bifurcation diagrams built from membrane B response. Note the broken axis.

a period-doubling route to chaos structure [Lee et al., 1985] although the chaotic regime now occurs around $V_p \approx 2$V. We observe several chaotic regions that are separated by small windows of periodic or quasiperiodic regimes as captured by the zero values of the associated LLE. An example of such regime is show in fig. 6.6g at value $V_p = 2.6$V with a period-4 motion. All experimental diagrams share a common dynamics but the bifurcation points significantly differ whether the eigenmode $(-)$ to $(+)$ is driven. This quantitative differences between the eigenmodes dynamics result from the imbalanced energy injection in the normal modes since we advantage the eigenmode $(+)$ by driving the membrane B.

Although the bifurcation diagrams are very similar whether A or B is read, a small shift in the bifurcation points positions can be observed and even a regime of periodic oscillations is present around V_p =2.3V in fig. 6.6f that is not present in fig. 6.6e. This is a consequence of the photothermal shift induced by the laser on the eigenfrequency dominated by the probed membrane [Gao et al., 2019]. This shift is lower than 3 kHz but leads to a significant modification of the bifurcation diagram. When driving a given normal mode, we expect the membrane responses to be perfectly correlated. The normal modes result from the strong coupling interaction between the membranes and the fact that they both are identically affected by the dynamics of a normal mode should not be understood as synchronization. This can not be confirmed without a simultaneous lecture of both membranes although it was corroborated by our numerical simulations.

The Duffing-Duffing model developed previously is used to reproduce the bifurcation diagrams for both the $(-)$ and the $(+)$ mechanical mode using the driving frequencies $\omega_d = 2\pi \times 2.167380$ MHz and $\omega_d = 2\pi \times 2.37940$ MHz (see resp. fig. 6.6d and fig. 6.6h). The simulations implement an adaptative step-size RK4 method to solve the ordinary differential equations (ODEs) shown in eq. (6.1) by including the time dependent strength and inject the experimentally determined parameters.

$$\tilde{f_B}(t) \rightarrow \tilde{f_B}\left[1 + \frac{V_p}{V_{dc}} \cos(\omega_p t)\right] \tag{6.3}$$

The resulting time traces are analyzed with the same protocol used for our experimental data. In particular, the effect of the 40 kHz bandwidth demodulation is reproduced by applying an identical low-pass filter on the time traces. The route to chaos by period doubling cascade is well captured by our model. The quantitative comparison with experiments yields a satisfactory agreement given all the experimental parameter uncertainties. Thanks to the model, it is possible to track the origin of the chaotic dynamics in the force modulation and not in the coupling: indeed uncoupled membranes should also display chaos under modulation [Miles, 1984; Houri et al., 2020].

6.2.5 Modulation frequency domain

The modulation frequency plays an important role in the dynamics. It seems indeed intuitive, in the framework of the theoretical model, that this frequency should not exceed the damping rate of the system for the stationary equation to remain valid. Somehow the mechanical system would not be able to react with a very fast modulation. In order to experimentally check this consideration, a bifurcation diagram is built with parameter ω_p ranging from 2 to 20kHz. The previous experiment has shown that the eigenmode $(+)$ has a higher amplitude for a given set of excitation parameters. Therefore this study focuses on this eigenmode. The static and resonant voltages stay unchanged: $V_{dc} = 2$ V and $V_{ac} = 3$ V. The modulation amplitude V_p is set at 2.5 V which clearly permit chaos to emerge as shown at this particular value in fig. 6.6f. The time traces sampling rate is adapted to the modulation frequency along the measurement so a satisfactory number of points is recorded per modulation period.

The experimental bifurcation diagram (see fig. 6.7a) evidence a large frequency window of chaotic dynamics as pointed out by the largest Lyapunov exponents. At low modulation frequency, the dynamics is generally periodic with small frequency windows of chaos. A large windows including chaotic intermittency starts around 6.7 kHz and stops at 17.5 kHz. At this value, a reverse cascade period-doubling leads to a single loop limit cycle oscillation whose amplitude decays as the modulation frequency increases. This effect is partly due to the passband demodulation bandwidth that is set to 40 kHz. Nevertheless, it is experimentally verified that for a high frequency (e.g 80kHz) and with an adapted bandwidth (200 kHz), the amplitude still decreases. Anyway no particular dynamics is observed after this reverse period-doubling.

The chaotic dynamics is clearly confined to a range of frequency neighboring the damping rate $\Gamma_+ = 2\pi \times 5$ kHz. The observed reverse cascade suggests that an increase ω_d acts as a decrease of V_p. As the system does not have the time to react to fast force modulation, it reduces its travels through a shorter range of response amplitude. The resulting dynamics therefore compares with what is obtained for lower modulation amplitude.

A numerical simulation is performed in the same modulation frequency range (see fig. 6.7b). The qualitative dynamics evolution is well captured by the model. In particular, the chaotic intermittency and the reverse period-doubling route to chaos clearly appears in the diagram. However, a quantitative difference is found as the system does not show anymore peculiar dynamics as soon as the modulation frequency gets over 12 kHz. The reason for this discrepancy is not perfectly clear but it might be that the force is not well scaled as already suspected with the previous simulation on eigenmode $(+)$ with parameter V_p. In both cases, it looks like the parameters injected in the model leads to underestimated driving force.

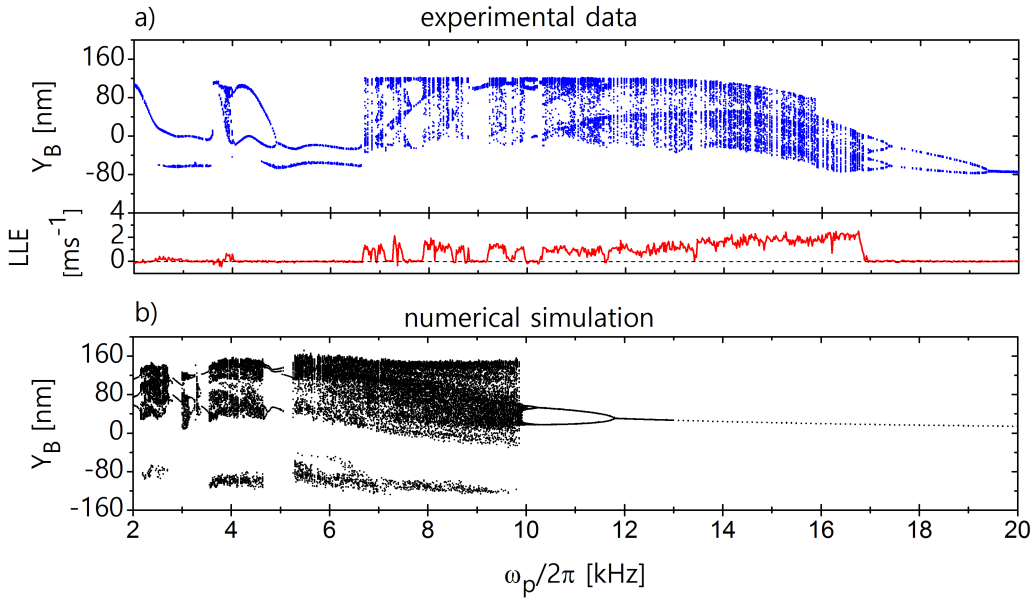

Figure 6.7 – a) Experimental bifurcation diagram with parameter ω_p. Settings: $\omega_d = 2\pi \times 2.379$ MHz, $V_{dc} = 2$ V, $V_{ac} = 3$ V and $V_p = 2.5$ V. Associated largest Lyapunov exponent (red). Measurement performed at ambient pressure. b) numerical simulation using identical settings. $\mathrm{BW} = 40$ kHz

Another way to check the influence of the dissipative timescale on the dynamics of the system consist in checking the bifurcation diagram at different pressure conditions in the vacuum chamber. It has been discussed in section 5.3.4 that the mechanical damping rate exponentially grows with the pressure and is limited to its internal component at low pressure (below 10^{-3} mbar). For 3 different pressure values, the mechanical hysteretic response of eigenmode $(+)$ is obtained by applying $V_{dc} = 2$ V and $V_{ac} = 3$ V on membrane B and by reading B (see fig. 6.8a). The bifurcation diagrams associated to these measurement are shown in fig. 6.8b. It appears clearly that the dynamics is getting poorer as the pressure is increased. In fact, a chaotic region is still found at 15 µbar but this is not the case for lower pressure. By comparing this particular diagram with fig. 6.7a, one finds that the chaotic region still starts at 6.7 kHz but now ends at lower modulation frequency, around 16.5 kHz. For higher pressure, no chaos is diagnosed in the diagrams but a reverse period doubling occurs and the position ω_{PD} of this bifurcation (red dot in each diagram) can be used as a key-criterion in this discussion.

Increasing the mechanical damping rate dramatically deteriorates the displacement amplitude and therefore leads to a lower mechanical saturation. In other words, the hysteresis frequency span is degraded with lower mechanical quality factor. In the meantime, the bifurcation dynamics that is discussed in this chapter relies on the mechanical nonlinearity. Therefore it seems natural that this dynamics vanishes when the bistability disappear. The direct conclusion of this reasoning is that the cut-off frequency ω_{PD}

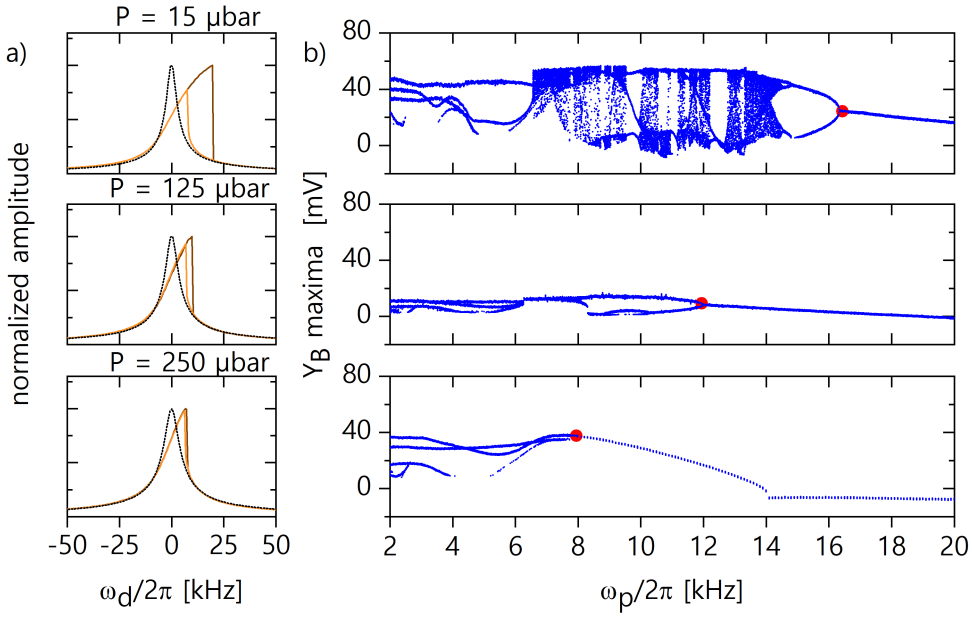

Figure 6.8 – For 3 different pressure in the vacuum chamber : a) Normalized mechanical displacement with forward (brown) and backward (orange) sweep of the driving frequency on eigenmode (+) centered at $\omega_+ = 2\pi \times 2.327$ MHz. The linear response is indicated for reference (back dashed). b) Experimental bifurcation diagram with parameter ω_p. The period-doubling bifurcation position is highlighted with a red dot.

should be anti-correlated with the damping rate Γ_+, which could seem in conflict with the previous discussion. In fact there is a competition between the system nonlinearity and the dissipation rate. Overall, it turns out that the impact of an higher damping rate on the hysteresis span is so important that it dominates the dynamics of the system.

6.3 Imperfect synchronization with two-drive excitation

The chaotic dynamics emerging from the force modulation has been observed in the coupled Duffing system. However this peculiar dynamics does not rely on the coupling between the membranes and could be observed in a single Duffing nanomechanical system. Moreover the period-doubling route to chaos has been observed independently on each eigenmode. Although the bifurcation diagrams have the same structure, we observe a significant difference in the position of the bifurcation points and in the response amplitude. This contrast is caused by the strong natural frequency mismatch which limits the energy enabled to transit from membrane B to membrane A and leads to imbalanced amplitudes of the eigenmodes.

In this section we show that the eigenmodes can couple and synchronize when si-

multaneously driven. The orthogonality breaking that allows this coupling is preliminary explained and described in the frame of the Duffing-Duffing model. Then we experimentally investigate the different synchronization regimes standing in periodic and in chaotic dynamics.

6.3.1 Orthogonality breaking

In the linear regime, the normal modes resulting from the spring coupling between the nano-membranes have properties given by the eigenvalues of the Jacobian J that has been extensively used in the previous chapter chapter 5. As soon as the system enters in the Duffing regime, this diagonalization can not be performed and the eigenmodes are no longer orthogonal to each other. In consequence an energy transfer is expected between the eigenmodes as soon as they are driven in a nonlinear regime. Here we will use the coupled Duffing resonators model to evidence this coupling.

The notation $(-)$ and $(+)$ respectively refer to the symmetrical and anti-symmetrical eigenmodes. We assume here that the eigenmodes are driven with strengths f_B^+ and f_B^- and driving frequencies ω_d^- and ω_d^+ applied on membrane B. The master equations of the system now reads:

$$\begin{cases} \ddot{x}_A + \Gamma_A \dot{x}_A + \omega_A^2(1+\beta x_A^2)x_A - G x_B = 0 \\ \ddot{x}_B + \Gamma_B \dot{x}_B + \omega_B^2(1+\beta x_B^2)x_B - G x_A = f_B^- \cos(\omega_d^- t) + f_B^+ \cos(\omega_d^+ t) \end{cases}$$

Solving these coupled nonlinear equations does not require additional technique than what is shown in section 6.1.1. However, since the system is now expected to respond both at ω_d^- and ω_d^+, we modify the ansatz :

$$\begin{aligned} x_A = & \, v_A^- \cos(\omega_d^- t) + w_A^- \sin(\omega_d^- t) \\ & + v_A^+ \cos(\omega_d^+ t) + w_A^+(\omega_d^+ t) \end{aligned}$$

The rest of the calculations are essentially the same. The nonlinear coupling between $r_{A,B}^-$ and $r_{A,B}^+$ comes from the development of the cubic terms x_A^3 and x_B^3. We neglect all off-resonant terms including the ones oscillating at $2\omega_\pm - \omega_\mp$. Following the exact same procedure than before, we derive a system of 8 equations for the normal modes $(-)$ and $(+)$ amplitudes and phases accessed either through the membrane A (r_A^-, r_A^+, ϑ_A^- and ϑ_A^+) or B (r_B^-, r_B^+, ϑ_B^- and ϑ_B^+). It writes :

$$\begin{cases} \dot{r}_A^- = \dfrac{-\gamma_A}{2} r_A^- + \dfrac{g}{2} r_B^- \sin(\vartheta_A^- - \vartheta_B^-) \\ \dot{r}_B^- = \dfrac{-\gamma_B}{2} r_B^- - \dfrac{g}{2} r_A^- \sin(\vartheta_A^- - \vartheta_B^-) + \dfrac{\tilde{f_B^-}}{2} \sin(\vartheta_B^-) \\ r_A^- \dot{\vartheta}_A^- = \dfrac{-r_A^-}{2} \left[2(\delta^- - \Delta\omega) + \dfrac{3}{4}\tilde{\beta}(r_A^{-^2} + 2r_A^{+^2}) \right] + \dfrac{g}{2} r_B^- \cos(\vartheta_A^- - \vartheta_B^-) \\ r_B^- \dot{\vartheta}_B^- = \dfrac{-r_B^-}{2} \left[2\delta^- + \dfrac{3}{4}\tilde{\beta}(r_B^{-^2} + 2r_B^{+^2}) \right] + \dfrac{g}{2} r_A \cos(\vartheta_A^- - \vartheta_B^-) + \dfrac{\tilde{f_B^-}}{2} \cos(\vartheta_B^-) \end{cases}$$

$$\begin{cases} \dot{r}_A^+ = \dfrac{-\gamma_A}{2} r_A^+ + \dfrac{g}{2} r_B^+ \sin(\vartheta_A^+ - \vartheta_B^+) \\ \dot{r}_B^+ = \dfrac{-\gamma_B}{2} r_B^+ - \dfrac{g}{2} r_A^+ \sin(\vartheta_A^+ - \vartheta_B^+) + \dfrac{\tilde{f}_B^+}{2} \sin(\vartheta_B^+) \\ r_A^+ \dot{\vartheta}_A^+ = \dfrac{-r_A^+}{2} \left[2(\delta^+ - \Delta\omega) + \dfrac{3}{4}\tilde{\beta}(r_A^{+^2} + 2r_A^{-^2}) \right] + \dfrac{g}{2} r_B^+ \cos(\vartheta_A^+ - \vartheta_B^+) \\ r_B^+ \dot{\vartheta}_B^+ = \dfrac{-r_B^+}{2} \left[2\delta^+ + \dfrac{3}{4}\tilde{\beta}(r_B^{+^2} + 2r_B^{-^2}) \right] + \dfrac{g}{2} r_A^+ \cos(\vartheta_A^+ - \vartheta_B^+) + \dfrac{\tilde{f}_B^+}{2} \cos(\vartheta_B^+) \end{cases}$$

With the detunings $\delta^\pm = (\omega_B - \omega_d^\pm)/\omega_d^\pm$ and the strengths $\tilde{f}_B^\pm = f_B^\pm/\omega_d^\pm$.

These two systems of 4 equations contains new terms that allow the eigenmode response amplitudes $r_{A,B}^+$ and $r_{A,B}^-$ to couple. By developing the 4 expressions of the phases derivatives ($r_A^\pm \dot{\vartheta}_A^\pm$ and $r_B^\pm \dot{\vartheta}_B^\pm$) we note that this coupling is of the form $\tilde{\beta} r^\pm r^{\mp^2}$. Interestingly we recover an nonlinear coupling that goes like a cubic displacement. This form of nonlinear coupling is sometime used in the description of nonlinearly coupled resonators, additionally to the Duffing nonlinearity [Truitt et al., 2013].

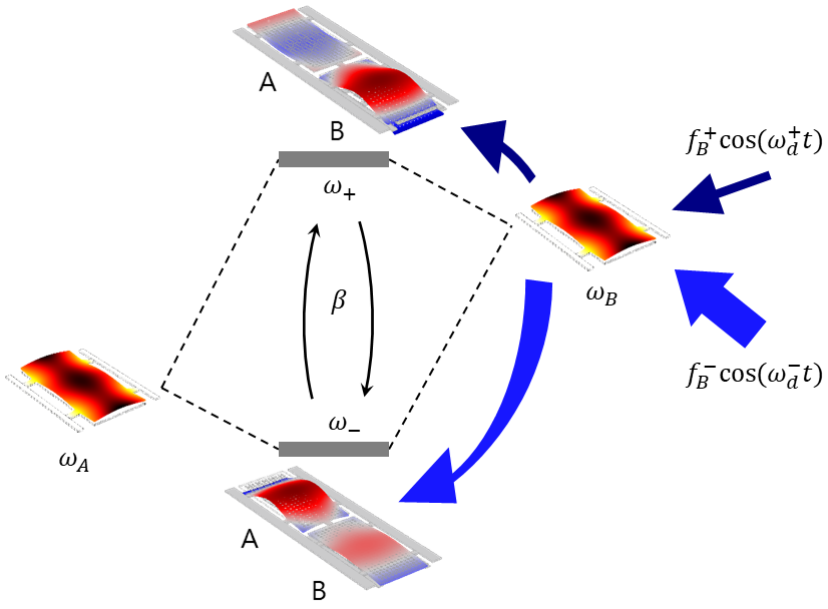

Figure 6.9 – The imbalance in each eigenmode displacement field distribution is caused by the intrinsic natural frequency mismatch $\omega_B - \omega_A$. The energy injected in each normal mode is balanced by choosing $f_B^- > f_B^+$. Additionally the Duffing nonlinearity β breaks the orthogonality between the eigenmodes and allows them to couple.

6.3.2 Correlated bifurcation diagrams

A measurement of the bifurcation diagrams is performed with $V_{dc} = 2V$, $V_{ac}^- = 3.5V$, $\omega_d^- = 2\pi \times 2.177$ MHZ, $V_{ac}^+ = 0.5V$, $\omega_d^+ = 2\pi \times 2.410$ MHz and $\omega_p = 2\pi \times 5$ kHz. We choose $V_{ac}^+ < V_{ac}^-$ in order to compensate the response amplitudes imbalance that

results from the membranes frequency mismatch (see fig. 6.9). We place the laser spot on membrane B and use two independent demodulators to simultaneously access the signal amplitude and phase at ω_d^- (R_B^- and θ_B^-) and at ω_d^+ (R_B^+ and θ_B^+). By sweeping the bifurcation parameter V_p, a new diagram is built from the local maxima of signal quadratures $Y_B^- = R_B^- \sin(\theta_B^-)$ and $Y_B^+ = R_B^+ \sin(\theta_B^+)$ that we record with demodulation bandwidth of 40 kHz. This allows a reduction of the crosstalk between the channels below -20 dB. We note that the diagram branches are broader than in the single-excitation case. This is caused by the remaining crosstalk between the two demodulation channels. In fig. 6.10a the qualitative comparison of the bifurcation diagrams shows a clear match of the dynamical regimes in which the normal modes $(-)$ and $(+)$ settle, and more importantly the bifurcation points are the same. After a limit-cycle region, both display identical period-doubling route to chaos structure confirmed by the LLE computed for each diagram. The chaotic regions are highlighted with blue stripes.

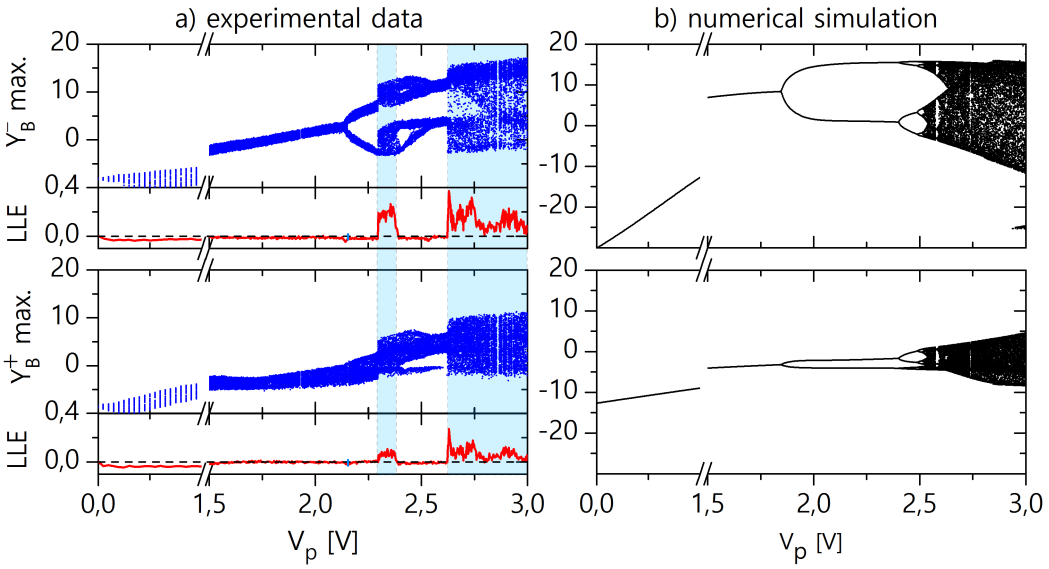

Figure 6.10 – Experimental (a) and simulated (b) bifurcation diagrams made from the Poincaré section of the eigenmode $(-)$ (top) and $(+)$ (bottom) amplitudes under double-excitation. The bifurcation parameter is the modulation amplitude while the modulation frequency is set to 5 kHz. The simulation inputs $\omega_d^- = 2.168500$ MHz and $\omega_d^+ = 2.370280$ MHz

A numerical simulation is performed from the model using our experimental parameters and reproduce a bifurcation diagram with the amplitude response of both normal modes (see fig. 6.10b). The period-doubling structure followed by chaotic intermittency is recovered. The period doubling occurs for $V_p = 2.176$ V which compares accurately with the experimental period doubling at $V_{PD} = 2.140$ V. However the response amplitude of mode $(-)$ is higher than the response of mode $(+)$ contrary to what was

observed experimentally. This can be explained by a limitation in the several experimental calibrations we have performed due to a degradation of some of the electromechanical properties with time. Indeed we have noted that the quality factor tend to decrease when using too high input laser power[3], or irreversible mechanical frequency modification when stopping and restarting the vacuum pump.

6.3.3 Amplitude synchronization

The typical dynamical regimes are illustrated with the phase portraits of eigenmode $(-)$ infig. 6.11a and eigenmode $(+)$ in fig. 6.11b as well as with the Fourier spectra of their respective amplitudes in fig. 6.11c. At low modulation amplitude (top: $V_p = 1.5$ V), a period-1 limit-cycle oscillation regime is established and the spectra display a main peak at the modulation frequency as well as low-intensity sub and super-harmonics. In the route to chaos (center: $V_p = 2.425$ V), the eigenmode $(-)$ clearly displays a period-4 motion while it is less obvious for the eigenmode $(+)$ due to its low amplitude. However both the Fourier spectra display more peaks, and with higher amplitude, than in the period-1 motion. However the noise floor is still quite flat between the peaks. Finally in the chaotic regime (bottom: $V_p = 2.750$ V), it is not so relevant to compare the phase portraits. However, the Fourier spectra appearance qualitatively change compared to the previous regimes. Their look noisier as well as lightened from most of the dominant peaks. Nonetheless both Fourier spectra are strongly correlated between the eigenmode amplitudes.

In fig. 6.11d (top), the phase portraits showing the eigenmodes normalized amplitudes relative dynamics are shown for three singular dynamical regimes. The normalization is meant to get rid of the unbalanced amplitudes still present despite the compensation. We show $\tilde{R}^{\pm} = (R_B^{\pm} - \langle R_B^{\pm} \rangle)/\sigma^{\pm}$ with $\langle R_B^{\pm} \rangle$ and $\sigma^{\pm}$ respectively the mean value and the standard deviation of $R_B^{\pm}(t)$ calculated over the entire time trace. The dashed black lines correspond to the synchronization regime where both normalized amplitudes are equal. Below the period-doubling bifurcation, for $V_p < V_{\mathrm{PD}}$, a master-slave relation is established between the drive and each resonance so these two inescapably move in synchrony. For $V_p > V_{\mathrm{PD}}$ the responses are now driven in a high-order synchronization regime. Nevertheless the amplitudes are clearly correlated to each other. This is even more manifest in the chaotic regime where the amplitudes are still correlated despite their asynchronous behavior with the drive. This regime corresponds to the chaotic synchronization of the nonlinearly coupled eigenmodes.

[3] The membrane degradation was particularly pronounced when using a 800 nm laser, which we did when attempting to photothermally tune the membranes' natural frequencies.

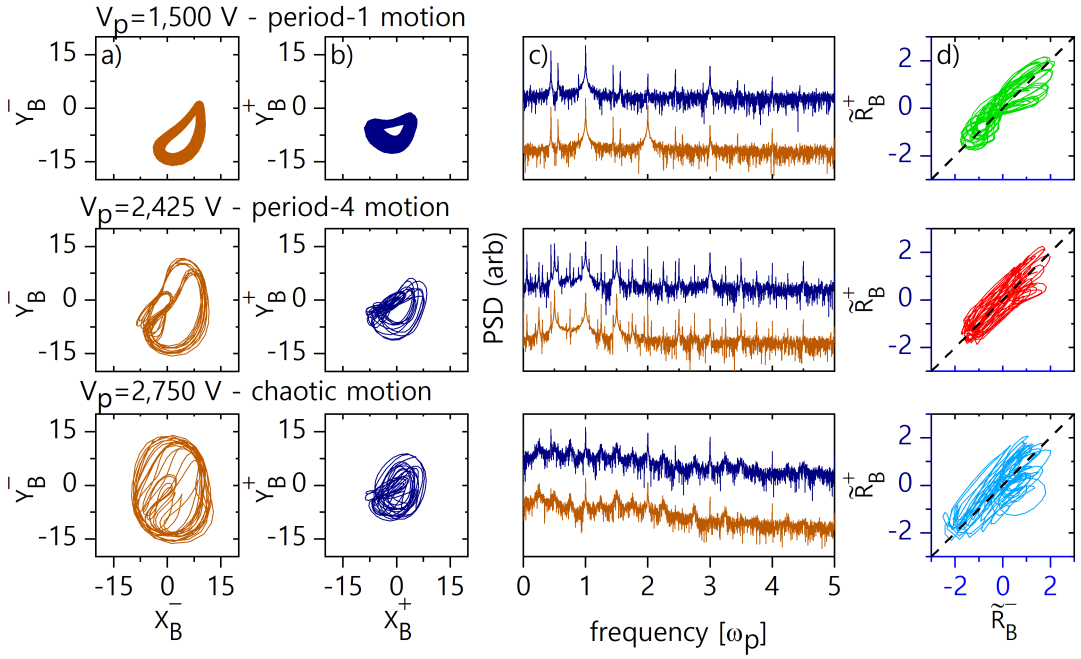

Figure 6.11 – In a period-1 (top), period-2 (middle) and a chaotic regime (bottom), a)-b) the respective phase portraits of the modes $(-)$ and $(+)$, c) the fft power spectra computed from their amplitude responses, d) the relative amplitude dynamics with the exact synchronization reference (black dashed). Note the color code in this figure: brown for eigenmode $(-)$ and dark blue for eigenmode $(+)$. The Fourier spectra noise floor are shifted for an easier comparison.

6.3.3.1 Lag synchronization

In chaotic synchronization regime, it is often interesting to take a look at the lag synchronization properties [Boccaletti et al., 2002]. A lag synchronization between two dynamical variables $x(t)$ and $y(t)$ is established whenever $x(t) = y(t - \tau)$ with τ the lag. In order to check such feature in the experimental data, one can plot a phase portrait showing the normalized amplitudes with a lag e.g $\tilde{R}^+(t - n \times dt)$ as a function of $\tilde{R}^-(t)$ with dt the experimental time step and n an integer. Then the distance between the points and the diagonal given by $\sqrt{\sum_t |\tilde{R}^+(t - n \times dt) - \tilde{R}^-(t)|^2}$ is estimated for several values of n. The lag is given by the delay which minimizes this distance. In practice, in order not to be limited by the experimental time step, we interpolate this distance with a sub-pixel precision.

This procedure is applied for each trace processed in fig. 6.10a. The lag is shown as a function of the modulation amplitude in fig. 6.12a in units of modulation period. As V_p is increased, the lag tends to reduce which indicates that the synchronization regime is set by this parameter. After the period-doubling, the lag essentially stay close to zero. Some small but sudden jumps occur at the edges of the bistable regions. Generally

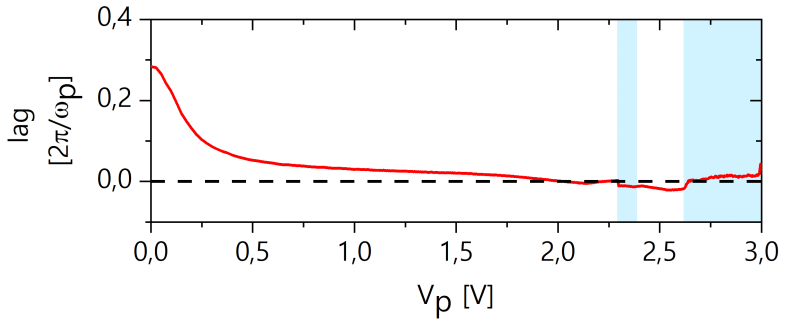

Figure 6.12 – Lag between the normal mode amplitudes as a function of the modulation amplitude. The chaotic regions found in fig. 6.10a are reported here for reference.

speaking the lag is never found to be very high as the maximum value in this study is below 30% of one modulation period. We conclude that this feature is not central in the present dynamics.

6.3.4 Phase dynamics

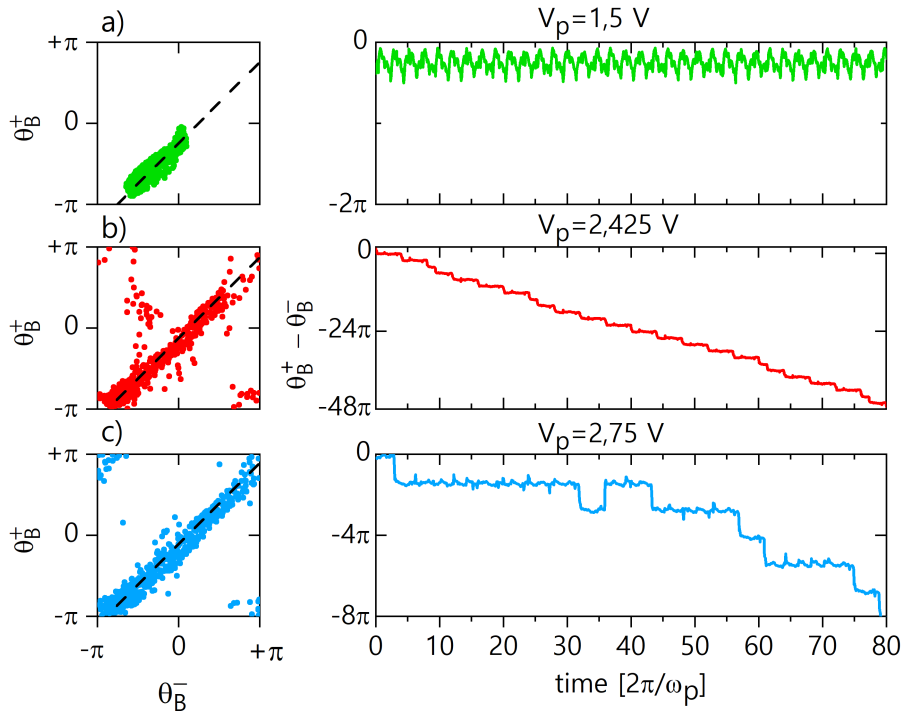

Figure 6.13 – a) Phase portraits showing the normal modes relative response normalized phase with phase synchronization references (black dashed lines). b) Measurement of $\theta_B^+ - \theta_B^-$ over 80 modulation periods (16 µs). We identify phase synchronization at $V_p = 1.5$V (green), phase desynchronization at $V_p = 2.425$V (red) and imperfect phase synchronization at $V_p = 2.75$V (blue).

We now focus on the phase responses correlations shown in fig. 6.13a. In each case, we fit the data with an unit-slope line (black-dashed) corresponding to the synchronization regime $\frac{d}{dt}(\theta_B^+ - \theta_B^-) = 0$. These plots show a tendency of synchronous evolution of θ_B^- and θ_B^+ under force modulation for $V_p < V_{\mathrm{PD}}$. Contrary to the amplitudes, the synchronization of the phases is not maintained for $V_p > V_{\mathrm{PD}}$ as the trajectory does not only lie on a unit-slope line.

By studying the real-time dynamics of the phase difference in fig. 6.13b, we find that 2π phase slips occur when $V_p > V_{\mathrm{PD}}$ while the resonators are phase synchronized for $V_p < V_{\mathrm{PD}}$ (green trace). When high-order synchronization is established between each mode and the drive [Pikovsky et al., 2001], phase slips resulting from desynchronization can come up even if the amplitudes stay correlated. This process leads to phase slips occurring regularly (red trace) – in this situation, the phases periodically execute one more (or one less) cycle regarding the drive – or chaotically (blue trace). In the latter case, the resonators stay phase synchronized over several modulation periods and this regime is interrupted by occasional phase slips. This corresponds to the imperfect phase synchronization scenario [Boccaletti et al., 2002]. In the general case of non-identical chaotic oscillators, complete synchronization of the amplitudes and phases is expected only for strongly coupled systems. For smaller coupling strength, either phase synchronization (PS) or imperfect phase synchronization (IPS) [Park et al., 1999] is observed. This phenomenon has received a large theoretical interest [Zaks et al., 1999; Blackburn et al., 2000; Lifshitz and Cross, 2003] with few experimental demonstrations only at the macroscopic scale, in electronic circuits [Pujol-Peré et al., 2003; Pisarchik et al., 2008] or Nd:YAG lasers [Volodchenko et al., 2001].

The different phase synchronization regimes can be described through a statistical study of the durations between two successive phase slips. For a given time trace, we list all the phase synchronization durations τ and calculate both the mean value $\langle\tau\rangle$ as well as the standard deviation σ_τ. In fig. 6.14a, the mean duration is plotted together with the standard deviation as a function of V_p while the scaled mean duration $\langle\tau\rangle/\sigma_\tau$ is shown in fig. 6.14b. No value can be estimated below the bifurcation to chaotic regime at $V_p = 2.3$ V since phase synchronization is established and therefore we do not observe any phase slip in the data. The durations found to be lower than $2\pi/\omega_p$ are ignored because it can not be qualified as synchronization.

The desynchronization regime is identified by the regularity of the phase slips which implies that σ_τ nears zero and leads to a peak in the scaled mean duration that can be seen around $V_p = 2.425$ V. The traces corresponding to this situation (included in the red stripe) are used to built an histogram in fig. 6.15 (left) showing the distribution of the phase synchronization durations probabilities with the associated 95% confidence interval. In order to compare the statistics of τ between the different traces, i.e. for different V_p, we normalize all the durations found in a given trace by the mean duration

value for this trace. By construction, the mean value of this histogram is 1 and here the probability is concentrated around this value. The corresponding mean duration is $\langle\tau\rangle = 3.6$ modulation periods. The histogram displays a 63% probability for the phases to synchronize during 4 modulation periods (see bar at position $\tau/\langle\tau\rangle = 1.2$) because this desynchronization occurs while the systems sets in a period-4 motion dynamics.

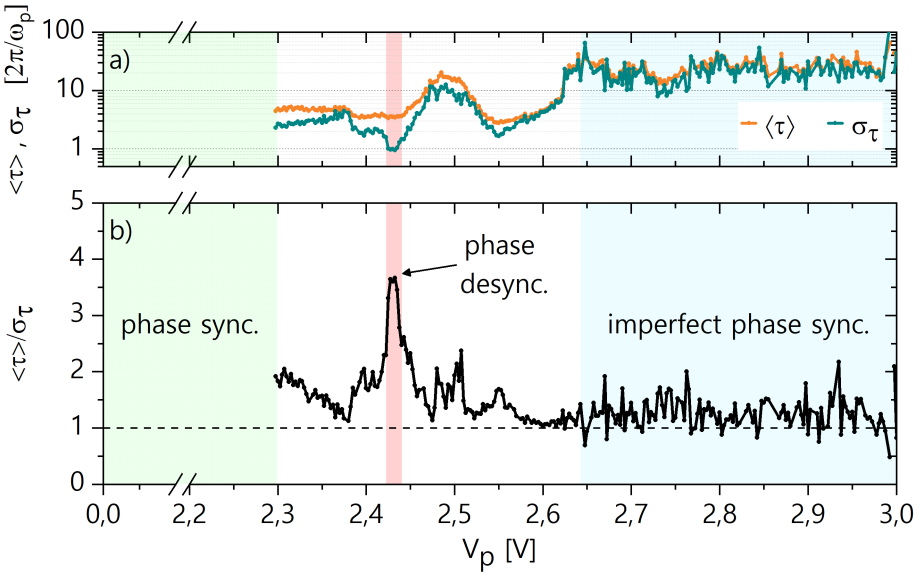

Figure 6.14 – a) Phase synchronization (PS) duration mean value τ and standard duration σ_τ, in units of modulation periods, as a function of the modulation amplitude. b) Scaled mean PS duration $\langle\tau\rangle/\sigma_\tau$.

In the chaotic regime (blue stripe in fig. 6.10a) we find that the scaled mean duration remains constant and slightly over 1 which tends to indicate an exponential decay of the probability distribution of $\tau/\langle\tau\rangle$ shown in fig. 6.15 (right). In this regime the mean phase synchronization duration is $\langle\tau\rangle = 26$ modulation periods. The probability indeed decays exponentially but we find that the probability for short phase synchronization durations is higher than predicted with such distribution. We conclude that the phase slips occur in a non-Poissonian process due to the chaotic dynamics and do not result from noise. The experimental histogram is reproduced using a numerical simulation realized from the new non-autonomous system of equations. We recover a similar bifurcation diagram with a robust scaling of the modulated force as shown in fig. 6.10b. We observe 2π slips of the phase difference when the system dynamics is chaotic. From these simulations, we reproduce a histogram of the phase synchronization durations in fig. 6.15. We find a good agreement with the experimental distribution.

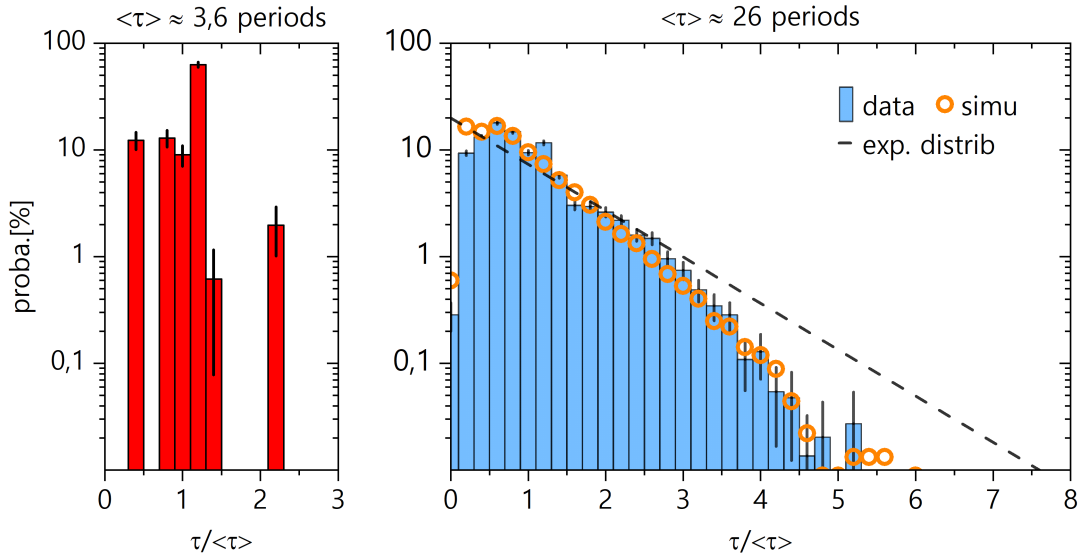

Figure 6.15 – Experimental probability distributions of the PS durations within the phase desynchronization (PDS) regime (red) or the imperfect phase synchronization (IPS) regime (blue). Distribution given by numerical simulation in the chaotic regime (orange circles). The exponential distribution (black dashed) is shown for comparison.

6.3.5 Perfect synchronization

In the previous results, the synchronization dynamics has been deeply investigated. It comes out that in the chaotic regime the oscillators experience imperfect phase synchronization. The mean phase synchronization (PS) duration is a statistical signature of this regime. The data show that this feature is quite constant with V_p in the chaotic regime (see fig. 6.14a). However, it has been noticed in the numerical simulations that the mean PS duration is extremely sensitive to the driving frequencies ω_d^- and ω_d^+. In particular, when the system is set close to a bifurcation point, it happens that the PS durations increase up to *perfect synchronization*, where chaos and phase synchronization cohabit.

In fig. 6.16a, we simulate the mean PS duration in a small region of the parameter space $\{\omega_d^-, \omega_d^+\}$ and with the modulation amplitude locked to $V_p = 3$ V. The study is centered around the values $\{\omega_d^{-,\mathrm{ref}} = 2.168500, \omega_d^{+,\mathrm{ref}} = 2.370280\}$ which were kept for the simulated bifurcation diagram shown in fig. 6.10b. Thus this point matches with the dynamics we experimentally observe. For each trace, the phase slip are recorded such that the PS durations can be recorded. The mean value can not be estimated when no phase slip is recorded: this the phase synchronization regime spotted in the top-left quarter of the contour plot. Ideally, we would like highlight the chaotic regions of this map using the largest Lyapunov exponent. Unfortunately, an accurate computation enabling the delimitation of a precise frontier between periodic and chaotic motion would be extremely long. Instead, we point at three typical dynamical regimes that illustrate

the present discussion. These three regimes set at the positions A, B and C highlighted by colored cross on the map. For each of them, the dynamics of mode $(+)$ and the phase dynamics $\vartheta_B^+ - \vartheta_B^-$ are both shown in figs. 6.16a and 6.16b. Note that we only show the dynamics of mode $(+)$ but it is verified that the mode $(-)$ experiences the same dynamics: amplitude synchronization is maintained.

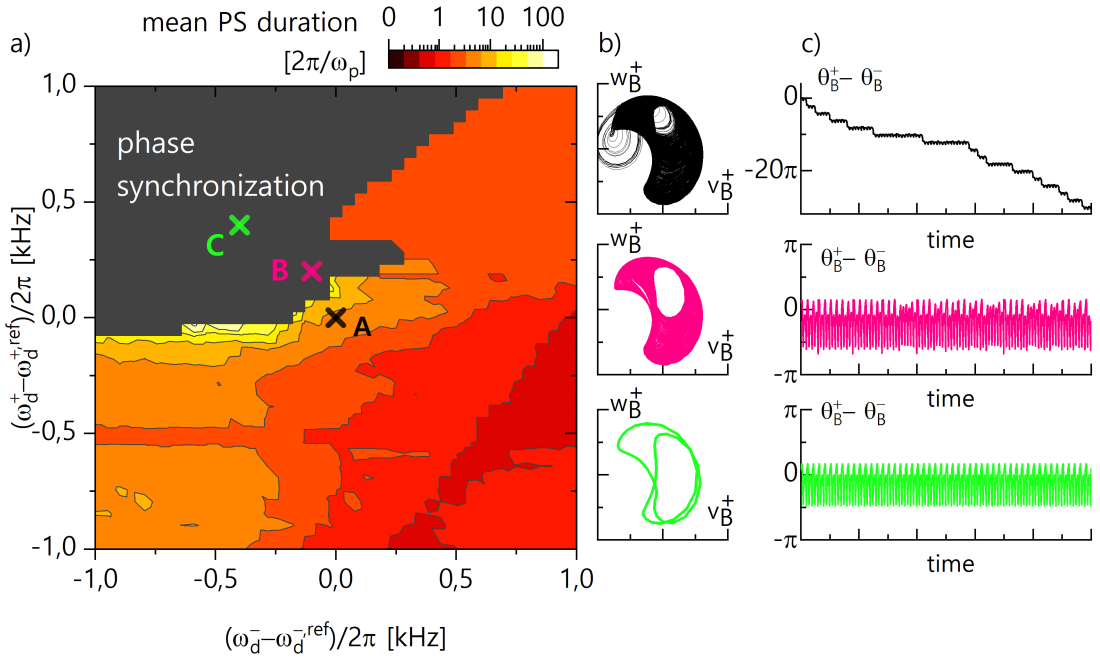

Figure 6.16 – Numerical simulation: a) estimation of the mean PS duration in the parameter space $\{\omega_d^-, \omega_d^+\}$. The center position (black cross) corresponds to the experimental conditions $\{\omega_d^{-,\mathrm{ref}} = 2.168500, \omega_d^{+,\mathrm{ref}} = 2.370280\}$ MHz (blue cross). No phase slip are found in the grey region and we deduce that phase synchronization is established. At three particular positions, we plot a) the normal mode $(+)$ dynamical phase portrait and b) the phase dynamics.

At point A (black), we recover the experimental regime when $V_p = 3$ V. Indeed the normal modes set in chaotic regimes and the phase difference experience phase slips such that the mean PS duration is around 26 modulations periods. Observing how the mean PS duration evolves in the transition towards the PS regime, it appears that it can be either brutal (see position $\{0.5, 0.75\}$) or smooth with a quick increase the mean PS duration (e.g. between points A and B). The first situation corresponds to a transition through a phase desynchronization (PDS) non-chaotic regime. The second enables phase synchronization despite the presence of chaos. This is the case in point B (magenta). The mode $(+)$ dynamics is chaotic but the phase difference stays bound. The simulation shows that no phase slip occur in several thousands of modulation periods. Finally, when moving deeper into the map's top-left quarter at point C (green), the PS

is maintained but the dynamics turns to periodic motion. As not PDS regime is spotted in this transition, it has be involve a brutal bifurcation, or *crisis*.

With this numerical exploration of the subspace $\{\omega_d^-, \omega_d^+\}$, we have noted a very rich dynamics. Surprisingly, the dynamical regime can evolve very quickly when shifting these parameters by less than 1 kHz. More importantly, our model predict a small region in which the chaotic regime is compatible with phase synchronization. With an experimental precision of the order of 10 Hz on each driving frequency, which is achievable, one could observe such behavior.

6.4 Chaos-aided generation of random bit sequences

The generation of random numbers is essential in many computing applications and communication encryption protocols. Therefore Random Number Generators (RNG) have been widely studied both on the hardware (True RNG) and software (Pseudo RNG) sides.

Here we apply a procedure enabling to extract a random binary sequence from our experimental chaotic time traces. We study the influence of two key parameters involved in this procedure – the sampling frequency and the delay – on the sequence randomness. Finally we discuss the integration of this method on our two synchronized chaotic oscillators for the implementation of a secure communication protocol.

6.4.1 Principles

The procedure enabling the generation of random bits from a chaotic time trace is explained in [Sciamanna and Shore, 2015]. To illustrate each step of the procedure, we focus on the normalized experimental trace shown in fig. 6.17a. These data are obtained in the 2 modulated-driven Duffing-Duffing configuration discussed in section 6.3. We apply $V_{dc} = 2$ V, $V_{ac}^- = 3.5$, $V_{ac}^+ = 0.5$, $\omega_d^- = 2\pi \times 2.177$ MHz, $\omega_d^+ = 2\pi \times 2.410$, $V_p = 2.5$ V and $\omega_p = 2\pi \times 3.77$ kHz. The normal modes experience an imperfect phase synchronization dynamics although this does not matter as we focus on the chaotic amplitude response of mode $(-)$. The interest of synchronization regarding the RNG will be discussed further on. The trace is normalized with $X(t) = (R_B^-(t) - \langle R_B^- \rangle)/\sigma^-$ with $\langle R_B^- \rangle$ and σ^- respectively the mean and standard deviation of $R_B^-(t)$ calculated over the whole trace.

i Delayed time trace The trace is delayed by an amount τ and can be compared to the original trace. In fig. 6.17b, both traces $X(t)$ and $X(t-\tau)$ are plotted together.

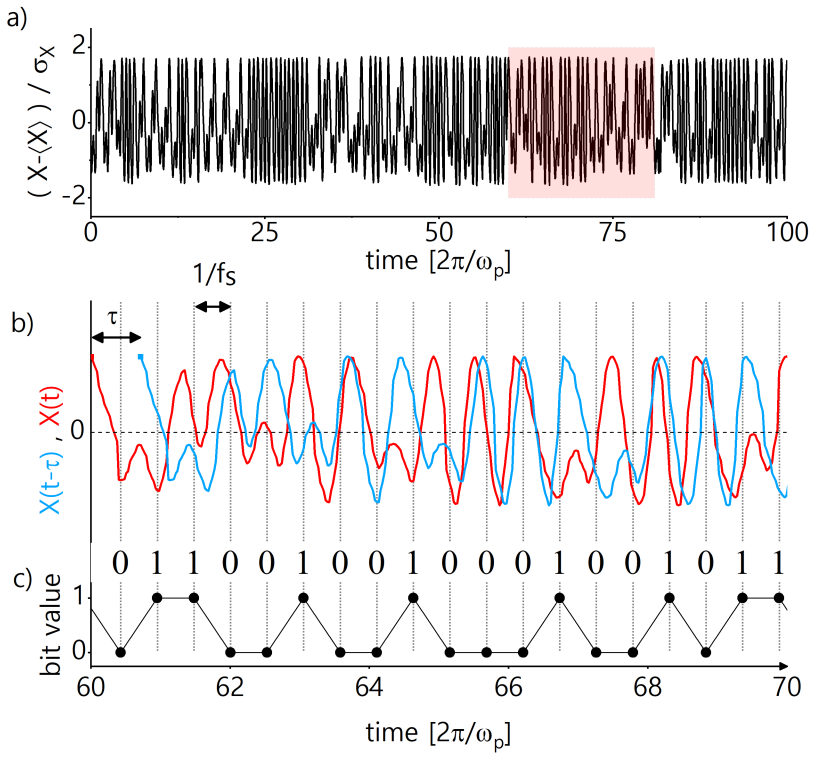

Figure 6.17 – a) Experimental chaotic time trace. b) The trace $X(t)$ is compared to its delayed self $X(t-\tau)$. c) The XOR logical gate is periodically applied to the traces relative sign. It results in a binary sequence.

ii Periodic XOR logical gate At any time, the traces sign are either equal or opposite. Applying an exclusive-OR (XOR) logical gate therefore permits to generate respectively either a 0 or a 1. The binary sequence is then obtained by periodically sampling the data and applying the XOR function. It results in a binary sequence generated at rate f_s (see fig. 6.17c).

Using this method, the bits can be generated at frequency f_s. However, the randomness is not guaranteed for all values of the delay and of the sampling frequency. We study the influence of these two parameters.

6.4.2 Randomness characterization

The randomness of a binary sequence can be verified by applying a certain number of statistical tests. The NIST Statistical Test Suite [Bassham et al., 2010] provides 14 randomness tests, each focusing on one particular statistical property of randomness. E.g one test checks the longest run of ones (or zeros), another test measured the entropy of the sequence, another focuses on the cumulative sum of the sequence, etc. Each test returns a p-value that can be interpreted as the probability for the sequence to be random according to the corresponding test. The p-value validates the test if it value is

above 0.1. In the following we simply apply all these algorithms on our binary sequence and check the p-values. If all the p-values valid the sequence as random, we consider that this sequence passes the randomness test. On the contrary, if at least one test fails, we consider the sequence as not random. In principle, this series of tests is statistically valid for a large number of bits in the sequence ('at least 1000' according to [Bassham et al., 2010]).

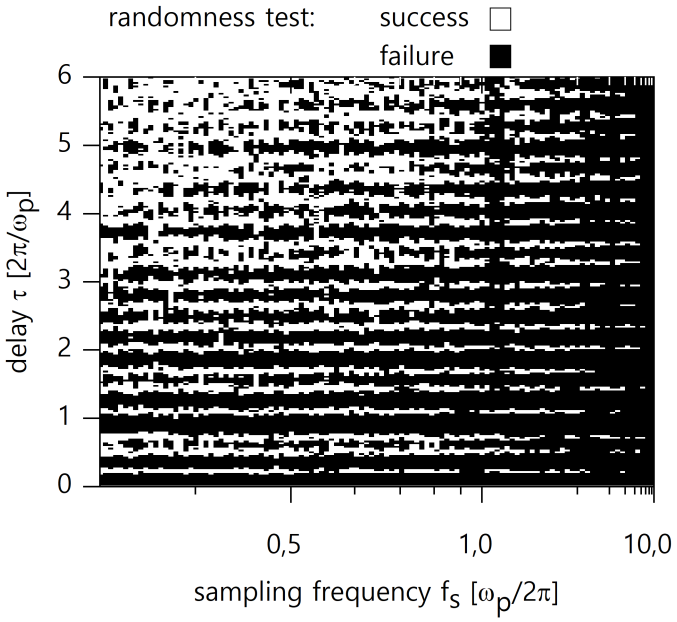

Figure 6.18 – Randomness test suite result as a function of the delay τ and the sampling frequency f_s applied to the trace presented in fig. 6.17a. Both quantities are shown in units of modulation period.

Now the objective is to characterize the randomness test success as a function of the delay τ and the sampling frequency f_s. By generating a binary sequence for several values of τ and f_s, we plot a matrix showing the randomness test result in fig. 6.18. The white (resp. black) pixels correspond to a successful (resp. unsuccessful) test. We observe an increase of the randomness quality toward low sampling frequencies (towards the left side of the map). This is related to trace typical frequency which is the modulation frequency ω_p in the present case. Indeed at high sampling frequencies, the trace does not have enough time to evolve between to samples. This favors the apparition of runs of ones and zeros ('00','11','000','111',etc.) and break the sequence randomness. Moreover the randomness quality shows oscillations with the delay, and also increases for higher values. Overall, low sampling frequency and high delay improve the randomness of the sequence. This involves the Lyapunov time (invert Largest Lyapunov Exponent) of the trace. It corresponds to the time required for the dynamical system to lose its memory and can also be understood as the typical decay time of the trace auto correlation function.

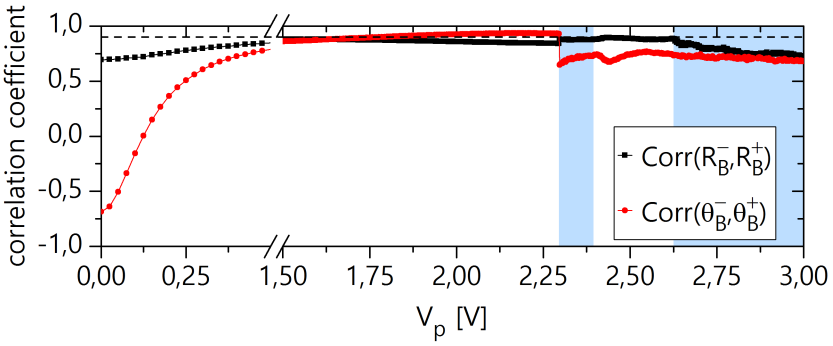

Figure 6.19 – Correlation between the normal mode amplitudes (black) or phases (red) as a function of the modulation amplitude V_p. Chaos (blue transparent stripes) comes with imperfect phase synchronization which results in a degradation of the phases correlation. The dashed line indicate 90% correlation.

In summary our coupled-membrane system enables the generation of random bits at a rate limited to the force modulation frequency. A delay of few periods of modulation is enough for sequence to pass all the randomness tests. Interestingly in our system, the bits are encrypted in the optical field which is used for the readout. The signal has a carrier given by the driving frequency at which a demodulation operation permits to access the random binary sequence. Moreover, we only use one quadrature of the signal here: the response amplitude. It could be advantageous to use both X and Y signal quadratures in order to multiply the bit-rate by two.

The use of two coupled membranes submitted to two modulated forces permits to reach chaotic regimes of both resonators. It implies they can both be exploited for the generation of random numbers. Moreover the synchronization dynamics that the normal mode responses experience lead to strong correlations between the two binary sequences. Such situation is of great interest for secure communication based on RNG [Liao et al., 2019]. In our data, we have observed up to 90% correlations between the sequences generated identically from mode $(-)$ and mode $(+)$ responses, i.e. with the same delay and sampling frequency. Unfortunately the too short experimental times traces do not permit to perform a robust statistical demonstration of randomness with our sequences. Nonetheless, we believe that the correlation is limited by imperfect phase synchronization and could be improved by setting the system in a perfect synchronization regime as numerically predicted (see section 6.3.5).

6.5 Conclusion

The experiments presented in this chapter all rely on the intrinsic nonlinearities of the two-coupled micromechanical nanomembranes. This phenomenon can be accurately modeled in the framework on the Duffing model. Using an amplitude modulation of the driving force, we show that a complex dynamics can be activated. The experimental bifurcation diagrams evidence period-doubling cascade route to chaos. Thanks to the calibrations developed in chapter 5, the dynamics is qualitatively and quantitatively reproduced numerically. The following experiment consist in driving both normal modes near their respective resonances. Thus the balanced energy injection enables the normal modes to couple via the Duffing nonlinearity. A simultaneous amplitude modulation of both forces highlight this orthogonality breaking mechanism. We investigate the synchronization of the normal modes amplitude and phase quadratures. In the chaotic regimes, the phase are imperfectly synchronize, which is subject of a statistical analysis. Finally we focus on the random number generation enabled by the observed chaotic dynamics. The synchronization of several random number generators in a key-aspect in several encryption protocols and the conciliation of chaos and synchronization, perfect synchronization predicted by our model, seems an interesting path towards this kind of applications. Overall this physical system is demonstrative of the ability of nano-systems to explore fundamental and ubiquitous concepts of nonlinear sciences.

Table of variables for Part II

Symbol : Meaning	Typical value (Units)
Electro-optomechanics platform geometry	
ℓ : coupling junction length	1.5 (μm)
w : coupling junction width	0.5-2 (μm)
a : IDE digit separation	3 (μm)
$\varnothing$: IDE digit width	1.5 (μm)
$\varnothing$: PhC membrane dimensions	10×20 (μm^2)
Coupled Duffing oscillators model	
$x_{A,B}$: displacement of membrane A,B	
$r_{A,B}$: response amplitude of membrane A,B	
$\vartheta_{A,B}$: response phase of membrane A,B	
$\Omega_{A,B}/2\pi$: natural frequency of membrane A,B	~ 2 (MHz)
$\omega_{A,B}/2\pi$: self-coupled frequency of membrane A,B	
$\Gamma_{A,B}/2\pi$: damping rate of membrane A,B	~ 4 (kHz)
G : bidirectionnal spring coupling between the resonators	
$F_{A,B}$: force applied on A,B	$\frac{1}{2}\frac{\partial C}{\partial x}V_{tot}^2$
$f_{A,B}$: amplitude of force applied on A,B	
$\omega_{\pm}/2\pi$: center frequency of normal mode $\pm$	
$\Gamma_{\pm}/2\pi$: damping rate of normal mode $\pm$	
β : Duffing mechanical nonlinearity	$(2\pi)^2 \times 6.71 \times 10^{-6}$ (MHz^2.nm^{-2})
for the normalized parameters, see table 6.1	
Experimental parameters	
electromechanical actuation	
$C(x)$: position-dependent electromechanical capacitance	$\lvert\frac{\partial C}{\partial x}\rvert \approx 2.2$ (μN.V^{-2})
V_{dc} : DC voltage	< 5 (V)
V_{ac} : AC voltage	< 5 (V)
$\omega_d/2\pi$: static voltage	$\sim \omega_{A,B}/2\pi$
V_p : modulation voltage	< 3 (V)
$\omega_p/2\pi$: modulation frequency	< 20 (kHz)
$V_{tot} = V_{dc} + V_{ac}\cos(\omega_d t) + V_p \cos(\omega_p t)$: total applied voltage	
$V_{\rm int}$: internal stress equivalent voltage	0.07 (V)
$V_{dc}^{\rm eff} = V_{dc} + V_{\rm int}$: effective DC voltage	
optomechanical readout	
λ : helium neon laser wavelength	633 (nm)
$P_{\rm in}$: incident laser intensity	~ 100 (μW)
L : Fabry-Pérot cavity length	380 (nm)
$\mathcal{G}/2\pi$: Fabry Pérot optomechanical coupling (theory)	1230 (GHz)
$Q_{\rm opt}$: Fabry Pérot optical quality factor	(10)

Symbol : Meaning	Typical value (Units)
signal demodulation scheme	
$R_{A,B}$: detected mechanical response amplitude of membrane A,B	
$\theta_{A,B}$: detected mechanical response phase of membrane A,B	
$\eta = R_B/r_B$: calibration constant	0.5 (mV.nm^{-1})
BW : demodulation bandwidth	
Bichromatic excitation scheme	
$\omega_d^{\pm}$: driving frequency near the resonance of mode $\pm$	
$V_{ac}^{\pm}$: AC voltage associated to $\omega_d^{\pm}$	
$R_B^{\pm}$: amplitude response of membrane B demodulated at $\omega_d^{\pm}$	
$\theta_B^{\pm}$: phase response of membrane B demodulated at $\omega_d^{\pm}$	
$X_B^{\pm}$, $Y_B^{\pm}$: quadratures' response of membrane B demodulated at $\omega_d^{\pm}$	
τ : phase synchronization duration	
$\langle\tau\rangle$: mean phase synchronization duration	
σ_τ : standard deviation of the phase synchronization duration	
RNG discussion	
f_s : bit sampling frequency	
τ : lag between the compared traces	

Chapter 7

Conclusion and perspectives

This research aimed to study the behaviors of coupled resonators, at the nanoscale, and using optomechanical or electromechanical systems. Relying on the knowledge acquired thanks to previous doctoral works for both cases, a new design has been proposed, fabricated and experimentally studied. In this conclusion, we summarized the main results of this work. Focusing on the benefits and limits offered on each side, we will extend the discussion with two perspectives interesting to explore. The first is the investigation of an integrated opto-electromechanical system. The second concerns the conception of arrays of nanomechanical resonators. In line with these novel systems of study, we conclude on few examples of experiments that could be carried out in the short to medium term.

7.1 Summary of the optomechanics experiments

In the first part of this thesis, the mechanical properties of a micro-membrane are investigated through a waveguide-coupled 2D photonic crystal molecule. In chapter 2, we describe how the optical resonances result from a coupling between two defect cavities. Thus, each mode corresponds to a specific electromagnetic field distribution spread over both defects. The respective cavity amplitude can not be experimentally observed as only the transmission waveguide is measured. It constitutes as indirect readout of the optical system. Using the coupled mode theory, a theoretical analysis of the system enables a full characterization of the waveguide transmission. This way, the frequency splittings are compared with FDTD simulations in the case of different geometries which yield a correct agreement.

By resonantly driving given optical mode, the mechanical noise spectrum of the suspended photonic crystal are characterized in chapter 3. The mechanical peaks have frequency and amplitude that depend on the detuning between the driving laser and the resonance spectral position. We find that the mechanical frequency shift is not strictly

speaking an optomechanical feature but a thermo-mechanical effect related to the cavity temperature increase caused by photo-thermal absorption. However, the mode amplitude is given by the dispersive and dissipative optomechanical couplings whose relative contribution are experimentally determined. Interestingly in this multimode optomechanical system, we show that a given mechanical mode can be dissipatively coupled to a first optical mode, but dispersively coupled to the second. Such configuration is presumably not exploitable in our system without a consequent improvement on the optical quality factors. Generally speaking this aspect constitutes the main limit to the study of singular optomechanical effects. It also probably explains why the L3-defect confined mechanical modes, expected in the GHz domain, could not be observed in this thesis.

Despite these limitations, the system provides an engaging platform for nonlinear dynamics experiments. By using a periodic modulation on the input laser field, we observe replica of the mechanical resonance in the noise spectrum (chapter 4). The optomechanical sidebands have balanced low-amplitudes for weak input power, as predicted by the theory. For higher input power, the thermo-optic nonlinearity comes with higher-imbalanced sidebands amplitudes. The experimental results are qualitatively understood from the adapted model. As the thermo-optic effect also leads to bistability of the optical resonance, we finally perform an experimental demonstration of vibrational resonance amplification. Here, the mechanical domain is only exploited for the bistable system characterization.

7.2 Summary of the electromechanics experiments

The second part of the thesis focuses on a pair of coupled electro-optomechanical cavities. This system turns out to be an ideal platform for the study of driven coupled resonators. The motion of these latter can be independently measured by probing the optical Fabry-Pérot cavity available under each membrane. The optical properties of these optomechanical cavities are far from providing the displacement sensitivity enabled by the 2D photonic crystal cavities studied in the first part. Nonetheless, it enables an efficient read-out of the membranes displacement under resonant excitation. In addition, this cavity offers a straightforward mean to transfer mechanical features to the optical domain. Here, contrary to the study of the waveguide-coupled photonic molecules, the mechanical normal modes are studied through a direct observation. In chapter 5, the mechanical properties, including the frequencies, the dissipative damping and the mechanical coupling, are experimentally characterized via a simple model of driven coupled harmonic oscillators. We highlight the importance of the natural frequency mismatch on the coupling. Contrary to the photonic molecule where the cavities can be considered as identical, the disorder in the mechanical frequencies must be taken into account

and can not necessarily be artificially compensated if the mismatch is too important. With reasonable mismatch (typically of 5% or less), it is often possible to use either a photothermal absorption technique or a dielectric tuning technique to tune the natural frequencies. The characterization in the linear regime is achieved by the calibration of the membranes' displacement and the applied force.

The chapter 6 focuses on the nonlinear dynamics arising from a strong electrocapacitive drive. Relying on the Duffing model, we model the nonlinear response of the system. As an echo to the optomechanics experiment, we show the effect of amplitude modulation applied to the driving resonant force. Here the system displays a period-doubling route to chaos structure with both the modulation amplitude and frequency. Thanks to the force calibration, the model numerical resolution yields a very good agreement. This dynamics can be generated by driving one of the two mechanical normal modes. By injecting a modes in its nonlinear regime, the initial orthogonality is broken such that the other mode can be excited. We use a bichromatic scheme to drive both modes such that a bidirectional nonlinear coupling is established between the modes. Through this mechanism, their responses synchronize. The synchronization of chaotic systems is a really peculiar phenomenon gathering two fundamental concepts. Most of the experimental demonstrations have been performed on electrical circuits or macroscopic lasers. Our work therefore constitutes the first study of chaos synchronization at the nanoscale. Finally, in order to exploit this dynamics, we apply a protocol of random bit generation to the experimental chaotic time traces. For this purpose, the exploration of perfect phase synchronization regime, that are predicted by the numerical simulations, might be relevant.

7.3 New generation of devices

This thesis deals with two systems that share at the same time many similarities and important conceptual differences. Now the idea is to propose novel systems based on the present designs, such that it would not imply an important effort on the nanofabrication. At first, we focus on an electro-optomechanical system enclosing both the integrated SOI waveguide and the IDEs. Secondly, we discuss the generalization from two coupled resonators to larger arrays. In both cases, the designs have been established and fabricated.

7.3.1 Nano-opto-electromechanical platform

The association of a sensitive optomechanical cavity with an electro-capacitive transducer on the same micromechanical resonator is a stimulating choice for the next generation of designs [Midolo et al., 2018]. Indeed, the introduction of the waveguide-accessed photonic

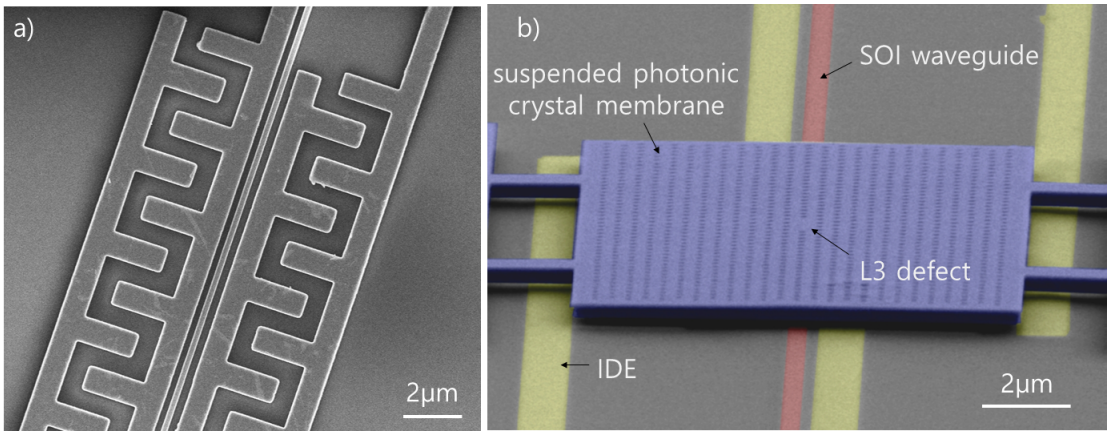

Figure 7.1 – a) SEM image of the gold IDE surrounding the SOI waveguide before the BCB bonding of the InP layer. b) colorized SEM image of the fully integrated electro-optomechanical platform.

crystal cavity enables a much lower displacement sensitivity. In fact, it would allow not only to probe the mechanical displacement under resonant electrostatic excitation, but also the Brownian noise of the membrane. On the other side, the motion can be resonantly driven with the electro-capacitive actuation. New nonlinear regimes are expected when the strongly driven mechanics couples with the optical cavity field [Olga, 2017; Jin et al., 2017; Wang et al., 2016].

In terms of fabrication, the main challenge to be answered is the compatibility of the SOI waveguide and the gold electrical lines below the same micro-membrane. In particular, the need of a straight SOI waveguide below the photonic crystal implies a change of design for the interdigitated electrodes. The chosen solution consists in the use of two pairs of IDE on both sides of the waveguide (see fig. 7.1a). In the course of this thesis, we have converged towards a reproducible fabrication protocol for the nano-opto-electro-mechanical system. We show a colorized SEM image in fig. 7.1b. Nonetheless the structure has not been investigated yet because the gold electrical line have been designed too close from the optical waveguide. Therefore the injected laser field is completely absorbed such that no transmission is observed. This problem can be easily overcome by increasing the electrical line to optical waveguide distance over 4 µm. If, the meantime, the optical quality factors of the L3 defect cavities can be improved, the resulting device would provide an extremely versatile testbed for electro-optomechanics experiments.

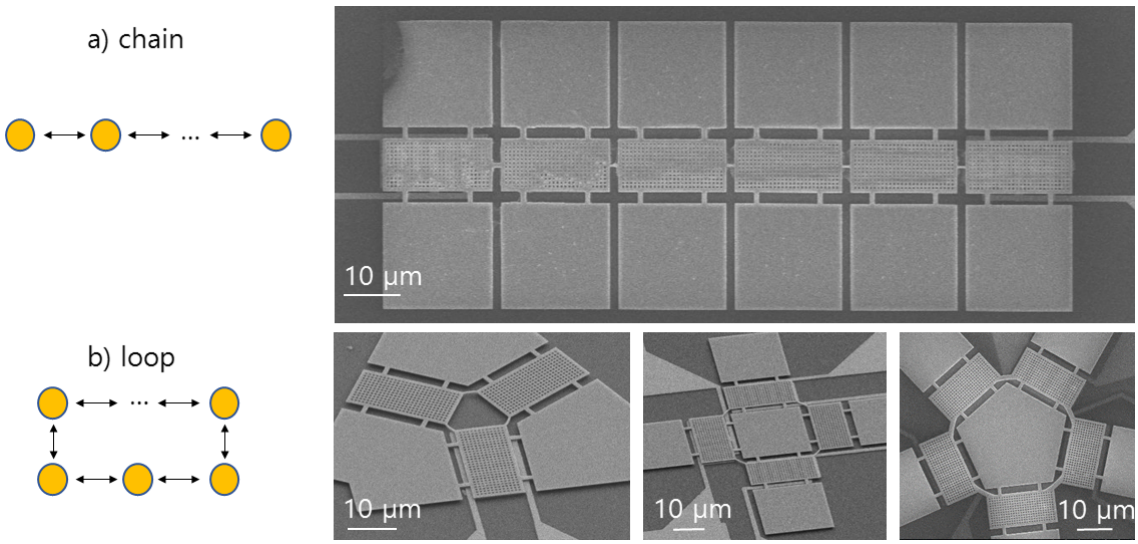

Figure 7.2 – SEM images of the coupled nanomechanical resonator arrays proposed for future collective dynamics experiments. As schematized on the left, each resonator (colored disk) is coupled (arrow) to its closest neighbors. Thus the 1D array can be a chain (a) or a loop (b).

7.3.2 Array of coupled resonators

The transfer from macro to nano-scaled resonators is very convenient at many levels. Obviously nano-devices present numerous interests for technological applications: compactness, low energy-consumption, high frequency operations, etc. But they also naturally provide a large variety of properties through which fundamental physics can be tested. The case of optomechanics is particularly indicative since the coupling mechanism itself relies on the low mass of the nanomechanical resonators. Another extraordinary advantage of working at the micro or nanoscale is the possibility to reproduce a large number of nearly-identical elements in a small area. As soon as these elements are designed in order to interact with each other, it becomes possible to study the collective dynamics of the overall system. Interestingly, this field can be studied at different levels of natural sciences e.g. in sociology [Strogatz et al., 2005; Moussaid et al., 2009] or biology [Coffey, 1998]. In the particular case of oscillators array, the collective dynamics can be modeled with the Kuramoto model. This latter was introduced in the context of chemical oscillations [Kuramoto and Yamada, 1976] but was found fruitful in many other contexts [Acebrón et al., 2005] including with nanomechanical systems [Matheny et al., 2019]. In these systems, the topological aspect of the coupling distribution strongly influence on the synchronization dynamics of the array.

As a continuation of this work, we design new geometries where 3 to 10 nanomembranes are mechanically coupled into an array. In these 1D arrays, the membranes can

communicate with their nearest neighbors in two topological configurations. In fig. 7.2a, the array is a chain where both extremities are possibly driven with integrated electrodes. Such chains of driven Duffing oscillators have recently been proposed as interesting candidates for the observation of chimera states [Clerc et al., 2018]. In fig. 7.2b, the membranes are coupled in a loop and only few of them can be driven. These small arrays might be an ideal platform of study halfway between two coupled resonators and large arrays, where individual properties are fully statistically diluted.

7.4 Physics in perspective

Now that novel designs are proposed, what physics could be interesting to study ? We end this thesis with few perspectives that lie in the continuity of the present research. We gather these suggestions in two groups. One contains applications of signal processing or metrology using chaos in bistable resonators. The second concerns the study of coupled resonators – possibly in large arrays – in which the coupling itself might be controlled.

7.4.1 Taking advantage of chaos

The perspective of a fully integrated electro-optomechanical platform opens the way to efficient transduction from an electrical signal to the optical field via the mechanical motion. Moreover the resonance of both the photonic crystal microcavity and of the mechanical membrane can be driven in bistable regimes. For these two reasons among others this novel system is versatile and can probably help to perform a given operation in several manners. As an example, we have seen that vibrational resonance amplification can be achieved optically in a photonic molecule, but similar results were also obtained using an electrically driven mechanical resonator [Chowdhury et al., 2020]. Similarly we could expect chaos to emerge from a nonlinear optical resonator under an amplitude modulation of the drive, as it was described with our electromechanical systems. Actually the Duffing model that set the frame of this dynamics has an equivalent in photonics, generally refereed as the Kerr model. Interestingly, if the mechanism behind chaotic dynamics in a modulated Kerr resonator would be the same, the dynamics timescale would however be much lower. Beside the interest of this electro-optomechanical system for the novel physics mentioned previously, it also gives the opportunity to perform different type of signal processing operation within the same system. A basic example is given in fig. 7.3a. Here, a first nonlinear resonator is used to generate random bits by modulating its input field, and a second is exploited to amplify the random bit sequence. Assuming that the first operation is obtained by electro-capacitive modulation, the mechanical displacement is therefore encrypted in the optical microcavity and can be amplified by vibrational (or stochastic) resonance via a Kerr-type nonlinearity. Generalizing such chain

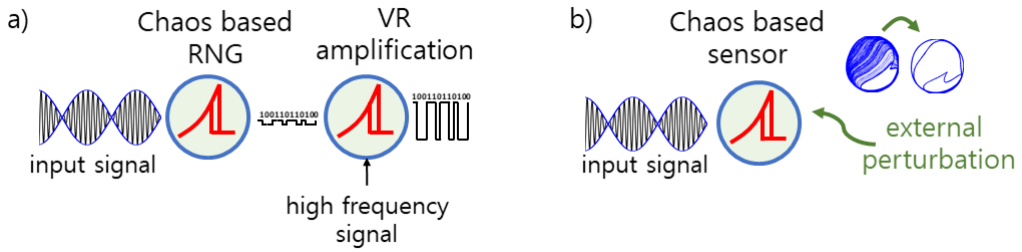

Figure 7.3 – a) Bistabilities have proven useful for several applications e.g. here vibrational resonance (VR) amplification or random number generation (RNG). Here we propose to perform several operations in a row on nonlinear resonators of possibly different nature. b) Set near a crisis, the system experience a sudden change of its dynamics under small external perturbation, thus enabling sensing experiments to be performed.

of operation in multimode systems, such as coupled or array of oscillators, opens the path to multispectral encryption protocols [Argyris et al., 2005; Annovazzi-Lodi et al., 1996; Mirasso et al., 1996; Cuomo et al., 1993].

In our electromechanical system, the chaotic dynamics emerge via a period doubling cascade. However the following bifurcations can also separate a chaotic dynamics from a simple limit cycle regime. These abrupt bifurcations, or crisis, are very sensitive to any perturbation of the system. Relying on this observation, the perspective of chaos based sensing emerges. In such experiment, depicted in fig. 7.3b, the system is preliminary stabilized in a given regime, e.g. chaotic in this schematic, and then submitted to external perturbation. For example we have notice that a tiny modification of the probe laser intensity – inducing a mechanical frequency shift of only few Hertz – is enough to pass a bifurcation point and dive the system in a different dynamics. This proposal therefore consists in using chaos in an electro-optomechanical system for metrology applications [Fiderer and Braun, 2018].

7.4.2 Control of the coupling

In coupled oscillators, the experimental control of the subsystems intrinsic properties can be extremely useful. Unfortunately it is generally hard to achieve as these parameters are usually set by the material properties or by the geometry. In the electromechanical systems, we have shown how the membranes natural frequencies can be controlled by induced an additional internal stress either with a photo-thermal absorption process or via an applied electrical field. Such control reveals extremely useful in the exploration of exceptional points [Miri and Alù, 2019]. These singularities of the parameter space of coupled oscillator, are found when the system eigenvalues coalesce. Physically, this occurs when the loss and the gain of the system equalize. Several interesting features are

expected near these exceptional points, e.g. in metrology [Wiersig, 2014], chiral mode conversion [Peng et al., 2016] or multimode laser cavities [Miri et al., 2012]. As the characterization and exploitation of an exceptional point relies on the fine control of either loss or gain in the system, we propose two mechanisms through which the coupling between two resonators can be continuously modified. They are both schematically represented in fig. 7.4a. First (i) we consider two electromechanical membranes A and B simultaneously probed with independent laser beams. Each converted optical response can then be amplified and injected in the opposite structure electromechanical actuator. Thus the resonators and both driven by the opposite subsystem. Here the coupling – which not necessarily balanced – can be fully controlled through the amplification gain ($\eta_{A,B}$ and $\eta_{B,A}$). The second proposal (ii) has already been discussed in section 2.5. We have indeed described how the phase shift experienced by the circulating light between two optical resonators leads to both energy and loss splitting. This phase shift is not easily tunable in integrated photonic circuits. The control of the phase shift could be obtained through a phase modulator placed between the resonators.

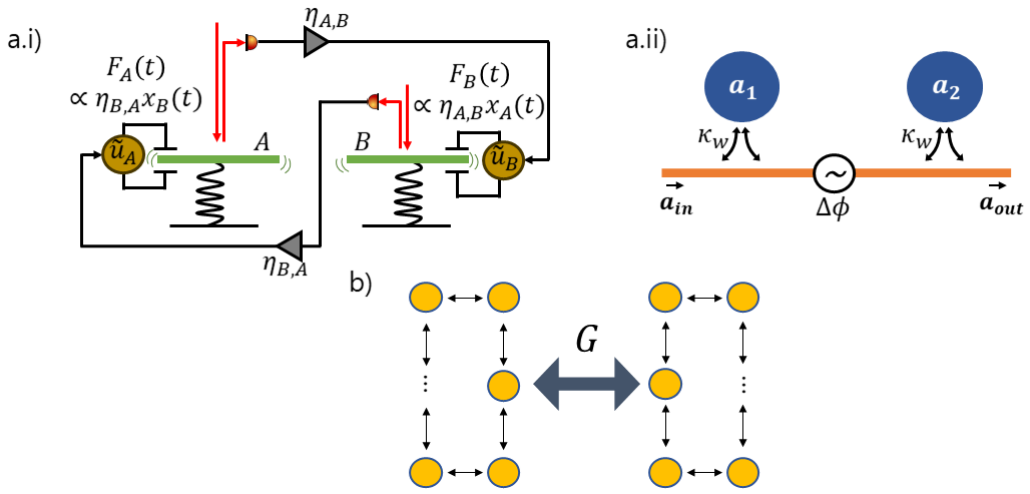

Figure 7.4 – a) Coupling control examples: i) In coupled electromechanical systems,each resonator is forced with the response of the other. The amplification gains $\eta_{A,B}$ and $\eta_{B,A}$ respectively determine the influence from A to B and from B to A. ii) The optical coupling between two optomechanical oscillators is controlled via a phase shifter. b) The coupling control (G) between two arrays of identical resonators (yellow disks) has a strong impact on the subsystems dynamics.

The control of coupling can also be useful in the context of the oscillator arrays that were discussed previously. For example in the investigation of synchronization patterns formation [Lauter et al., 2015] or chimera states [Pelka et al., 2020] using optomechanical systems, the Kuramoto dynamics strongly depends on the coupling. The previous examples

for coupling control could be applied not between resonators but between two arrays as depicted with the schematic in fig. 7.4b. Here the oscillators could be either optical, mechanical or optomechanical objects.

Appendix A

Larger 2D photonic crystal molecules

The photonic molecules presented in section 2.1.2 are made of two L3 defects inserted in a 2D photonic crystal (PhC) membrane. Such bi-directional arrangement of the refractive index is conductive to the study of coupled resonators in different coupling topologies. By using only two cavities, different geometries can be studied as soon as the integrated waveguide is added to the system, since the positions of the cavities regarding this latter can result in asymmetrical designs. Then the indirect coupling processes happening through the waveguide can be exploited. Considering only the direct couplings[1], the full potential of 2D PhC is however not fully exploited with only cavities. Indeed, with more than two cavities, it is possible to set a more complex topology of coupling in which the cavities are not only coupled to their nearest neighbors. For examples the cavities can be coupled in a circle such that each cavity couples to two others. They can also be coupled in a row, such that the ends cavities couple only with one cavity. This difference results in the degeneracy of several eigenmodes. For example, in a four-cavities molecule, the normal mode frequencies are given by the eigenvalues of the following matrices, respectively for the "row" and the "loop" configurations:

$$M^{(4)}_{\text{row}} = \begin{pmatrix} \omega_0 & \mu & 0 & 0 \\ \mu & \omega_0 & \mu & 0 \\ 0 & \mu & \omega_0 & \mu \\ 0 & 0 & \mu & \omega_0 \end{pmatrix} \qquad M^{(4)}_{\text{loop}} = \begin{pmatrix} \omega_0 & \mu & 0 & \mu \\ \mu & \omega_0 & \mu & 0 \\ 0 & \mu & \omega_0 & \mu \\ \mu & 0 & \mu & \omega_0 \end{pmatrix} \tag{A.1}$$

The cavities have identical frequency ω_0 and are coupled to their neighbors with a strength μ. Here the matrix $M^{(4)}_{\text{row}}$ has four distinct eigenvalues $\omega_1 = \omega_0 - \frac{\sqrt{5}+1}{2}\mu$, $\omega_2 = \omega_0 - \frac{\sqrt{5}-1}{2}\mu$, $\omega_3 = \omega_0 + \frac{\sqrt{5}-1}{2}\mu$ and $\omega_4 = \omega_0 + \frac{\sqrt{5}+1}{2}\mu$ while the matrix $M^{(4)}_{\text{loop}}$ has only three $\omega_1 = \omega_0 - 2\mu$, $\omega_2 = \omega_3 = \omega_0$ and $\omega_4 = \omega_0 + 2\mu$. Considering now the fact that a cavity might be able to couple also with the non-neighboring cavities of adding

[1] The "direct coupling" refers to the evanescent coupling occuring within the PhC, between the cavities.

the indirect coupling introduced by the integrated waveguide to the model, one can see how these new configurations are more complex to model.

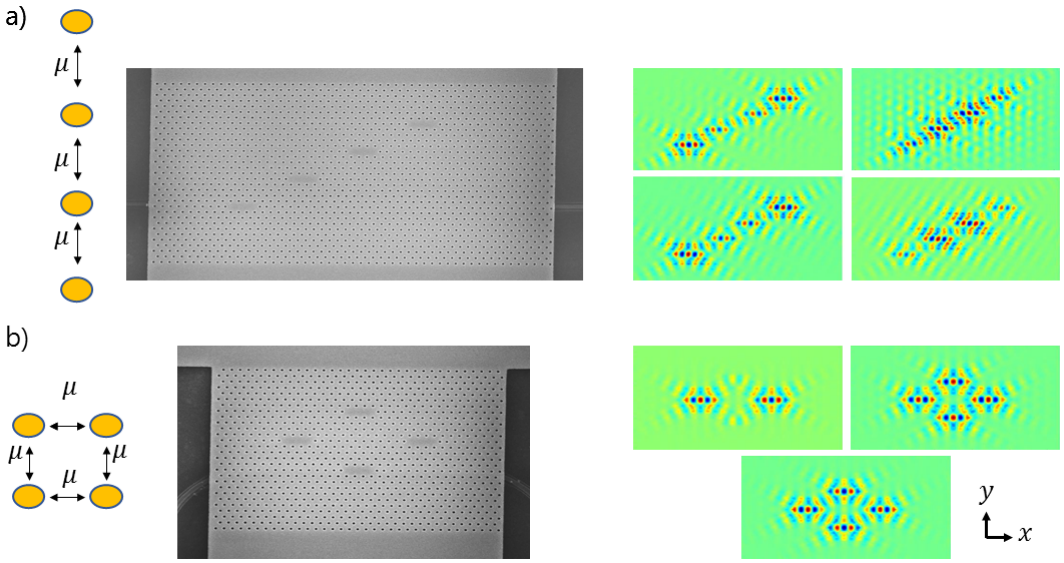

Figure A.1 – a) 4D4 photonic molecules: four cavities are coupled diagonally in a row configuration, schematically described on the left. b) 4R4 photonic molecules: four cavities are coupled diagonally in a loop configuration. For each case on the right: FDTD simulation of the photonic eigenmodes electric field y component distribution.

These bigger photonic molecules are designed in line with the diatomic molecules presented previously. We show two examples corresponding respectively to the "row" configuration in fig. A.1a with the SEM image of a 4D4 structure. Here, the four cavities are diagonally spaced by 4 lines of holes. On the right, we show the electric field y component distribution corresponding to the four photonic eigenmodes found with FDTD simulations. Each mode has its own symmetry. The "loop" configuration is shown in fig. A.1b with four cavities diagonally coupled to their neighbors such that the direct coupling between two adjacent cavities are presumably equal. Only three eigenmodes are found in the FDTD simulations are discussed above and here again, each mode has its own symmetry. More designs have been fabricated, introducing three or four cavities in the molecules, with different coupling geometries: vertical, horizontal, diagonal or circular, and different cavity-to-cavity separations.

Appendix B

Indirect optomechanical readout

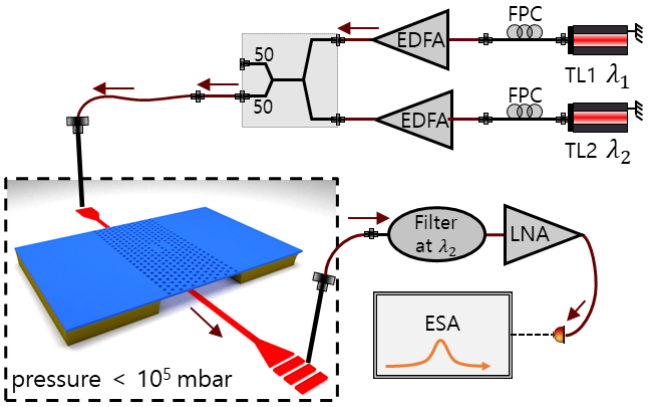

Figure B.1 – Experimental setup including a second tunable laser (TL). The TL1 is used for scanning a given optical mode while the TL2 probes the mechanical mode at fixed wavelength near the other optical mode resonance. The TL1 is filtered out as only the TL2 is used for the readout of the mechanical noise spectrum.

The following measurement are made in the continuation of the experiments detailed in section 3.3. In this section we discuss the influence of the laser frequency, or detuning on the noise power at the mechanical resonance. By relating the evolution of this amplitude to the partial derivative of the optical transmission as a function of the frequency, we extract the dissipative and dispersive optomechanical contributions. To do so only one optical mode was used for a given measurement of the mechanical noise spectrum. Here we propose to use a first tunable laser to scan an optical resonance while a second laser has a fixed detuning near the second optical resonance. Thus the mechanical mode is read through the second laser but is submitted to the influence of the change in the 1st laser detuning. The second laser (TL2) in added to the experimental setup and amplified with a second EDFA (see fig. B.1. The laser field are both injected in the waveguide using the inection fiber and 50/50 fiber coupler. At the output, both fields are collected

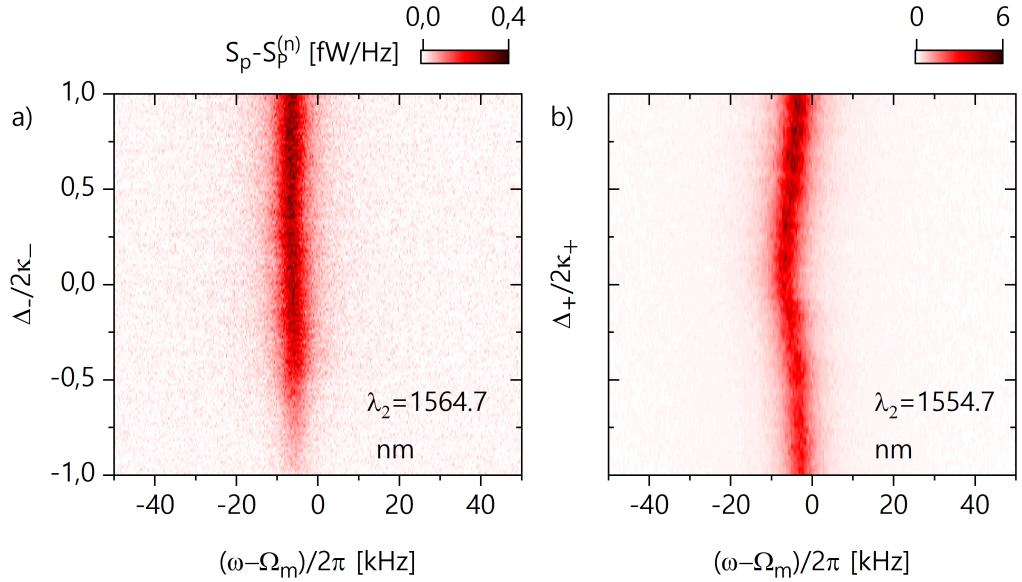

Figure B.2 – Mechanical noise spectrum at fundamental resonance as a function of the relative detuning a) from the $(-)$ optical resonance and b) from the $(+)$ optical resonance. The readout is performed through a second laser probing the opposite normal mode in each configuration. In the probe laser has a wavelength a) $\lambda = 1554.7$ nm and b) $\lambda = 1564.7$ nm

but only the TL2-field is kept for the the photodetector by filtering out the TL1-field.

At first, the TL1 is used to scan the optical mode $(-)$ while the TL2 has fixed wavelength $\lambda_2 = 1564.7$ nm such that the fundamental mechanical mode has an maximum amplitude. The reduced noise amplitude is plotted in a colormap in fig. B.2a. The mechanical peak amplitude is determined by the relative detuning of the probe laser (TL1) that is fixed here. Therefore, the amplitude is quite constant along the map. The mechanical frequency is shifted from the zero-power resonance frequency by an offset but stays also constant. This indicates that the thermo-mechanical shift is dominated by the field stored at the probe wavelength λ_2. On the other hand in the opposite situation - when the TL1 scans the optical mode $(+)$ while the noise spectrum is recorded via the TL2 with $\lambda = 1664.7$ nm (see fig. B.2b)- the mechanical frequency follows a shift that is proportional to the cavity energy as the thermo-mechanical effect is now dominated by the load in the optical mode being scanned.

These types of measurement, although interesting for the exploration of many concepts in multi-mode optomechanics [Malz and Nunnenkamp, 2016], have revealed to be particularly complicated to achieve. The main experimental issue is the overload at the waveguide input fiber that tends to twist when the input power passes a certain threshold. It is probable that a stabilization of these fibers could help for performing stable

and reproducible mechanical characterization via a 2-laser drive method.

Appendix C

Chaotic traces analysis: technical tools

This part is meant to introduce some tools that will be useful to deal with our experimental time traces and investigate the dynamical regimes in which our system settles. We discuss the representation of the system trajectories in the phase space and how a Poincaré crossection can be built from a time trace, and how chaos can be identified with the largest Lyapunov exponents.

i Measured data The lockin-amplifier outputs the phase quadratures of the demodulated signal $X(t)$ and $Y(t)$ as well as the time vector t. Physically, let's recall here that $X(t) = R(t)\cos\theta(t)$ and $Y(t) = R(t)\sin\theta(t)$ where $R(t)$ refer to the amplitude of the detected signal, which is proportional to the probed resonator amplitude. $\theta(t)$ is the phase between the probed resonator and a reference clock that is set by the driving force, i.e. by the lockin-amplifier.

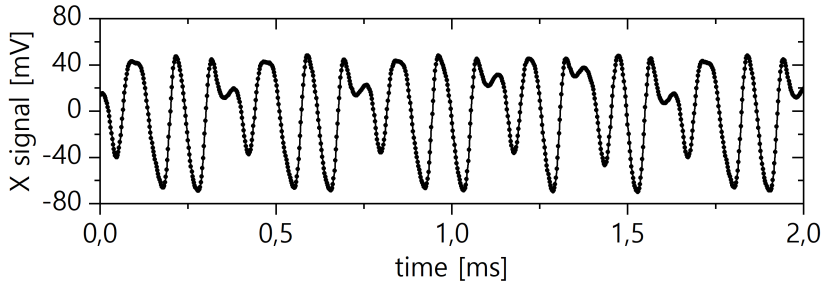

Figure C.1 – example of experimental time trace $X(t)$ recorded over 2 ms.

Since we dispose a discrete flow of data, it will be more convenient in this section to use the time vector in units of the time resolution dt rather than in physical units.

ii Delay embedding phase space reconstruction It is possible, under certain conditions, to reconstruct the full phase space of a d dimensions deterministic dynamical system from the observation of a single component of this phase space. This is the Takens's theorem and this method is the time-embedding phase space reconstruction [Packard et al., 1980]. The method is the following: with one time trace (line-vector) $X(t)$ that is measured, the following matrix can be built:

$$\overrightarrow{S}(t) = \begin{pmatrix} x_0(t) \\ x_1(t) \\ \dots \\ x_{d-1}(t) \end{pmatrix} \quad \text{with} \quad x_k(t) = X(t + k\tau) \tag{C.1}$$

The embedding delay τ choice is described later. $\overrightarrow{S}(t)$ is the delay-embedding the signal $X(t)$. Experimentally, we only have a limited number of uniformly time distributed samples. The reconstruction of the delay-embedding will cost at least $(d-1)\tau$ data points so that all traces $s_k(t)$ have the same length. Note also that it is necessary for the observed component to be coupled with the other components in order to apply the Takens's theorem.

iii Phase portrait and choice of τ It is convenient to plot a projection of trajectory on 2 or 3 dimensions. It often gives a qualitative feeling of the dynamics of the system. After proceeding the reconstruction of the phase space, one can easily draw a parametric plot $\{x_1(t), x_2(t), x_3(t)\}$. The choice of τ is not submitted to a general method. It is often found in the literature that the optimal τ corresponds to the first zero of the auto-correlation function of the signal $X(t)$. It is also interesting to plot the phase portrait for different values of τ and to observe the trajectory amplitude getting distorted. Increasing τ, the trajectory is first appearing with a wider angle, which makes its reading easier. Then the distortion gets too important and the trajectory becomes messy, even for a simple limit cycle. In fig. C.2, the 3D phase portrait of the time trace plotted before in fig. C.1 is given for different delay τ.

iv Poincaré section By observing a single component of a d dimensional dynamical system, the full phase-space can be reconstructed using time embedding. A phase portrait is a representation of the trajectory of a system in the phase space. for $d > 3$, the phase portrait has to be projected on 2 or 3 dimensions but the flow of data will be fully observed with such a plot. In the case of chaotic behavior, the time flow data are not the best suited for graphical representation. Indeed, one might have to plot data over large time to illustrate the dynamics, which will unavoidably overload the figure. Another representation mean is the Poincaré section. It consists in the intersection of a $(d-1)$-dimensional hyperplane with the in-time trajectory in the d-dimensional

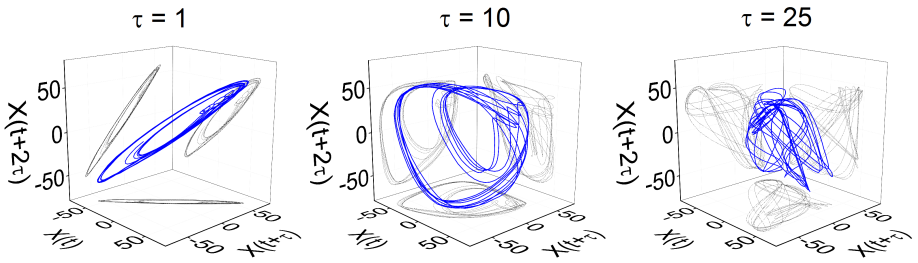

Figure C.2 – 3D phase portrait plotted using $x_1(t)$, $x_2(t)$ and $x_3(t)$ (blue) and its projections over the (xy), (xz) and (yz) planes (gray dashed).

embedding space. The choice of this hyperplane is arbitrary, but in practice one need to choose wisely both the intersection and the orientation of the trajectory in order to obtain a useful Poincaré section. In the context of chaotic systems, the mathematical limit of the Poincaré section for an infinite number of points is called an attractor.

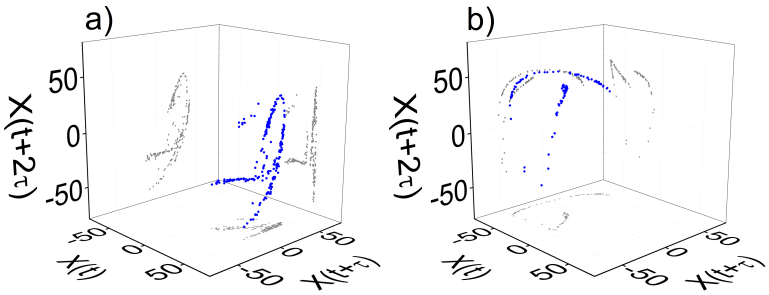

Figure C.3 – Poincaré section in 3d (blue) and its projections in 2D on the (xy), (xz) and (yz) planes (gray dots). a) using the maxima of $X(t)$. b) using a stroboscopic picture at $\omega_p = 8$ kHz.

v Contruction from extrema Usually, our Poincaré section will be built by taking the maxima of $X(t)$ (see fig. C.3). This means that we choose the plane ($\dot{X}$=0). The minima are not kept. This method is very sensitive to noise which can generate additional extrema in the signal. In some cases, the obtained plot can be unsatisfying, because the points are accumulated in a narrow surface of the subspace. This can be fixed by changing the orientation of the phase space. For example, if 2 time traces $x(t)$ and $y(t)$ are used to evaluate the Poincaré section of a system based on the maxima of $x(t)$, the following transformation can be tried:

$$\begin{aligned} x_r(t) &= x\cos(\phi) + y\sin(\phi) \\ y_r(t) &= -x\sin(\phi) + y\cos(\phi) \end{aligned} \tag{C.2}$$

Maybe for a properly picked angle $\phi \in [0, 2\pi]$, it is possible to maximize the occupied surface in the Poincaré map. A Poincarré section can also be built from the delays separating periodic pulses in the context of biology for example [Hegger and Kantz, 1997].

vi Contruction from a stroboscopic poll It is also current, in the context of periodically driven non autonomous oscillators, to built a Poincaré section from a stroboscopic picture of the phase space. In principle, it is quite straight forward: the Poincaré map is built from all points $\{x_1(t_0+p\Delta t, x_2(t_0+p\Delta t, ...\}$. Here Δt is the driving period and p in an integer that can be as large as possible. t_0 can be chosen arbitrarily but, here again, it must be carefully chosen for a better readability. In analogy with the orientation of the phase space when the extrema are picked to draw a map, the instant t_0 must be chosen so that the variance of the Poincaré section along the different axis of the subspace is maximized.

vii Lyapunov exponent and neighbor trajectories The Lyapunov exponent quantifies the divergence rate between two close trajectories of a dynamical system [Mawhin, 2005]. It is a straightforward mean of diagnosing chaos. Chaos emerge from deterministic dynamical systems whose high sensitivity to initial conditions makes unpredictable with a finite computing memory. In a chaotic regime, two close trajectories will exponentially diverge with time. Let's consider two trajectories $\overrightarrow{S}(t)$ and $\overrightarrow{S'}(t)$ in a d-dimensionnal phase space. The error function is defined as[1]:

$$\delta(t) = ||\overrightarrow{S'}(t) - \overrightarrow{S}(t)|| \tag{C.3}$$

Assuming that initially $\overrightarrow{S'}(0) - \overrightarrow{S}(0)$ is an infinitesimal d-sphere, the error function will grow exponentially in the i^{th} dimension as $10^{\lambda_i t}$ leading to a d-ellipsoid at instant $t > 0$. The λ_i are the Lyapunov exponents ordered in descending order and can be interpreted as the divergence rate of the i^{th} component. Therefore the largest Lyapunov exponent is λ_1 and and is given by:

$$\lambda_1 = \lim_{t\to\infty} \frac{1}{t} \log_{10}\left(\frac{||\delta(t)||}{||\delta(0)||}\right) \tag{C.4}$$

The positivity of λ_1 implies a chaotic dynamics. This expression relies two mathematical limits: $t \to \infty$ and $\delta_0 \to 0$. Therefore, this formula can not be applied to finite experimental data. However, this problem has been widely discussed in the literature and several algorithms have been presented [Wolf et al., 1985; Rosenstein et al., 1993; Eckmann et al., 1986; Sano and Sawada, 1985].

[1] $||\cdot||$ is the 2-norm: $||\overrightarrow{r}|| = (\sum_{i=1}^{d} r_i^2)^{1/2}$

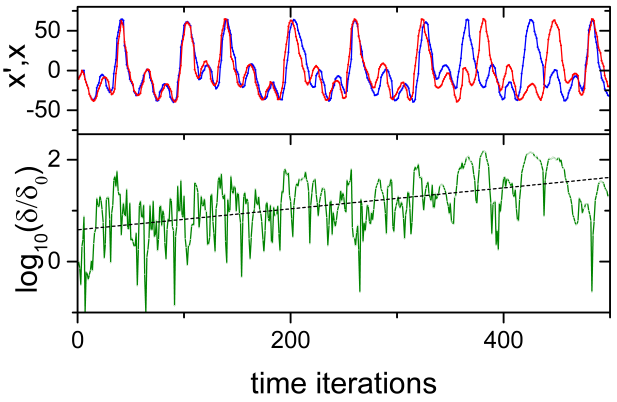

Figure C.4 – After finding t_0 so that $X(t_0)$ is the closest neighbor of $X(0)$ in a 3D reconstructed phase space. $X(t)$ (red) and $X(t_0+t)$ (blue) are plotted as well as the associated exponentially growing error function.

viii Numerical computation of the Largest Lyapunov Exponent (LLE) We use the TISEAN package [Hegger et al., 1999] which is a software project based on C/FORTRAN routines allowing time series analysis. Basically, this routine finds the closest neighbors of each point and outputs the delay and the associated logarithm of the averaged error functions. After a transient time, the trajectories are oriented in the most unstable directions, and this logarithm shows a linear variation. The slope is the LLE. The detailed method for Lyapunov exponent estimations using this package is presented in [Kantz, 1994].

ix Find closest neighbors Given an instant t_0 and the trajectory $\overrightarrow{S}$ in the d-dimensional phase space, one seeks for all the instant t_k such as $||\overrightarrow{S}(t_k) - \overrightarrow{S}(t_0)|| < \varepsilon$. ε is chosen arbitrarily and defines a small hypersphere centered in $\overrightarrow{S}(t_0)$ and containing all its closest neighbors $\overrightarrow{S}(t_k)$. The error function $\delta_k(t) = ||\overrightarrow{S}(t_0+t) - \overrightarrow{S}(t_k+t)||$ can be plotted for $t > 0$. An exponential growth of δ_k can be checked as shown in fig. C.4. This trace is therefore chaotic.

Résumé en français

L'optomécanique traite de l'interaction entre un résonateur mécanique et une cavité optique. L'utilisation de ces deux composantes à l'échelle nanométrique permet d'exalter les interactions lumière-matière qui s'y manifestent. Les résonateurs optomécaniques permettent, entre autres, d'accéder avec une grande sensbilité aux modes de vibrations de la structure mécanique. Il est également possible de manipuler un résonateur nanomécanique en le couplant à un dispositif d'actuation électrique. Cette approche, l'électromécanique, est d'ores et déjà largement exploitée dans l'industrie des MEMS (*Micro Electro-Mechanical Systems*), notamment pour des fonctions de métrologie dans des systèmes embarqués, smartphones, etc. Ce domaine de recherche reste néanmoins très actif avec le développement de systèmes à complexité croissante.

Parmi les nombreux défis émergeant dans la communauté ces dernières années, l'intégration d'un grand nombre de systèmes opto-électromécanique couplés les uns aux autres en réseaux est prometteuse. Dans cette optique, il s'agit d'abord de bien comprendre les mécanismes sous-jacents à l'interaction entre deux systèmes couplés. C'est dans ce cadre que s'incrit ce travail de thèse. Deux approches sont étudiées. Dans les deux cas, nous bénéficieront de la versatilité des cristaux photoniques. Ces structurations périodiques de l'indice de réfraction d'un matériau permettent de guider la lumière à l'échelle nanométrique avec une grande précision. La première approche consiste en l'étude d'une plateforme optomécanique d'InP (phosphure d'indium) à cristal photonique (voir fig. 7.6a). Ce dernier comporte deux microcavités optiques dont les modes photoniques localisés peuvent être sondés à l'aide d'un laser injecté dans un guide de silicium intégré sous la membrane, permettant ainsi d'accéder au mouvement brownien du cristal photonique suspendu (voir fig. 7.8a). La deuxième approche consiste à coupler mécaniquement deux nano-membranes électromécaniques par l'intermédiaire d'une jonction nanométrique (voir fig. 7.6b). Chaque membrane peut être excitée électrocapacitivement de façon indépendante par l'intermédiaire de deux paires d'électrodes inter-digitées placées sous les membranes.

Pour chacun de ces systèmes, il est possible d'en étudier la dynamique sous l'effet d'une excitation modulée par un signal harmonique. Dans le cas du système optomécanique, le laser incident est modulé à l'aide d'un modulateur électro-optique en intensité.

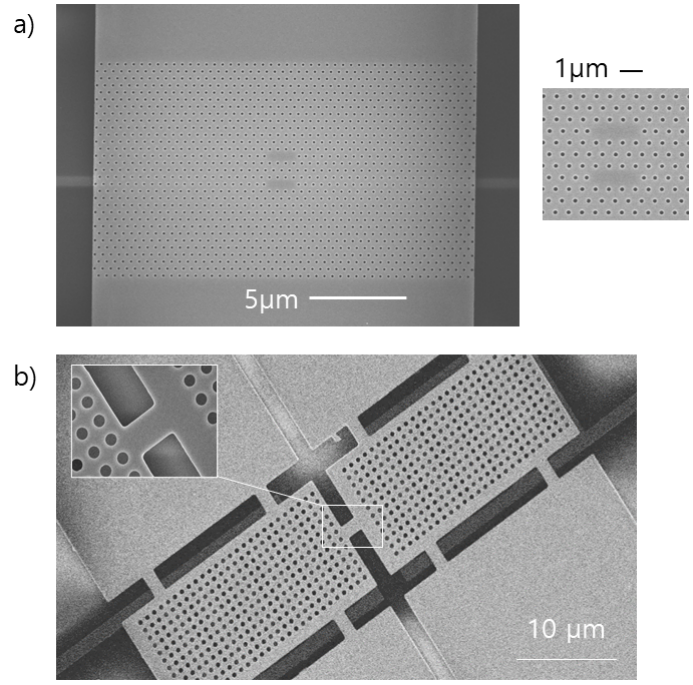

Figure 7.5 – Images de microscopie électronique à balayage des deux systèmes étudiés. a) plateforme optomécanique comportant le cristal photonique suspendu et le guide de silicium intégré passant sous la structure. La géométrie des microcavités optiques est montrée à doite. b) Les deux membranes couplées par une jonction mécanique (voir le zoom). On distingue les paires d'électrodes inter-digitées.

L'interaction entre le laser modulé et le résonateur mécanique peut être modélisée par une dynamique de Floquet. Le modèle prédit alors le transfert du peigne de modulation depuis le domaine optique vers les fréquences des modes mécaniques. Des bandes de modulation sont ainsi observées autour de chaque mode mécanique (voir fig. 7.8b). La présence de nonlinéarités thermo-optiques dans le matériau complexifie cette intéraction lorsque la puissance du laser incident est augmentée. En particulier, les bandes de modulation se retrouvent dissymmétrisées (voir fig. 7.8c). La gamme de fréquences de modulation permettant d'observer cet effet est limitée par les propriétés photothermales de l'InP. En effet une modulation trop rapide ne laisse pas le temps à la cavité optique de thermalisée, ce qui tend à détruire l'effet thermo-optique. En perspective, cette dynamique de Floquet suggère l'utilisation d'un système optomécanique comportant plusieurs modes mécaniques. L'utilisation d'une fréquence de modulation égale à la séparation spectrale de ces modes permettrait, en régime de fort couplage optomécanique, de réaliser l'amplification paramétrique de plusieurs modes mécaniques à la fois. Cette configuration serait utile à la réalisation de portes logiques. Nous démontrons également, indépendamment des modes mécaniques du système, que la réponse bistable du résonateur optique peut être utilisée pour amplifier un signal de faible amplitude. Il

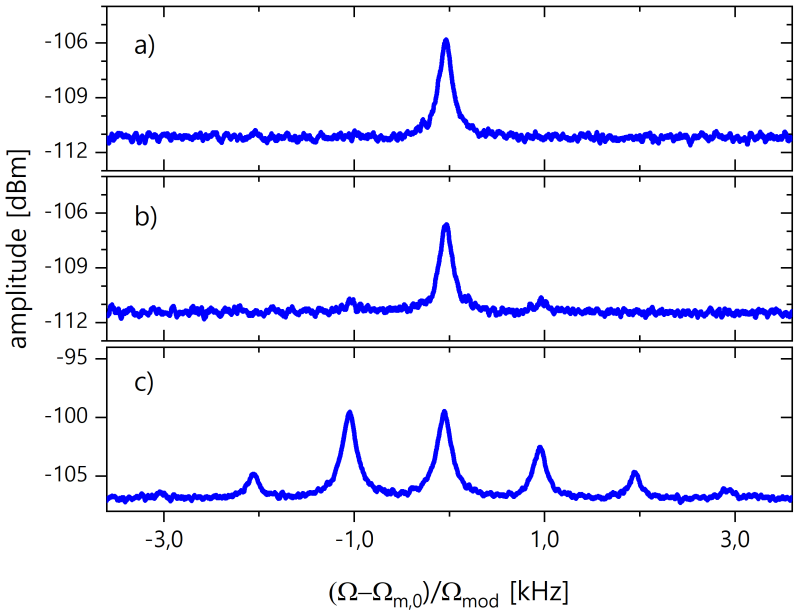

Figure 7.7 – Mesures du spectre de bruit du champ optique en sortie du dispositif optomécanique. Le mode mécanique fondamental, de fréquence $\Omega_m \approx 4.34$ MHz, est observé a) sans modulation du champ incident et à puissance optique faible, b) avec une modulation de fréquence Ω_{mod}; le peigne de modulation est transféré du domaine optique vers les modes mécaniques; et c) avec une modulation et une puissance incidente plus élevée, menant à la dyssymétrisation du peigne de modulation.

s'agit du phénomène de résonance vibrationnelle.

La seconde série d'expériences réalisées dans ce travail de thèse est basée sur la paire de membrane électromécaniques couplées mécaniquement. Ce couplage mène à une hybridization des modes de déplacement des membranes, avec deux *modes normaux*: un mode symétrique – les membranes se déplacent en phase – et un mode anti-symétrique – les membranes se déplacent en opposition de phase. Nous réalisons différentes calibrations du système dans son régime linéaire, permettant de déterminer efficacement les fréquences des structures, leur couplage, les mécanismes de pertes et la force électro-capacitive. Lorsque cette dernière passe un certain seuil, la réponse mécanique des membrane devient nonlinéaire, ce qui peut être décrit théoriquement par un modèle d'oscillateurs de Duffing couplés. L'utilisation d'une modulation cohérente de l'excitation électrique permet ici de générer une dynamique chaotique pour chacun des modes normaux. L'excitation simultanée, ou *bichromatique*, des deux modes normaux permet de synchroniser leurs réponses chaotiques. Alors que la synchronisation chaotique est bien maintenue en amplitude, les réponses en phases sont, quant à elles, imparfaitement synchronisées. On observe effectivement, on jouant avec un paramètre de contrôle (l'amplitude de la modulation) une transition d'un régime de "blocage en phase" (fig. 7.10a) vers un régime de "désynchronisation" (voir fig. 7.10a). Enfin, en dy-

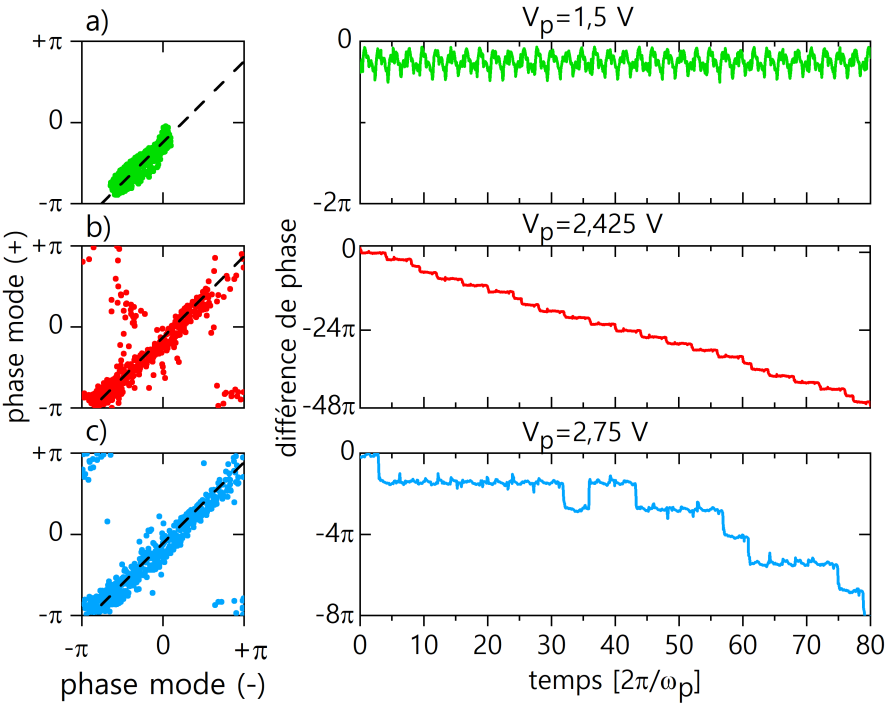

Figure 7.9 – Mesures de trois régimes dynamiques observés sur les modes normaux (-) et (+) des membranes couplées sous excitation bichromatiques (excitation simultanée des modes). Le paramètre de contrôle, l'amplitude de la modulation V_p, est augmenté de a) à c). À gauche, les portraits de phases montrant la réponse en phase du mode (+), θ^+ en fonction de celle du mode (-), θ^-. À droite: la trace temporelle de la différence de phase $\theta^+ - \theta^-$. a) régime de phase lockée, les modes sont synchronisés en phase. b) régime de désynchronisation, les modes évoluent chacun dans un régime quasipériodique. c) régime de synchronisation imparfaite, avec des dynamiques chaotiques pour chaque mode.

namique chaotique, les phases sont " imparfaitement synchronisées", c'est-à-dire qu'elles se désynchronisent de temps en temps mais irrégulièrement (fig. 7.10c). Les durées de synchronisation en phase font l'objet d'une analyse statistique permettant de prouver que ces "sauts" résultent du chaos et non du bruit présent dans les dispositifs expérimentaux: la dynamique observée est bien déterministe et non stochastique! Le chaos permet par ailleurs de générer du désordre, de l'aléatoire. Nous discutons ainsi de l'exploitation de notre dynamique de chaos bichromatique synchronisé pour généner des nombres aléatoires. Cette possibilité ouvre, en perspective, l'exploitation du mécanisme décrit ici pour de nouveaux protocoles de communication multi-spectrale.

Bibliography

Abrams, D. M. and Strogatz, S. H. (2004). Chimera States for Coupled Oscillators. *Phys. Rev. Lett.*, 93(17):174102. 3

Acebrón, J. A., Bonilla, L. L., Pérez Vicente, C. J., Ritort, F., and Spigler, R. (2005). The Kuramoto model: A simple paradigm for synchronization phenomena. *Rev. Mod. Phys.*, 77:137–185. 3, 158

Akahane, Y., Asano, T., Song, B.-S., and Noda, S. (2003). High-Q photonic nanocavity in a two-dimensional photonic crystal. *nature*, 425(6961):944–947. 23

Albrecht, T. R., Grütter, P., Horne, D., and Rugar, D. (1991). Frequency modulation detection using high-Q cantilevers for enhanced force microscope sensitivity. *Journal of Applied Physics*, 69(2):668–673. 54

Annovazzi-Lodi, V., Donati, S., and Scire, A. (1996). Synchronization of chaotic injected-laser systems and its application to optical cryptography. *IEEE Journal of Quantum Electronics*, 32(6):953–959. 160

Antoni, T., Kuhn, A. G., Briant, T., Cohadon, P.-F., Heidmann, A., Braive, R., Beveratos, A., Abram, I., Le Gratiet, L., Sagnes, I., et al. (2011). Deformable two-dimensional photonic crystal slab for cavity optomechanics. *Optics letters*, 36(17):3434–3436. 8

Antoni, T., Makles, K., Braive, R., Briant, T., Cohadon, P.-F., Sagnes, I., Robert-Philip, I., and Heidmann, A. (2012). Nonlinear mechanics with suspended nanomembranes. *EPL Europhysics Letters*, 100(6):68005. 5

Argyris, A., Syvridis, D., Larger, L., Annovazzi-Lodi, V., Colet, P., Fischer, I., García-Ojalvo, J., Mirasso, C. R., Pesquera, L., and Shore, K. A. (2005). Chaos-based communications at high bit rates using commercial fibre-optic links. *Nature*, 438(7066):343–346. 160

Ashkin, A. (1970). Acceleration and Trapping of Particles by Radiation Pressure. *Phys. Rev. Lett.*, 24(4):156–159. 5

Ashkin, A., Dziedzic, J. M., Bjorkholm, J. E., and Chu, S. (1986). Observation of a single-beam gradient force optical trap for dielectric particles. *Opt. Lett.*, 11(5):288–290. 5

Aspelmeyer, M., Kippenberg, T. J., and Marquardt, F. (2014). Cavity optomechanics. *Rev. Mod. Phys.*, 86(4):1391–1452. 5, 49, 56, 101

Atlasov, K. A., Rudra, A., Dwir, B., and Kapon, E. (2011). Large mode splitting and lasing in optimally coupled photonic-crystal microcavities. *Opt. Express*, 19(3):2619–2625. 24

Bagheri, M., Poot, M., Li, M., Pernice, W. P. H., and Tang, H. X. (2011). Dynamic manipulation of nanomechanical resonators in the high-amplitude regime and non-volatile mechanical memory operation. *Nature Nanotechnology*, 6(11):726–732. 5, 73

Bassham, L. E., Rukhin, A. L., Soto, J., Nechvatal, J. R., Smid, M. E., Barker, E. B., Leigh, S. D., Levenson, M., Vangel, M., Banks, D. L., Heckert, N. A., Dray, J. F., and Vo, S. (2010). SP 800-22 Rev. 1a. A Statistical Test Suite for Random and Pseudorandom Number Generators for Cryptographic Applications. Technical report, NIST, Gaithersburg, MD, USA. 148, 149

Bayer, M., Gutbrod, T., Reithmaier, J. P., Forchel, A., Reinecke, T. L., Knipp, P. A., Dremin, A. A., and Kulakovskii, V. D. (1998). Optical Modes in Photonic Molecules. *Phys. Rev. Lett.*, 81(12):2582–2585. 23

Blackburn, J. A., Baker, G. L., and Smith, H. J. T. (2000). Intermittent synchronization of resistively coupled chaotic Josephson junctions. *Phys. Rev. B*, 62(9):5931–5935. 143

Boccaletti, S., Kurths, J., Osipov, G., Valladares, D. L., and Zhou, C. S. (2002). The synchronization of chaotic systems. *Physics Reports*, 366(1):1–101. 141, 143

Braginski, V. and Manukin, A. (1967). Ponderomotive effects of electromagnetic radiation. *Sov. Phys. JETP*, 25(4):653–655. 5

Braginsky, V., Gorodetsky, M., and Ilchenko, V. (1989). Quality-factor and nonlinear properties of optical whispering-gallery modes. *Physics letters A*, 137(7-8):393–397. 3

Branicio, P. S., Rino, J. P., Gan, C. K., and Tsuzuki, H. (2009). Interaction potential for indium phosphide: a molecular dynamics and first-principles study of the elastic constants, generalized stacking fault and surface energies. *Journal of Physics: Condensed Matter*, 21(9):095002. 59

Brunstein, M., Braive, R., Hostein, R., Beveratos, A., Robert-Philip, I., Sagnes, I., Karle, T. J., Yacomotti, A. M., Levenson, J. A., Moreau, V., Tessier, G., and De Wilde, Y. (2009). Thermo-optical dynamics in an optically pumped Photonic Crystal nanocavity. *Opt. Express*, 17(19):17118–17129. 40, 73, 80

Bunch, J. S., van der Zande, A. M., Verbridge, S. S., Frank, I. W., Tanenbaum, D. M., Parpia, J. M., Craighead, H. G., and McEuen, P. L. (2007). Electromechanical Resonators from Graphene Sheets. *Science*, 315(5811):490–493. 53

Cepkauskas, M. M. and Jianfeng, Y. (2005). *Equivalent properties for perforated plates An analytical approach*. Atomic Energy Press, China. MATERIALS SCIENCE. 43

Chan, J., Safavi-Naeini, A. H., Hill, J. T., Meenehan, S., and Painter, O. (2012a). Optimized optomechanical crystal cavity with acoustic radiation shield. *Applied Physics Letters*, 101(8):81115. 7

Chan, J., Safavi-Naeini, A. H., Hill, J. T., Meenehan, S., and Painter, O. (2012b). Optimized optomechanical crystal cavity with acoustic radiation shield. *Applied Physics Letters*, 101(8):081115. 61

Chaste, J., Eichler, A., Moser, J., Ceballos, G., Rurali, R., and Bachtold, A. (2012). A nanomechanical mass sensor with yoctogram resolution. *Nature Nanotechnology*, 7(5):301–304. 4

Childress, L., Schmidt, M. P., Kashkanova, A. D., Brown, C. D., Harris, G. I., Aiello, A., Marquardt, F., and Harris, J. G. E. (2017). Cavity optomechanics in a levitated helium drop. *Phys. Rev. A*, 96(6):63842. 5, 6

Chizhevsky, V. N., Smeu, E., and Giacomelli, G. (2003). Experimental Evidence of "Vibrational Resonance" in an Optical System. *Phys. Rev. Lett.*, 91(22):220602. 78

Chowdhury, A. (2016). *Mechanical nonlinear dynamics of a suspended photonic crystal membrane with integrated actuation*. Phd thesis, Université Paris-Saclay. 10, 93, 120

Chowdhury, A., Barbay, S., Clerc, M. G., Robert-Philip, I., and Braive, R. (2017). Phase Stochastic Resonance in a Forced Nanoelectromechanical Membrane. *Phys. Rev. Lett.*, 119(23):234101. 5, 93

Chowdhury, A., Clerc, M. G., Barbay, S., Robert-Philip, I., and Braive, R. (2020). Weak signal enhancement by nonlinear resonance control in a forced nano-electromechanical resonator. *Nature Communications*, 11(1):2400. 5, 78, 93, 159

Chowdhury, A., Yeo, I., Tsvirkun, V., Raineri, F., Beaudoin, G., Sagnes, I., Raj, R., Robert-Philip, I., and Braive, R. (2016). Superharmonic resonances in a two-dimensional non-linear photonic-crystal nano-electro-mechanical oscillator. *Applied Physics Letters*, 108(16):163102. 93

Cleland, A. N. (2013). *Foundations of Nanomechanics: From Solid-State Theory to Device Applications*. Advanced Texts in Physics. Springer Berlin Heidelberg. 42

Clerc, M. G., Coulibaly, S., Ferré, M. A., and Rojas, R. G. (2018). Chimera states in a Duffing oscillators chain coupled to nearest neighbors. *Chaos: An Interdisciplinary Journal of Nonlinear Science*, 28(8):83126. 119, 159

Clerk, A. A., Marquardt, F., and Jacobs, K. (2008). Back-action evasion and squeezing of a mechanical resonator using a cavity detector. *New Journal of Physics*, 10(9):95010. 64

Coffey, D. S. (1998). Self-organization, complexity and chaos: The new biology for medicine. *Nature Medicine*, 4(8):882–885. 158

Cohadon, P. F., Heidmann, A., and Pinard, M. (1999). Cooling of a Mirror by Radiation Pressure. *Phys. Rev. Lett.*, 83(16):3174–3177. 5

Colombano, M. F., Arregui, G., Capuj, N. E., Pitanti, A., Maire, J., Griol, A., Garrido, B., Martinez, A., Sotomayor-Torres, C. M., and Navarro-Urrios, D. (2019). Synchronization of Optomechanical Nanobeams by Mechanical Interaction. *Phys. Rev. Lett.*, 123(1):17402. 9

COMSOL (2018). COMSOL Multiphysics (v.5.2), Solid Mechanics Module User's Guide. 43

Cuomo, K. M., Oppenheim, A. V., and Strogatz, S. H. (1993). Synchronization of Lorenz-based chaotic circuits with applications to communications. *IEEE Transactions on Circuits and Systems II: Analog and Digital Signal Processing*, 40(10):626–633. 160

Dargys, A. and Kundrotas, J. (1994). *A Brief History of Time: From the Big Bang to Black Holes*. Vilnius, Lithuania : Science and Encyclopedia Publishers, 1994, Vilnius. 87

Della Corte, F. G., Cocorullo, G., Iodice, M., and Rendina, I. (2000). Temperature dependence of the thermo-optic coefficient of InP, GaAs, and SiC from room temperature to 600 K at the wavelength of 1.5 um. *Applied Physics Letters*, 77(11):1614–1616. 39, 87

Deng, B., Wang, J., Wei, X., Tsang, K. M., and Chan, W. L. (2010). Vibrational resonance in neuron populations. *Chaos: An Interdisciplinary Journal of Nonlinear Science*, 20(1):13113. 78

Deotare, P. B., McCutcheon, M. W., Frank, I. W., Khan, M., and Lončar, M. (2009). Coupled photonic crystal nanobeam cavities. *Applied Physics Letters*, 95(3):31102. 8, 9

Dong, X., Dykman, M. I., and Chan, H. B. (2018). Strong negative nonlinear friction from induced two-phonon processes in vibrational systems. *Nature Communications*, 9(1):3241. 123

Dorsel, A., McCullen, J. D., Meystre, P., Vignes, E., and Walther, H. (1983). Optical Bistability and Mirror Confinement Induced by Radiation Pressure. *Phys. Rev. Lett.*, 51(17):1550–1553. 5

Doster, J., Hoenl, S., Lorenz, H., Paulitschke, P., and Weig, E. M. (2019). Collective dynamics of strain-coupled nanomechanical pillar resonators. *Nature Communications*, 10(1):5246. 9

Dykman, M. I., Luchinsky, D. G., Mannella, R., McClintock, P. V. E., Stein, N. D., and Stocks, N. G. (1995). Stochastic resonance in perspective. *Il Nuovo Cimento D*, 17:661–683. 77

Eckmann, J.-P., Kamphorst, S. O., Ruelle, D., and Ciliberto, S. (1986). Liapunov exponents from time series. *Physical Review A*, 34(6):4971. 171

Eichenfield, M., Chan, J., Safavi-Naeini, A. H., Vahala, K. J., and Painter, O. (2009). Modeling dispersive coupling and losses of localized optical and mechanical modes in optomechanical crystals. *Opt. Express*, 17(22):20078–20098. 61

Eichler, A., del Álamo Ruiz, M., Plaza, J. A., and Bachtold, A. (2012). Strong Coupling between Mechanical Modes in a Nanotube Resonator. *Phys. Rev. Lett.*, 109(2):25503. 9

Esmann, M., Lamberti, F. R., Harouri, A., Lanco, L., Sagnes, I., Favero, I., Aubin, G., Gomez-Carbonell, C., Lemaître, A., Krebs, O., Senellart, P., and Lanzillotti-Kimura, N. D. (2019). Brillouin scattering in hybrid optophononic Bragg micropillar resonators at 300 GHz. *Optica*, 6(7):854–859. 6

Fan, S., Suh, W., and Joannopoulos, J. D. (2003). Temporal coupled-mode theory for the Fano resonance in optical resonators. *J. Opt. Soc. Am. A*, 20(3):569–572. 25

Farace, A. and Giovannetti, V. (2012). Enhancing quantum effects via periodic modulations in optomechanical systems. *Phys. Rev. A*, 86(1):13820. 64

Faust, T., Rieger, J., Seitner, M. J., Krenn, P., Kotthaus, J. P., and Weig, E. M. (2012). Nonadiabatic Dynamics of Two Strongly Coupled Nanomechanical Resonator Modes. *Phys. Rev. Lett.*, 109(3):37205. 9

Fiderer, L. J. and Braun, D. (2018). Quantum metrology with quantum-chaotic sensors. *Nature Communications*, 9(1):1351. 160

Galayko, D. (2018). Cours 1 : bases theoriques des mems. bases de la mecanique, transduction capacitive, résonateur mécanique à paramètres localisés. 102

Gao, N., Luo, W., Yan, W., Zhang, D., and Liu, D. (2019). Continuously tuning the resonant characteristics of microcantilevers by a laser induced photothermal effect. *Journal of Physics D: Applied Physics*, 52(38):385402. 133

Gao, Y., Zhou, W., Sun, X., Tsang, H. K., and Shu, C. (2017). Cavity-enhanced thermo-optic bistability and hysteresis in a graphene-on-Si_3N_4 ring resonator. *Optics Letters*, 42(10):1950–1953. 37

Garrett, C. (1972). Tidal resonance in the Bay of Fundy and Gulf of Maine. *Nature*, 238(5365):441–443. 1

Gavartin, E., Braive, R., Sagnes, I., Arcizet, O., Beveratos, A., Kippenberg, T. J., and Robert-Philip, I. (2011). Optomechanical coupling in a two-dimensional photonic crystal defect cavity. *Physical review letters*, 106(20):203902. 8, 43

Ghorbel, I., Swiadek, F., Zhu, R., Dolfi, D., Lehoucq, G., Martin, A., Moille, G., Morvan, L., Braive, R., Combrié, S., and De Rossi, A. (2019). Optomechanical gigahertz oscillator made of a two photon absorption free piezoelectric III/V semiconductor. *APL Photonics*, 4(11):116103. 7

Glazov, V. M., K., D., Nashelskii, A. Y., and Mamedov, M. M. (1977). Ternary Alloys Based on III-V Semiconductors. *Zh. Fiz. Khim*, 51(10). 57, 59, 87

Gorodetksy, M. L., Schliesser, A., Anetsberger, G., Deleglise, S., and Kippenberg, T. J. (2010). Determination of the vacuum optomechanical coupling rate using frequency noise calibration. *Opt. Express*, 18(22):23236–23246. 49

Halioua, Y., Bazin, A., Monnier, P., Karle, T. J., Sagnes, I., Roelkens, G., Thourhout, D. V., Raineri, F., and Raj, R. (2010). III-V photonic crystal wire cavity laser on silicon wafer. *J. Opt. Soc. Am. B*, 27(10):2146–2150. 11

Hamel, P., Haddadi, S., Raineri, F., Monnier, P., Beaudoin, G., Sagnes, I., Levenson, A., and Yacomotti, A. M. (2015). Spontaneous mirror-symmetry breaking in coupled photonic-crystal nanolasers. *Nature Photonics*, 9(5):311–315. 8, 9

Hargrove, L., Fork, R. L., and Pollack, M. (1964). Locking of He–Ne laser modes induced by synchronous intracavity modulation. *Applied Physics Letters*, 5(1):4–5. 126

Hauer, B., Doolin, C., Beach, K., and Davis, J. (2013). A general procedure for thermomechanical calibration of nano/micro-mechanical resonators. 42, 58

Haus, H. A. (1984). *Waves and Fields in Optoelectronics*. Series in Solid-State Physical Electronics. Prentice Hall, 1983, hardcover edition. 25

Hegger, R. and Kantz, H. (1997). Embedding of sequences of time intervals. *Europhysics Letters ({EPL})*, 38(4):267–272. 171

Hegger, R., Kantz, H., and Schreiber, T. (1999). Practical implementation of nonlinear time series methods: The TISEAN package. *Chaos: An Interdisciplinary Journal of Nonlinear Science*, 9(2):413–435. 172

Houri, S., Asano, M., Yamaguchi, H., Yoshimura, N., Koike, Y., and Minati, L. (2020). Generic rotating-frame-based approach to chaos generation in nonlinear micro- and nanoelectromechanical system resonators. *Phys. Rev. Lett.*, 125:174301. 133

Hryniewicz, J. V., Absil, P. P., Little, B. E., Wilson, R. A., and Ho, P. . (2000). Higher order filter response in coupled microring resonators. *IEEE Photonics Technology Letters*, 12(3):320–322. 8, 9

Hsuan, H., Ajmera, R., and Lonngren, K. (1967). The nonlinear effect of altering the zeroth order density distribution of a plasma. *Applied Physics Letters*, 11(9):277–279. 119

Jang, C.-H. and Chen, R. T. (2003). Polymer-Based 1 {\texttimes} 6 Thermooptic Switch Incorporating an Elliptic TIR Waveguide Mirror. *J. Lightwave Technol.*, 21(4):1053. 81

Jin, L., Guo, Y., Ji, X., and Li, L. (2017). Reconfigurable chaos in electro-optomechanical system with negative Duffing resonators. *Scientific Reports*, 7(1):4822. 157

Joannopoulos, J. D., Johnson, S. G., Winn, J. N., and Meade, R. D. (2008). *Photonic Crystals: Molding the Flow of Light (Second Edition)*. Princeton University Press, 2 edition. 6

Joe, Y. S., Satanin, A. M., and Kim, C. S. (2006). Classical analogy of Fano resonances. *Physica Scripta*, 74(2):259–266. 108

Johnson, S. G., Ibanescu, M., Skorobogatiy, M. A., Weisberg, O., Joannopoulos, J. D., and Fink, Y. (2002). Perturbation theory for Maxwell's equations with shifting material boundaries. *Phys. Rev. E*, 65:066611. 44

Johnson, S. G., Villeneuve, P. R., Fan, S., and Joannopoulos, J. D. (2000). Linear waveguides in photonic-crystal slabs. *Phys. Rev. B*, 62:8212–8222. 7

Kantz, H. (1994). A robust method to estimate the maximal Lyapunov exponent of a time series. *Physics Letters A*, 185(1):77–87. 172

Karabalin, R. B., Cross, M. C., and Roukes, M. L. (2009). Nonlinear dynamics and chaos in two coupled nanomechanical resonators. *Phys. Rev. B*, 79:165309. 9

Kenfack, A. (2003). Bifurcation structure of two coupled periodically driven double-well Duffing oscillators. *Chaos, Solitons & Fractals*, 15(2):205–218. 3

Kirkendall, C. R. and Kwon, J. W. (2016). Multistable internal resonance in electroelastic crystals with nonlinearly coupled modes. *Scientific Reports*, 6(1):22897. 123

Kittel, C. (2005). *Introduction to Solid State Physics*. Wiley, 8th ed edition. 42

Korsch, H. J., Jodl, H.-J., and Hartmann, T. (2008). *The Duffing Oscillator*, pages 157–184. Springer. 119

Kozłowski, J., Parlitz, U., and Lauterborn, W. (1995). Bifurcation analysis of two coupled periodically driven Duffing oscillators. *Phys. Rev. E*, 51:1861–1867. 3

Kuramoto, Y. and Yamada, T. (1976). Pattern Formation in Oscillatory Chemical Reactions. *Progress of Theoretical Physics*, 56:724–740. 158

Landa, P. S. and McClintock, P. V. E. (2000). Vibrational resonance. *Journal of Physics A: Mathematical and General*, 33(45):L433—-L438. 77

Lauter, R., Brendel, C., Habraken, S. J. M., and Marquardt, F. (2015). Pattern phase diagram for two-dimensional arrays of coupled limit-cycle oscillators. *Phys. Rev. E*, 92(1):12902. 161

Lee, C. H., Yoon, T. H., and Shin, S. Y. (1985). Period doubling and chaos in a directly modulated laser diode. *Applied Physics Letters*, 46(95). 133

Li, Q., Wang, T., Su, Y., Yan, M., and Qiu, M. (2010). Coupled mode theory analysis of mode-splitting in coupled cavity system. *Opt. Express*, 18(8):8367–8382. 30

Liao, T.-L., Wan, P.-Y., and Yan, J.-J. (2019). Design of Synchronized Large-Scale Chaos Random Number Generators and Its Application to Secure Communication. *Applied Sciences*, 9(1). 150

Lifshitz, R. and Cross, M. C. (2003). Response of parametrically driven nonlinear coupled oscillators with application to micromechanical and nanomechanical resonator arrays. *Physical Review B*, 67(134302). 143

Lifshitz, R. and Cross, M. C. (2009). *Nonlinear Dynamics of Nanomechanical and Micromechanical Resonators*, chapter 1, pages 1–52. John Wiley & Sons, Ltd. 3, 120

Limonov, M. F., Rybin, M. V., Poddubny, A. N., and Kivshar, Y. S. (2017). Fano resonances in photonics. *Nature Photonics*, 11(9):543–554. 108

Lin, Q., Rosenberg, J., Chang, D., Camacho, R., Eichenfield, M., Vahala, K. J., and Painter, O. (2010). Coherent mixing of mechanical excitations in nano-optomechanical structures. *Nature Photonics*, 4(4):236–242. 9

Liu, J., Yang, H., Wang, C., Xu, K., and Xiao, J. (2016). Experimental distinction of Autler-Townes splitting from electromagnetically induced transparency using coupled mechanical oscillators system. *Scientific Reports*, 6(1):19040. 3

Lousse, V., Suh, W., Kilic, O., Kim, S., Solgaard, O., and Fan, S. (2004). Angular and polarization properties of a photonic crystal slab mirror. *Opt. Express*, 12(8):1575–1582. 7

Makles, K. (2015). *Optomechanic's photonic crystal nano-membranes*. Phd thesis, Université Pierre et Marie Curie - Paris VI. 97

Makles, K., Antoni, T., Kuhn, A. G., Deléglise, S., Briant, T., Cohadon, P.-F., Braive, R., Beaudoin, G., Pinard, L., Michel, C., Dolique, V., Flaminio, R., Cagnoli, G., Robert-Philip, I., and Heidmann, A. (2015). 2D photonic-crystal optomechanical nanoresonator. *Opt. Lett.*, 40(2):174–177. 8

Malz, D. and Nunnenkamp, A. (2016). Floquet approach to bichromatically driven cavity-optomechanical systems. *Phys. Rev. A*, 94(2):23803. 65, 166

Marconi, M., Javaloyes, J., Raineri, F., Levenson, J. A., and Yacomotti, A. M. (2016). Asymmetric mode scattering in strongly coupled photonic crystal nanolasers. *Opt. Lett.*, 41(24):5628–5631. 11

Mari, A. and Eisert, J. (2009). Gently Modulating Optomechanical Systems. *Phys. Rev. Lett.*, 103(21):213603. 64

Mason, D., Chen, J., Rossi, M., Tsaturyan, Y., and Schliesser, A. (2019). Continuous force and displacement measurement below the standard quantum limit. *Nature Physics*, 15(8):745–749. 4

Matheny, M. H., Emenheiser, J., Fon, W., Chapman, A., Salova, A., Rohden, M., Li, J., de Badyn, M., Pósfai, M., Duenas-Osorio, L., Mesbahi, M., Crutchfield, J. P., Cross, M. C., D\textquoterightSouza, R. M., and Roukes, M. L. (2019). Exotic states in a simple network of nanoelectromechanical oscillators. *Science*, 363(6431). 158

Mawhin, J. (2005). *Alexandr Mikhailovich Liapunov, The general problem of the stability of motion (1892)*, pages 664–676. Elsevier. 171

Midolo, L., Schliesser, A., and Fiore, A. (2018). Nano-opto-electro-mechanical systems. *Nature Nanotechnology*, 13(1):11–18. 156

Miles, J. (1984). Chaotic motion of a weakly nonlinear, modulated oscillator. *Proceedings of the National Academy of Sciences*, 81(12):3919–3923. 133

Miller, S. E. (1954). Coupled wave theory and waveguide applications. *The Bell System Technical Journal*, 33(3):661–719. 25

Mirasso, C. R., Colet, P., and Garcia-Fernandez, P. (1996). Synchronization of chaotic semiconductor lasers: application to encoded communications. *IEEE Photonics Technology Letters*, 8(2):299–301. 160

Miri, M.-A. and Alù, A. (2019). Exceptional points in optics and photonics. *Science*, 363(6422). 3, 160

Miri, M.-A., LiKamWa, P., and Christodoulides, D. N. (2012). Large area single-mode parity–time-symmetric laser amplifiers. *Opt. Lett.*, 37(5):764–766. 161

Mitchell, M., Khanaliloo, B., Lake, D. P., Masuda, T., Hadden, J. P., and Barclay, P. E. (2016). Single-crystal diamond low-dissipation cavity optomechanics. *Optica*, 3(9):963–970. 5, 6

Moussaid, M., Garnier, S., Theraulaz, G., and Helbing, D. (2009). Collective Information Processing and Pattern Formation in Swarms, Flocks, and Crowds. *Topics in Cognitive Science*, 1(3):469–497. 158

Mukaiyama, T., Takeda, K., Miyazaki, H., Jimba, Y., and Kuwata-Gonokami, M. (1999). Tight-Binding Photonic Molecule Modes of Resonant Bispheres. *Phys. Rev. Lett.*, 82(23):4623–4626. 23

Najer, D., Söllner, I., Sekatski, P., Dolique, V., Löbl, M. C., Riedel, D., Schott, R., Starosielec, S., Valentin, S. R., Wieck, A. D., Sangouard, N., Ludwig, A., and Warburton, R. J. (2019). A gated quantum dot strongly coupled to an optical microcavity. *Nature*, 575(7784):622–627. 4

Navarro-Urrios, D., Gomis-Bresco, J., El-Jallal, S., Oudich, M., Pitanti, A., Capuj, N., Tredicucci, A., Alzina, F., Griol, A., Pennec, Y., Djafari-Rouhani, B., Martínez, A., and Sotomayor Torres, C. M. (2014). Dynamical back-action at 5.5 GHz in a corrugated optomechanical beam. *AIP Advances*, 4(12):124601. 7

Niemczyk, T., Deppe, F., Huebl, H., Menzel, E. P., Hocke, F., Schwarz, M. J., Garcia-Ripoll, J. J., Zueco, D., Hümmer, T., Solano, E., Marx, A., and Gross, R. (2010). Circuit quantum electrodynamics in the ultrastrong-coupling regime. *Nature Physics*, 6(10):772–776. 4

Norte, R. A., Moura, J. P., and Gröblacher, S. (2016). Mechanical Resonators for Quantum Optomechanics Experiments at Room Temperature. *Phys. Rev. Lett.*, 116:147202. 8

O'Connell, A. D., Hofheinz, M., Ansmann, M., Bialczak, R. C., Lenander, M., Lucero, E., Neeley, M., Sank, D., Wang, H., Weides, M., Wenner, J., Martinis, J. M., and Cleland, A. N. (2010). Quantum ground state and single-phonon control of a mechanical resonator. *Nature*, 464(7289):697–703. 3

Okamoto, H., Gourgout, A., Chang, C.-Y., Onomitsu, K., Mahboob, I., Chang, E. Y., and Yamaguchi, H. (2013). Coherent phonon manipulation in coupled mechanical resonators. *Nature Physics*, 9(8):480–484. 4, 126

Olga, S. (2017). *Nonlinear Microwave Optomechanics*. Phd thesis, TU Delft QN. 157

Packard, N. H., Crutchfield, J. P., Farmer, J. D., and Shaw, R. S. (1980). Geometry from a Time Series. *Phys. Rev. Lett.*, 45(9):712–716. 169

Park, E.-H., Zaks, M. A., and Kurths, J. (1999). Phase synchronization in the forced lorenz system. *Phys. Rev. E*, 60:6627–6638. 143

Pelka, K., Peano, V., and Xuereb, A. (2020). Chimera states in small optomechanical arrays. *Phys. Rev. Research*, 2(1):13201. 161

Peng, B., Özdemir, b. S. K., Liertzer, M., Chen, W., Kramer, J., Y\ilmaz, H., Wiersig, J., Rotter, S., and Yang, L. (2016). Chiral modes and directional lasing at exceptional points. *Proceedings of the National Academy of Sciences*, 113(25):6845–6850. 161

Pernpeintner, M., Schmidt, P., Schwienbacher, D., Gross, R., and Huebl, H. (2018). Frequency Control and Coherent Excitation Transfer in a Nanostring-resonator Network. *Phys. Rev. Applied*, 10(3):34007. 4

Pettit, G. D. and Turner, W. J. (1965). Refractive Index of InP. *Journal of Applied Physics*, 36(6):2081. 22, 39, 87

Pikovsky, A., Rosenblum, M. G., and Kurths, J. (2001). *Synchronization, A Universal Concept in Nonlinear Sciences*. Cambridge University Press, Cambridge. 143

Pisarchik, A. N., Jaimes-Reátegui, R., and García-López, J. H. (2008). Synchronization of coupled bistable chaotic systems: experimental study. *Philosophical Transactions of the Royal Society A: Mathematical, Physical and Engineering Sciences*, 366(1864):459–473. 143

Pujol-Peré, A., Calvo, O., Matias, M. A., and Kurths, J. (2003). Experimental study of imperfect phase synchronization in the forced lorenz system. *Chaos: An Interdisciplinary Journal of Nonlinear Science*, 13(1):319–326. 143

Qiu, C., Yang, Y., Li, C., Wang, Y., Wu, K., and Chen, J. (2017). All-optical control of light on a graphene-on-silicon nitride chip using thermo-optic effect. *Scientific Reports*, 7(1):17046. 81

Qiu, L., Shomroni, I., Ioannou, M. A., Piro, N., Malz, D., Nunnenkamp, A., and Kippenberg, T. J. (2019). Floquet dynamics in the quantum measurement of mechanical motion. *Phys. Rev. A*, 100(5):53852. 64

Rabi, I. I., Zacharias, J. R., Millman, S., and Kusch, P. (1938). A New Method of Measuring Nuclear Magnetic Moment. *Phys. Rev.*, 53(4):318. 1

Rajasekar, S., Used, J., Wagemakers, A., and Sanjuan, M. A. F. (2012). Vibrational resonance in biological nonlinear maps. *Communications in Nonlinear Science and Numerical Simulation*, 17(8):3435–3445. 78

Ren, H., Matheny, M. H., MacCabe, G. S., Luo, J., Pfeifer, H., Mirhosseini, M., and Painter, O. (2020). Two-dimensional optomechanical crystal cavity with high quantum cooperativity. *Nature Communications*, 11(1):3373. 7, 8

Rodriguez, S. R. K., Casteels, W., Storme, F., Carlon Zambon, N., Sagnes, I., Le Gratiet, L., Galopin, E., Lemaître, A., Amo, A., Ciuti, C., and Bloch, J. (2017). Probing a Dissipative Phase Transition via Dynamical Optical Hysteresis. *Phys. Rev. Lett.*, 118(24):247402. 39

Rosenstein, M. T., Collins, J. J., and De Luca, C. J. (1993). A practical method for calculating largest Lyapunov exponents from small data sets. *Physica D: Nonlinear Phenomena*, 65(1-2):117–134. 171

Roy, A. and Devoret, M. (2016). Introduction to parametric amplification of quantum signals with Josephson circuits. *Comptes Rendus Physique*, 17(7):740–755. 119

Rugar, D., Budakian, R., Mamin, H. J., and Chui, B. W. (2004). Single spin detection by magnetic resonance force microscopy. *Nature*, 430(6997):329–332. 4

Russell, P. (2003). Photonic Crystal Fibers. *Science*, 299(5605):358–362. 7

Safavi-Naeini, A. H., Alegre, T. P. M., Winger, M., and Painter, O. (2010). Optomechanics in an ultrahigh-Q two-dimensional photonic crystal cavity. *Applied Physics Letters*, 97(18):181106. 7, 8

Safavi-Naeini, A. H. and Painter, O. (2010). Design of optomechanical cavities and waveguides on a simultaneous bandgap phononic-photonic crystal slab. *Opt. Express*, 18(14):14926–14943. 9

Sano, M. and Sawada, Y. (1985). Measurement of the Lyapunov Spectrum from a Chaotic Time Series. *Phys. Rev. Lett.*, 55(10):1082–1085. 171

Satpathy, S., Roy, A., and Mohapatra, A. (2012). Fano interference in classical oscillators. *European Journal of Physics*, 33(4):863–871. 2, 3

Sauvan, C., Lalanne, P., and Hugonin, J. P. (2005). Slow-wave effect and mode-profile matching in photonic crystal microcavities. *Phys. Rev. B*, 71(16):165118. 23

Schliesser, A., Rivière, R., Anetsberger, G., Arcizet, O., and Kippenberg, T. J. (2008). Resolved-sideband cooling of a micromechanical oscillator. *Nature Physics*, 4(5):415–419. 49

Sciamanna, M. and Shore, K. A. (2015). Physics and applications of laser diode chaos. *Nature Photonics*, 9:151–162. 147

Shim, S.-B., Imboden, M., and Mohanty, P. (2007). Synchronized Oscillation in Coupled Nanomechanical Oscillators. *Science*, 316(5821):95–99. 9

Shomroni, I., Youssefi, A., Sauerwein, N., Qiu, L., Seidler, P., Malz, D., Nunnenkamp, A., and Kippenberg, T. J. (2019). Two-Tone Optomechanical Instability and Its Fundamental Implications for Backaction-Evading Measurements. *Phys. Rev. X*, 9(4):41022. 64

Spreeuw, R. J. C., van Druten, N. J., Beijersbergen, M. W., Eliel, E. R., and Woerdman, J. P. (1990). Classical realization of a strongly driven two-level system. *Phys. Rev. Lett.*, 65(21):2642–2645. 3

St-Gelais, R., Bernard, S., Reinhardt, C., and Sankey, J. C. (2019). Swept-Frequency Drumhead Optomechanical Resonators. *ACS Photonics*, 6(2):525–530. 56, 109

Stambaugh, C., Xu, H., Kemiktarak, U., Taylor, J., and Lawall, J. (2015). From membrane-in-the-middle to mirror-in-the-middle with a high-reflectivity sub-wavelength grating. *Annalen der Physik*, 527(1-2):81–88. 8

Stassi, S., Chiadò, A., Calafiore, G., Palmara, G., Cabrini, S., and Ricciardi, C. (2017). Experimental evidence of Fano resonances in nanomechanical resonators. *Scientific Reports*, 7(1):1065. 108

Strogatz, S. H., Abrams, D. M., McRobie, A., Eckhardt, B., and Ott, E. (2005). Crowd synchrony on the Millennium Bridge. *Nature*, 438(7064):43–44. 158

Tagantsev, A. K., Sokolov, I. V., and Polzik, E. S. (2018). Dissipative versus dispersive coupling in quantum optomechanics: Squeezing ability and stability. *Phys. Rev. A*, 97(6):63820. 61

Tamayo, J., Kosaka, P. M., Ruz, J. J., San Paulo, Á., and Calleja, M. (2013). Biosensors based on nanomechanical systems. *Chem. Soc. Rev.*, 42(3):1287–1311. 4

Teufel, J. D., Donner, T., Li, D., Harlow, J. W., Allman, M. S., Cicak, K., Sirois, A. J., Whittaker, J. D., Lehnert, K. W., and Simmonds, R. W. (2011). Sideband cooling of micromechanical motion to the quantum ground state. *Nature*, 475(7356):359–363. 5, 6

Truitt, P. A., Hertzberg, J. B., Altunkaya, E., and Schwab, K. C. (2013). Linear and nonlinear coupling between transverse modes of a nanomechanical resonator. *Journal of Applied Physics*, 114(11):114307. 138

Tsvirkun, V. (2015). *Optomechanics in hybrid fully-integrated two-dimensional photonic crystal resonators*. Phd thesis, Universite Paris-Sud. 10, 22, 52

Tsvirkun, V., Surrente, A., Raineri, F., Beaudoin, G., Raj, R., Sagnes, I., Robert-Philip, I., and Braive, R. (2015). Integrated III-V Photonic Crystal – Si waveguide platform with tailored optomechanical coupling. *Scientific Reports*, 5(1):16526. 8, 51

Tsvirkun, V., Surrente, A., Raineri, F., Beaudoin, G., Raj, R., Sagnes, I., Robert-Philip, I., and Braive, R. (2016). External control of dissipative coupling in a heterogeneously

integrated photonic crystal—soi waveguide optomechanical system. In *Photonics*, volume 3, page 52. Multidisciplinary Digital Publishing Institute. 11, 48

Uesugi, T., Song, B.-S., Asano, T., and Noda, S. (2006). Investigation of optical nonlinearities in an ultra-high-Q Si nanocavity in a two-dimensional photonic crystal slab. *Opt. Express*, 14(1):377–386. 37

Ullner, E., Zaikin, A., Garcia-Ojalvo, J., Bascones, R., and Kurths, J. (2003). Vibrational resonance and vibrational propagation in excitable systems. *Physics Letters A*, 312(5):348–354. 78

Unterreithmeier, Q. P., Weig, E. M., and Kotthaus, J. P. (2009). Universal transduction scheme for nanomechanical systems based on dielectric forces. *Nature*, 458(7241):1001–1004. 103

Vahala, K. J. (2003). Optical microcavities. *Nature*, 424(6950):839–846. 7

Venstra, W. J., Capener, M. J., and Elliott, S. R. (2014). Nanomechanical gas sensing with nonlinear resonant cantilevers. *Nanotechnology*, 25(42):425501. 5

Verhagen, E., Deléglise, S., Weis, S., Schliesser, A., and Kippenberg, T. J. (2012). Quantum-coherent coupling of a mechanical oscillator to an optical cavity mode. *Nature*, 482(7383):63–67. 5, 6

Volodchenko, K. V., Ivanov, V. N., Gong, S.-H., Choi, M., Park, Y.-J., and Kim, C.-M. (2001). Phase synchronization in coupled nd:yag lasers. *Opt. Lett.*, 26(18):1406–1408. 143

Wang, D.-Y., Bai, C.-H., Wang, H.-F., Zhu, A.-D., and Zhang, S. (2016). Steady-state mechanical squeezing in a double-cavity optomechanical system. *Scientific Reports*, 6(1):38559. 157

Weiss, T. and Nunnenkamp, A. (2013). Quantum limit of laser cooling in dispersively and dissipatively coupled optomechanical systems. *Phys. Rev. A*, 88(2):23850. 61

Wiersig, J. (2014). Enhancing the Sensitivity of Frequency and Energy Splitting Detection by Using Exceptional Points: Application to Microcavity Sensors for Single-Particle Detection. *Phys. Rev. Lett.*, 112(20):203901. 161

Wirkus, S. and Rand, R. (2002). The dynamics of two coupled van der Pol oscillators with delay coupling. *Nonlinear Dynamics*, 30(3):205–221. 3

Wolf, A., Swift, J. B., Swinney, H. L., and Vastano, J. A. (1985). Determining Lyapunov exponents from a time series. *Physica D: Nonlinear Phenomena*, 16(3):285–317. 171

Wu, M., Hryciw, A. C., Healey, C., Lake, D. P., Jayakumar, H., Freeman, M. R., Davis, J. P., and Barclay, P. E. (2014). Dissipative and dispersive optomechanics in a nanocavity torque sensor. *Physical Review X*. 51

Wu, M., Wu, N. L.-Y., Firdous, T., Fani Sani, F., Losby, J. E., Freeman, M. R., and Barclay, P. E. (2017). Nanocavity optomechanical torque magnetometry and radiofrequency susceptometry. *Nature Nanotechnology*, 12(2):127–131. 4

Yang, W., Gerke, S. A., Ng, K. W., Rao, Y., Chase, C., and Chang-Hasnain, C. J. (2015). Laser optomechanics. *Scientific Reports*, 5(1):13700. 8

Yariv, A. (1965). Internal Modulation in Multimode Laser Oscillators. *Journal of Applied Physics*, 36(2):388–391. 126

Yeo, I., de Assis, P.-L., Gloppe, A., Dupont-Ferrier, E., Verlot, P., Malik, N. S., Dupuy, E., Claudon, J., Gérard, J.-M., Auffèves, A., Nogues, G., Seidelin, S., Poizat, J.-P., Arcizet, O., and Richard, M. (2014). Strain-mediated coupling in a quantum dot–mechanical oscillator hybrid system. *Nature Nanotechnology*, 9(2):106–110. 4

Zaikin, A. A., López, L., Baltanás, J. P., Kurths, J., and Sanjuán, M. A. F. (2002). Vibrational resonance in a noise-induced structure. *Phys. Rev. E*, 66(1):11106. 78

Zaks, M. A., Park, E.-H., Rosenblum, M. G., and Kurths, J. (1999). Alternating locking ratios in imperfect phase synchronization. *Phys. Rev. Lett.*, 82:4228–4231. 143

Zanette, D. H. (2018). Energy exchange between coupled mechanical oscillators: linear regimes. *Journal of Physics Communications*, 2(9):95015. 94

Zanotto, S. (2018). *Weak Coupling, Strong Coupling, Critical Coupling and Fano Resonances: A Unifying Vision*, chapter 23, pages 551–570. Springer International Publishing, Cham. 95

Zhang, M., Wiederhecker, G. S., Manipatruni, S., Barnard, A., McEuen, P., and Lipson, M. (2012). Synchronization of micromechanical oscillators using light. *Physical Review Letters*. 9

Zhang, W.-M., Hu, K.-M., Peng, Z.-K., and Meng, G. (2015). Tunable micro- and nanomechanical resonators. *Sensors (Basel, Switzerland)*, 15(10):26478–26566. 4, 108


C2N


université
PARIS-SACLAY


NanoSaclay
Laboratoire d'Excellence
en Nanosciences et Nanotechnologies

université PARIS-SACLAY | ÉCOLE DOCTORALE Ondes et matière (EDOM)

Title: Coherent modulation in coupled electro-optomechanical photonic crystal resonators: Floquet dynamics and chaos

Keywords: optomechanics, nanophotonics, photonic crystals, nonlinear dynamics

Abstract: Nanomechanical systems are useful to inspect some fundamental aspects of physics such as the relations between the elastic, thermal and electromagnetic properties of solid-state objects. When interacting with an optical cavity or coupled to an electrostatic actuator, these systems can be studied in the wide topic of electro-optomechanics. This work takes advantage of photonic crystal versatility to investigate the nonlinear optical and mechanical dynamics of such electro- or optomechanical systems under coherent modulation.

The first experiment uses a nanophotonic platform combining a suspended InP membrane and an integrated underneath silicon waveguide. The membrane is etched with a 2D photonic molecule whose electromagnetic eigenmodes can be driven with a laser thus enabling a sensitive access to the mechanical noise spectrum of the membrane. Using a coherent modulation of the input laser field, we show how the input modulation comb is transferred to the mechanical frequency domain via the optomechanical interactions. The presence of thermo-optic nonlinearities further leads to a desymmetrization of this modulation comb, thus suggesting the use of modulation to parametrically amplify and even synchronize several mechanical modes. The experiment is described theoretically via Floquet theory. Relying on thermo-optic bistability, a bistable photonic mode is finally used to amplify a small signal by vibrational resonance.

In a second part, we study two mechanically coupled electro-optomechanical nanocavities. The bistable mechanical responses evidence the strong intrinsic Duffing nonlinearities of the material. In this context, the use of coherent modulation of the input force interestingly reveals a period-doubling cascade route to chaos. The simultaneous excitation of both normal modes in their nonlinear regime allows them to couple such that their responses, although chaotic, can synchronize. As chaotic systems can be used to generate random numbers, this bichromatic synchronized chaotic dynamics could be exploited in novel multispectral data encryption protocols.

This work open the way toward the exploration of large optomechanical arrays, in which collective dynamics could be studied.

Université Paris-Saclay
Espace Technologique / Immeuble Discovery
Route de l'Orme aux Merisiers RD 128 / 91190 Saint-Aubin, France

université PARIS-SACLAY | ÉCOLE DOCTORALE Ondes et matière (EDOM)

Titre: Modulation cohérente dans des résonateurs couplés électro-optomécaniques à cristal photonique: dynamique de Floquet et chaos

Mots clés: optomécanique, nano-photonique, cristaux photoniques, dynamique non-linéaire

Abstract: Les systèmes nanomécaniques permettent d'explorer les relations physiques fondamentales entre les propriétés élastiques, thermiques et électromagnétiques des solides. Mis en interaction avec une cavité optique ou couplés à des actuations électrostatiques, ils peuvent être étudiées dans le cadre de l'électro-optomécanique. Dans ce travail de thèse nous mettons à profit la versatilité des cristaux photoniques pour étudier la dynamique non linéaire optique et mécanique induite par la modulation cohérente de l'excitation appliquée à des systèmes électromécaniques ou optomécaniques.

Dans un premier temps nous utilisons une plateforme nanophotonique combinant une membrane d'InP suspendue au-dessus d'un guide de silicium intégré. La membrane comprend une molécule à cristal photonique dont les modes électromagnétiques peuvent être sondés par un laser, permettant ainsi d'accéder au spectre de bruit mécanique de la membrane. Nous démontrons, via l'utilisation d'une modulation cohérente du champ optique, le transfert des bandes de modulations depuis le domaine optique vers le domaine fréquentiel mécanique. La présence de nonlinéarités thermo-optiques dans le système mène à une désymétrisation du peigne de modulation, suggérant l'utilisation de la modulation pour amplifier, voire synchroniser, plusieurs modes mécaniques. Finalement, en se plaçant dans un régime de bistabilité thermo-optique, nous démontrons l'amplification d'un signal de faible amplitude dans un mode photonique par résonance vibrationnelle.

Dans une seconde partie, nous étudions deux membranes couplées entre elles mécaniquement. Les fortes nonlinéarités Duffing du matériau se manifestent par de larges bistabilités dans la réponse mécanique. Dans ce cas l'utilisation d'une modulation cohérente de l'excitation induit une dynamique de route vers le chaos par doublement de périodes. L'excitation simultanée de deux modes mécaniques dans leur régime non linéaire leur permet de se coupler de telle sortes que leurs réponses, bien que chaotiques, se synchronisent. Le chaos pouvant être exploiter pour générer des nombres aléatoires, cette synchronisation chaotique bichromatique pourrait servir à développer de nouveaux protocoles de communication multi-spectrale.

En perspective, ce travail ouvre notamment la voie à l'étude de la dynamique collective dans de plus larges réseaux de systèmes optomécaniques.

Université Paris-Saclay
Espace Technologique / Immeuble Discovery
Route de l'Orme aux Merisiers RD 128 / 91190 Saint-Aubin, France